SILICON NANOSTRUCTURES FOR ELECTRO-OPTICAL AND PHOTOVOLTAIC APPLICATIONS

A THESIS SUBMITTED TO
THE GRADUATE SCHOOL OF NATURAL AND APPLIED SCIENCES
OF
MIDDLE EAST TECHNICAL UNIVERSITY

BY

MUSTAFA KULAKCI

IN PARTIAL FULFILLMENT OF THE REQUIREMENTS
FOR
THE DEGREE OF DOCTOR OF PHILOSOPHY
IN
PHYSICS

FEBRUARY 2012

Approval of the thesis:

SILICON NANOSTRUCTURES FOR ELECTRO-OPTICAL AND PHOTOVOLTAIC APPLICATIONS

Submitted by **Mustafa KULAKCI** in partial fulfillment of the requirements for the degree of **Doctor of Philosophy in Physics Department, Middle East Technical University** by,

Prof. Dr. Canan Özgen _____
Dean, Graduate School of **Natural and Applied Sciences**

Prof. Dr. Mehmet T. Zeyrek _____
Head of Department, **Physics, METU**

Prof. Dr. Raşit Turan _____
Supervisor, **Department of Physics, METU**

Examining Committee Members:

Assoc. Prof. Dr. Ceyhun Bulutay _____
Department of Physics, Bilkent University

Prof. Dr. Raşit Turan _____
Department of Physics, METU

Assoc. Prof. Dr. Uğur Serincan _____
Department of Physics, Anadolu University

Assoc. Prof. Dr. Hakan Altan _____
Department of Physics, METU

Assist. Prof. Dr. Alpan Bek _____
Department of Physics, METU

Date: 20.02.2012

I hereby declare that all information in this document has been obtained and presented in accordance with academic rules and ethical conduct. I also declare that, as required by these rules and conduct, I have fully cited and referenced all material and results that are not original to this work.

Name, Last name : Mustafa KULAKCI

Signature :

ABSTRACT

SILICON NANOSTRUCTURES FOR ELECTRO-OPTICAL AND PHOTOVOLTAIC APPLICATIONS

KULAKCI, Mustafa

Doctor of Philosophy, Department of Physics

Supervisor: Prof. Dr. Raşit TURAN

February 2012, 221 pages

Recently extensive efforts have been spent in order to achieve all silicon based photonic devices exploiting the efficient light emission from nanostructured silicon systems. In this thesis, silicon based nanostructures have been investigated for electro-optical and photovoltaic applications. The thesis focused on three application areas of silicon nanostructures: Light emitting diode (LED), light modulation using quantum confined Stark effect (QCSE) and photovoltaic applications.

In the context of LED applications, ZnO nanocrystal/silicon heterojunctions were investigated. Contrary to observation of pure ultraviolet photoluminescence (PL) from ZnO nanocrystals that were synthesized through vapor liquid solidification (VLS) method, visible emissions were observed in the electroluminescence (EL) due to defect states of ZnO. The discrepancy between these emissions could be ascribed to both change in excitation mechanisms and the defect formation on ZnO nanocrystals surface during device fabrication steps. EL properties of silicon nanocrystals embedded in SiO_2 matrix were also systematically studied with and without Tb doping. Turn-on voltage of the Tb doped LED structures was reduced below 10 V for the first time.

Clear observation of QCSE has been demonstrated for the first time in Si nanocrystals embedded in SiO_2 through systematic PL measurements under external

electric field. Temperature and size dependence of QCSE measurements were consistently supported by our theoretical calculations using linear combination of bulk Bloch bands (LCBB) as the expansion basis. We have managed to modulate the exciton energy as high as 80 meV with field strength below MV/cm. Our study could be a starting point for fabrication of electro-optical modulators in futures for all silicon based photonic applications.

In the last part of the thesis, formation kinetics of silicon nanowires arrays using a solution based novel technique called as metal assisted etching (MAE) has been systematically studied over large area silicon wafers. In parametric studies good control over nanowire formation was provided. Silicon nanowires were tested as an antireflective layer for industrial size solar cell applications. It was shown that with further improvements in surface passivation and contact formation, silicon nanowires could be utilized in very efficient silicon solar cells.

***Keywords*:** Silicon nanocrystal, silicon nanowire, LED, QCSE, solar cell

ÖZ

SİLİSYUM NANOYAPILARIN OPTO-ELEKTRONİK VE FOTOVOLTAİK UYGULAMALARI

KULAKCI, Mustafa
Doktora, Fizik Bölümü
Tez Yöneticisi: Prof. Dr. Raşit TURAN

Şubat 2012, 221 sayfa

Son zamanlarda, nanoyapılı silisyumun etkin ışımasını kullanarak, tamamı silisyum tabanlı fotonik aygıt geliştirmek için çok büyük çaba sarfedilmektedir. Bu tez çalışmasında, silisyum nanoyapılar elektro-optik ve fotovoltaik uygulamalar için incelenmiştir. Tez silisyum tabanlı nanoyapıların üç temel uygulama alanı üzerine yoğunlaşmıştır. Bunlar: Işık yayan diyotlar (LED), kuvantum sınırlandırılmış Stark etkisini (KSSE) kullanarak ışık modulasyonu ve fotovoltaik uygulamalrdır.

LED uygulamaları kapsamında: ZnO nanokristal/silisyum farklı eklemler incelenmiştir. Buhar sıvı katılaştırma yöntemiyle üretilen ZnO nanokristallerden fotolüminesans ölçümlerinde saf UV ışıma elde edilmesine karşın, LED lerden gelen ışımaların görünür bölgede ZnO kusurlarından kaynaklandığı gözlemlenmiştir. Bu iki ışıma arasındaki farkın nedeninin hem uyarma mekanizması ve hemde aygıt fabrikasyonu sırasında nanokristal yüzeyinde oluşan kusurlardan kaynaklandığı anlaşılmıştır. LED çalışması kapsamında ayrıca SiO_2 içine gömülmüş silisyum nanokristallerin katkısız ve Tb katkılı olarak elektrolüminesansları detaylı olarak incelenmiştir. Işıma başlama gerilimi SiO_2 içine gömülü Tb katkılı yapılarda ilk defa 10 voltun altına indirilebilmiştir.

Bu tez kapsamında ayrıca, SiO_2 içerisinde oluşturulmuş silisyum nanokristallerde ilk defa KKSE bariz bir şekilde fatolüminesans tekniğiyle gözlemlenmiş ve rapor edilmiştir. KSSE etkisi sıcaklık ve nanokristal büyüklüğüne gore incelenmiş ve deneysel bulgular teorik hesağlarla bire bir uyumlu şekilde desteklenmiştir. Teorik hesaplarda Kristal Bloch bandlarının doğrusal birleşimi açma bazı olarak alınmıştır. Yapılan ölçümlerde ekziton enerjisi elektrik-alan altında 80 meV kadar module edilebilmiştir. Bizim bu çalışmamız geleceğin silisyum tabanlı fotonik uygulamaları için gerekli elektro-optik modülatörleri için önemli bir başlangıç oluşturmaktadır.

Tezin son bölümünde, yeni bir teknik olan metal yardımlı kazıma (MYK) yöntemiyle silisyum nanotellerin oluşum kinetiği büyük alan silisyum yongalar üzerinde sistematik bir şekilde çalışılmıştır. Detaylı çalışmalar sonucunda nanotel oluşturma üzerine çok iyi control sağlanmıştır. Üretilen silisyum nanoteller endüstriyel ölçekte güneş gözesi uygulamalrı için test edilmiştir. Nanotellerin silisyum tabanlı güneş gözelerinde etkin bir şekilde kullanılabilmesi için nanotellerin yüzeyinin çok iyi pasifize edilmesi ve ön kontak yapısının iyileştirilmesi gerektiği anlaşılmıştır.

Anahtar kelimeler: Silisyum nanokristal, silisyum nanotel, LED, KSSE, güneş gözesi

To my family, to the memory of my uncle Kerim Mermi and to the memories of my grand parents Fazli Mermi and Ayse Mermi

ACKNOWLEDGEMENT

First of all, I would like to give a very special thank you to my supervisor Dr. Raşit Turan for giving me the opportunity to work with you, giving financial support and especially giving the freedom in my studies that I could not find anywhere. I owe my deepest gratitude to Dr. Ceyhun Bulutay for his endless support during my PhD. Studies. I am also very grateful to the examining committee members Dr. Hakan Altan, Dr. Uğur Serincan and Dr. Alpan Bek for their valuable comments along in this thesis. And I am also very grateful to Dr. Mehmet Parlak, who always was with me in my diffucult days, his invaluable moral supports always gave me good feelings when I was in trouble. I would like to thank Harun Tanık and Dr. Nader Asghar Pour Moghaddam for their good friendship and their encouragements.

During my life that was constrained in the basement of the physics department at METU, I spent good days with several dearest friends whose memories will always be with me. Therefore I need to single out them: technician Yücel Eke, Fazlı Çağrı Mermi, Dr. Uğur Serincan, Dr. Bülent Aslan, Dr.Tahir Çolakoğlu, Umut Bostancı, Dr. Murat Kaleli, Dr. Hakan Karaağaç, Barış Özdemir, Fırat Es, Mehmet Karaman, Olgu Demircioğlu, Yasin Ergunt, Kutlu Kutluer, İlker Doğan, İlker Yıldız, Seçkin Öztürk, Sedat Canlı, from VAKSİS company: Mehmet Emre Kabadayı, Urcan Güler, Dr. Selçuk Yerci, Arif Sinan Alagöz, technician Nevzat Görmez, technician Tayfun Demir, technician Dursun Erdoğan, Hasan Hüseyin Güllü, İdris Candan, Hayrettin Un, İsmail Kabaçelik, Hisham Nasser and finally Engin Özkol. I could not draw a border between them. However, Fazlı Çağrı Mermi, Yücel Eke, Tahir Çolakoğlu and Uğur Serincan were the four special close friends for me throughout in my basement life; I could not describe my feelings with any words towards them. Together with Uğur Serincan, I would also like to thank thanks Bülent Aslan again for making me feeling valuable, I do not know whether I deserve their positive attitudes towards me.

I also want to give my thanks to my lab-mates, old colleagues and friends for spending good times with them, Mustafa Arıkan, Dr. Tacettin Kuru, Dr. Ali Murat

Ceyhan, Adem Yenisoy, Şahin Coşkun, Can Koral, Dr. Yusuf Selim Ocak, rahmetli Oben Sezer, Dr. Tunay Tansel, Özgür Selimoğlu, Dr. Mustafa Anutgan, Dr. İsmail Atılgan, Dr. Bayram Katırcıoğlu, technician Mustafa Yıldırım, Dr. Kadir Gökşen, Nuh Sadi Yüksek, Dr. Levent Kurt, Dr. Koray Yılmaz, Sedat Bekir Yıldırım, Dr. Münir Dede, Dr. Terje Finstad, Savaş Ulucan, Koray Ürkmen, Turhan Uçar, from NUROL company Erdem Katı, Nejdet Kurşun, Mustafa Çubuk, Yalçın İslamzade, Nihat Kurşun, members of VAKSİS company: Sadık Yenilmez, Murat Güney, Durmuş Sakcı, Gökhan Doğan, Dr. Baybars Oral and I also want to thank all members of our goat flock over the twenty years that I spent during my vacations with them in the mountains of my village.

The author devotes his special thanks to the three little special people who gave him an opportunity of reflecting his childish side while spending time with them in the basement of the physics department. The son of Dr. Mehmet Parlak **Sarp Parlak,** the son of our technician Tayfun Demir **Metehan Demir** and to the pretty lovely girl; **Deniz Eke** the daughter of our generous technician Yücel Eke. I still keep my first special agreement with this little girl Deniz Eke that was signed by me, her, and her father. Under the assignment; during the preparation time to the qualifying exam, she woke me up at 8.30 and got a big pocket of chocolate every morning. Now this job was substituted by my dearest friend Fırat Es, for just a few nuts, but when I look at the past that little girl was more successful than him.

And finally the deepest and special thanks go to my family; my parents Teslime and Bayram, my sisters Esin and Elif, my brother Erkan and his wife Hilal, my nephew Ahmet Kerim, my aunts and their family, my Uncles Kerim Mermi and Süleyman Kulakcı and their family.

TABLE OF CONTENTS

LIST OF TABLES

LIST OF FIGURES

CHAPTER 1

INTRODUCTION

"Nanostructured Silicon opens a new era in silicon based electro optical and photovoltaic devices"

"Who dominates materials dominates technology"

Dr. Sekimoto

1.1. Silicon; Technology and Current Status

Since the invention of the first semiconductor transistor in 1947 at Bell Labs, the semiconductor industry has grown incredibly. Even though the first semiconductor transistor was made from germanium (Ge), silicon (Si) became the material of choice due to the low melting point of Ge that limits high temperature processes and the lack of a natural occurring germanium oxide for the formation of a highly isolating dielectric for complementary large area planar circuitry.

Silicon is the primary material in today's microelectronic and photovoltaic technology. The current level of knowledge of Si properties and the sophistication of Si technology are impressive. Ultrapure single crystal Si can be grown in mass production almost dislocation free up to several tens of centimeters in diameter, no other semiconductor material can support these features. Furthermore, it is the second most abundant element in the earth crust after oxygen, nonpolluting and economically feasible and retains its semiconducting properties in a wide temperature range. In the last 60 years, our modern life and changing cultures have directly been shaped by innumerable products of Si integrated circuits whose performance dramatically increase with exponential decrease in the manufacturing cost.

There is an almost exponential progress in the complexity of Si integrated circuits, which directly imply the increasing number of transistors per unit area with scaling down of individual transistor. Scaling is the engine of progress in micro-electronic technology generating more powerful chips with reasonable price and sustained only by the intense research and development [1]. However, there is an expectation of the problem "interconnect bottleneck" in the horizon as the number of transistors in integrated circuits (IC) increases, more and more metallic interconnect lines are required to link each component to the network of other components (the ICs today are made of several tens of kilometers of metallic wiring already) [2]. Signaling along these complex wiring consumes significant power as resistive heating and causes major delay in today's modern Si chips. Moreover, with further scaling, RC charging delays in the wires will dominate the performance of the coming future microelectronic circuitry. In the past, the problems of wiring that threaten the chip performance were overcome by replacing only the interconnect material. The replacement of the resistive aluminum wiring with more conductive copper lines would be a solution to this problem. However, since the copper is a very diffusive material in Si matrix, it is hard to prevent shorting with further scaling down of the integrated elements. One of the big efforts of the microelectronic industry in recent years has been to find a reliable barrier layer to prevent copper diffusion and adaptation of these layers into the existing production line in an effective manner.

To sustain ongoing progress in microelectronic industry and find an ultimate solution to the interconnect problem, optical interconnect schemes have been proposed to replace copper wirings both in- and inter-chip signal processing [3,4] . Although the introduction and integration of photonics elements into the very mature and sophisticated electronic technologies will bring out new challenging problems, it is worth facing them as the optical interconnection offers very attractive potential benefits like the elimination of RC delays and cross talks between inter-connecting lines, reducing power dissipation during signal processing etc. For the realization of optical interconnections, stable light sources (especially lasers), photo detectors, low loss planar optical wave guides and electro optical modulators with a high contrast

ratio will be necessary [3]. In addition, the additional cost of the integration should be at an acceptable level.

In a macroscopic scale, data transfer rates of optical fiber networks have been improved dramatically over the last few decades and reached a quality which is much superior than the metallic counterparts. The optical networks stretch between continent, cities and down to computers and in some special cases chip to chip. However, the connected photonic components are still typically packaged separately. The establishment and integration of photonic components into the Si complementary metal oxide semiconductor (Si-CMOS) electronic platform of future chips requires not only the compact miniaturization of photonic elements but also integration to the current Si platform without drastic changes in the existing electronic fabrication processes. If optical interconnects become feasible for scaling progression in micro/nano electronics, an enormous development will be seen in the integrated photonic-electronic circuit technology. As a result, new devices for the high density optical system will open a road for quantum computation which will be a new era in computer sciences. Considering the historical development of the electronic industry from vacuum tubes to present technology, this dream seems not far from the horizon.

Nowadays there are two distinct routes that have been followed separately to develop, improve and utilize Si photonics for the realization of reliable cost effective devices of the future. The first one is the hybrid incorporation of the III/V semiconducting materials in to the Si-CMOS platform [5, 6]. The reliability, speed and high efficiency of III/V compound semiconductors have been proved in the optoelectronic area and large number of practical devices based on these materials has already been used in either domestic, space or military applications. However, until now, the reliability and compatibility of hybrid integration of optical interconnect systems are quite far from realization in practical applications. The difficulties mainly come from fabrication of III/V optical devices on Si substrate due to high lattice mismatch between host and guest material, where the optical active devices are very sensitive to the defects generated by lattice mismatch [3]. The other difficulty is that the Si chip production requires several high temperature treatment

cycles under which III/V materials face serious deteriorations leading to functional losses. Moreover, as the Si-CMOS and III/V materials require different production techniques, the cost of the fabrication becomes very expensive.

With these difficulties in the hybrid technology, solutions that are based on Si based materials, where the photonic components are made of Si devices, have become very attractive. To achieve monolithically integrated all Si based photonics, several optoelectronic devices such as light emitting diodes (LED), lasers or modulators have already been demonstrated. However, they are far from realistic practical applications due to their inefficient and/or unreliable operations. Over the years, huge efforts has been dedicated to overcome these problems for practical Si based photonic device applications and to understand theoretical background of these structure. Along with the research efforts on the development of basic Si based components, there have been diversely branched research interests to integrate them to the CMOS environment. One of the approaches to obtain photonic components is based on the band gap and band structure engineering through SiGe strained materials or Si-Ge quantum wells and super lattices [7-9]. Using Si itself is another approach to build light emitting devices. In these attempts, although it is not sufficiently efficient, the band gap recombination has been demonstrated in both p-n junction and in a simpler form of MOS like hetero-junctions with transparent conductive oxides [10-12]. The most astonishing achievement in pure Si has been the laser emission through the Raman Effect [13, 14]. In this laser type, the light emission does not depend on the recombination of electron hole pairs. The laser operation directly depends on Raman scattering of sub wave length pump laser light with Si phonons and the required population inversion occurs in excited virtual phonon states. However, the requirement of an intense optical pump for lasing leads to significant number of two photon absorption and carrier excitation into the conduction band and the laser performance is reduced by free carrier absorption. Therefore Raman laser is far from practical applications in Si optical interconnect technology which strongly requires electrical pumping for population inversion and modulation. Recently, dispersion of Rare Earth (RE) elements into Si environment has become another route in the Si based photonic research [15-17]. In this approach, instead of Si, light emission originates directly from RE element’s atomic transitions.

Depending on the type of the added RE (Tb, Er, Gd, Yb etc.), the wavelength of emitted light can span a range between ultraviolet to infrared. RE elements can be either directly dispersed in Si substrate or dispersed in stochiometric/un-stochiometric SiO_2, Si_3N_4 etc. on the Si substrates. The strategy of inclusion of RE into Si environment is compatible with the CMOS production line and could find a place in a practical applications. Efficient Si based LED devices exploiting RE atomic emission have already been demonstrated in several studies and it is expected that numerous domestic applications like full color displays/micro displays, lab on chip diagnostic devices and even electrically driven Si based lasers will flourish in near future.

However, over the last twenty years, light emission from Si nanocrystals has been the most remarkable potential candidate for Si photonic applications. Quantum mechanical effects bring out new phenomena leading to efficient and tunable light emission from nanostructured Si. In this thesis, a new approach coupling RE to Si nanocrystals has been studied extensively.

1.2. Silicon nanocrystals

Contrary to its superior electronic properties that govern today's current technology, Si is a very poor material in optical properties especially in light emission. The main limitation of Si as a light emitter is directly related to its energy band structure i.e. to the indirect band gap structure of Si. Either light absorption or emission requires higher order processes i.e. optical transitions that take place with at least one phonon involvement to satisfy energy and momentum conservations which is seriously hampering light emission/absorption. As seen in Figure 1.1. the bottom of the conduction band is displaced in k (momentum) space relative to the top of the valence band. As the indirect transitions require simultaneous phonon absorption or emission to compensate momentum difference between the extremum of the bands, the probability of radiative recombinations is much less than that of the non-radiative recombinations. The necessity of phonon coupling results in a very long spontaneous radiative life time (around ms) compared to fast non-radiative channels (ns or less), i.e. this huge difference results in very low internal quantum efficiency and prevents

the Si from being a light emitting material. The internal quantum efficiency of radiative recombination is around 10^{-6} for Si.

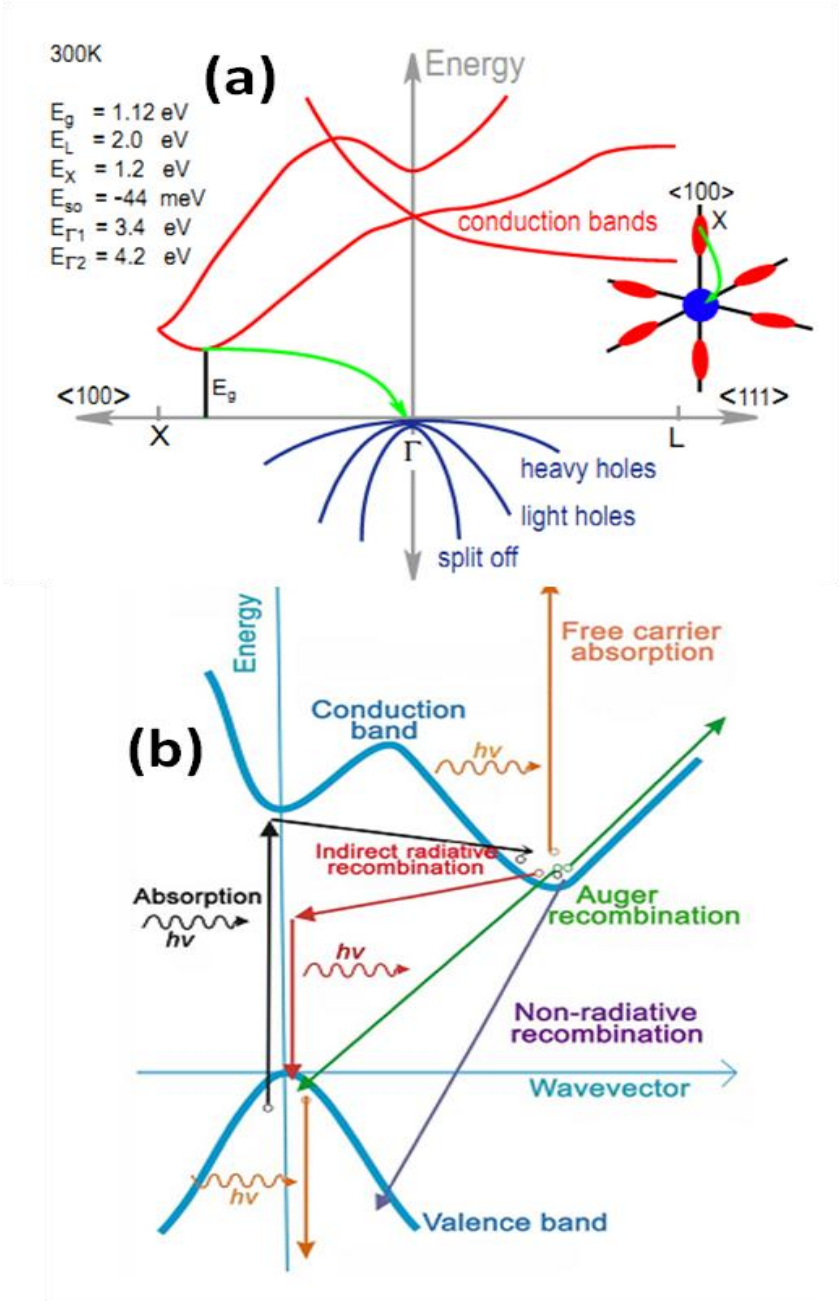

Figure 1.1. (a) Representative energy band structure of Si in momentum space in the Brilloine zone. The energy gap is indirect with lowest value 1.12 eV at room temperature in <100> direction at around X point. There are six equivalent conduction bands with ellipsoidal constant energy surface in ±x, ±y, ±z directions. (b) Schematic illustration of various absorption and recombination paths occurring in Si [18,19]**.**

This fundamental physical obstacle, that prevents Si from being a luminescent material was overcome at the beginning of nineties with the observation of intense photo luminescence (PL) from electrochemically etched Si done by Canham [20]. The new structures were called porous Si and opened a new era in photonic research and a new terminology has been added to literature as Si photonics or Si micro- and nano-photonics. The pioneering work of Canham's has excited most of the scientists and engineers over the world for the realization of the big utopia of science; ***"Si light emitters"***. With this excitement more than 10000 scientific papers have been published on both porous Si and Si nanostructures buried in a dielectric matrix that try to understand light emission mechanisms and exploit them for practical device applications.

Following the pioneering work of Canham on porous nanostructured Si, the synthesis of Si nanocrystals within a different insulating matrix has been accomplished. It was later recognized that, porous Si is not stable in time due to its active unpassivated surface; the high energetic surface makes nanostructured porous Si susceptible to the environment resulting in either partial or total oxidation of nanocrystals and/or adsorption of water molecules on the surface. Moreover porous nanostructures are very brittle to handle and this causes difficulties in further processes like device fabrication and characterization. On the other hand, Si nanocrystals produced in an insulating matrix by phase separation of excess Si inclusion through high temperature annealing process offers more stable and robust material systems for applications. Several types of matrices have been chosen for nanocrystal encapsulation: SiO_2, Si_3N_4, SiC, Al_2O_3 etc. [21-24]. Among these, SiO_2 has been found the most suitable matrix for nanocrystal formation. Si nanocrystals distributed in SiO_2 synthesized via annealing of Si rich SiO_2 above 900 ^{c}C has been produced by these methods: ion implantation, sputtering, plasma enhanced chemical vapor deposition, laser ablation, thermal evaporation etc. [25-29]. The excess Si concentration, duration and temperature of annealing treatment determine the size and crystallinity of the nanocrystals. Both electrical and optical properties of nanocrystals are directly determined by those production parameters. One of the curial concerns is the uniformity of the size of nanocrystals that are scattered in the matrix.

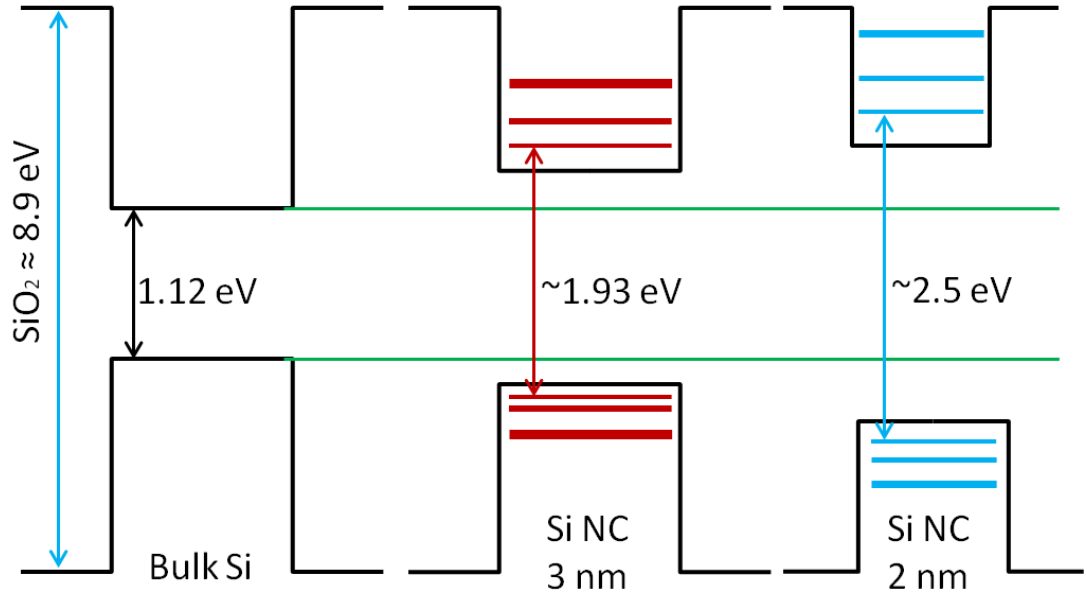

Figure 1.2. Simple illustration of increasing band gap of Si nanocrystals due to quantum confinement effect on charged carriers. Si nanocrystal is assumed to be embedded in a SiO_2 matrix. Nanocrystal sizes chosen are below exciton Bohr radius of the Si. The potential depth seen by the carrier due to band alignment with SiO_2 is decreasing with increasing carrier energy.

The change in physical properties of Si from bulk to nm sizes can be described by the quantum confinement effect. Free carrier motions are quantized in a quantum dot or in nanocrystal when the dot/nanocrystal size becomes comparable to the exciton Bohr radius of a given material. The Bohr radius of exciton can be thought of as the average separation of electron and hole wave functions in space. The ground state exciton Bohr radius of Si is around a bit less than 5 nm. Therefore we can expect that, to observe the quantum confinement effect in Si nanocrystals, the radius of the nanocrystal should be at least around 5 nm. The confinement by the boundaries raises the ground state of the carriers (Figure 1.2.) and creates discrete density of states. For an ideal system of nanocrystals, these energy levels are well separated from each other (like an atomic energy levels) especially for the states with lower energies. However, in reality due to the inter dot couplings, and interactions between nanocrystals and host matrix cause a broadening in those energy levels.

As a result of Heisenberg uncertainty principle, the carrier localization in the nanocrystal volume can bring uncertainty to the carrier's momentum. Then

momentum is not a good quantum number to describe electron/hole as in the case of bulk form of the material. The relaxation in momentum conservation rule converts inefficient light emitter Si to technologically important efficient luminescent material. Also under the context of Fermi's Golden rule, as the electron-hole pairs are localized in a dot volume spatially, their wave functions overlap more in position space and allow increase in oscillator strength for more geminate recombinatios. Despite the efficient radiative transition observed from Si nanocrystal, the transition is assumed to be a quasi direct transition, and the transition rate of this system could not compete with any direct gap III/V semiconductors switching speed. Fortunately it is observed that through the coupling with field of plasmons near metal nanoparticles, the radiative rate could be increased by several orders with an optimum design criteria [30].

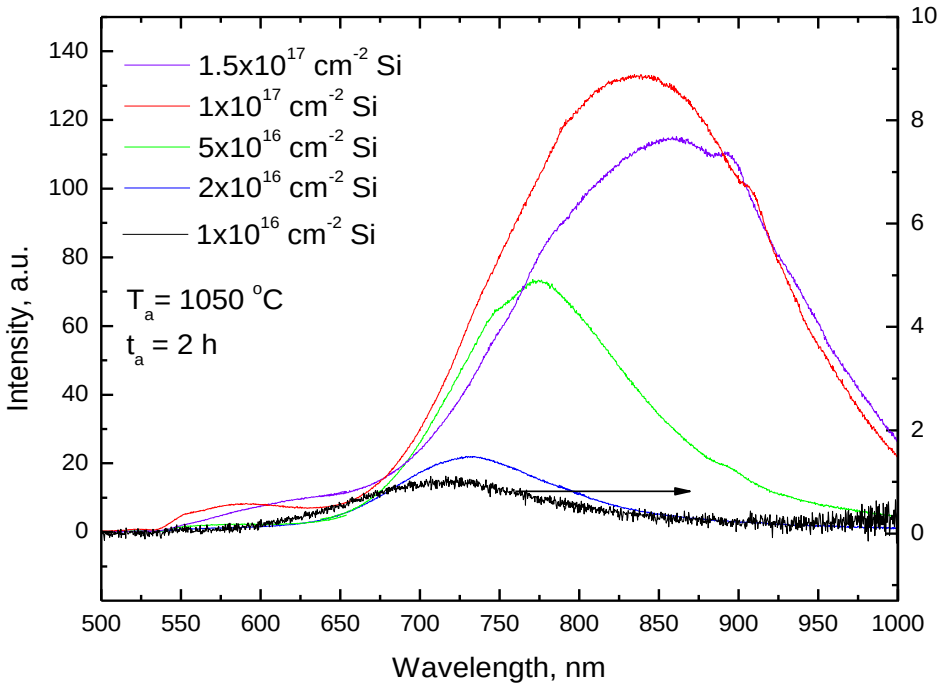

Figure 1.3. PL spectra of Si nanocrystals formed in SiO_2 dielectric. The average size of nanocrystals increased through increasing Si implantation dose. The peak position of the emission shifted from around 725 nm to 875 nm following average size of nanocrystals. This data were obtained through studies carried out at METU.

The emission/absorption of light can be manipulated through engineering the average size of the formed nanocrystals, following the size dependence of the quantum confinement effect. As the nanocrystal size is reduced, the energy of emitted or absorbed photon increases due to the increase in band gap. The typical photo

luminescence spectrum is shown in Figure 1.3. for the illustration of size dependence of light emission from Si nanocrystals embedded in a SiO_2 matrix.

Typical light emission from Si nanocrystal formed in SiO_2 varying between 700 nm to 1000 nm depending on nanocrystal size, and in general, the peak position of the emission and structure of the spectrum is almost independent from the production methods. The light emission mechanism from nanocrystal in an oxide matrix has actually not been understood totally. Although a consensus on the light generation by the electron-hole pair recombination due to transitions between nanocrystal energy levels has been achieved, the effect of surface states involvements could not be entirely disregarded. As the nanocrystal size is reduced, the increased surface to volume ratio makes the nanocrystal surfaces chemically more active. It is suggested that the trap states formed by oxidation of nanocrystals could trap (localize) excitons and recombinations occur over those trapped excitons. This model can be convincing for the smaller nanocrystals (less than 3 nm) with enhanced coupling between excited carriers and surrounding matrix or thin shell region around nanocrystals composed of sub-stoichiometric oxide region. This sub-oxide region can either produce exciton trap levels on the surface like multiple Si-O double bands, or directly creates energy levels inside nanocrystals. To avoid surface states due to the oxidation, there is a controversial suggestion of producing nanocrystals in Si-nitrate instead of SiO_2. The controversy is that, Si has a large solubility limit in nitrate which prevents the phase separation for nanocrystal formation. The achieved and scaled light emissions would be due to band tail recombinations in Si rich nitrate and the energy of the emissions directly modified by concentration of excess Si inclusion.

1.3. Applications of Si nanocrystals for photonics

The most astonishing achievement in Si nanocrystals has been the observation of gain by L. Pavesi and later other groups, which can be considered as the first small step for future Si nanocrystal based lasers [31,32]. However the stimulated emissions were observed only under intense pulsed laser pump that could achieve population inversion. Under strong excitation, the concentration of excitons in nanocrystal

increases, hence consequently both Auger recombination and population inversion enhance with the excited states. Therefore, there occurs a vital competition between Auger recombination and stimulated emission, which makes Si nanocrystals very difficult media for reliable and repeatable lasing. Moreover, for practical applications in optical interconnect technology, lasing should be observed under electrical injection of carriers into the nanocrystals, which still remains a dream for the future.

Following the PL observation from porous Si, both porous Si and nanocrystals embedded in dielectric matrices have been tested for practical LED applications. Due to the stability problem of porous nanostructured Si as discussed above, most of the attention has been focused on Si nanocrystals in SiO_2 matrix. Many groups have demonstrated working devices operating either by charge injection or by field effect [33-37]. Although successfully operating LED structures from Si nanocrystals have demonstrated, the efficiency and luminosity could not compete with today's conventional devices in the market. The main limitation of Si nanocrystal based devices is the surrounding dielectric layers which prevent carrier injection into nanocrystals and cause an increase of turn on voltage. The LED operations generally stand on impact excitation of nanocrystals by hot electron injection under high field regime near breakdown, which prevents stable device operation. Moreover, emission from nanocrsytals are limited to red and near infrared region of the spectrum and it is very broad, can not be easily tuned to cover the visible region effectively and the infrared region window of the waveguide devices.

Nowadays to adapt the light emission from the Si nanocrystal based LEDs to the regions of interest; intensive efforts have been spent on doping of Si nanocrystal system with RE elements. In reality, although the LED structures operating with RE incorporation do not require the involvement of Si nanocrystals, it is believed that Si nanocrystals improve LED efficiencies by behaving as energy transfer host for RE atoms. The Ion Beam Research Center in Dresden, Germany, hosts a leading research group on RE doped Si based LED fabrication by ion implantation. They announced efficient devices that can compete with conventional ones in efficiency. However the turn-on voltage is extremely high for practical applications. Recently, we have managed to reduce turn on voltage below 10 volts with Tb doped Si rich

oxide structures. The advantage and the flexibility of using RE elements as light emitting centers in Si platform is that they have very sharp emission lines due to the atomic nature of emissions, and by changing type of incorporated elements one can scan full range from ultraviolet (by using Gd) to infrared region of low loss fiber transmission window (by Er).

Besides the applications discussed above, new physical phenomena that have been observed in Si nanocrystals may find place for practical applications in the future. These include optical memory effect, nonlinear optical properties, multi exciton generation, Quantum Confined Stark Effect (QCSE) etc. [38-41]. QCSE is one of the major research topics of this thesis study. It can form the physical basis for the fabrication of the light modulators using the light emission from Si nanocrystal (including porous Si). Although this topic has been studied by several other groups, first clear and systematic observation of QCSE in Si nanocrystals has been demonstrated in our studies. The theoretical aspects of QCSE have been studied in collaboration with Dr. Ceyhun Bultay's group from Bilkent University [42]. Signal modulation is the heart of the today's optical data transferring lines, practical self electro-optic modulators using QCSE based on III/V semiconductors have been already used in practical applications. In the future for all Si based optical interconnect systems, Si based modulator devices are needed for processing optical signals. In that context QCSE in Si nanocrystal would be exploited for either in self electro-optic modulators or in modulators of Mach-Zender type structures.

1.4. Si nanostructures for photovoltaic applications

One of the measures of development is considered to be the degree of energy consumption. The demand for energy has been increasing to sustain healthy growth in economies and to sustain modern life styles. Today main energy sources are fossil fuels like coal, oil, and natural gas. The energy is obtained by burning these products, which creates unsolvable and extremely harmful environmental problems like global warming and air pollution. Moreover, the sources of fossil fuels are available only in a few countries. This causes both uncertainties in the supply and price of these products, and political conflicts between supplying and demanding countries.

Nowadays, these problems have directed most countries to invest on renewable energy sources either to insure the supply stability or fulfill the increasing energy gap that cannot be easily compensated in a short term. Among the alternative renewable energy sources, direct conversion of the solar energy into the electrical energy by solar cell technologies stand as the most attractive one due to the availability of huge amount of clean energy that we are receiving from the sun every day.

In recent years, many different types of solar cells have been developed. Among them all Si based solar cells dominate the market with a percentage of over 90 % whose main slice is occupied by the crystalline Si. There are several advantages of Si over other competitors in photovoltaic industry: Si is abundant in earth crust, production of high volume defect free crystal with an affordable price is possible, it has a suitable band gap with tunable physical properties, it is nonpolluting and Si solar cell technology is based on the huge knowledge that has been gathered by Si micro-electronics industry in the last 50 years. Nowadays researchers have been intensively focusing on both increase of the efficiencies of conventional solar cells in a cost effective way with novel design strategies, and more affordable new solar materials or new heterostructures with superior performance under the flourishing availability and flexibility of nanotechnology platform.

Nanotechnology has rapidly established itself as an interdisciplinary field of our age. It deals with the new physical and chemical properties of nanometer sized materials for novel applications. According to their geometries or the limitation in free carrier motion, nanostructured materials can be categorized as: quantum dots or nanocrystals (zero dimensional), nanowires (one dimensional), and quantum wells or some thin films (two dimensional). In this thesis, we worked with the one dimensional system defined by Si nanowires; a brief description of this system is given below.

Due to the technological success and the intensive knowledge accumulation on Si in the bulk form, Si nanowires have attracted a lot of attention in nano-technological

research studies. In particular, employment of Si nanowires in solar cell technologies may be the most promising one that can be commercialized in the near future. Si nanowires can be produced in horizontal networks, vertically standing arrays, and stacked arrays with extremely high aspect ratios. Among the production techniques, nanowire formation by metal assisted/electroless etching (MAE) of Si substrates is very promising for industrial size solar cell applications. The method is very simple and can be easily adapted to the crystal Si solar cell production line. The superiority of the MAE technique over the other methods can be listed as: it does not require costly process equipments, it is suitable for large area applications, and it offers flexibility in the temperature range between 0 to 60 ^{o}C. Moreover, as the nanowires are produced from bulk Si, they have same crystal quality and same uniform doping characteristics with pristine substrate. Vertically aligned Si nanowires were first demonstated by Peng in a solution containing Hf/$AgNO_3$ [43]. It was later demonstrated that other metals like Au, Fe, Pt, Cu, Ni can be also used for MAE etching. The etching process takes place through galvanic replacement between metal and Si substrate.

Si nanowires that can be produced by galvanic replacement can be used as either active or passive layers in solar cell applications. As an active component, Si nanowires could be utilized in both homo junction and heterojunction device fabrications. It was predicted that the three dimensional or radial homo/hetero-junctions provided by Si nanowires would offer better performance over the planar counterparts. One of the most important features of vertically aligned silicon nanowires fabricated by MAE is the remarkable antireflectivity. As the black and dull appearance of the surface containing silicon nanowires suggests, the optical reflectivity of the silicon substrate dramatically decreases following the etching procedure. This is due to the fact that both the optical path that incoming photons have to travel and the number of scattering events are increased substantially. In this study, the optical reflectivity measurements were carried out and it was found that the samples had as low as 1% reflectivity. However, as an antireflective layer on top of the solar cell, Si nanowires were mostly employed as a passive component. It is crucial that, good passivation of nanowires is required to decrease the surface

recombination which is enhanced by the large defective surface area of the nanowires.

This thesis is organized as 6 chapters. After the introduction in Chapter 1, Chapter 2 presents results on ZnO nanocrystal/Si heterojunction devices for LED applications. In Chapter 3, Electroluminescence properties of Si nanocrystal based MOS-LED structures are given. Chapter 4 is devoted to the experimental observations of QCSE in Si nanocrystals along with theoretical findings. In Chapter 5, Si nanowire production by a novel method so called MAE has been presented along with large area solar cell applications. And the last chapter is devoted to the general conclusion of the thesis.

CHAPTER 2

Si BASED LIGHT EMITTING DIODES WITH AND WITHOUT ZnO NANOSTRUCTURES: EFFECTS OF SiO_2 BUFFER LAYER

2.1. Introduction

2.1.1. ZnO and its properties

Zinc oxide (ZnO) is an inorganic compound in a white powder form that is insoluble in water. As a semiconductor, ZnO has gained much interest due to its large exciton binding energy (60 meV) that could allow lasing action based on exciton recombination and possibly polariton/exciton interaction even above room temperature [44,45]. It is a member of II/VI binary compound semiconductors with a direct gap and has band gap energy of 3.37 eV which makes it transparent in the visible part of the spectrum. With the high energy gap value, ZnO can be useful for device operation for the UV to blue wavelengths (Figure 2.1.). Band gap of ZnO can be tuned between 3 to 4 eV by alloying with CdO and MgO [46]. Moreover, a broad defect related peak extending from ~1.9 to ~2.8 eV is also a common optical feature of ZnO. The origin of this luminescence, known as green band, is still not well understood and has been attributed to variety of different impurities and defects.

ZnO has intrinsically n-type conduction. The cause of this inherent doping is still not very well understood so far. The background carrier concentration varies with the type of the production techniques and with the quality of the grown layers. However, in most cases this is around 10^{16} cm^{-3}. Intentional n-type doping of ZnO is relatively easy to accomplish with elements such as Al, Ga or In, wheras, reliable p-type doping is very difficult to achieve [47]. Usually group I and group V elements are used as acceptor in ZnO. So far, the most common acceptor atom has been nitrogen because it readily substitutes oxygen and does not distort the lattice significantly. Actually lacking complementary doping is a problem for most of the wide band gap

semiconductors i.e. conductivity type is limited to either n-type or p-type and generally limited to n-type.

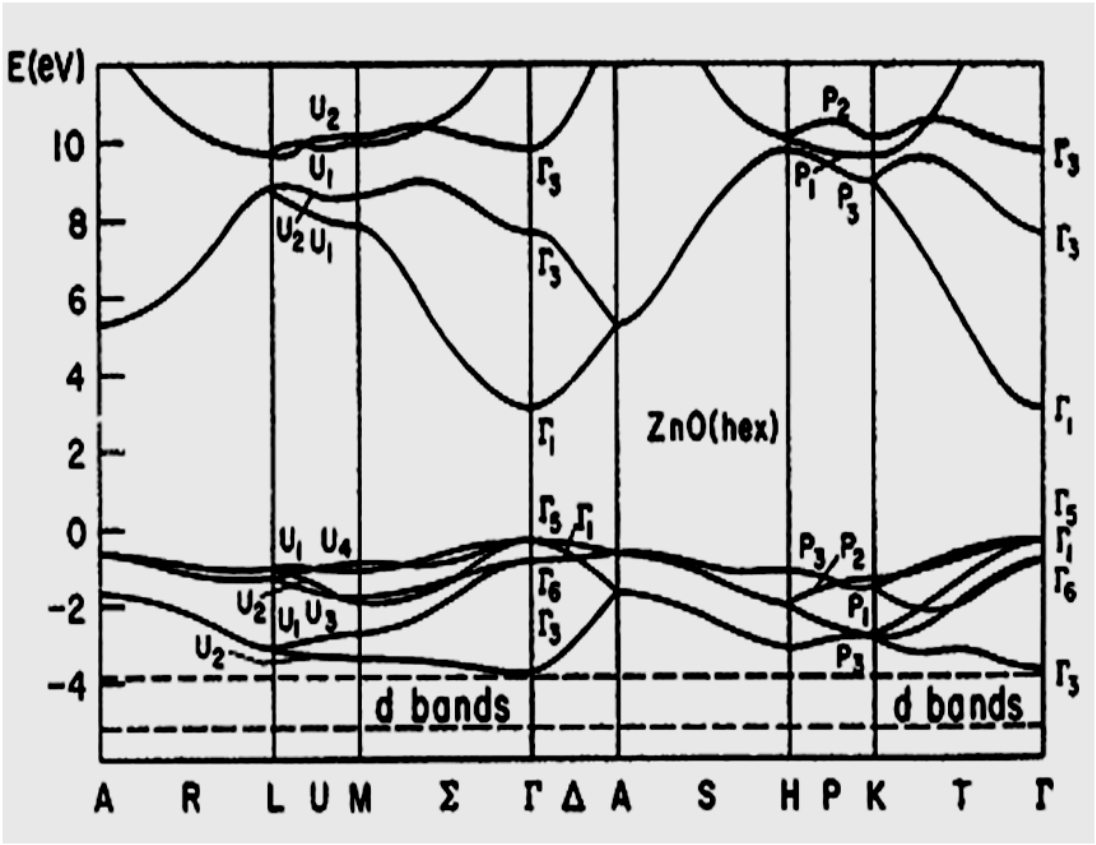

Figure 2.1. Calculated energy band structure of ZnO. Both the valence and conduction bands extremes occur at the Γ point K= 0 indicating that ZnO is a direct band gap semiconductor [48].

At ambient pressure and temperature, ZnO crystallizes in the Wurtzite structure, as illustrated in Figure 2.2. This hexagonal lattice structure is characterized by two interconnecting sub lattices of Zn^{2+} and O^{2-}, such that each Zn ion is surrounded by a tetrahedral of O ions, and vice versa. This tetrahedral coordination results in a polar symmetry along the hexagonal axis. This polarity is responsible for a number of the properties of ZnO, including its piezoelectricity and spontaneous polarization, and is also a key factor in crystal growth, etching and defect generation.

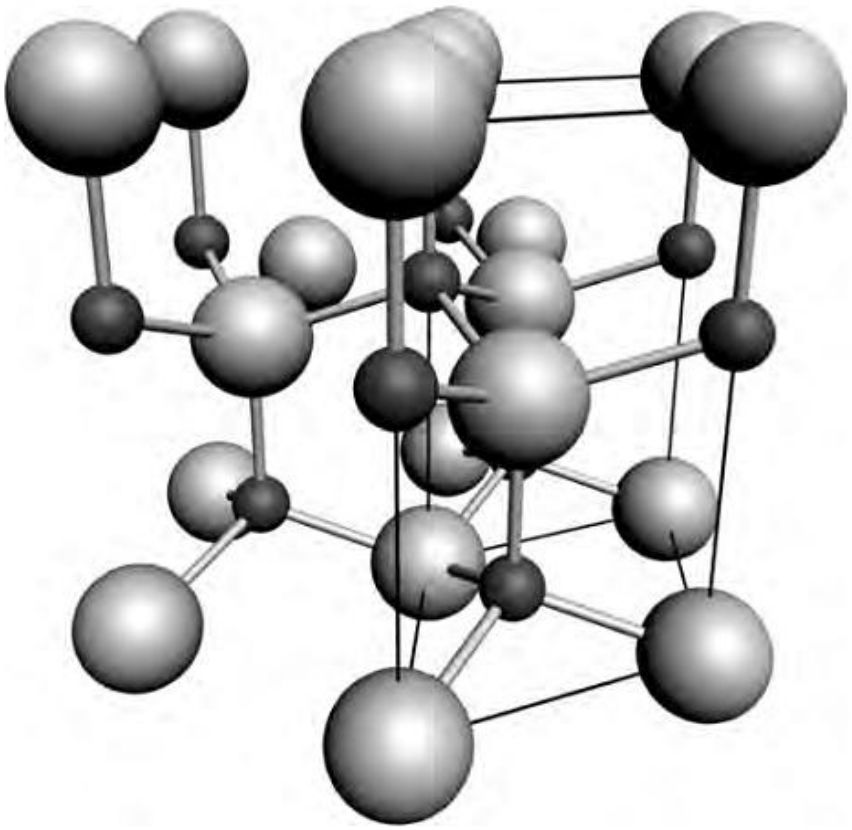

Figure 2.2. Hexagonal Wurtzite structure of ZnO. Zn atoms are shown as large sphere, O atoms are smaller ones [49].

2.1.2. Applications of ZnO

The use of ZnO dates back to the ancient times, when it was used for medical treatments and for the production of first brass metal. It has been used for almost 150 years in the industry as a white paint pigment and processing chemical. First application as a semiconductor material was seen in the fabrication of a detector in 1920s during the early times of the electronic industry. Today, ZnO is a very versatile compound for variety of applications. Application areas of ZnO includes rubber industry (50 % of total), concrete industry, corrosion prevention in nuclear industry for coatings of various metals, lubricants, paints, ointments, pigments, foods, batteries, various medical treatments, root improver in agriculture, etc. [50,51]. Moreover, due to its unique electrical, mechanical and optical properties;

ZnO is suitable for utilization in numerous device applications in electronic, photovoltaic and optoelectronic technologies.

Recently ZnO has been considered as one of the important materials for the fabrication of UV LEDs, lasers and photo detectors [44]. It is assumed to be a competitor of GaN due to its superior properties like high exciton binding energy (60 meV for ZnO and 25 meV for GaN), single crystal substrate producibility, and durability to environmental and radiation effects [52]. It is also a good substrate for epitaxial growth of GaN. ZnO has very high piezoelectric coefficient and strong spontaneous polarizability, which has lead to the developments of various piezoelectric transducers and surface acoustic wave devices [53]. Moreover ZnO can be utilized as transparent conductive layer window for several types of solar cells, transparent thin film transistors, electrode for flat panel display and transparent display applications, biological and chemical sensors [54-56]. And finally ZnO can be a good candidate for spintronic applications [57]. The number of application areas for ZnO has being growing with the new emerging properties of ZnO at nanoscale, which are briefly described below.

2.1.3. ZnO nanostructures

Under specific growth conditions, ZnO probably has the richest family of nanostructures among all materials both in terms of structure and physical-chemical properties. Nanostructured ZnO materials have received broad attention due to their distinguished performances (which are largely believed to be the result of surface and quantum confinement effects) and they could have novel applications in optoelectronics, photovoltaics, sensors, transducer, and bio-medical sciences [58]. ZnO nanostructures have been identified and classified according to their morphologies: nanocrystals, nanowires, nanocages, nanocombs, nanorings, nanohelixes, nanosprings, nano tetrapods, nanoneedles, nanosaws, nanoflowers, seamless nanorings, and nanodumbbells. In Figure 2.3 below, several types of nanostructures made from ZnO are shown. The morphology of the grown nanostructures is determined by physical parameters of growth techniques. There are several growth methods adapted for ZnO nanostructure synthesis: Vapor-Liquid-

Solid or Vapor Transport (VLS), Metal Organic Chemical Vapor Deposition (MOCVD) and Molecular Beam Epitaxy (MBE). These three gas phase approaches are employed at relatively high temperatures and require expensive equipment. Fortunately, cost effective, low temperature wet chemical synthesis methods such as electrodeposition, sol-gel aqueous chemical or hydrothermal methods have been either developed or adapted for ZnO nanostructures. However, the control of morphology and the positioning of nanostructures using wet chemical techniques are challenging. In all of the techniques listed above, VLS appears to be the most versatile technique for morphology engineering.

Figure 2.3. ZnO nanostructures in different morphologies types using VLS methods [49].

2.1.4. ZnO based light emitting diodes

ZnO has ben considered as a promising material for LED applications in the UV-blue region for a long time. The first ZnO based LED structure was introduced by Drapak in 1967, the fabricated device was heterojunction of n-ZnO with p-Cu_2O [59]. Lacking p-type ZnO forced scientists to search a substitution for the p-ZnO to facilitate the fabrication of heterojunction LED structures. Later Tsurkan et al. succeeded to grow p-ZnTe on n-ZnO, and later Ohta et al. fabricated p-$SrCu_2O$/n-ZnO heterojunctions for the realization of electroluminescence (EL) [60,61]. After these pioneering works, there has been much interest in ZnO based LED applications using ZnO with a suitable p-type conjugate material. Due to the similarity in their lattice constants (1.8 % mismatch), GaN has been considered as a good alternative for the p-type layer in heterojunction and many working devices have been demonstrated so far [62,63]. Besides GaN, AlGaN, SiC, NiO, GaAs, organic materials and Si have been extensively studied for p-type substitution of ZnO [64-69]. Although, not reliable and convincing yet, a few groups have announced electroluminescence emission from the homojunction of ZnO [70,71].

Recently ZnO based nanostructures (especially nanowires) have been extensively studied for LED applications. Beyond the ease of growth of ZnO in nanostructured form, the main advantage introduced by nanostructures is that matching the lattice constant is no longer required. The stress developed at the interface due to the lattice mismatch can be easily relieved by the large surface area of the nanostructures. However, this advantage of nanostructures is diminished by increased defect states in ZnO as a result of increase in surface to volume ratio, which also cause a decrease in the ratio of UV to visible light emitted from the device. By using nanostructured ZnO (mostly nanowires), both homo and numerous type of heterostructures have been fabricated for LED applications [72-76]. As a substrate and p-type layer for nanostructured ZnO, Si is an attractive material for cost effective and reliable UV/visible hybrid device for future lightining [77-79].

In this part of the thesis, we report on the fabrication of ZnO nanocrystal/Si based heterojunction LEDs and on their electroluminescence properties. ZnO nanocrystals were synthesized by using VLS technique using Au as a catalyst metal.

Electroluminescence behaviour of ZnO nanocrystals grown on both p- and n-type Si substrates was observed at room temperature under both forward and reverse bias conditions.

2.2. Experimental Details

2.2.1. ZnO nanocrystal synthesis through VLS method on Si substrates

2 nm Au layer was deposited on both p- and n-type Si as a catalyst metal using the thermal evaporation technique. Four different kinds of samples were processed: two of them were on p-type Si substrate (one of them had 3 nm SiO2 buffer layer between ZnO and Si), other two were on n-type Si substrate (one of them had 3 nm SiO2 buffer layer between ZnO and Si). Au coated samples were placed in a horizontal quartz tube furnace for nanocrystal growth over them. As a source material, an alumina crucible filled with 2 grams mixture of ZnO-C in 1:1 ratio was placed at the center of the furnace heated to a temperature of 900 ^{o}C while the samples were located 10 cm away from the source and kept at 850 ^{o}C in the direction of carrier gas flow. As a carrier gas, argon was used with a flow rate of 100 sccm. The duration of the growth was about 10 s for the nanocrytals. Further growth resulted in the nanowire formation.

2.2.2. Catalytic vapor-liquid-solid (VLS) method

The VLS crystal growth mechanism was first proposed by Wagner and Ellis in 1964 for Si whisker growth [80]. This method has been adapted for nanostructure growth of many types of semiconductors such as ZnO. This technique allows for a great control over the resultant structure and as a consequence, it has been the most widely preferred technique to produce very high quality ZnO nanostructures. The VLS processes are usually carried out in a horizontal tube furnace as illustrated in Figure 2.5. It is simply the transport of carrier reactant vapors by carrier gas (Ar or N_2) on to the specified substrate where they react to form desired structures. For the ZnO growth, the reactant source is a mixture of generally ZnO-C (graphite) powders where C lowers the ZnO decomposition temperature significantly. At high temperatures C reacts with ZnO to form Zn, CO, and CO_2 vapors which are carried

by Ar on to the substrate. The spatial distribution of the catalyst metal particles determines the pattern of the grown nanostructures. A continuous metal Au layer turns into a layer of small droplets on the surface. Reactant metal Zn form liquid alloy with Au and ZnO growth begins in the presence of oxygen after the alloy liquid becomes supersaturated with reactant materials and it continues as long as the catalyst alloy remains in the liquid state and the reactants are available. Since the liquid droplet catalyzes the incorporation of material from the gas source to the growing crystal, the deposit grows anisotropically as a whisker whose diameter is dictated by the diameter of the liquid alloy droplet. The nanowires are thus obtained with a high purity, except for the end containing the solidified catalyst as an alloy particle. As a source material for VLS growth of ZnO nanostructures, sometimes ZnO and Zn have also been used. However the decomposition of ZnO to reactant vapors requires extremely high temperatures (~1975 ^{o}C) in the absence of C. When Zn is used as the starting material, a partial O_2 gas should be mixed to the carrier gas. The use of Zn significantly reduces the vaporization temperature (~420 ^{o}C).

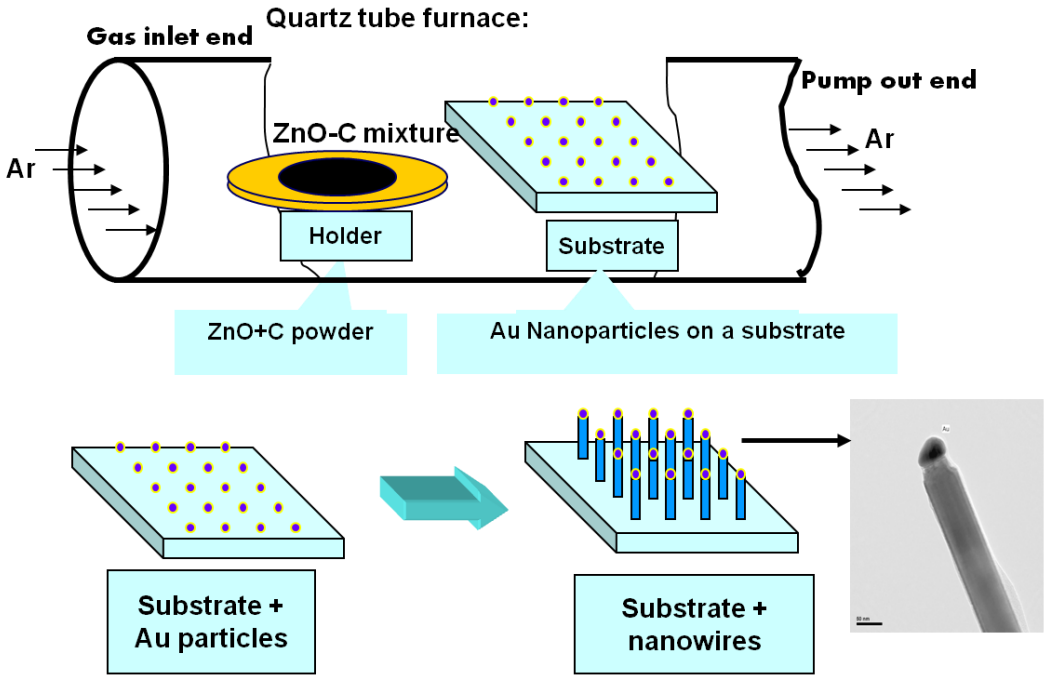

Figure 2.4. A typical growth oven set up used for the catalytic growth of ZnO nano-wires. When the growth time is limited to few seconds nanocrystals are formed. The inset shows a transmission electron microscope image of a single ZnO nano-wire with Au dot on the top of the wire [81].

2.2.3. Light emitting device fabrication

Following the growth process of ZnO nanorystal on four different types of Si substrates by VLS method, further processes have been done for the fabrication of LED structures. In addition to these samples, devices with pristine Si substrates and Si substrates having 3 nm of thermally grown SiO_2 were also fabricated as test devices to understand the EL properties of nanocrystalline ZnO.

About 100 nm of indium-tin-oxide (ITO) layer was grown using sputtering technique through copper shadow mask having many circular apertures with a radius of 1.2 mm that allow circular electrodes on the surface of the samples. The deposited ITO layer serves as transparent optical window for light extraction as well as a current spreading layer for devices. Aluminum (Al) and gold-antimony (Au-Sb) alloy were evaporated onto the back side of devices as an ohmic contact to p- and n-type Si substrates, respectively. The concentric Au top contact with a radius of 200 μm was deposited on the ITO layer again using thermal evaporation technique. In order to decrease the resistivity of the ITO window and back contact layers, samples were annealed at 450 ^{o}C under nitrogen ambient for 20 minutes. Following the annealing, devices were mounted on a handmade chip carrier using silver paste and each device was wired to respective copper pads of carriers by 25 μm gold wire. The schematic cross sectional views of fabricated different devices are shown the Figure 2.5.

EL measurements were conducted at room temperature under DC biasing condition of both polarities (reverse and forward). MS-257 type monochromator of Oriel Instrument Company and a Hamamatsu CCD camera were used for the detection of the emission. The data collected from the measurements were corrected for the sensitivity of the CCD camera and grating in the monochromator.

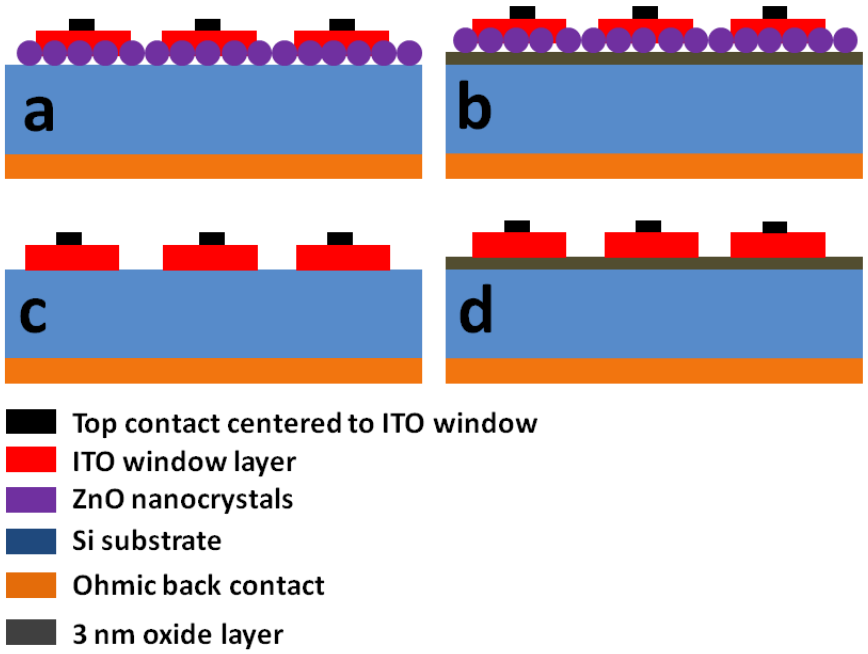

Figure 2.5. Representative cross-sectional schematic of the fabricated devices, (a) and (b) represent the devices with ZnO nanocrystals as an active layer on bare Si surface and on buffer 3 nm oxide layer, (c) and (d) represents the test devices without ZnO nanocrystals on pristine Si and on Si with buffer oxide layer.

2.3. Results and discussions

2.3.1. SEM and photoluminescence results

Scanning electron microscope (SEM) images of the VLS grown ZnO nanocrystals from the top view are shown in Figure 2.6. Almost the same spatial distributions of nanocrystals were observed in both samples. The shape and the size of the nanocrystals are not entirely homogenous. We see some elongated nanocrystals as well as spherical ones. The size of the nanocrystals are distributed between 5 to 40 nm, while a few of them are abit larger than 50 nm. The droplet formation of catalyst Au is spontaneous in agglomeration. The shape and the size of the nanocrystal take the morphological structure of catalyst droplets.

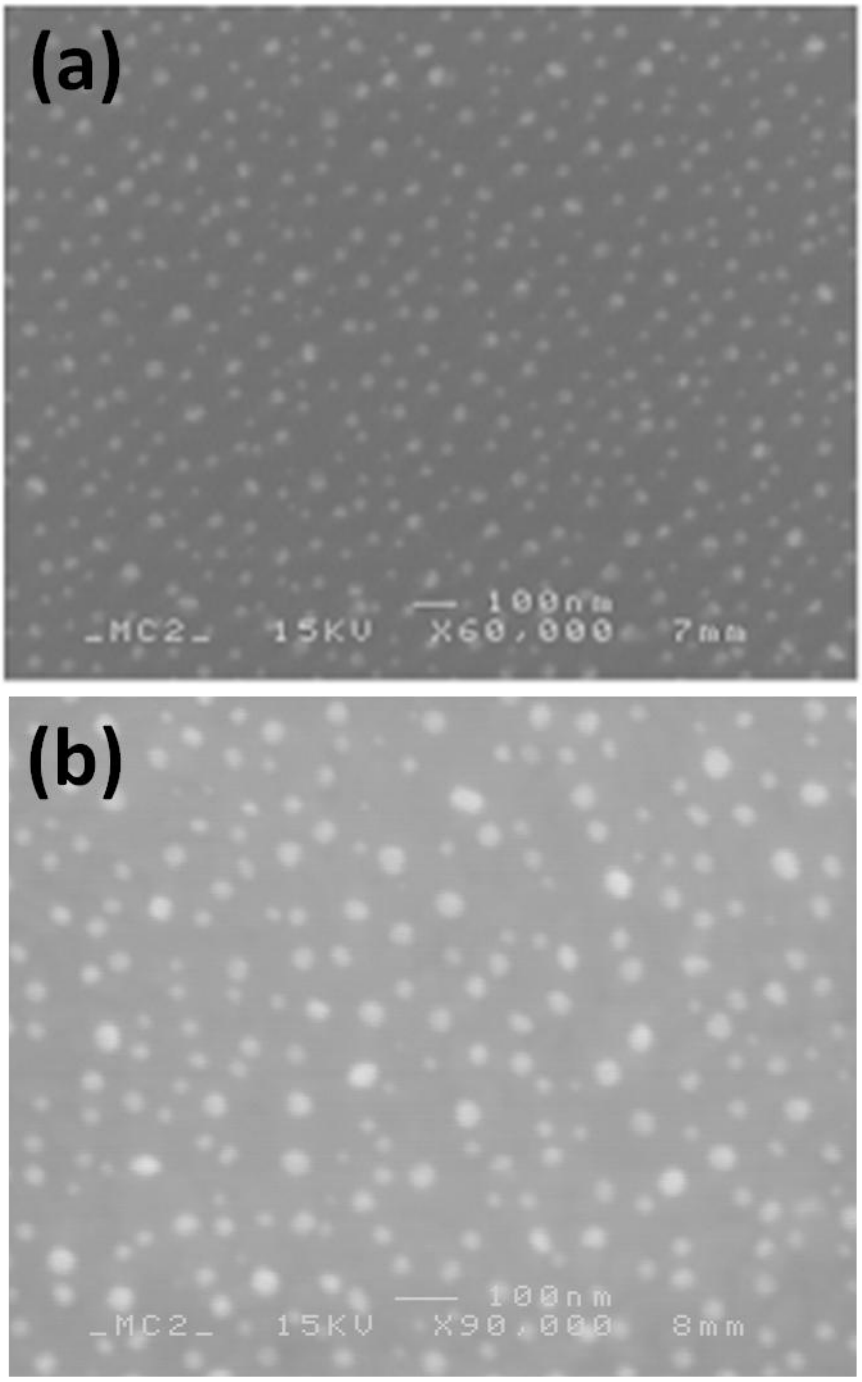

Figure 2.6. SEM images of the ZnO nanocrystal sythesized through VLS technique at 850 ^{o}C. ZnO nanocrystals on (a) pristine Si, and (b) on oxide covered Si substrates.

Photoluminescence (PL) of the samples were measured at room temperature with same set up that was used for EL studies. The only change was the excitation source. A He-Cd ion laser generating a light beam at 325 nm was used as an excitation source for the PL emission.

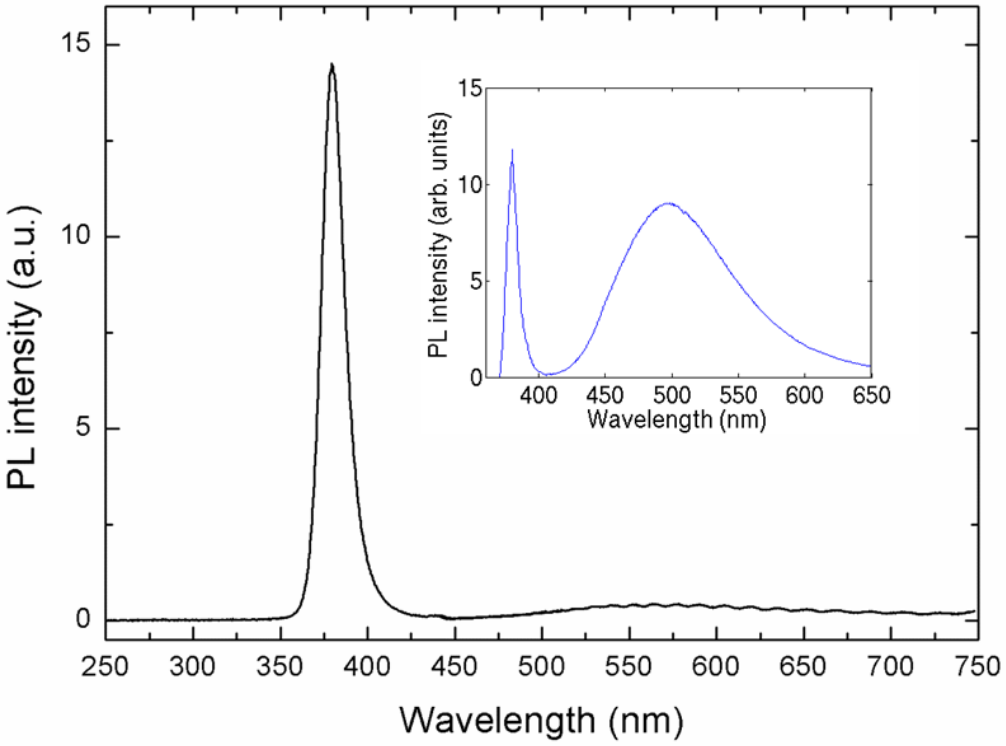

Figure 2.7. Room temperature PL spectrum of ZnO nanocrystals on Si substrate. PL spectrum of defective nanostructure is given for comparision in the inset.

PL spectrum of the synthesized nanocrystals is a given in Figure 2.7. The band edge emission from ZnO is clearly seen at around 478 nm accompanying weak and broad light emission covering the visible region from 425 to 800 nm due to the defect related energy states in the band gap of ZnO. The mechanisms of emissions from defect states are not well understood. However, several types of defect formation such as Zn, O interstitials and vacancies or Zn-O anti-cites could be identified Moreover, external impurities may also create band gap states which generate visible emission. The increasing role of surface over the volume in nanostructures inevitably results in low energy broad tail emissions which are generally more intense than narrow UV band edge emission. Looking at PL spectra, we can conclude that, the

samples studied here can be accepted to be a good quality with small intensity of defect emissions in the band gap. Illustration of more defective emission from ZnO nanostructure is given as an inset in Figure 2.7. A combination of these two emission bands can be exploited for white LED applications in domestic area without requiring any phosphorus layers.

2.3.2. Current voltage (I-V) chararteristics of fabricated LEDs

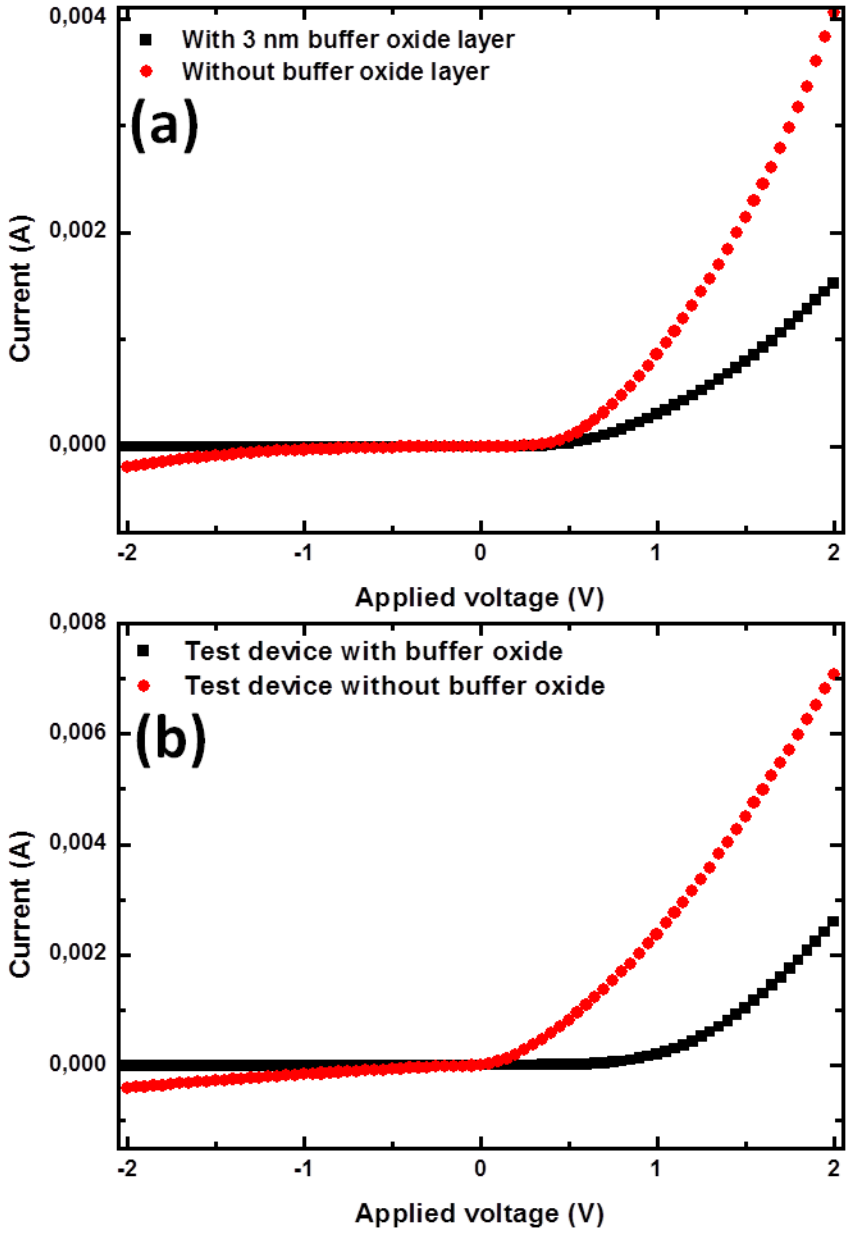

Figure 2.8. Current-Voltage characteristics of LEDs, (a) LEDs with ZnO nanocrystals built on p-type Si, and (b) test LEDs built on p-type Si.

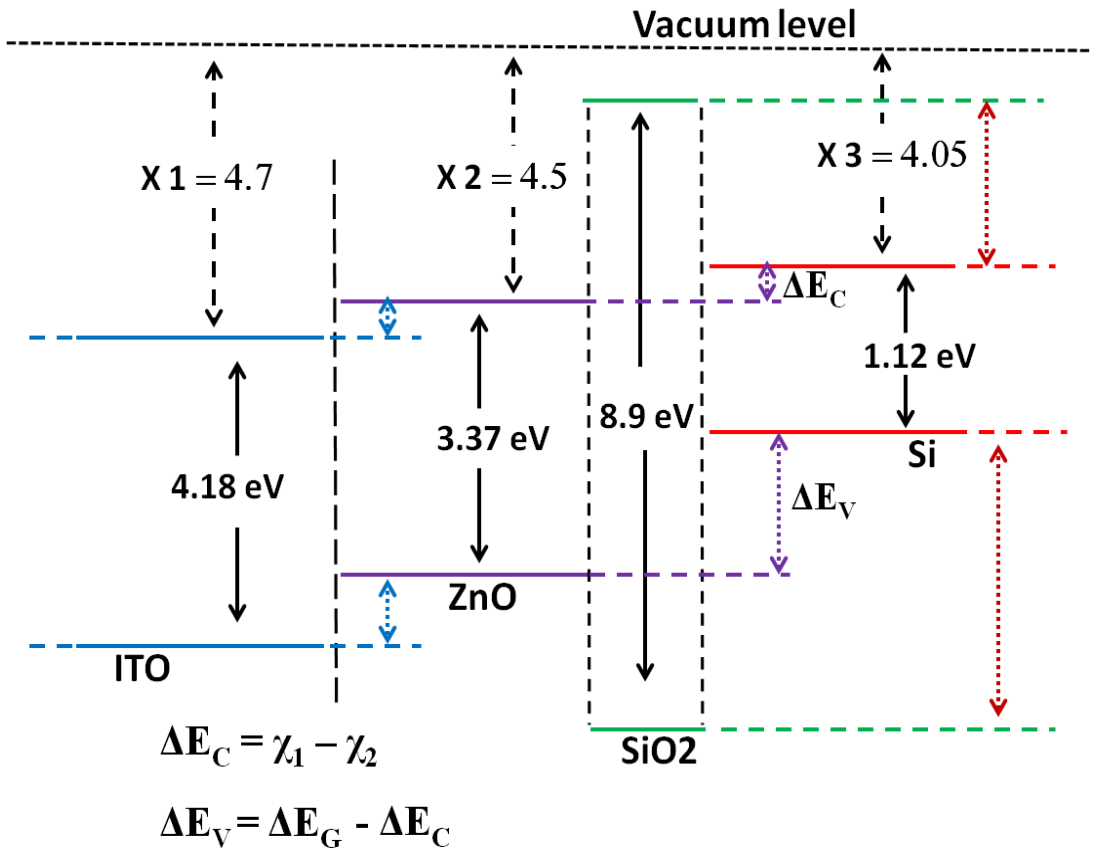

Figure 2.9. Illustrative schematic showings band alignment of different layers constituting LED structures having no contact with each other with respect to vacuum level.

Figure 2.8 shows rectifying diode behavior for different LEDs fabricated in this study. We have built LEDs on p-type substrates for the sake of convenience. Similar diode behavior can also be observed from the devices on n-type Si. Introduction of thin SiO_2 buffer layer greatly enhances diode behavior at the expense of injected current level. For the comparison of the test devices, an insertion of extra ZnO layer (active layer of our LED) significantly reduces injection current level further at the same bias voltages as one can expect. Approximate band alignment of the layers is given in the contactless mode in Figure 2.9. Except for the SiO_2 buffer layer, all materials are aligned in type II or staggered heterojunction scheme. This representative schematic will help understanding the EL mechanisms as discussed in following sections.

2.3.3. Electroluminescence of test devices

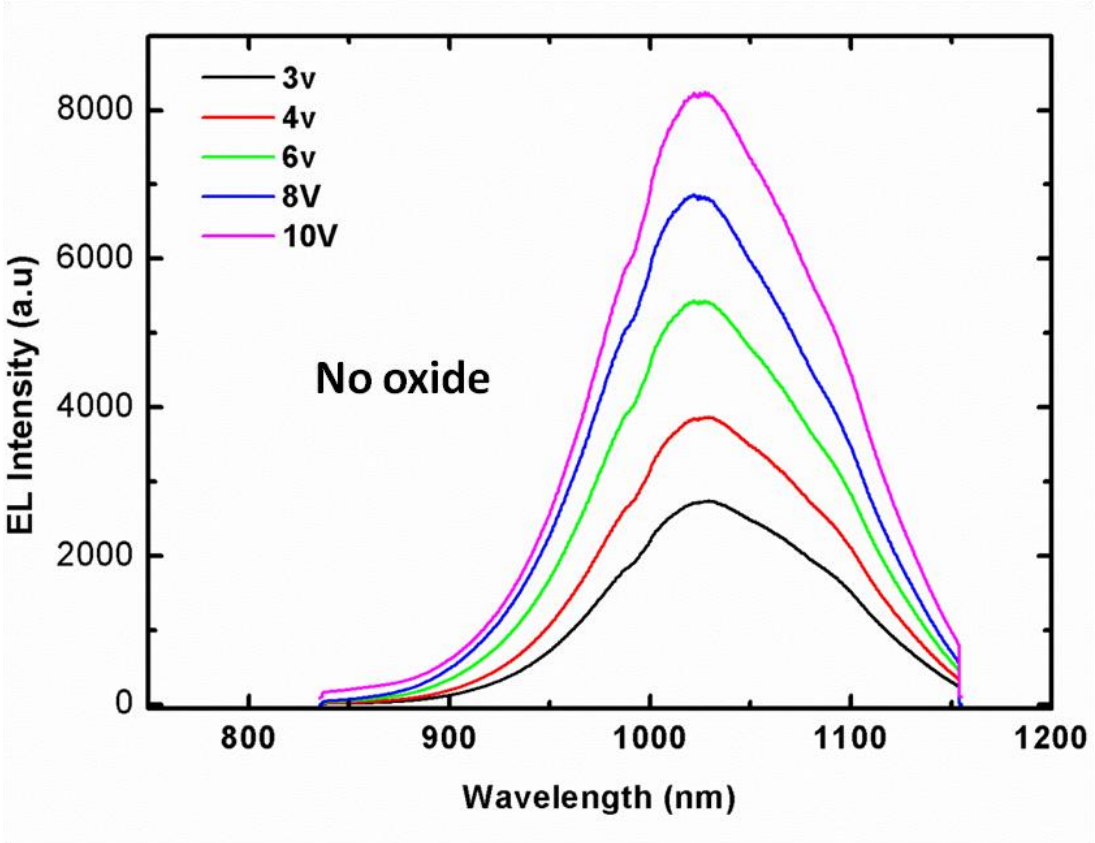

Figure 2.10. EL results of the test device with various voltage values under the forward bias. This test device has no oxide barrier between ITO and Si.

In order to understand the light emission from the ZnO nanocrystal/Si heterojunction LED structures and exclude the interference of the possible parasitic contributions in the emitted light; test devices were fabricated on p-type Si substrate with the same conditions and structures without any ZnO layer. Two types of test devices were fabricated: without and with an oxide layer between ITO and Si substrate. Their EL results are given in Figure 2.10 and 2.11, respectively.

Device without barrier layer is a simple staggered hetero junction of ITO and Si where ITO constitutes n-side and Si p-side. Band edge discontinuities at valence band and conduction band edges of this junction are around 0.65 eV and 2.41 eV, respectively. This means that electrons from ITO side to Si and holes from Si side to ITO see the some potential barrier under forward bias. Therefore one can expect electron accumulation at the ITO side and hole accumulation at the Si side of the

interface as a result of band bending under forward bias. This charge accumulation is more pronounced in the case of the device having oxide barrier. Details of this aspect are given in the discussion below.

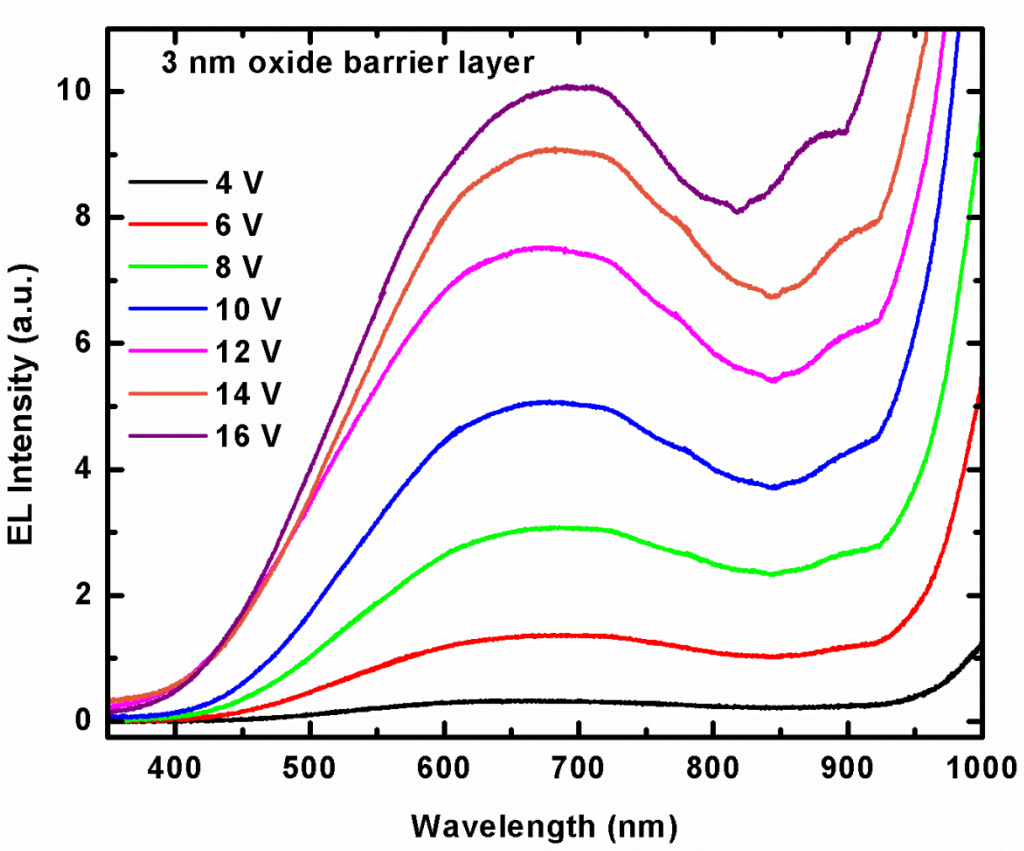

Figure 2.11 EL results of the test device with 3 nm oxide layer under forward bias

Room temperature EL emission from the electron hole recombination through the Si band gap was observed under the forward bias as presented in Figure 2.10. Due to phonon involvement, the peak energy of the emitted light spectrum is a bit lower than the Si band edge. The turn-on (emission threshold) voltage of the EL emission is around 1.5 V in the measured samples and the reliable device operation window was found between 1.5 to maximum 10 V. In the case of the device with barrier oxide layer, the situation is different, there is a broad high energy tail band whose peak position is located around 675 nm and due to the presence of much higher potential barriers seen by the carriers, the turn on voltage level also increased compared to other devices. Moreover the infrared part of the spectrum (not shown here) is hundred times lower than the emission intensity of ITO/Si junction. The visible

emission could be attributed to the luminescence centers (defects, impurities or self trapped excitons) being in the oxide layer. Although not proven conclusively, there is a general acceptance that red luminescence from oxide is due to the non-bridging oxygen-hole-centers (NBOHC) [82]. Either the co-carrier tunneling into these centers (especially in low fields or voltages) or excitation of these centers by impact ionization due to hot electrons can be the mechanism generating the observed EL emission. The latter mechanism is more likely in very high electric fields which provide the electrons with sufficient energy to surmount the oxide conduction band. Besides, injected hot electron hole recombination in the Si may also cause visible emission from the Si substrate [83]. The emission intensity of both devices increases as the gate current (or bias voltage) increases. In the case of reverse biasing, the infrared emission vanishes in the ITO/Si structure while for the sample with an oxide barrier, the visible emission is observed at the same peak energy with reduced intensity and increased turn on voltage. The observation of visible emission under reverse bias excludes the hot electron-hole recombination mechanisms at least for our device.

Now we should address how it could be possible to have such a high EL emission from indirect band Si while we have not observed any detectable PL signal at room temperature. The answer to this question can be found by considering the energy band alignment and the formation of quantum well structure on the surface of Si which leads to carrier confinement. The valence band discontinuity between ITO/Si and SiO_2/Si are around 2.5 and 4.5 eV, respectively. Under a forward bias i.e. negative potential applied to the ITO with respect to Si substrate, holes are accumulated at the ITO/Si and SiO_2/Si junction interface, where a potential well is created for holes due to the bending upwards of Si band. Therefore, holes are accumulated and localized at the interface in a narrow triangular potential well in the Si side. As one can predict, the potential well at the SiO_2/Si interface is more populated because it is deeper than that at the ITO/Si interface. The localization of the holes to a narrow region at the interface causes the spreading of momentum of holes in the reciprocal space along the growth direction. Then the momentum of holes does not have discrete values, instead they have distributed momentum values, which results in involvement of more phonon states to compensate momentum

difference in the radiative emission of indirect Si. Since the radiative recombination takes place in the interfacial region, hole-electron scattering due to surface roughness could also satisfy the momentum conservation in the radiative transition [84]. In addition to scattering from the surface roughness and momentum spreading due to localization, the scattering between majority carriers (between holes) in the accumulation layer can enhance EL property of the Si. Electrons injected from ITO window into the conduction band of Si could radiatively recombine with holes confined at the interface.

We have observed that devices without barrier oxide are much more efficient for Si band edge emission. Although, we have not been able to identify the exact physical mechanism, this can be attributed to several effects: (1) Surface roughness scattering would be more significant than that of growth directional localization for momentum compensation in radiative recombination due to the fact that sputtered ITO/Si interface is rougher compared to thermally oxidized SiO_2/Si interface: As the surface roughness could cause a two dimensional localization of carriers over the whole surface in the interface plane. This results in widening of the momentum distribution with the aid of scatterings. (2) Strong hole accumulation formed at the interface can easily initiates Auger recombination processes for the device with barrier oxide. (3) Loss of some carriers generating visible emission in the barrier defect states.

2.3.4. Electroluminescence results of ZnO nanocrystals/p-Si heterojunction devices.

In this section, the room temperature EL observations of VLS grown ZnO nanocrystal/Si heterojunction LED structures have been presented and discussed. Two types of devices have been fabricated on n-type and p-type Si substrates with and without SiO_2 barrier layer between ZnO and Si. The EL measurements were carried out under forward and reverse biasing of devices.

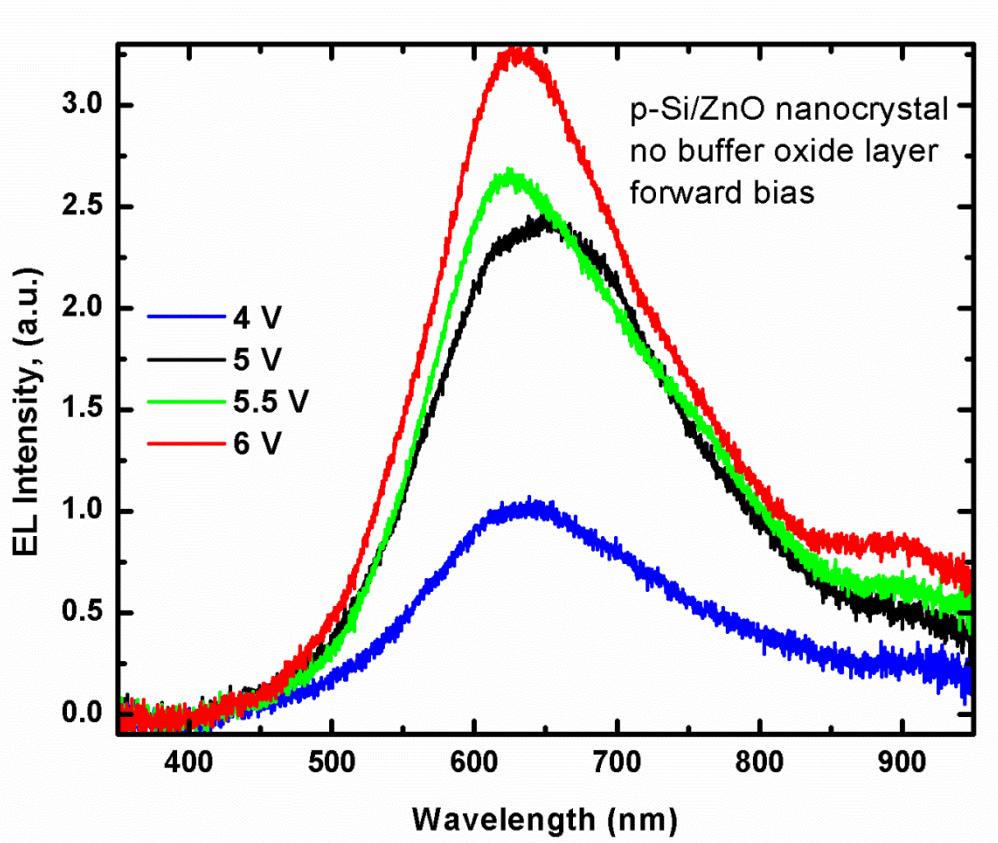

Figure 2.12. EL spectra of device on p-type Si substrate without SiO_2 buffer layer between Si and ZnO nanostructure layer observed under forward bias.

In Figures 2.12 and 2.13, EL spectra measured from devices having ZnO nanocrystal active layer on p-type Silicon substrates with and without SiO_2 buffer layer under forward bias condition (substrate was held at positive potential with respect to top contact (or ITO optical window)) are given. It was observed that for both devices, the detectable EL threshold voltage is below 3 V. An emission with orange-red color can be seen by naked eye when the bias voltage is above this value. For both devices it is seen from Figures 2.12 and 2.13 that, there is an asymmetric EL emission peaked at around 600 nm. For the devices without buffer oxide, EL emission peak is located at 620 nm, whereas emission from the device having buffer layer is a bit blue shifted with respect to other devices and located at 595 nm. EL spectrum exhibits a broad visible emission covering the whole visible region from 400-700 nm and even extends to the infrared region.

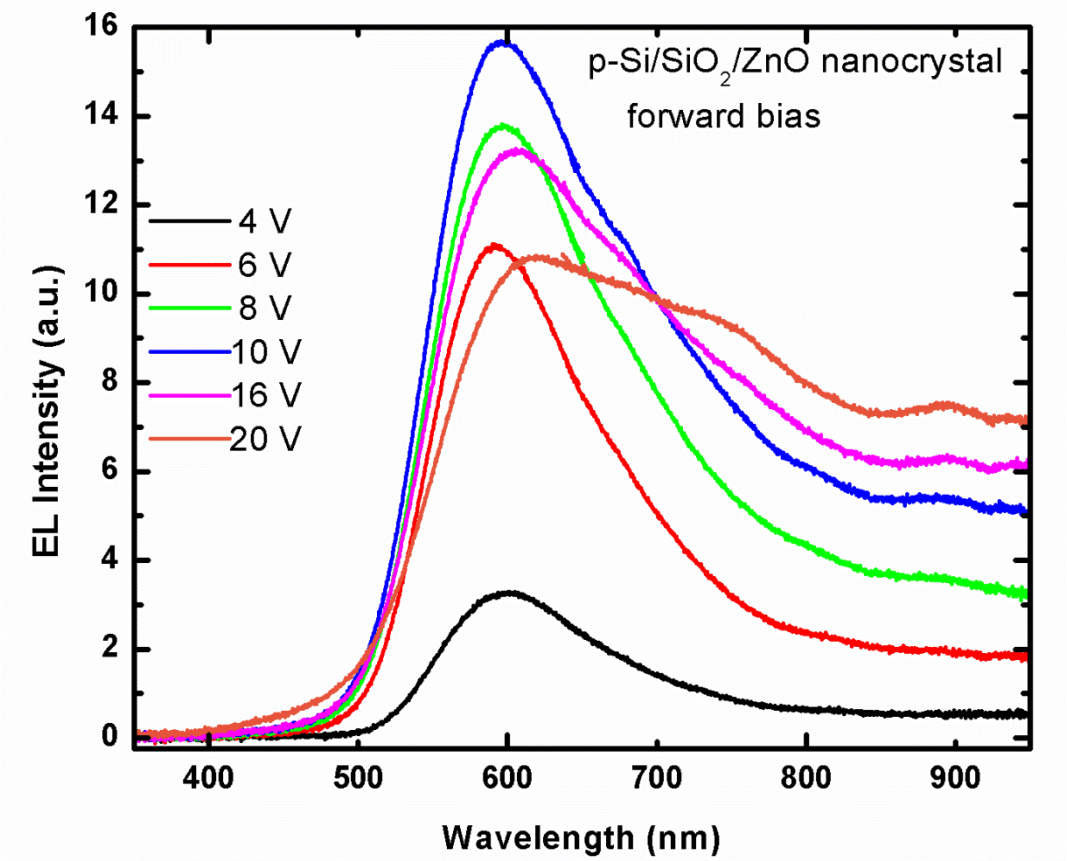

Figure 2.13. EL spectra of device on p-type Si substrate with a 3 nm SiO_2 buffer layer between Si substrate and ZnO nano structured film under forward bias.

EL intensity increases with increased bias voltage. However, it was observed that the intensity reaches a maximum and then tends to decrease after some voltage value. The voltage value for the maximum EL emission is higher for the device with buffer layer than other devices. Upper limit of applied voltage values for reliable operation of the devices also depends on the buffer layer. The forward bias voltage window for the device without SiO_2 layer was between 2.5 to 8 V. At voltages higher than 8 V the devices tended to degrade with a sudden increase of current passing through them, accompanying with a decrease in the EL intensity. For the device with a SiO_2 layer, upper limit of operation voltage could increase up to 30 volts or more without any degredation. It was observed that the presence of a SiO_2 layer could also enhance the EL intensity of the device. In the reverse bias (top contact hold positive potential with respect to Si substrate) both devices were inefficient compared to the forward bias case; especially for the device without SiO_2 buffer layer EL intensity was very

low and easily saturated (it is not shown here). In Figure 2.14, EL results of device having a SiO_2 layer is seen under reverse bias. While the detectable EL threshold was around 12-14 V in these samples, the EL spectra under reverse bias are almost same as the forward bias case, except that an additional emission band emerged at around 450 nm for the bias voltage values of 23 V and 26 V.

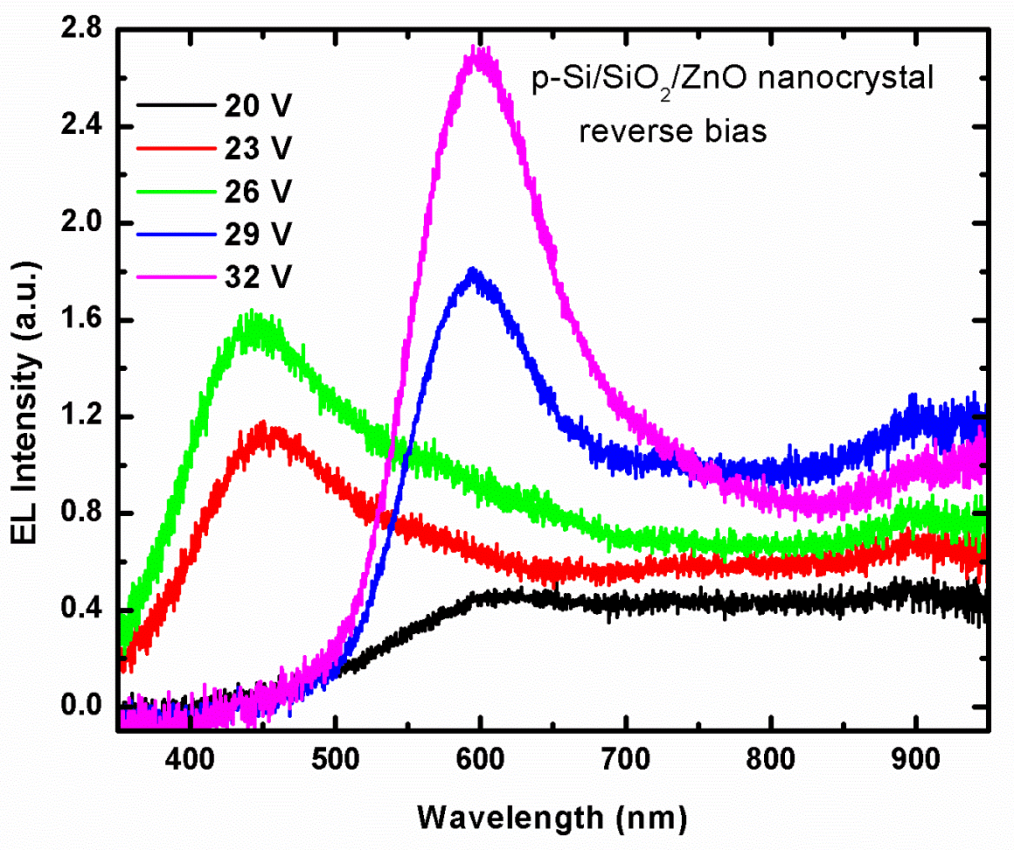

Figure 2.14. EL results of device build on p-type substrate with SiO_2 buffer layer between Si substrate and ZnO nanocrystalline layer, under reverse bias.

Devices fabricated on n-type silicon show almost same behavior with the devices built on p-type Si, only the bias voltage polarity was reversed. In the forward bias, EL spectra of the device without buffer layer is shown in Figure 2.15; it is seen that the band edge emission from ZnO nanostructure is observed at around 365 nm which is a slightly lower than that generated by bulk ZnO (for bulk it is around 375-380 nm). This small difference may be due to the quantum confinement effect occurring in smaller nanocrystals. This observation is the exceptional case in which UV

emission was observed in the EL spectrum, but it is too low in intensity. We also see a few other emission peaks at low energy side of the spectra which are related to the defect levels present in the band gap of the ZnO layer.

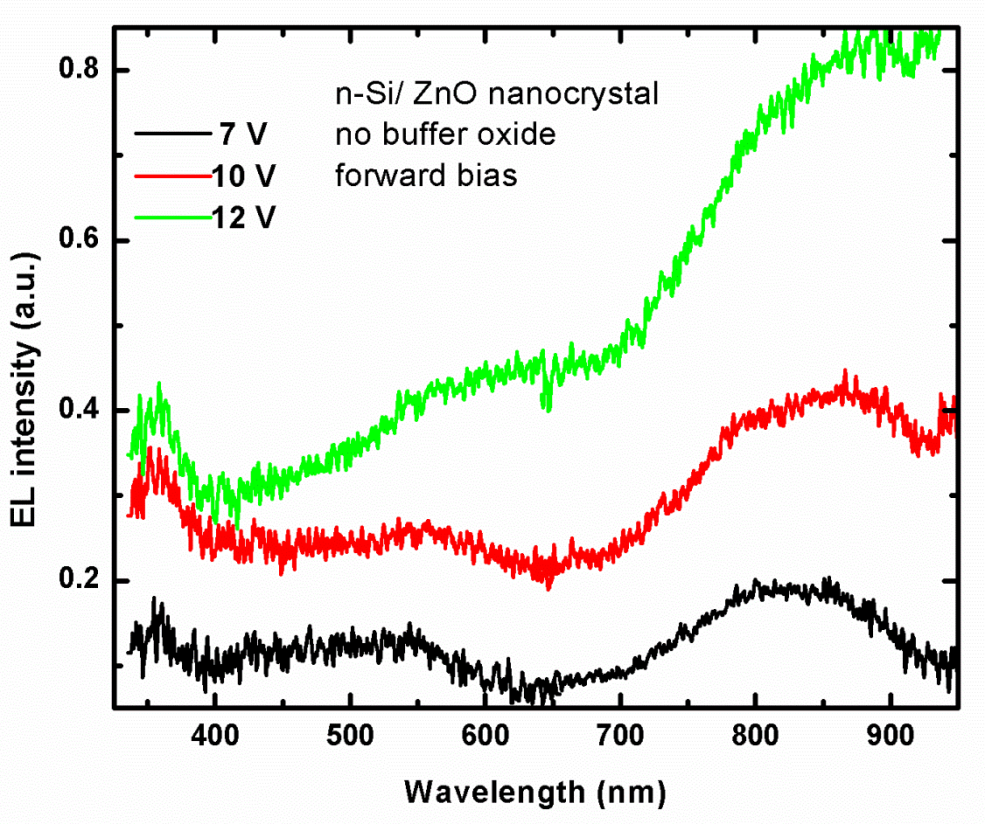

Figure 2.15. EL results of device fabricated on n-type substrate without SiO_2 buffer layer under forward bias.

In Figures 2.16 and 2.17, EL results measured from the devices on n-type Si substrate with and without buffer SiO_2 layer under reverse bias are given. When these EL spectra are compared, there are some differences that can be easily seen. In agreement with the results presented above, devices without buffer layer have a lower threshold voltage for EL emission than other devices having an oxide buffer layer. However, the upper operation voltage limit for un-buffered device is very low and its EL intensity first reaches a maximum at some voltage value and then decreases with increasing bias voltage. Looking at the results from device with buffer layer (Figure 2.17), we see that the emission threshold is higher (around 10-12 V)

than un-buffered one and the EL spectra is complicated due to the combination of few defect related emission levels whose peaks are located in between 550-700 nm.

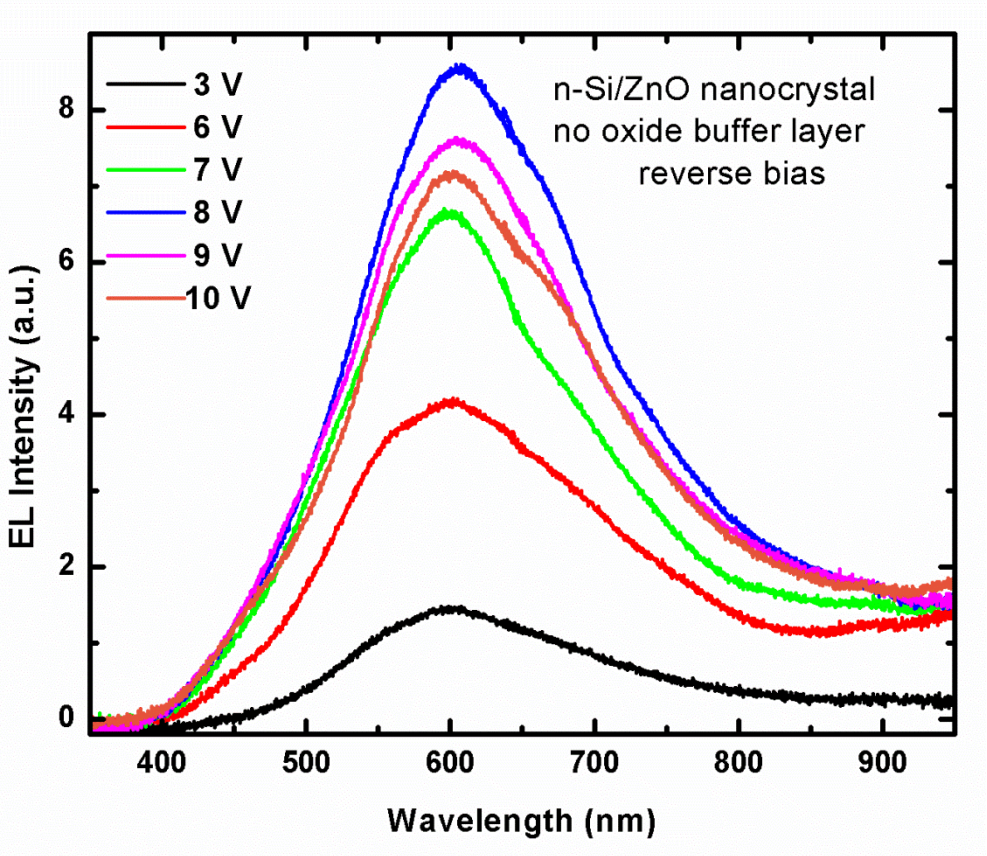

Figure 2.16. EL results of device fabricated on n-type substrate without SiO_2 buffer layer under reverse bias

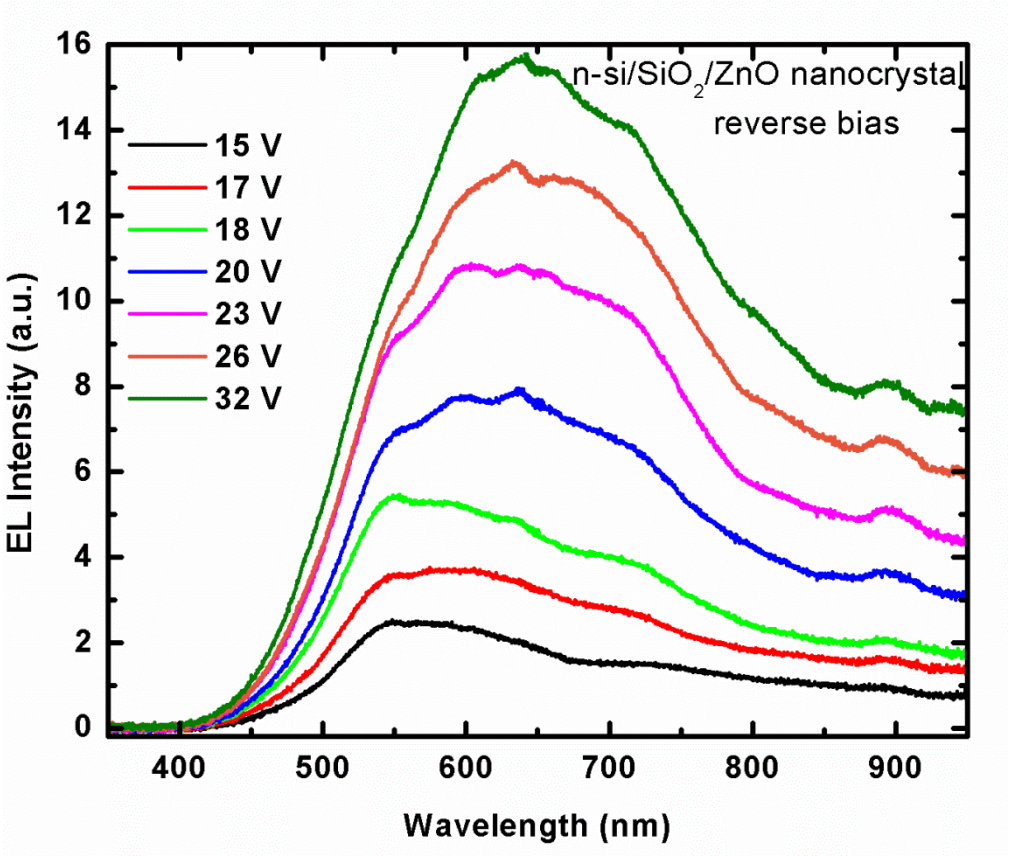

Figure 2.17. EL results of device fabricated on n-type Si substrate with buffer SiO_2 layer between substrate and ZnO nanocrytalline active layer, under reverse bias.

2.3.5. Discussions on EL results of ZnO nanocrystals/Si heterojunctions

Except for one device (Figure 2.15) with very low UV EL emission, we could not observe any UV emission generated by the band edge transition from the ZnO nanocrystals. Contrary to clear observation of UV emission due to ZnO band edge emission from PL the measurement which indicates good crystallinity of starting nanostructured active layer for successive device operation, EL measurements exhibited totally different behaviour. All EL emissions are broad in spectrum and cover whole visible region from 400 nm to near infrared due to radiative recombination of carriers in band gap states of ZnO. The visible emission from ZnO is directly related to the native point defects such as vacancies (V_O and V_{Zn}), self-interstitials (Zn_i and O_i) and also incorporation of impurity states might cause visible emissions [85,86]. In Figure 2.18, several native point defects that have been considered for origin of visible light emissions from ZnO are shown.

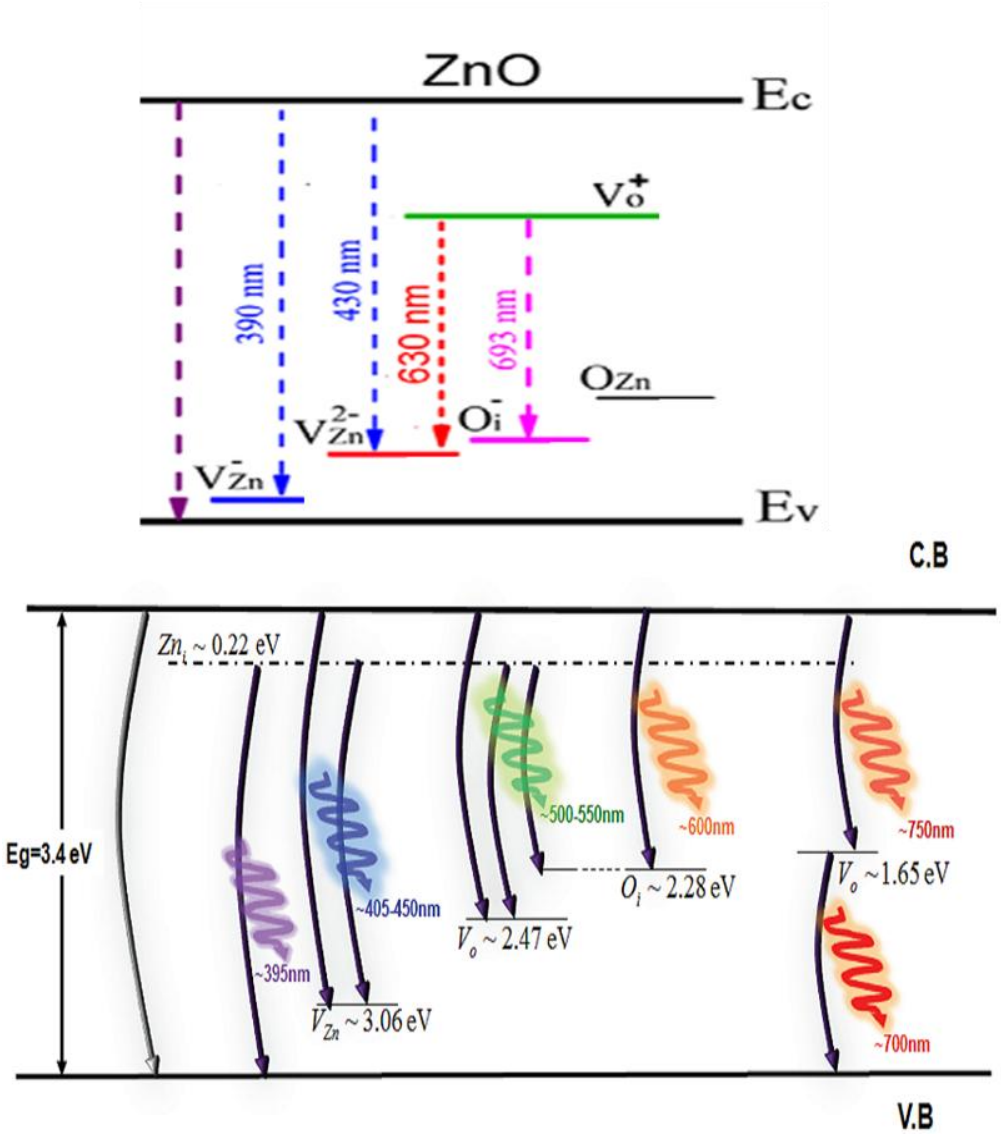

Figure 2.18. Various native point defects within the ZnO band gap that cause to visible emissions from ZnO [86].

From the data shown in this figure, one can easily expect that, depending on the growth condition and the type of the defects generated, the color of the visible emissions can be varied. Moreover, for the same defect structures the peak position can be either red or blue shifted. In the presence of those defect levels direct band gap transition path can easily be blocked. With this prediction, we suggest that either the nature of the excitation mechanisms for EL emission, or the defect formation in the fabrication processes that make large surface region of nanocrystals very defective, which prevent the successful device operation in UV region of the

spectrum. One particular process is the window deposition by the sputtering technique that would create high density of defects through the collision of energetic deposition materials with ZnO nanocrystal. Furthermore, annealing step for contact enhancement could change the compositional ratio in the nanocrystal layer and during this annealing; reaction with ITO layers might produce large defective surfaces. These processes should be systematically studied to understand their specific effects on the EL operation.

The presented EL observations show that Si band edge emission that was seen in the test devices are no longer observed in the devices that contain ZnO nanocrystal as the active emitting layer. This is most probably due to tunneling of holes in to the ZnO nanocrystals more easily due to the fact that the valance band offset between ZnO and Si is smaller (see Figure 2.9) which results in easy tunneling of holes to either valance the band or to the respective defect states directly at the ZnO/Si interface. Alternativaly, holes can move to the same energy levels by a direct or tunneling mediated transfer by the defect states located in the oxide layer. The presence of a thin barrier oxide layer between ZnO and Si regulates the tunneling (injection) of holes into the ZnO nanocrystals with an enhanced bias window which is much wider than that of the sample without an oxide layer at the expense of slight increase in turn on (threshold) bias value. Moreover, the spectra of devices with oxide barrier layer include few emission centers imposed on main band centered at about 600 nm (related with insterstial oxygen, sometimes attributed to oxygen vacancies) (Figure 2.13 and 2.17). Those bands are at about 550 nm which originate from the oxygen insterstitials and bands at about 700-750 nm are from the oxygen vacancies. However, we could not identify whether or not the barrier layer contributes to lower energy tails seen in the spectrum. In addition to the oxygen related visible emission bands, a blue emission band peak seen at around 440 nm is related to the insterstitial Zn point defect. This peak emerged at specific values of the applied voltage (Figure 2.14) under the reverse bias of the device fabricated with an oxide barrier on p-type Si. However, the origin of this voltage dependent color switching could not be understood. It can be suggested that, the appearance of these new peaks in EL spectrum could be due to two effects: First one is that the nature of the nanocrystals changes with the type of the underlying substrate or with the process to fabricate

them. Use of amorphous SiO_2 or crystalline may lead to differences in the nanocrystals properties. Another possible mechanism is that different charge injection mechanism and excitation dynamics are dictated by two different interfaces. This point needs to be studied in a more detailed and systematic way to understand the mechanism underlying the multicolor emission from the ZnO nanocrystals.

We have already proposed several charge injection mechanisms in order to explain the electrically driven light emission from ZnO structures. We have mainly discussed the models based on the bipolar carrier injection and impact excitation by unipolar injection of hot carriers, mostly the electrons. For the bipolar generation of EL model, electrons and holes are simultaneously injected into the active ZnO layer, and then the EL emission occurs via radiative recombination of these carriers within the emitting material. In the impact excitation model, electrons tunneling through the barrier that have sufficient energy could excite electron-hole pairs within the ZnO nanocrystal through inelastic scattering. Depending on the quality of the crystal, the created carriers relax to the valence band either by a band-to-band transition or by a transition through the energy levels located in the band gap. Besides, both mechanisms can work simultaneously depending on structure of the fabricated device and the strength of the applied voltage.

The EL results presented in this chapter suggest that under the condition in which holes could be supplied by the Si substrate into the ZnO nanocrystal layer, the efficiency of the devices is significantly higher than the electron injection case. Holes could be supplied under forward bias over the accumulation layer of the p-type substrate and supplied under reverse bias over inversion layer of the n-type substrate. This suggests that the dominant EL emission mechanism should be bipolar injection of carriers from their respective terminals into the ZnO nanocrystal layer, namely electrons from ITO side and holes from Si side into the ZnO layer. As the three materials used to fabricate the LED form a staggered (type-II) hetero junction, insertion of a barrier oxide layer leads to the formation of a blocking layer for electrons and the ITO/ZnO interface behaves as blocking layer for the holes. This means that the oxide layer acts as a carrier confinement barrier for carriers in ZnO nanocrystal region. Furthermore, as the barrier increases towards Si for electrons it

can also balance the carrier injections in favor of the holes. These two advantages of barrier layer enhance EL efficiencies significantly compared to the devices without barrier oxide. However, the contribution of impact ionization could also be involved at higher voltages.

In the case, when electrons are supplied from the Si substrate under reverse bias of p-type and forward bias of n-type devices, the impact ionization is expected to dominate the EL emission. In this bias scheme, as the ITO is degenerately n-type, hole injection from ITO to ZnO layer is very difficult and leaves the impact ionization as the dominant mechanism for EL emission with high turn on voltage values. For the impact ionization, the energy of electrons gained under high field is important, but sufficient energy can be supplied through available length space before an inelastic scattering. Therefore, the barrier oxide could supply higher energy path for the electrons travelling from Si side, and makes devices more efficient and reliable compared to the devices without barrier layer.

2.4. Conclusions

In conclusion ZnO nanocrystals were synthesized by VLS method on p- and n- type Si substrate with and without thin SiO_2 layer. Using these samples, LED structures were fabricated and EL measurements were carried out at room temperature. In addition to ZnO/Si heterojunction devices, control devices without any nanocrystals were also fabricated and tested to understand the EL mechanisms of LED structures. Throughout the EL study presented above, some conclusive results have been obtained.

Contrary to the clear observation of UV emission from the band edge of ZnO in PL measurements, almost all EL emissions were in the visible region, which are related to the native defect levels (vacancies and insterstitials) located in the band gap of ZnO. The dominance of these visible EL emissions was attributed to either to the structural changes during the device fabrication processes or to the different nature of the excitation mechanisms of electron hole pair under the applied voltage.

Devices having an oxide buffer layer seem to have more tolerance to higher voltage-applications and more reliable compared to the devices having no SiO_2 buffer layer. Therefore SiO_2 buffer layer acts as a controller and regulator for the charge transport which results in a more reliable and efficient EL device by preventing over injection and breakdown. For an efficient device operation; hole injection from the substrate is required (forward bias condition for the devices on p-type and reverse bias condition for the devices n-type Si substrate respectively) over the hole accumulation layer in the p-type substrate and from the inversion layer in n-type substrate. In this biasing scheme, the dominant mechanism for the EL emission is the bipolar injection of carriers in to the ZnO crystal layer. In the case of electron injection from the Si substrate, the light emission mechanism should be impact ionization, because of the difficulties of hole injection from ITO layer. In this case hot electrons should be supplied by the Si substrate.

Finally, ZnO nanocrystal/Si heterostructures can be exploited for fabrication of light emitting devices with optimized growth condition and device design. Because ZnO/Si heterostructures combine the advantages of the large band gap and exciton binding energy of ZnO with maturity of Si technology with cheap and large size substrate they have a great potential for future silicon based LED applications. By controlling defect to band edge emissions ratio with process control and non-defective encapsulation of ZnO nanocrystals with some delicate new approaches, efficient white LEDs, which do not require extra phosphor light converting layer, can be produced.

CHAPTER 3

LIGHT GENERATION BY Si NANOCRYSTALS AND APPLICATIONS TO MOS TYPE LED DEVICES

3.1. Introduction

Although Si is the leading material in microelectronics technology, as a photonic element it is rarely used in few photon absorbing devices and in the read-out circuitry of optoelectronic systems. Being an indirect gap material, the absorption and emission of light requires involvement of at least one phonon in bulk Si. Competitive non-radiative recombination rates are much higher than radiative ones and most of the excited pairs recombine nonradiatively. This condition makes Si an inefficient light emitter with very low internal quantum efficiency. For this reason, more complex and expensive semiconductors, such as GaAs, InP, GaN, ZnSe and etc. are used to make light emitting and high-speed telecommunication devices.

In 1990, Canham achieved the efficient luminescence from porous silicon [20] and this study attracted much interest towards the silicon nanocrystals. However, from the application point of view, difficulties arise from the instability problem of porous Si that consists of a network of nanocrystallites which are not isolated from each other. This is a very complex system that depends on a variety of its fabrication and storage conditions. Because porous silicon suffer from poor stability due to the fragile hydrogen surface passivation, where oxidation of nanostructures easily takes place even at room temperature, it is not suitable for existing technology and mass production. To overcome these drawbacks of porous silicon, many research groups around the world have been searching new techniques and approaches to produce efficient structures containing luminescent silicon nanocrystals [87-91].

The most promising approach has been the formation of nanocrystal inside silicon dioxide (SiO_2), that have the superior properties compared to porous silicon in

mechanical strength and good passivation of grown structures. These properties lead to a good resistance to ambient conditions and prevent non-radiative escape of excited carriers in the dots. Additionally, SiO_2 allows the fabrication of desired advanced devices in both electronic and optoelectronic area and gives a flexible tool of playing with the optical property of nanostructures by just changing the growth parameters easily. Today we know that many nanocrystalline structures of different materials can be fabricated in the SiO_2 matrix: Si, Ge, SiGe, SiC, some metals and some other kinds of compound semiconductor such as CdS and CdSe [87, 92-94]. From these materials, Si nanocrystals are the most studied structures due to the good interface conditions with SiO_2. Silicon nanocrystals are produced from the super saturated SiO_2 with Si atoms introduced either by ion implantation or during the growth of the oxide such as by sputtering, chemical vapor deposition (CVD) or electron beam deposition of SiO_x film.

Besides the light emission from Si nanocrystals in various matrix, incorporation of Rare Earth (RE) elements in to the Si platform active luminescent centers has recently been subject of intensive studies. Actually, RE ions in Si based structures do not require Si nanocrystal for light emission. Si, SiO_2, Si-nitrate could be a host matrix for those ions. However for ions dispersed in Si itself mostly suffer from back energy transfer to the host substrate (Si). It has been recognized that, doping the Si nanocrystal/SiO_2 systems increases the luminescence efficiencies of RE ions due to the energy sensitization role of nanocrystals for the RE atoms. Incorporation of RE elements in to the Si nanocrytal environment gives a tool for wavelength engineering from UV to IR with narrow spectral distribution through atomic transitions of different types of RE elements. With this method, wide and near infrared emission (mostly non-useful for various photonic applications) of nanocrystals can be converted to efficient atomic transitions for numerous practical applications.

This chapter is devoted to electroluminescent properties of different types of Tb doped SiO_2 either containing Si nanocrystal or in stochiometric form. We have also investigated the light emitting behaviors of the same system without Tb inclusion. EL results obtained on the MOS-LEDs based on Si nanocrystals only are given. As being the host matrix for Si nanocrystals, the basic properties of SiO_2 and the

formation mechanisms of nanocrystals in this matrix are presented for the sake of completeness. Moreover, general properties of RE elements and their interactions with each other and Si nanocrystal/oxide systems are also discussed.

3.2. SiO_2 and its properties

The general name called *silica* comprises all compounds of silicon and oxygen with the composition SiO_2 with a large number of polymorphic forms. These forms are determined by thermodynamic stability ranges; pressure, temperature, reaction dynamics etc. But all of these solids share a common composition, a common chemistry, and even a common structural element: substantially covalent [SiO_4] tetrahedral unit; but they are structurally very different [95]. Amorphous SiO_2 preserves much of the ordering present in the crystalline forms on a short or intermediate length scale. The origin of this surprising structural multiplicity lies in a parameter known as rigidity that is related to the structural topology i.e. the ways of atoms or group of atoms connected together [96].

The basic bonding unit for all these forms of silica is the SiO_4 tetrahedron. Four oxygen atoms surround each silicon atom with the Si-O distance ranging from 0.152 nm to 0.169 nm; the tedrahedral O-Si-O angle is 109.18˚. Each oxygen is bonded to two silicon atoms, with the Si-O-Si angle varying from 120˚ to 180˚ depending on the form of the SiO_2. All forms are constructed from the corner- sharing tetrahedra as the SiO_4 building block, tetrahedral units are connected together at the tetrahedron vertices through a common oxygen atom, but there are many ways to do so, in both regular and irregular arrangements. In crystalline forms, the tetrahedral arrangements are regular and exhibit long range orientational and translational order. For the amorphous structures orientational and translational invariances are relaxed slightly or totally with short order arrangements [97].

Silicon dioxide (with a band gap of 9 eV) has been one of the most extensively studied materials in material science and condensed matter physics. SiO_2 plays a central role in many of today's technologies, including fiber optics and satellite data bus applications, as the gate and field oxides in 95 % of all metal-oxide-

semiconductor (MOS) devices, as windows, photo masks, and tranmissive optics for ultraviolet-laser chip lithography, and as thin films for highly reflective (or highly transmissive) coatings for laser optics. Moreover, SiO_2 has been an important host matrix for the formation of nanocrystal structures of many elemental and compound materials. Despite the technological importance of SiO_2 and the amount of studies done on defects, color centers, kinetics etc. many puzzles still remain.

Today most of the studies on SiO_2 are about defects and their properties. Defects in SiO_2 can manifest their presence as e.g., by exhibiting luminescence and/or optical absorption bands or they may show themselves as charge trapping centers. Defects can be introduced in the manufacturing process or induced by ionizing radiation (X-ray, ultraviolet photons etc.) or particle irradiations e.g. ion implantation. If we consider the important applications above, it is easy to understand the control and the identifications of these defects could result in billions of dollars in cost savings to both photonics and semiconductor industries now and over the next decade.

There are lots of types of defects in silicon dioxide; some of them are luminescent centers at various colors from red to ultraviolet in the SiO_2 band gap. In the framework of this study, some of the absorbing and radiating/nonradiating (or luminescence bleaching) centers resulting from oxygen excess and deficiency in SiO_2 will be given briefly.

The oxygen excess centers are formed in SiO_2 either as excess number of oxygen or as displacement of oxygen by external excitations and radiations, such as ion implantation. The well known center of this type is the oxygen dangling bond or non-bridging oxygen hole centers (NBOHC)**.** NBOHC (≡Si−O•) is the best characterized intrinsic defect in SiO_2. This center has two absorption bands at 1.97 eV and 4.8 eV and a luminescence band at 1.91 eV [98,99]. Oxygen deficiency centers can be generated by the excess silicon in the oxide or due to the lack of the homogeneous oxidation of silicon atom on the substrate surface. Actually many defects can be described using a model based on the oxygen vacancy depending on the coordination number of silicon and paramagneticity of the center. Among them, P_b center (Si≡Si•) is the well known type which is created by the the dangling Si bond at Si/SiO_2

interface and the dangling bond towards the oxide [100]. This defect is generally assumed to play a major role in the luminescence quenching of the silicon nanocrystals. The other two important oxygen vacancy generated defects are E' (O≡Si•) and B_2 (O≡Si−Si≡O) centers having known absorption bands at 5.79 and 5.00 eV and luminescence bands at 3.1 and 2.7 eV [101,103].

3.3. Formation of Si nanocrystals with Si rich SiO_2

At the beginning of the twentieth century a biologist W. Ostwald discovered the ripening process in biosystems. After him, the theory has been elaborated and adapted to the formation dynamics of the almost all systems including the formation kinetics of the nanocrystals including Si nanocrystals in various matrices [104]. Ostwald ripening simply clarifies the increases in average size of islands or nanocrystals. The growth occurs as the exchanging of atoms between small and big neighbor islands by detachment of atoms from smaller ones and attachment to bigger ones. The decrease in surface energy is usually assumed as the driving force for the Ostwald ripening, so that when two microparticles interact with each other by exchanging mass, the larger one grows at the expense of the smaller one. Larger clusters or droplets are energetically more favorable due to their smaller interface curvature or smaller surface area to volume ratio. Thus they grow at the expense of smaller clusters which resolve again and finally disappear. This collective behavior leads to increase in average island size and simultaneously to decrease in the total number of nanocrystallites.

For the formation of the Si nanocrystals in SiO_2 the first requirement is the super saturation of the oxide by the silicon atoms, it can be done in two ways; either during the growth of Si rich oxide like in the co-sputtering or by high dose Si implantation into the thermally grown oxide. It means that Si incorporation into stochiometric oxide must be much higher than the solid solubility of Si in the SiO_2 to initiate phase separation of Si from the oxide for the nanocrystal evolution. When the dose of Si in SiO_2 exceeds 10^{21} cm^{-3} (~ 2%), the average distance between Si excess atoms is around 1 nm [105]. For such doses or more, the distance between the more closely spaced Si atoms becomes comparable with the Si − Si bond length and atoms are

then in interaction with each other. Even without any thermal treatment Si − Si bonds can be formed resulting with small clusters or percolation chains. For the concentration less than at 1%, small cluster formation requires temperature enhancement. Subsequent annealing is needed in phase separation of the Si from Si rich oxide. Since, thermal treatments can stimulate an onward growth of the induced precipitates up to the state of coalescence, where closed buried layers or nanocrystalline structures can be formed. In general, phase separation process is expected to be a consequence of few physical mechanisms; nucleation, growth and Ostwald ripening of Si precipitates. All these mechanisms are result of some randomly occurred elementary events like bond breaking, bond forming, diffusional jumps of atoms, chemical reaction etc [106].

There are several parameters that effect the formation of nanocrystalline Si structures in SiO_2: annealing temperature, annealing time, initial excess amount of Si atoms etc. Having a small diffusion constant of Si in SiO_2, the formation of Si nanocrystal in the oxide requires very high temperature treatments with long annealing time. Si nanocrystallites do not form below 900 ºC annealing temperature and very long period of time is needed between 900 ºC and 1000 ºC. Therefore we can accept that the threshold temperature for a well seperated Si nanocrystal in SiO_2 is at least 1000 º C [107,108].

For a fixed super saturation and temperature, the mean radius increases only very slowly when increasing the annealing time up to 16 hours. When annealing time and Si excess are fixed, the mean radius increases with the increase in temperature by decreasing nanocrystal density. At very high temperature annealing (over 1100 ºC) the mean radius will be stable for some period of time of annealing because at this temperature there is a competition between the Ostwald ripening process and the dissolving process of nanocrystals with migration of Si atoms to the substrate Si/SiO_2 interface. This Si loss to the interface decreases the density of nanocrystal, but Ostwald ripening is more effective than Si loss to the interface, so at the end, the size of the nanocrystal increases with decreasing number in the oxide. In the case of varying degree of supersaturation, as other fixed parameters (annealing temperature and time), both size and the density of nanocrystal increase with the concentration of

excess Si. This situation can be easily seen for ion implantation method due to the Gaussian concentration distribution of the Si atoms. The highest concentration is seen at the peak of distribution and it decreases toward the tails at both sides, then one can expect that the larger nanocrystals will be formed at the middle of the implantation range and they reduce in size and in density toward the tails in accordance with the concentration profile.

3.4. Optical properties of Si nanocrystals

Before discussing the general predictions of the quantum confinement effect on the basic light emission/absorption behavior of Si nanocrystal in the oxide, it will be meaningful to give general optical properties of bulk Si. Simplified energy band structure of Si was given in Figure 1.1. The top of the valance band is located at the Γ point (k=0) at the center of Brillouine zone and six equivalent conduction band minima in the symmetries of directions, centered at the Δ= (0.85, 0, 0) π/a points, where **a** is the lattice constant of Si. Therefore direct absorption and emission of light are impossible and require the emission or absorption of phonon to supply the discrepancy in the momentum between these extreme points. The only possible scenario for the optical transitions is the following: a photon causes a vertical virtual transition at k=0 (top of the Γ point) or 0.85π/a with subsequent electron phonon scattering process. So with these secondary processes the probability of absorption and especially the emission of photons in the Si stay very low compared with any direct band material. Since the radiative time of indirect transitions are very long, excitons can travel very long distances in their thermalization process and the chance of finding nonradiative recombination channels become very high. The only possible direct transition is the Γ- Γ absorption of the photons with and energy of ~3.1 eV between valance band maxima and conduction band minima.

However, in the case of nanocrystalline structure of the silicon in SiO_2, the spatial confinement cause to spreading of exciton wave function in momentum space that result in the breakdown of k- conservation rule in Si nanocrystals. Therefore, no-phonon (NP) optical transitions become possible with increased oscillator strength which is directly proportional to the reciprocal space overlap i.e size of the

nanocrystal. It is reported that for the same confinement energy no-phonon (NP) transitions are about three times stronger in Si nanocrystals in SiO_2 or having a SiO_2 shell [109,110]. Two effects of opposite nature can be accounted for the observed tendency depending on the quality of the Si-SiO_2 interface. First one is the carrier scattering at the Si nanocrystal oxide heterointerface, responsible for the suppression of the k-conservation rule and it is assumed to be strongly dependent on the interface abruptness. Second one is the confining potential (for a fixed size) is lower for a Si nanocrystal surrounded by SiO_x compound ($x<2$) than SiO_2. To achieve the same confinement energy, smaller size nanocrystals are required, giving rise to a relative increase of NP transitions. The lower confinement potential leads also to the smaller size dependent variation of the photoluminescence (PL) maximum [88]. To obtain good confinement effects, Si nanocrystals must be well separated from each other, where there is a low limit of distance to avoid cross-talk between neighbor nanocrystals to produce efficient emission.

Although Si nanocrystals have high PL yield, they behave as indirect semiconductors, keeping some properties of bulk Si with long radiative lifetime. In the photon absorption-emission cycles both NP and phonon-mediated processes take place simultaneously. Therefore optical properties of Si nanocrystals have to be considered on the basis of competition between indirect and quasidirect recombination channels [111]. As nanocrystal size decreases, it can be predicted from the confinement theory that the probability of NP transitions should increase with respect to the phonon-assisted (PA) transitions which imply the radiative oscillator strength and absorption cross section per nanocrystal are much larger for smaller size Si nanocrystal than larger ones [112]. However, it is rather complicated to find accurately the exact ratio of NP/PA transitions because the exact shape and size distribution of the nanocrystals and the energy dependence of the absorption/emission process in Si nanocrystals are not known. The major scaling parameter in all these effects is the size of the nanocrystal R [113,114] and NP transitions which are expected to be proportional to the volume of crystallite inversely $(1/R)^3$. With this expectation, NP transitions begin to dominate at the confinement energies of the order of 0.65 – 0.7 eV.

In addition to the enhancement in the optical transitions in Si nanocrystal relative to the bulk case, the important feature related with the quantum confinement is the increasing of band gap energy as a function of the nanocrystal size. The band gap variation as a function of size can be simply written from the confinement theory for a three dimensionally confined Si nanocrystal as;

$$E(eV) = E_{bulk} + \frac{C}{R^2} \tag{3.1}$$

Where E_{bulk} is the bulk silicon band gap, R is the dot radius, and C is the confinement parameter [115]. Therefore the expected result from the theory is that, as the size of the nanocrystal decrease there is a blue shift in both absorption and emission of the photons. Theoretically calculated optical energy gap dependence of Si nanocrystal size is given below with several groups [116].

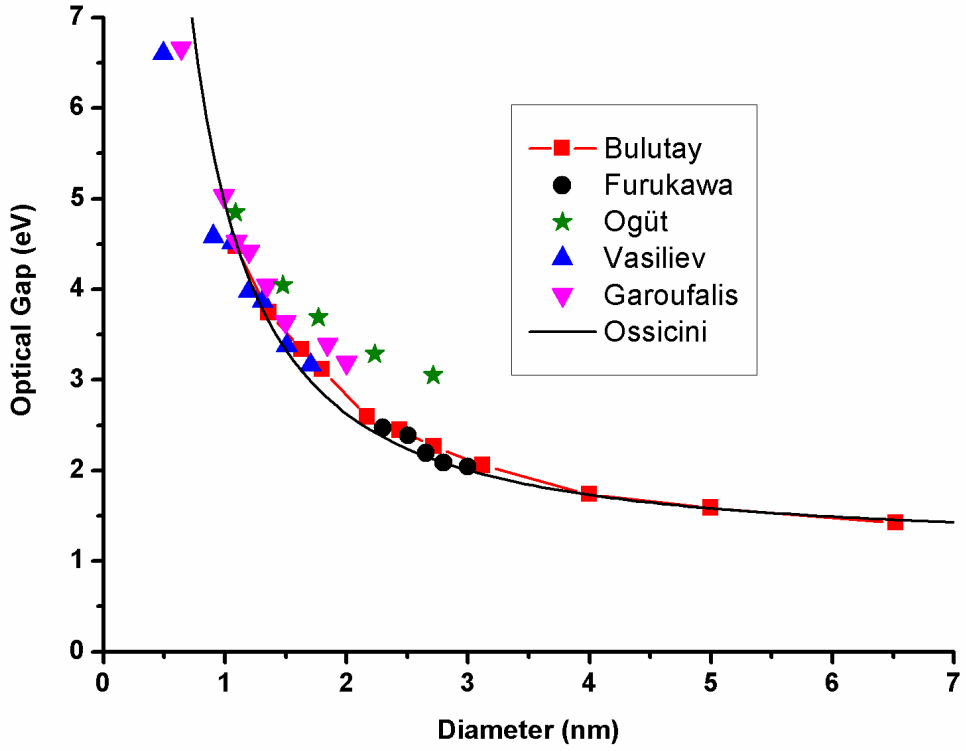

Figure 3.1. Theoretical calculated results of size dependence of optical gap of Si nanocrystals by several groups [116].

3.5. Si nanocrystal/SiO_2 based light emitting devices (LED)

So far, different types of Si based electrically driven devices have been demonstrated using different approaches: Si p-n junction, MOS structure using thin layer of SiO_2 tunneling layer, introduction of dislocation loops, $FeSi_2$ precipitation in Si, rare earth incorporation, nanocrystalline porous Si, Si rich SiO_2 etc [117-128]. As a pioneering material of intense Si based light emitter researches, porous Si was tested for wavelength engineered Si LED applications, but the biggest obstacle of mechanical robustness and stability of structures has been preventing the application of porous Si to commercial industrial products such as LEDs. On the other hand, light emitting devices (LED) using the system of Si nanocrystals distributed in SiO_2 systems has been considered as a viable option that is compatible with the Si CMOS based technologies for variety of photonic applications. Si nanostructures embedded in SiO_2 are superior over porous Si due to fairly strong and stable light emission with easy modification of emission from visible to infrared. In the two decades, many different Si nanocrystal/SiO_2 LED structures have been reported using a variety of different production techniques. In the device operation, it is reported that application of AC/pulsed voltage could be more advantageous than DC biasing, especially for the stability of the devices for long term operations [129].

EL emission from Si rich SiO_2 can be classified depending on the spectral regions where the EL emission depends on the type of emission centers: it is either related to the matrix defects or to the excess Si, Si nanocrystals or defect states at the nanocrystal surface. Generally, emission bands at green, blue and even UV are attributed to the point defects in the oxide band gap. Whereas red and near infrared EL from Si rich SiO_2 are mostly ascribed to the electron-hole pair recombination in Si nanocrystals [130,131]. However, there is no exact demarcation line for the red emission which is either from nanocrystal or from well known oxide defects of NBOHC due to excess oxygen mentioned before. The only clue for discrimination might be that the peak position of the emission generated by the matrix defects is almost independent of the fabrication conditions. The intensity of different EL bands strongly depends on the fabrication details such as excess Si concentration, annealing conditions and annealing time.

Usually, LED structures of Si nanocrystal/oxide systems are in the form of standard Si-MOS device. The EL active Si rich oxide layer(s) is sandwiched between Si substrate and transparent optical window (ITO, semitransparent metal or poly-Si), and the device is driven by injection of carriers into the active layer under either DC or AC bias. Generally, the excitation mechanism works through impact ionization by hot carriers under high field conditions [132]. However, a few research groups have reported devices working on field effect phenomena [133], where electron and holes sequentially tunnel into the nanocrystals through thin oxide layer from underlying Si substrate under AC bias, and recombine there radiatively.

3.6. Excitation and charge injection mechanisms in Si NC/SiO_2 MOS-LEDs

In traditional p-n junction LEDs, EL occurs in depletion (or sandwiched active region) region through recombination of electrons and holes diffused from n and p side of the junction under forward bias. In a MOS device, the leakage of electrons in valence band or holes does not exist, so light must be produced by other means. In Si nanocrystal-MOS LED, this may be the case, since hole injection from Si valence band to the SiO_2 valence band is difficult because of the larger energy barrier than for electrons from window layer to the conduction band, as illustrated in Figure 3.2. As the injected current strongly depends on the barrier heights seen by carriers, the electron hole recombination is much more improbable in MOS based LEDs.

Electroluminescence is explained by mechanisms that include field ionization of the luminescent centers, charge trapping and impact excitation by hot carrier and radiative recombination. In these descriptions, different conduction mechanisms can be considered as shown in Figure 3.2. However, two of them, namely, direct tunneling and Fowler-Nordheim (FN) tunneling, have been widely used to explain the experimental observations. Having high threshold voltage of EL, the dominant mechanism is likely to be the tunneling of hot carriers (FN) from a nanocrystal to another one through insulating matrix. A way to reduce the high voltage requirement, is to narrow the oxide thickness. In this case, good quality oxide layers are needed to minimize the leakage current near the breakdown operating conditions of the oxide layer, and to produce enough hot carriers. On the other hand, high concentration of Si

precipitates (or nanocrystal) is needed to generate enough number of efficient luminescence centers inside the oxide. Another disadvantage of using the thin oxide layer is the reduced possibility of carriers to recombine radiatively.

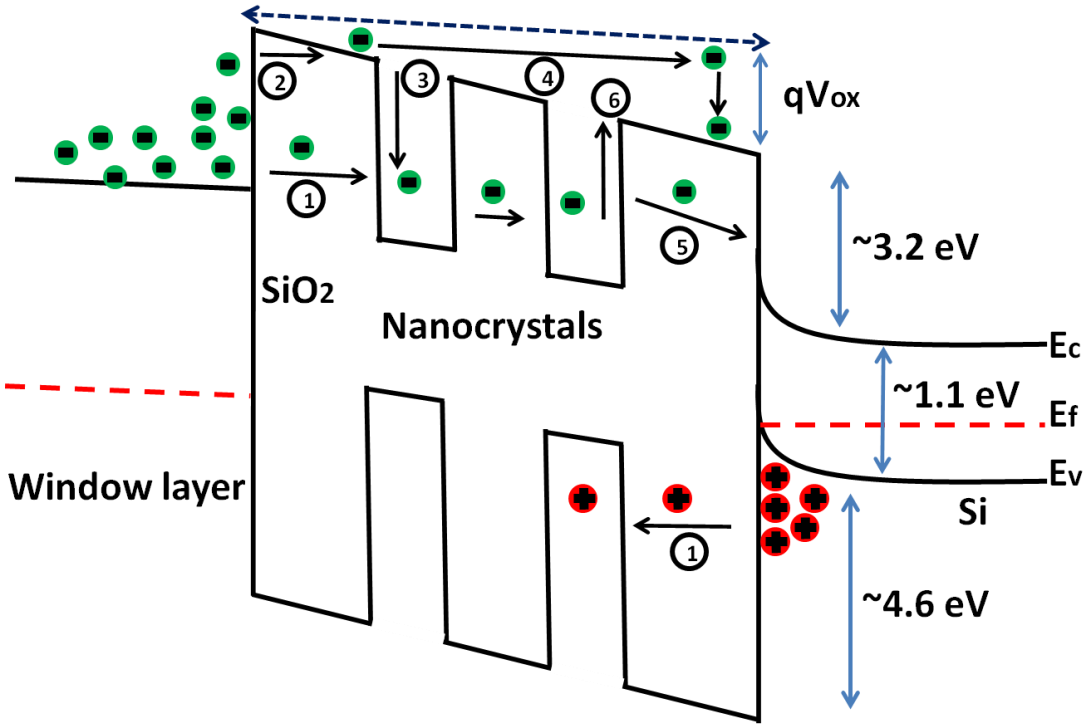

Figure 3.2. Transport mechanisms in Si-NC/SiO_2 MOS structure: (1) Direct tunneling (2) Fowler-Nordheim tunneling, (3) trapping at cluster (NC) and tunneling from cluster (NC) to another, (4) quasi free movement of electrons within the conduction band of SiO_2, (5) hopping conduction, (6) Poole-Frenkel tunneling.

Because the oxide (active layer containing nanocrystals) is thinner, the number of Si nanocrystals in the direction of current flow is reduced. If the current injection occurs via percolation paths, it could be assumed that impurities near the oxide-silicon barrier may lower the voltages needed to inject holes to the oxide layer. In this situation, the trade off with higher doping of Si would be made at least with lower breakdown voltage. However, reducing the excess Si at the favor of threshold voltage will cause the reduction in the number of emitted photons. Hence, the nanocrystal/oxide structure represents a complicated material system whose optimization requires extensive and careful studies.

The direct tunneling is a typical characteristic of very thin oxide layers (< 4 nm) [134]. The analytical equation that presents the current density passing through an oxide layer with thickness t_{ox} under an applied voltage V can be written as:

$$j = \frac{AE^2}{\left[1-\sqrt{1-\frac{qV}{\phi_B}}\right]^2} \exp\left\{-\frac{B}{E}\left[1-\left(1-\frac{qV}{\phi_B}\right)^{3/2}\right]\right\} \tag{3.2}$$

$$\text{where } A = \frac{q^2}{2\pi h} \qquad \text{and} \qquad B = \frac{4\pi\sqrt{2m^*}}{h} \tag{3.3}$$

ϕ_B is the effective barrier height, m^* effective electron mass in SiO_2, E is the electric field and *q*, *h* are the elementary electron charge and Planck constant. The direct tunneling is possible between Si nanocrystals and the substrate if the separation is less than 4 nm. For this case, electrons see a higher barrier than the voltage drop across the SiO_2 layer and the potential barrier appears as trapezoidal form. The electrons, with the presence of this trapezoidal barrier, can travel between a nanocrystal to another one and so move through the SiO_2 matrix.

Fowler-Nordheim tunneling in Si MOS structures has been studied extensively [135]. It is assumed that, this is the dominant current injection mechanism in to the SiO_2 matrix, especially for the thick oxide. The tunneling of highly energetic particles can occur by FN injection. The analytic equation for FN conduction mechanism is:

$$J_{FN} = \frac{A}{4\phi_B} E^2 . \exp\left(-\frac{2B\phi_B^{3/2}}{3E}\right) \tag{3.4}$$

Where the constants *A* and *B* are same given in the Eq. (3.11). The electrons pass through the barrier, due to the high electric field, which is the triangular barrier of oxide band under high voltage.

As the dominant excitation mechanism for EL emission under high field levels, impact ionization may involve other transport mechanisms coupled to the FN: trap assisted tunneling, Poole-Frenkel contribution. In high current injection limits, strong contribution from space charge limited current (SCLC) might be expected. Therefore the total resultant current and recombination channels can not be predicted easily. Requirement of hot carrier injection into the Si NC/SiO_2 active layer results in vulnerable devices. Long term operations lead to breakdown of the device which is an important problem to be overcome along with high turn on voltage limits. Moreover excitation mechanism require extra dead zone that does not contribute to EL of about 10-15 nm to supply sufficient energy for injected carriers to generate impact ionization, pushing the operation voltage to higher values.

3.6. Incorporation of Rare Earth (RE) elements in to Si environment for LED applications

3.6.1. Rare Earths (RE) and properties

RE elements are the metals whose ores are found often together with oxides of the alkaline earths (Ca, Mg) and usually compromise about 15 elements (Eu, Gd, Yb, Nd, Tb, Er, Ce, Tm, Sm etc.). In general, the electronic structure of neutral RE atoms is composed of a Xe electronic configuration, the electronic configuration of RE^{3+} ions can be written as $[Xe]4f^n$ with n being the numbers of electrons in the 4f shell [136]. These f shell electrons are well screened from the local chemical environment by outer 5S and 5P electrons. As a result, their characteristic atomic emissions resulting from the intra f shell transitions are narrow and almost fixed in the optical spectrum. In reality, this intra 4f transitions are parity forbidden, but in host matrices like SiO_2 their interactions with ligand field make RE elements unique light emitters with well defined characteristics [137]. The energy transfer processes are often used in practical phosphors in order to enhance the emission efficiency of REs. Therefore, the band positioning of RE atoms and host are crucially important for effective energy transfer from host (energy donor) to RE (energy acceptor).

RE elements have been intensively used as an active phosphor for visible and infrared applications that are technologically very important over the last 50 years [138]. Nowadays they are one of the hot topics in electrically driven light emitting structures in optoelectronic and sensor fields by dispersing them in numerous host matrices. Those host mediums include variety of glasses and oxides, organic materials, and semiconductors [17,139-144].

3.6.2. RE doping of Si environment for optoelectronic applications

Dispersion of RE elements into Si environment as an active phosphor have been one of the routes for Si photonics. Er is the main RE ion of interest, as allowing suitable IR emission which is very suitable for existing telecommunication window. Huge efforts have been devoted to doping Si with Er for the emission line at about 1.5μm. Although some promising results from bulk Si have been obtained at room temperature the efficiency of the luminescence is limited due to energy back transfer and other non-radiative coupling with host Si substrate [145]. Besides, the solubility of Er atoms in Si is very low for creating sufficient number of phosphor centers.

Recently, instead of bulk Si, SiO_2, Si rich SiO_2 and Si rich Si_3N_4 grown on Si substrate have been proposed as a host medium for light harvesting from RE ions [146,147]. It has been demonstrated that, Si nanocrystals behaving as sensitizer enhances the RE luminescence compared to the stochiometric oxide [148,149]. The energy transfer is evidenced by the increase of the RE related PL intensity with increasing density of nanocrystals and simultaneously decrease in the PL emission originating from Si nanocrystal [150,151]. It could be due to higher excitation cross section of nanocrystal, much more than the RE elements. Using this approach, light generation from Si nanocrystal/SiO_2 systems could be converted to more useful structure through RE ions.

Fortunately, non optical methods (including energy transfer from nanocrystals) for excitation of RE ions where the optical selection rules do not apply, and for this reason the electrically driven luminescence has the potential to reach much higher efficiencies than that of PL. This is mainly due to the fact that EL emission is

generated generally by the impact excitation via hot electrons whose energy distribution is very broad compared to PL excitation sources.

The interest in RE emissions goes beyond telecommunication applications. They find applications in LEDs, displays, lasers, radiation detection, data storage, bio-medical lab on chip and diagnostics, in which RE light emission plays an increasingly important role. Besides the Er doping, other RE elements are gaining importance in Si based photonic applications. In this context, various kind of RE elements have been incorporated into Si environment [152-155]. Among them, Tb doping has attracted special interest as it is having the various emission lines in the UV and visible parts of the light spectrum.

3.6.3. Tb related emissions and concentration quenching

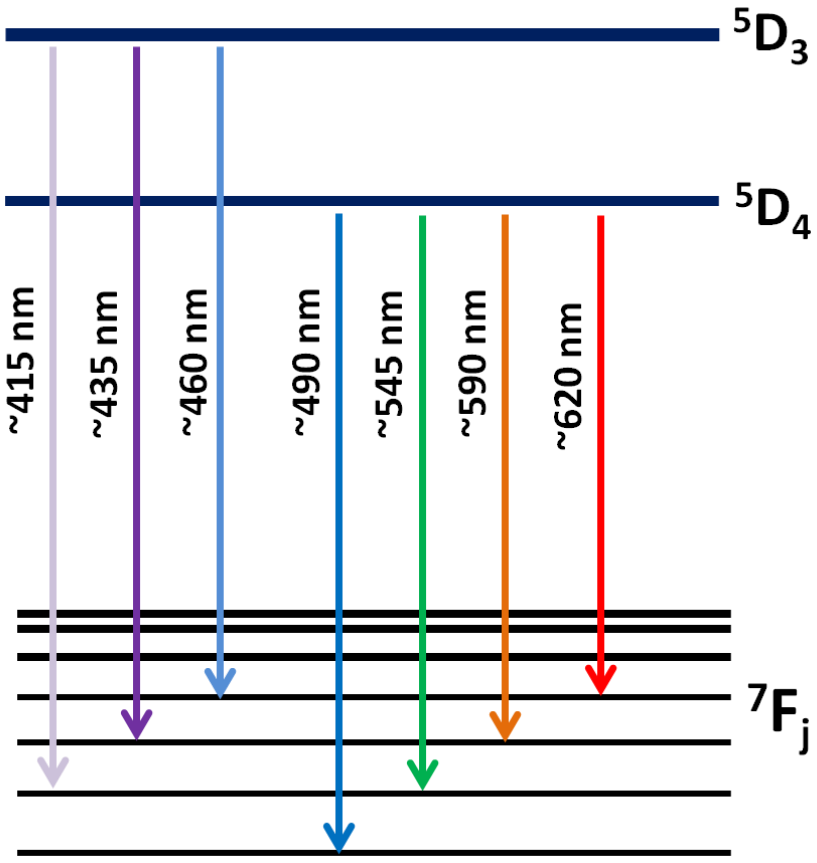

Figure 3.3. Emission lines due to 4f intra shell transitions of Tb^{3+} ion

Tb with 8 electrons in its 4f shell has several distinct emission lines due to intra f-f transitions that can be controlled through distributed concentration of Tb in a host matrix. Tb energy level system offers two excited states, $^5D_4$ and $^5D_3$ from which a couple of transitions to the states ^7F_j are possible. The main luminescence band $^5D_4 \rightarrow {}^7F_5$ around 545 nm constitute more than 50% of overall emission spectrum. The emissions line of Tb from intra 4f transitions is represented in figure 3.3.

If the concentration of a RE (or general manner activator phosphor) ion is higher than a threshold value (usually few wt %), the emission intensity is usually very low. This effect is called concentration quenching of the emission. The origin of this effect is based on the interaction between the phosphor (RE) ions through different interaction mechanisms that are technologically important depending on the practical applications. Although several other energy migration phenomena have been considered for a complete understanding the system, we discuss here the most favorable quenching mechanisms based on the cross relaxation as shown in Figure 3.4.

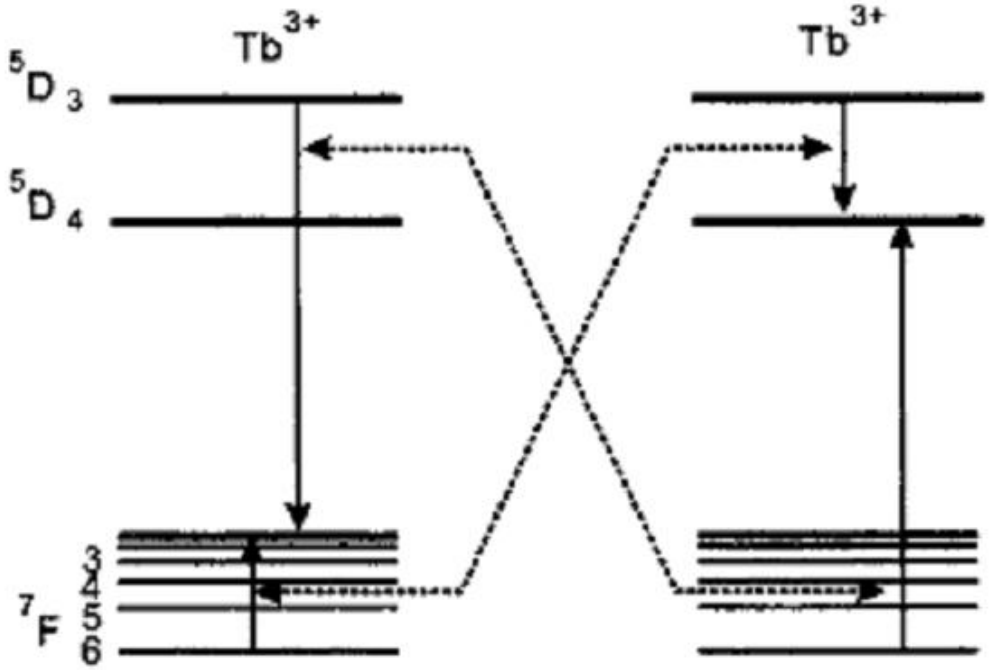

Figure 3.4. Illustration of cross relaxation phenomena between two terbium ions [156].

When the concentration quenching due to cross relaxation (relaxation due to resonant energy transfer between the same RE elements ions) occurs between several emitting energy levels, the emission color of the RE changes with the RE ion concentration in host media. For instance, while the emission color of Tb^{3+} ion is blue- white, due to mixing of the blue-UV emission from $^5D_3$ excited level and green emission from the $^5D_4$ level at concentration below 0.1-0.3 % [157], the color changes to green at higher RE concentrations. The change is caused by the cross relaxation between the $^5D_4$ and $^5D_3$ emitting levels, thereby diminishing the population of Tb^{3+} ion in $^5D_3$ excited state and increasing the one in the $^5D_4$ state. The onset of this concentration quenching could be varying depending on the type of host material system.

3.7. Experimental details

3.7.1. MOS-LED fabrication using Si implanted SiO_2 layers

Ion implantation is the introduction of controlled amount of energetic, charged particles into the solid substrate with ions energy of a few KeV to a few MeV energy range. By introducing such impurities, mechanical, electrical, optical, magnetic and superconducting properties of the host material can be changed in a desirable way. The main advantage of the ion implantation is precise control of the total number of impurity atoms with good reproducibility. Ion implantation is one of the major doping techniques of the microelectronic circuit production.

In this work, ^{28}Si ions were implanted into the thermally grown 100 nm and 40 nm thick SiO_2 on n-type and p-type Si substrates. Implanted ion dose was $5x10^{16}$ cm^{-2} with implant energy of 40 keV for n-type and 15 keV for p-type sample. The depth of peak positions of implanted ions distributions were estimated to be at 60 nm and 23 nm from SiO_2 surface by using SRIM code. SRIM code is actually a Monte Carlo simulation of 99999 ions inserted into target one by one considering the stopping mechanisms at the end gives the desired statistical distribution of the implanted atoms. The simulated distributions of implanted Si atoms into SiO_2 layers are given in Figure 3.5

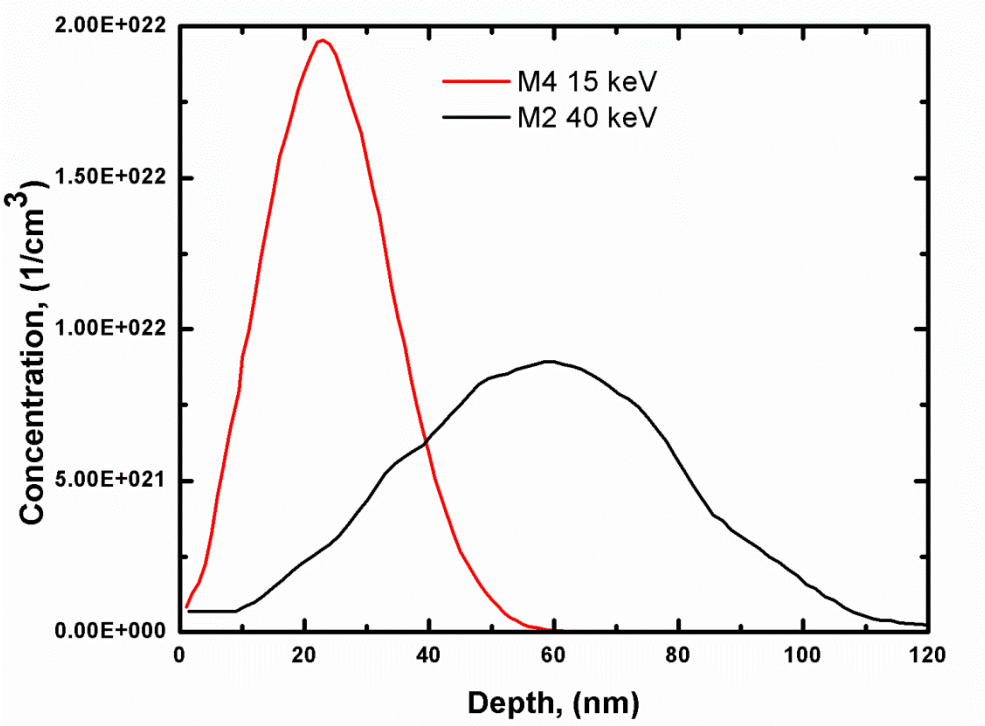

Figure 3.5. Implanted Si distributions in the SiO_2 layers of the samples simulated by using SRIM. The zero point indicates SiO_2/air interface.

Table 3.1. Tabulated annealing properties of Si implanted samples.

Series	Sample name	energy KeV	ion dose cm^{-2}	Anneal Temp ºC	Anneal Time (h)	Oxide thickness (nm)	Substrate type
M2	M2 AS	40	$5x10^{16}$	_	_	100	n
	2NM2900	40	$5x10^{16}$	900	2	100	n
	2NM21050	40	$5x10^{16}$	1050	2	100	n
	4NM21050	40	$5x10^{16}$	1050	4	100	n
M4	M4 AS	15	$5x10^{16}$	_	_	40	p
	2NM4900	15	$5x10^{16}$	900	2	40	p
	2NM41100	15	$5x10^{16}$	1100	2	40	p
	4NM41100	15	$5x10^{16}$	1100	4	40	p

Following implantation processes, samples were annealed at 900 ^{o}C for 2 h and at 1050 (1100) ^{o}C for 2 and 4 h under N_2 atmosphere in conventional quartz furnace to induce phase separation and NC formation. The temperature value indicated in parenthesis is for the p-type sample with 40 nm thick oxide layer. The annealing processes of the samples are tabulated in Table 3.1. PL experiments were conducted prior to MOS device fabrication at room temperature by using 532 nm line of Nd-YAG laser as an excitation source. Emission was measured with Oriel MS-257 monochromator and Hamamatsu CCD camera, and corrected for the measurement system's errors.

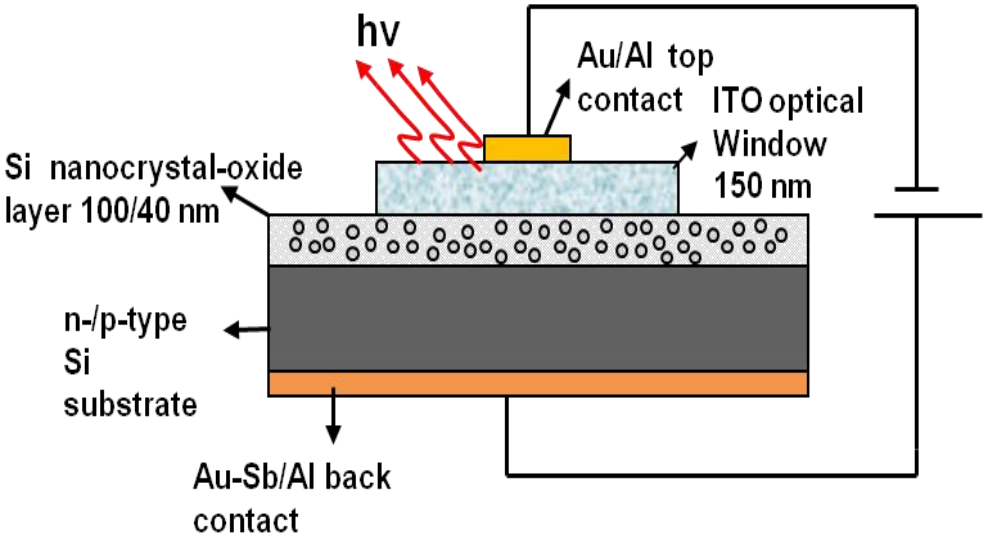

Figure 3.6. Crosssectional illustration of fabricated MOS-LED structures

Prior to device fabrication, samples were cleaned and back oxide layer removed. EL devices were fabricated using standard MOS fabrication technique. As shown in Figure 3.6., backside of the devices was covered with Au/Sb and Al for ohmic contact using electron beam and thermal evaporator system systems for n- and p-type substrates respectively. Metal evaporated samples were annealed in the quartz furnace around 20 minutes, in order to diffuse the metal atoms into the substrate for good Ohmic contact. Annealing temperatures for Al and for Au-Sb were ~ 400 ºC and 500 ºC, respectively. Indium Tin Oxide (ITO) layer with a thickness of 150 nm

were sputtered through shadow mask containing circular apertures with 2 mm diameter for optical window. Following sputtering of optical window, samples were annealed under nitrogen ambient at a temperature of 350 ^{o}C for 30 minutes to increase the conductivity of the ITO layer. Au and Al top contacts were evaporated on the ITO window centered through another shadow mask containing circular apertures again with a diameter of 0.5 mm. Fabricated devices were mounted on a handmade chip holder using printed circuit board (PCB) and bonded using 25 μm diameter gold wire to the copper pads defined on the chip holder. Fabricated MOS-LED device is schematically illustrated in Figure 3.6. EL measurements on fabricated devices were conducted at room temperature with the same set up that was used in PL measurements in a DC bias voltage range of 0-35 V.

3.7.2. Production of MOS-LED structures doped with Tb

Magnetron co-sputtering technique was used to fabricate Tb doped SiO_2 layer with or without excess Si. SiO_2 layers with about 40 nm in thickness were deposited on both n- and p-type, 1-10 ohm-cm Si wafers. For each substrate type, two kinds of film with or without excess Si were deposited. The co-sputtering process was carried out with independently controlled 3 targets: Si target with Tb pieces, Si target without Tb pieces, SiO_2 target with Tb pieces and 75 nm SiO_2 covered Si target with Tb pieces (four Tb pieces with 5 mm diameter were placed on respective targets).

For the samples with excess Si we have applied 50 watt DC power to the Si target, 175 watt RF power for SiO_2 target and 20 watt DC power for Si target with Tb pieces. In the sample with excess Si, the atomic Si concentration was found to be 25-27 % using X-ray photoelectron spectroscopy (XPS) measurement. For the sample without excess Si, 190 watt RF power applied to the SiO_2 target and 20 watt DC power to the SiO_2 covered Si target with Tb pieces. After the film deposition, samples were annealed at the temperatures of 900 and 1050 ^{o}C under nitrogen ambient for an hour. Following the annealing processes photoluminescence measurements were conducted at room temperature using 325 nm line of He-Cd ion laser as an excitation source and the signal was detected by a CCD camera installed on a monochromator. For the ohmic contact formation on the backside of the LED, Al (p-type) or Au-Sb (n-type) were evaporated and annealed at 500 ^{o}C under

nitrogen ambient for a half hour. 100 nm thick tin doped indium oxide (ITO) optical window serving also as a current spreading layer was deposited on to the front surface by an electron beam evaporator through a shadow mask having 800 μm diameter circular apertures. The resistivity of ITO film was measured to be 15 ohm-cm after annealing at 400 ^{o}C for 15 minutes. The fabricated MOS devices were mounted on a PCB chip holder and wired using a 25 μm diameter gold wire to the respective pads. The top view photograph of one of the fabricated device is shown in the Figure 3.7. The electroluminescence measurements were carried out at the room temperature using constant current source and detected by the same set up used in the PL measurements.

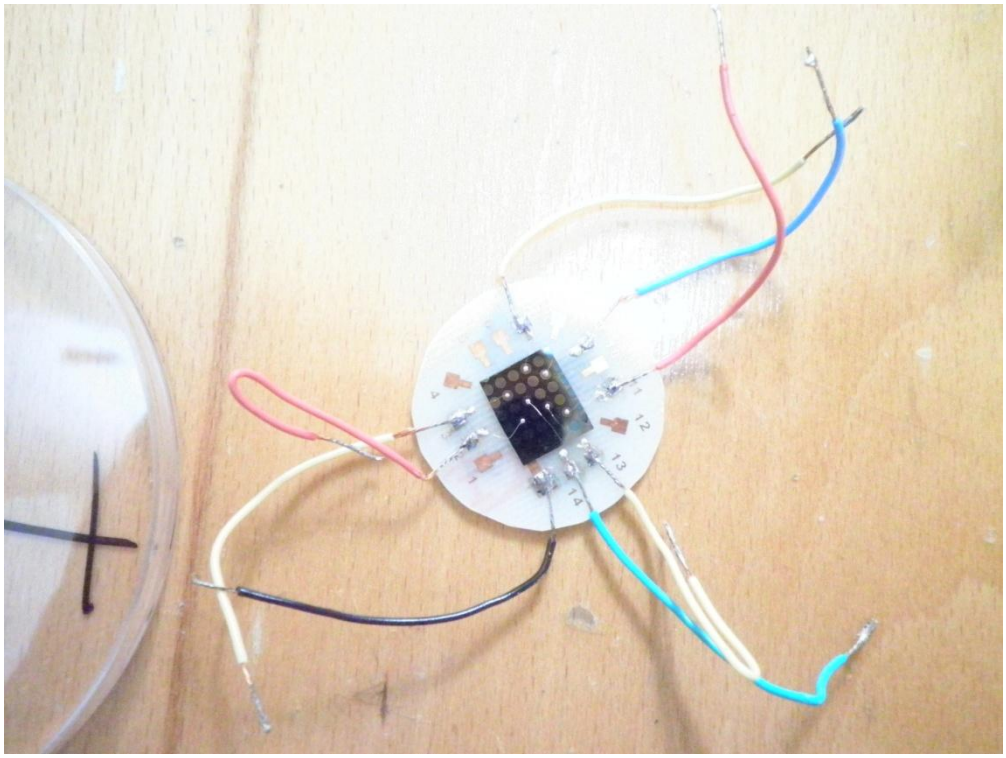

Figure 3.7. Top view photograph of the MOS-LED device mounted on a hand made chip holder.

3.8. Results and discussions

3.8.1. PL results and discussions on ion implanted Si rich SiO_2

PL spectroscopy is one of the simplest and non-destructive method used for the characterization of Si nanocrystals in the oxide matrix. By illuminating using a suitable light source, electron-hole pairs are created in the nanocrystal. When these electron hole pairs recombine radiatively, photons with energy equal to the difference between two energy levels are created. By measuring the spectrum of the released photons, the life time of excited carriers, type of recombination, etc. can be depicted.

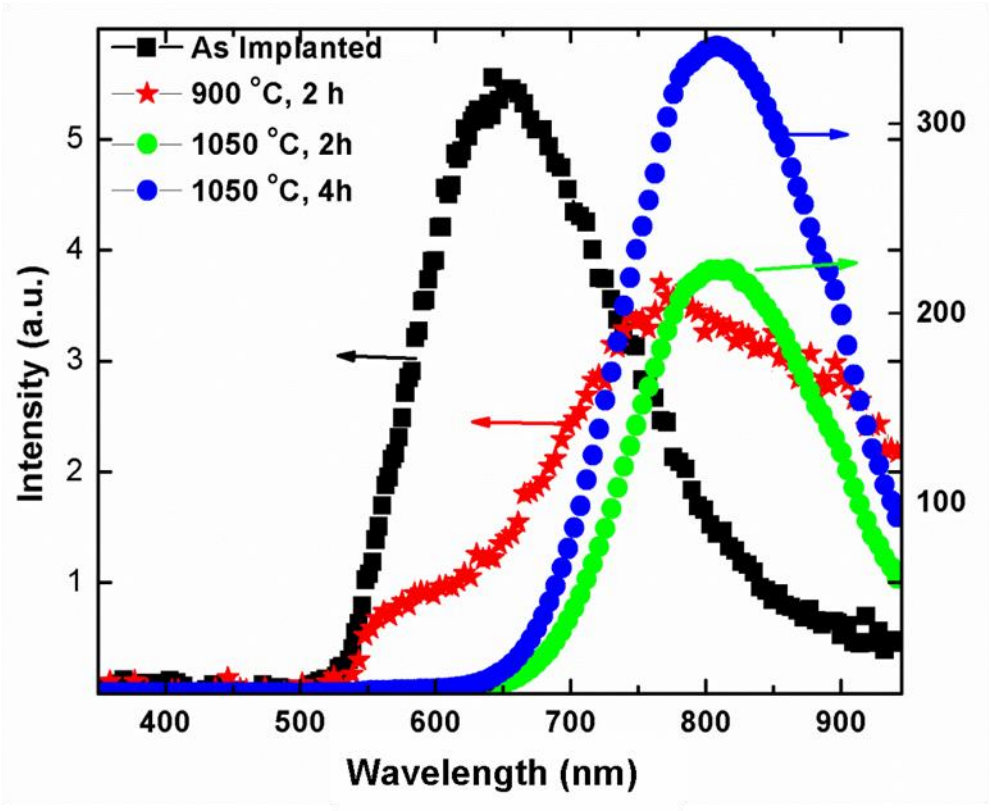

Figure 3.8. PL spectra of the sample (M2) before device fabrication at room temperature with varying annealing time and duration under N_2 atmosphere (as-implanted, 900 ^{o}C 2h, 1050 ^{o}C 2 h and 1050 ^{o}C 4 h). All samples were implanted with $5x10^{16}$ cm^{-2} Si ions at an energy of 40 keV.

A broad light emission is usually observed from Si nanocrystals, in the SiO_2 matrix in the wavelength range of 400-1000 nm. The emission band between 400-700 nm is usually attributed to the defects in the oxide matrix as a result of deformation in the oxide structure [158]. The other band seen in 700-1000 nm is a result of the recombination of excited carriers in/on Si nanocrystals and the peak position of this band can be varied depending on the size of nanocrystals through quantum confinement effect: as the nanocrystal size increases, wavelength of emission also increases approaching 1000 nm, meaning a red shift in the emission spectrum.

Figure 3.8. shows PL results of as-implanted and annealed samples with 100 nm oxide layer on n-type Si. In the as-implanted reference sample, very broad emission band is observed with the main peak at around 650 nm. This peak is commonly attributed to non-bridging oxygen hole centers (NBOHC) [82] formed as a result of Si implantation into the oxide. Upon annealing the sample at 900 ^{o}C, the peak at 650 nm disappears and a new peak emerges at around 780 nm in the PL spectrum showing that annealing process reduces the amount of optically active NBOHC and initiates the formation of Si nanoclusters. The new peak seen at around 780 nm can be attributed to the presence of the small amorphous crystallites surrounded with Si rich oxide [159]. The low intensity of this emission might indicate the presence of luminescence quenching center formation around clusters especially P_b centers whose dangling bonds directed into the Si reach oxide matrix from the cluster surface to the SiO_2. When the annealing temperature is increased to 1050 ^{o}C, it is expected that Si nanocrystals are formed in the oxide. Increasing the annealing temperature causes coalescence of clusters into larger well shaped nanocrystals, repairs the destroyed oxide matrix [160] and decreases the number of P_b centers on the nanocrystal surface. From 900 ^{o}C to 1050 ^{o}C, the PL peak position red shifted to 810 nm accompanied with narrowed spectrum due to the elimination of defect related emission at around 650 nm. An increase in the duration of the annealing from 2 hours to 4 hours at 1050 ^{o}C has not altered the peak position of emission. We however see an enhancement in the emission intensity with longer annealing time. The intensity enhancement is likely to result from the further reduction in the number of P_b centers (i.e. reduction in P_b centers on the nanocrystal surface may be promoted

by mild oxidation due to any trace amount of oxygen present in the nitrogen gas used during the annealing procedure, which saturate dangling Si bonds).

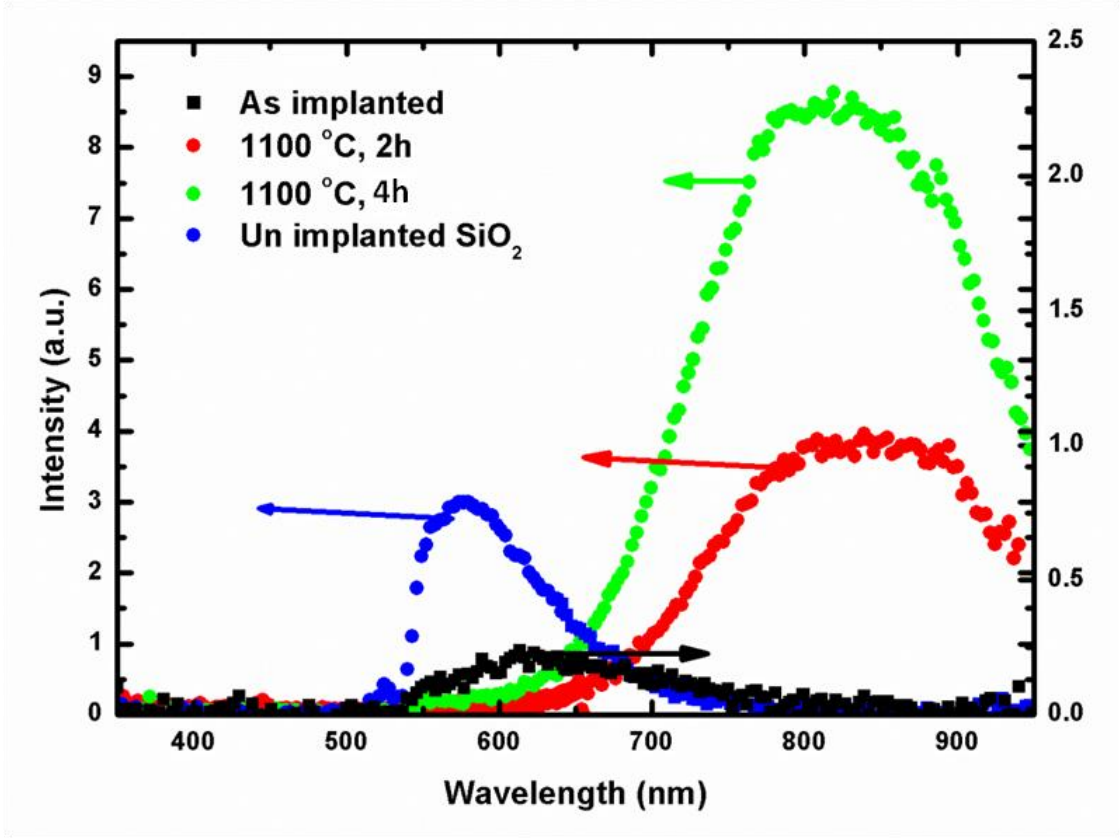

Figure 3.9. PL spectra of sample (M4) before device fabrication at room temperature with varying annealing time and duration under N_2 atmosphere (as-implanted, un-implanted reference oxide, 1110 ^{o}C 2 h and 1100 ^{o}C 4 h). All samples were implanted with $5x10^{16}$ cm^{-2} Si ions at an energy of 15 keV.

In Figure 3.9. PL spectra obtained at room temperature from p-type Si samples with a 40 nm oxide layer at different temperatures for different duration are given. It is seen that, the virgin oxide has an emission band at around 570 nm. This emission band is less studied for the Si nanocrystal/oxide system due to lack of reliable information on the possible sources of the emission. As evidenced by Barthou et al. and Sakurai et al. [99,102], upon comparing with the energy of the known defects types, we find it coinciding with the peroxy-radical defects due to high oxygen content in oxide. Like other samples, NBOHC emission is also clearly seen from the

as-implanted one. As pointed out above, defect emission is almost fixed in wavelength position and independent from the substrate type and the implantation dose. The intensity of this emission band can vary depending on the number of NBOHC created during the implantation.

From Figures 3.8 and 3.9, when we compare the spectra of these two types samples, we see that there is a red shift in peak position of the emission in M4 series with respect to M2, due to both higher Si content and higher annealing temperature, which induce larger nanocrystal in M4 accompanying with an emission at around 850 nm. Figure 3.9 shows ~ 25 nm blue shift in the 4 h annealed sample with respect to 2 h annealed one. There are two possible explanation of this blue shift that is not pronounced in the sample with low excess Si content of sample (M2): the first reason might be that further oxidation of nanocrystal surface results in a size reduction because of the higher annealing temperature. The second possible reason is the exciton migration effect which is expected for the case of M4 having higher excess Si content [161]. In the 2 h annealed (at 1100 ^{o}C) sample of M4 series excitons created in small nanocrystals can migrate to larger one by a tunneling mecahism due to higher Si excess and nanocrystal concentration, then recombine there radiatively by emitting a longer wavelength photons. Therefore, as the number of photon emission at high-energy side bleached, the PL spectrum exhibits a red shift. When annealing time has risen to 4 h, the oxide matrix becomes more resistive to the exciton tunneling between dots and thus created excitons recombine at their nanocrystals and total spectrum shows blue shift with increasing intensity of the emission. Exciton migration or energy transport effect can be also seen in other samples, but it is much more effective in series M4 due to higher density of nanocrystals, which enhances tunneling between dots. However, both mechanisms can take place at the same time, and to analyze exciton transport effect in this situation, careful analysis has to be done over temperature dependent PL experiments. Besides the two effects discussed above, dissociation of nanocrytstals (inverse Ostwald ripening) is another possible mechanism which leads to the lowering the nanocrystal size with diffusing of some excess Si back to the SiO_2 matrix. The EL results could shed a light on the evidences for this suggestion.

The PL results demonstrate clearly that very broad emission bands having a band width of ~375-400 nm originates from the Si nanocrystals formed in the oxide matrix by means of ion implantation method. The broadness of the peak might be attributed to two phenomena: first one is the Gaussian distribution profile of implanted ions, which creates nonuniformity in the size and distribution of the nanocrystals. Serincan et al, [158] supported this dependence on the nanocrystal size distribution, by etching the oxide including Si nanocrystals in a sequential way. Another broadening mechanism is inevitably peculiar to Si nanocrystal and oxide matrix relationships. Except for very small nanocrystals, the dominant recombination of excited excitons occurs at the surface or strained suboxide shell region through coupling with localized Si − O vibrations at the interface. Involvements of these vibrations result in further broadening in emission spectrum.

3.8.2. Current-voltage (I-V) characteristics of implanted samples

Understanding the carrier transport mechanisms is crucial for engineering improved devices (memory, light emitting devices etc.) that are based on Si nanocrystal-MOS structures. There are many transport mechanisms adapted to MOS structures without nanocrystal inclusions; some of them were given in Figure 3.2.

The most frequently discussed mechanisms in Si nanocrystal-MOS structures are single step tunneling processes which include the direct tunneling through trapezoidal barrier between anode and cathode and the Fowler-Nordheim (FN) tunneling through a triangular barrier of the oxide (also rarely two step tunneling process are considered; field assisted, trap assisted etc.). However, in reality, these mechanisms cannot give an accurate description of the transport processes in Si-nanocrystal/SiO_2. The main problems with the models based on these mechanisms can be summarized as follows: First, FN tunneling is developed for smooth barriers without any local field variation in oxide matrix. Second, the classical FN transport treats the carrier tunneling between Si substrate and top contact directly. Third, both direct and FN tunneling exclude size variation in Si nanocrystals and Coulomb blockade effect due to charge trapping in/on Si nanocrystal surface. Therefore, with such structural and electronic variations, resonant tunneling effects via quantized

energy levels between neighboring Si nanocrystals can be expected. As a result, transport properties of Si nanocrystals become very complex when all these different effects are taken into the account.

In this work, we have analyzed our I-V curves using Fowler-Nordheim, Poole-Frenkel [162], analytical two-step trap assisted tunneling (TAT) [163,164], Ohmic conduction and Space Charge Limited Current (SCLC) mechanisms [165]. Since the I-V curves were taken only at room temperature, hopping conduction mechanisms were excluded in the analysis. We will not give every detail or all the plots for conduction analyses but present representative examples to show which procedure we followed during our I-V analysis.

Table 3.2. Different kinds of current mechanisms studied to understand the injection and transport properties in the ion implanted Si nanocrystal/SiO_2 system.

Mechanism	Plotted Curve	Physical Parameter extracted
Fowler-Nordheim	J/E^2 vs. 1/E	Barrier height
Poole-Frenkel	J/E vs. $\sqrt{E}$	Oxide permittivity
TAT - Wang	J vs. 1/E	Trap energy
TAT - Fleischer	J*E vs. 1/E	Trap energy
Space charge limited current	Log J vs. Log V	-
Ohmic conduction	Log J vs. Log V	-

FN analysis (for all samples except for the unimplanted ones) revealed that although some field dependence can be attributed to FN mechanism, it does not dominate the total measured current. FN curves did not exhibit the expected field dependence and yields unacceptable barrier heights between 0.02 to 0.1 eV depending on the devices. These barrier values are far from any realistic value (3-4 eV) for the Si/SiO_2 interface. Poole-Frenkel (PF) analysis also gives unrealistic permittivity in the range of 31-186 depending on the bias scheme of the devices. The expected permittivity for SiO_2 is around 3.9. The inclusion of excess Si could not change the system

permittivity beyond the Si permittivity which is around 11.8. We followed similar procedures for the other models. TAT models gave a good linearity in the curves and the trap energies are found as 0.21-0.11 eV (Fleischer) and 0.17-0.08 eV (Wang) depending on the bias configuration of the devices. There are some differences between two models due to their assumptions on the definitions of traps, their locations and depths. We will not make any discrimination between these models since, firstly, they produce close trap energies, and secondly, an in-depth numerical analysis of the traps is out of scope of this thesis. These values for the trap energies can be acceptable somehow for an implanted and deformed oxide, but other models should also be tested before drawing a conclusion. This is especially important in our samples because except for the Fowler-Nordheim current, all other mechanisms include traps and use them as pathways for carriers one way or another.

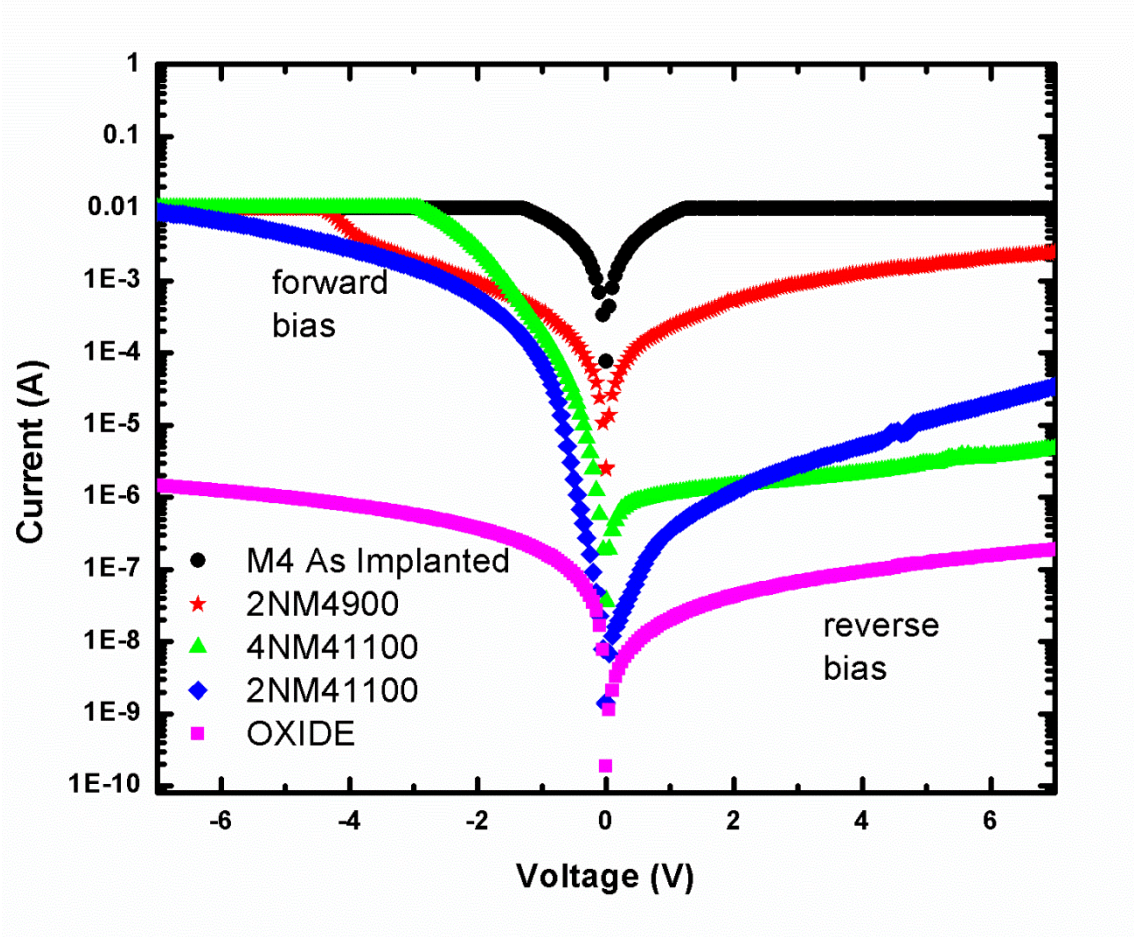

Figure 40. Measured I-V results from Series M4 for different annealing time and duration. The substrate is p-type, oxide thickness is 40 nm, the implant energy is 15 keV and the dose is $5x10^{16}$ cm^{-2}.

In Figure 3.10, I-V results measured from the sample series M4 (40 nm oxide on p-type substrate) is given along with the results of the un-implanted oxide under both forward and reverse bias conditions. The maximum allowed current through the devices was limited by the measuring set up to the 10 mA. Since the substrate is p-type, in the forward bias case, substrate voltage is positive with respect to top contact and negative for the reverse bias. Therefore, in the forward bias, electrons are injected from ITO window and holes are injected from the Si substrate. In the reverse bias case, injection of electrons occurs from the inversion region populated by minority carriers (electrons) accumulated at the Si/SiO_2 interface of the p-type Si substrate. From the I-V curves displayed in Figure 3.10, it is seen that there is a systematic change in the I-V spectra with the annealing temperature and time. The conductivity is highest for the as-implanted sample and decreases with the annealing treatment. The observed variations in the current through the oxide layer are more pronounced for the reverse bias. The conduction mechanism for as implanted sample could be a percolation type conductance through resistive network created across the implanted oxide layer, in which the current follow the least resistive paths. The I-V curve for as-implanted sample is just like a current passing through a regular resistor with an Ohmic conduction ($J \sim V^m$, m=1). The implantation process reduces the oxide band gap and thus the barrier height for charge injection by excess Si. The carrier injection can also be enhanced via created traps at interfaces and in the oxide. Upon annealing at a temperature of 900 ºC, both formation of small crystallites and reconstruction of destructed oxide matrix are expected. Therefore, resistance of oxide increases with the reduction of jumping states, resulting in a decrease in the measured current. We observe in the sample annealed at 900 ^oC that there is a jump in the current at the voltage value of 4 V in the forward bias, which indicates a change in the transport mechanism, probably from the trap assisted tunneling to SCLC ($J \sim V^m$, m=2 found) at high current levels. In the sample annealed at 1100 ^oC, the size of nanocrystals increases through the Ostwald ripening process at the expense of dissolved Si atoms and small crystallites in the matrix, resulting in a more stoichiometric oxide with even higher electrical resistance. This decrease in the conductivity is due to the increased tunneling barrier both at interface and between neighboring nanocrystals. However, comparing to virgin oxide, nanocrystals insert

large number of inherent quantum states for charge transport over them (we can imagine each nanocrystal as a macro defect in SiO_2 matrix with broad distribution of energy states). It is seen that, there is a distinct transport behavior between samples annealed for 2 and 4 h at 1100 ^oC, both at forward and reverse bias. We can conclude that different mechanisms like TAT, PF, Ohmic and NF tunneling contribute to the total measured current, however, for largest current values, the transport is dominated by the SCLC. Difference in the reverse bias case can be attributed to the Coulomb blockade effect due to the trapping of the electrons/holes in Si nanocrystals in SiO_2 especially at or near substrate/SiO_2 interface, and can be concluded that, in the 4 h case nanocrystals are well passivated. Differences in the forward bias case can also be governed by the degree of passivation through which tunneling (transport) mechanisms vary. Therefore, it is expected that direct tunneling should be more dominant over the trap assisted one and starts at low voltage values for 4 h annealing sample compared to 2 h annealed sample for which the situation seems to be opposite.

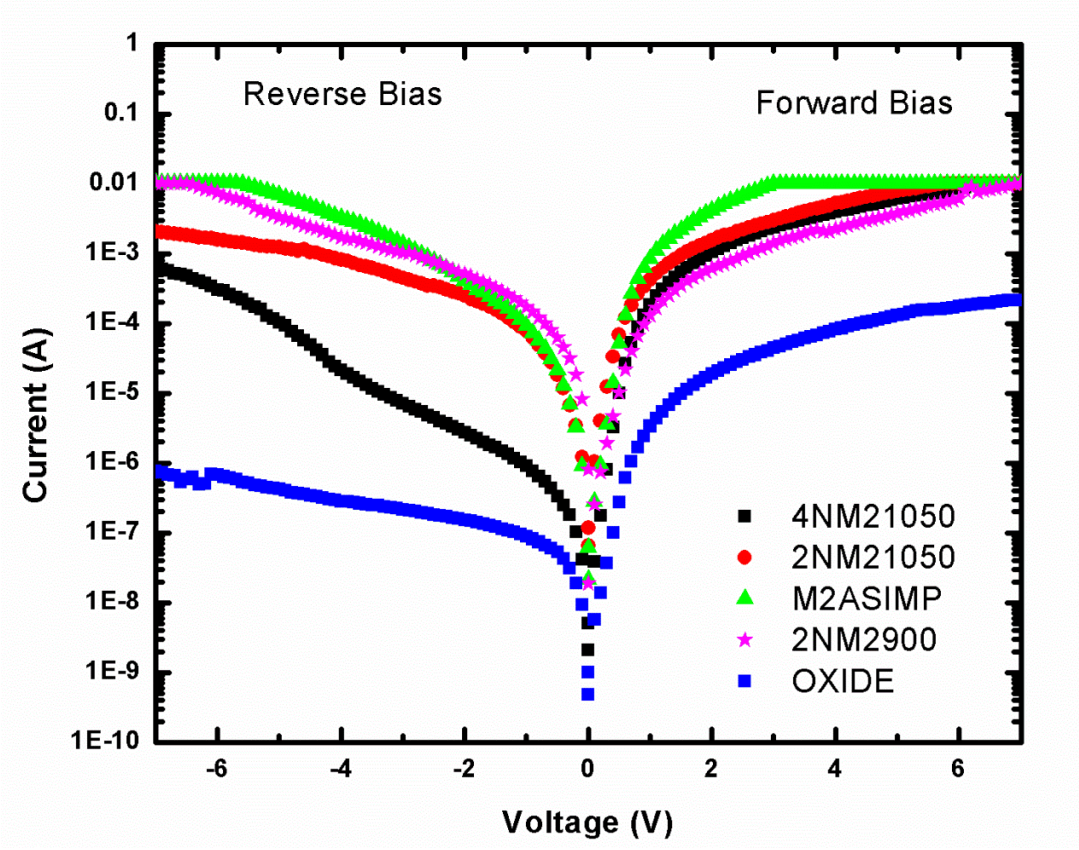

Figure 3.11. Measured I-V spectra of the sample series M2 at both forward and reverse bias range of 7 V. Substrate is n-type, oxide thickness 100 nm, implanted Si dose $5x10^{16}$ cm^{-2} with an implant energy of 40 keV.

I-V spectrum of series M2 is given in Figure 3.11. In this case the substrate is n-type with an oxide thickness of 100 nm, so in forward bias case, the voltage applied to the top contact is positive with respect to the substrate. In the forward bias, electron injection occurs from substrate into Si nanocrystal oxide layer, whereas in the reverse bias case, the electron injection takes place from the top contact to the oxide layer. In the reverse bias, the hole injection from the inversion region of the Si substrate into oxide layer is hardly possible. This is the main obstacle for efficient device operations. I-V spectra show that, for samples of M2, the change in the current level with changing annealing temperature and time is lower than p-type samples, especially in reverse bias regime due to the much thicker oxide and reduction in applied field. Rectifying property of p-type samples is enhanced for an applied voltage range as the annealing time and the temperature increase.

In both n and p-type samples, the majority of the current is expected from electron transport, and the hole current gives small contribution due to the higher barrier at SiO_2/ Si substrate interface for holes. Barrier height between oxide and Si for hole is 4.6 eV, for the case of electron it is 3.2 eV. In addition, mobility of hole is much smaller in the oxide compared with electron mobility; mobility of electron and hole is 20 cm^2/Vs, $4x10^{-9}$ cm^2/Vs respectively. However, it is expected that introducing large amount of energy states by excess Si could significantly enhance hole mobility throughout the active layer. Although implanted samples (both n and p-type) show enhanced current transport compared to unimplanted oxide, this is not enough to alter the asymmetry between electron and hole injection into Si nanocrystal oxide.

3.8.3. Electroluminescence properties of Si rich/SiO_2 produced using ion implantation technique

3.8.3.1. MOS-LEDs with lower excess Si on n-type substrate

EL devices were fabricated on the same samples used for PL measurements and all measurements were conducted at room temperature as in the case of PL. We observed that devices emitted light when the substrate was held at positive potential with respect to ITO transparent optical window (the MOS is in the inversion condition for n-type Si or in accumulation for p-type Si). Therefore, devices were light emitting when holes are accumulated under the oxide film. Figure 3.12(a) shows the EL results of the device made on the as-implanted sample of M2 under varying voltage bias up to 35 volts. It is seen that peak locations of EL and PL spectra (Figure 3.8) are almost the same, indicating the same origin for both PL and EL emission at 650 nm. However, EL peaks are broader than PL signals and the EL peak position is a bit red shifted with respect to the PL peak. This might be due to two reasons: first, the energy of the Nd-YAG laser operated at 532 nm is not sufficient to excite the luminescent centers with high energies, while they can easily be excited by the electrical signal; the high energy tail in the emission peak is then observable in the EL measurements only. Broadening at the low energy side can be attributed to the substrate emission resulting from the electron hole recombination in the inversion region. Peak position of this substrate emission is around 1050 nm which is coinciding with the Si substrate band gap energy and discussed in Chapter 2. However, it was speculated that this emission might partly result from Si nanocrystals whose band gap energy is close to Si bulk band gap energy [166].

For the sample annealed at 900 ^{o}C results are given in Figure 3.12 (b) where the peak position of EL emission almost coincides with PL peak position with a slight blue shift for low voltage values. Increasing voltage causes EL peak to shift slightly towards the PL peak positioned at 780 nm. The intensity of the EL band at 780 nm and the substrate emission increase with the increasing applied voltage. The emission peak seen at around 780 nm was attributed to emission generated by small nanocrystals (or chain like Si structures [167]) which are usually in amorphous phase of Si nanoclusters surrounded by the Si rich oxide.

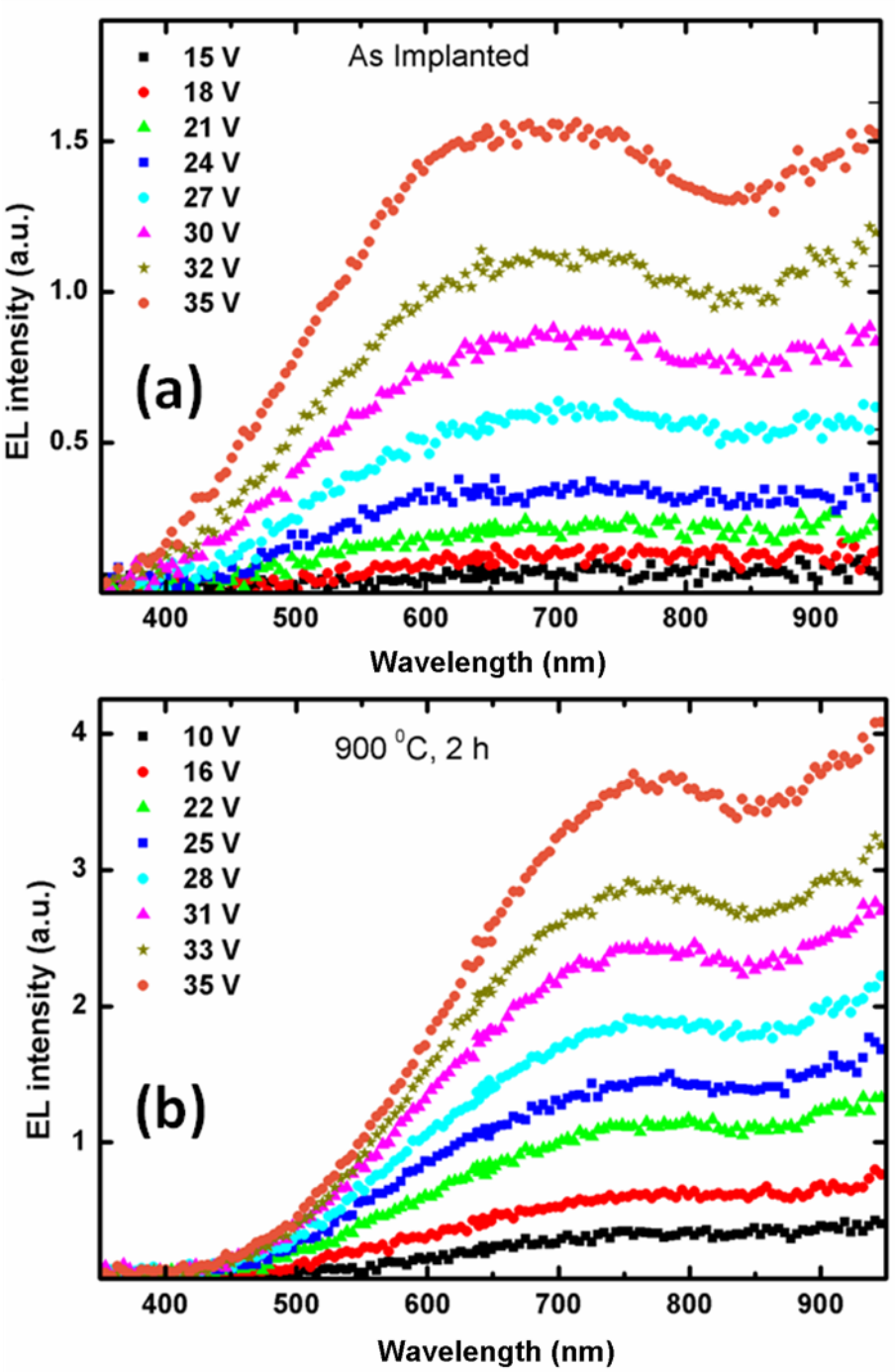

Figure 3.12. EL results of (a) as-implanted and (b) of sample that was annealed at 900 ^{o}C for 2h under reverse bias condition with varying voltage values at room temperature. Samples were implanted with dose of $5x10^{16}$ cm^{-2} Si ions at an energy of 40 keV into 100 nm thick SiO_2 on n-type Si substrate.

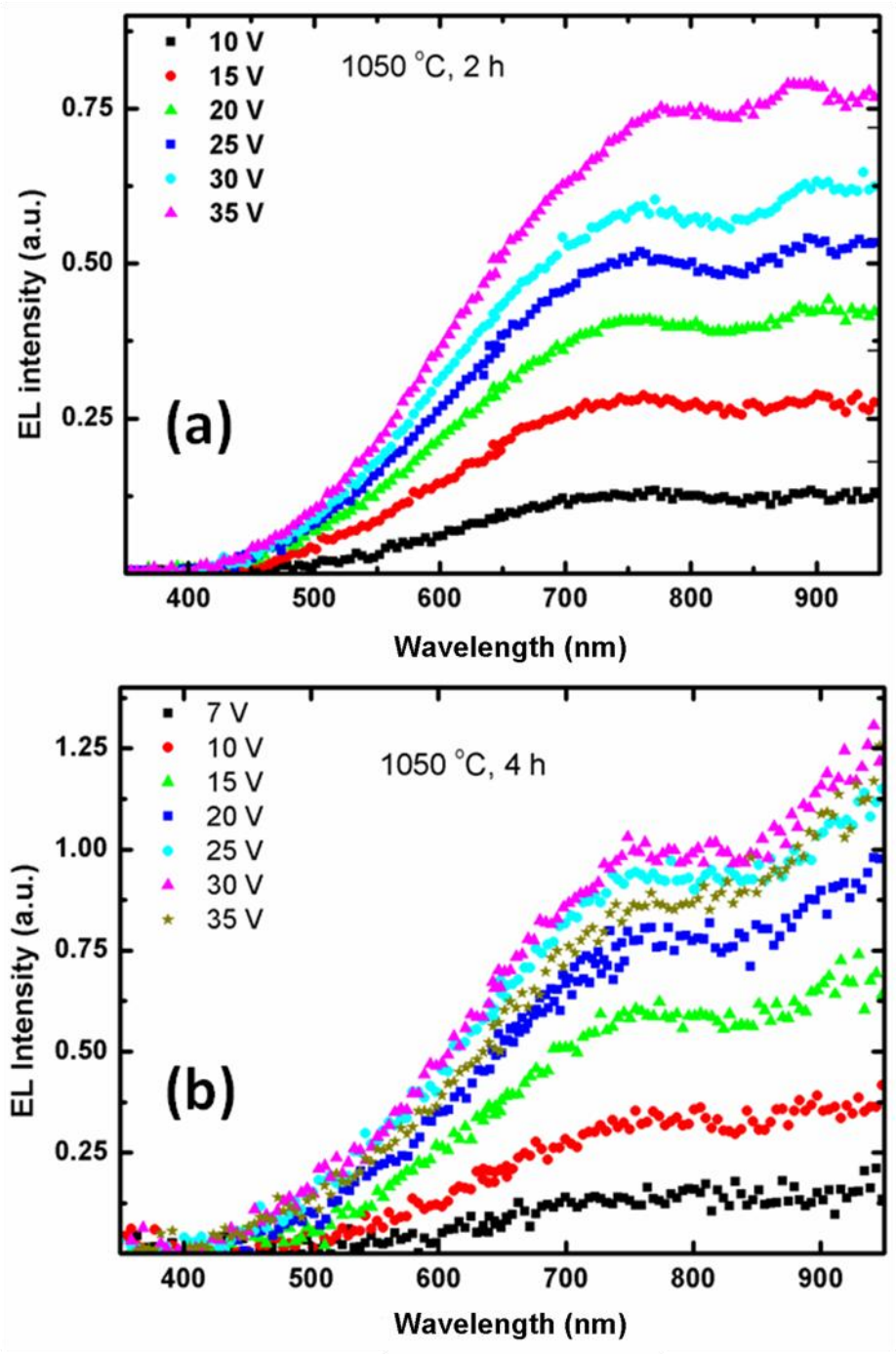

Figure 3.13. EL results of samples M2 (a) annealed at 1050 ^{o}C for 2h and (b) for 4h under reverse biasing with varying voltage values at room temperature. Samples were implanted with dose of $5x10^{16}$ cm^{-2} Si ions at an energy of 40 keV into 100 nm thick SiO_2 on n-type Si substrate.

When the annealing temperature is increased to 1050 ^{o}C, both 2 h and 4 h annealed samples exhibit recognizable distinct behaviors compared to as-implanted and 900 ^{o}C annealed samples. Peak positions of the EL signals of high temperature annealed samples stay at higher energy than PL peak, namely EL spectra are blue shifted with respect to PL signal. The sample annealed for 2 h shows an EL peak (see Figure 3.13 (a)) at around 750 nm at lower voltage values and it gradually shifts to red with increasing voltage, and at voltage value of 35 volts it reaches 795 nm that is closer to the PL peak position at 810 nm. On the other hand, the sample annealed for 4 hours starts emission at around 755 nm for the lowest voltage value and redshifts to 770 nm for 35 V as shown in Figure 3.13 (b). It is clearly seen that the intensity of the emission increases almost linearly with the applied voltage in the sample annealed for 2 h. However, in the sample annealed for 4 h, the intensity of the signal increases linearly up to 20 V after which the rate of increase becomes low and it reaches highest value at 30 V, and then falls down to lower values.

As mentioned above, two main mechanisms might be responsible for the light emission in MOS-LEDs containing nanocrystals: impact ionization of nanocrystals by hot electrons under high field, and co-tunneling of electrons and holes into nanocrystal-oxide system from top contact and from the Si substrate. In some recent reports, EL was observed under both forward and reverse bias conditions [168-170]. However we observed emission only under the reverse bias condition for n-type substrate (or forward bias for p-type as in M4 below), i.e. holes are supplied by Si substrate which is in the inversion condition and electrons are supplied by the top contact.

In the impact ionization model, EL should be observable for both reverse and forward bias conditions, because electrons can be supplied and can excite nanocrystals for both voltage polarities. However, in the case of co-tunneling model, hole injection is possible only for one bias condition. Having ITO as the top contact, holes can only be supplied from the substrate; therefore our results suggest the recombination of electrons and holes by means of tunneling into nanocrystals via holes from substrate and electrons from the optical window. Another important evidence for this conclusion is that an increase in applied voltage causes EL peak

shifts to larger wavelenghts. In the impact ionization model, excitation starts with larger nanocrystals having lower band gap relative to smaller ones, then with increasing voltage bias, blue shift would be observed in the emission spectrum due to the contribution of smaller nanocrystals at larger voltage values [171].

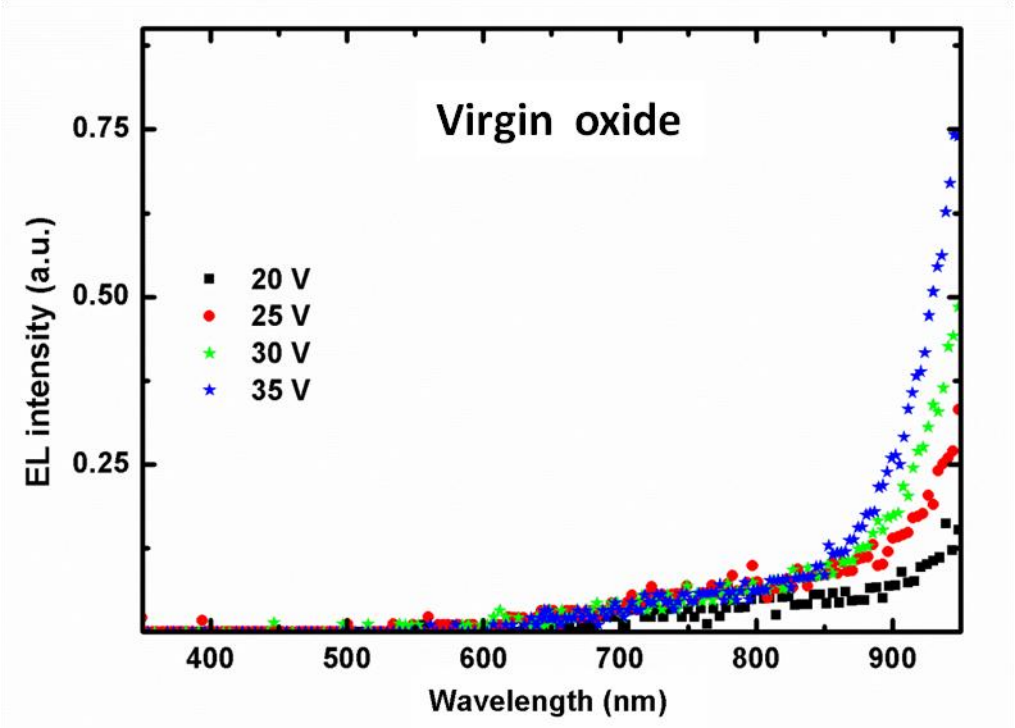

Figure 3.14. EL spectra of thin oxide layer with a thickness of 100 nm on n-type Si under reverse bias. Same behavior also was seen from the virgin oxide with a thickness of 40 nm on p-type Si under forward bias.

In order to test whether the virgin oxide and substrate have any contribution to the observed spectra we conducted measurements on the unprocessed control sample. As can be seen in Figure 3.14, virgin samples exhibits light emission above 900 nm with a peak at about 1050 nm under the same bias condition as the other samples. This emission is a result of the electron-hole recombination in the inversion region formed beneath the oxide layer. This emission from the Si substrate is discussed in Chapter 2 for a thinner oxide. We believe that, this kind of substrate emission reduces the efficiency of nanocrystal related emission in these devices due to the decrease in the number of holes at the inversion/accumulation region through both radiative and nonradiative electron-hole recombination. Facing with a higher oxide barrier and

having much lower mobility in the oxide [172], number of holes injected into the nanocrystalline oxide layer is very low with respect to the number of injected electrons. Therefore, a small fraction of injected electrons supplied by the optical window recombines with hole in Si nanocrystals, most of them reach hole rich inversion layer and destroy holes via radiative/non-radiative recombination there.

Concentration of implanted ions in the host material follows a Gaussian distribution [173] that results in the formation of nanocrystals with varying size. Larger nanocrystals are expected to be formed at a position closer to the center of the distribution while smaller ones are formed in the region where the tails of the distribution is located [158]. When devices are biased, nanocrystals near the oxide/ substrate interface are much more populated by holes than those located closer to the optical window. An increase in the applied voltage results in an increase in the hole population in nanocrystals in the central region and therefore, the contribution of larger nanocrystals becomes more important, and hence a red shift is seen in the EL spectrum. The amount of red shift depends on the resistivity of the implanted oxide via especially change in the injected hole distribution and number in nanocrystal/oxide matrix between substrate and ITO window. We observed from the I-V measurements that the resistivity of the implanted oxide increases with annealing temperature and duration due to the recovery of damaged oxide matrix. Samples annealed at 900 ^{o}C has a lower resistivity compared to the sample annealed at 1050 ^{o}C and the EL emission from this sample has a very small blue shift at lower voltage values and reaches PL peak position at higher applied voltages. This is because the emission in this sample results from small nanoclusters surrounded by the Si rich oxide which has lower resistivity and potential barrier for carriers. Therefore holes can easily populate nanoclusters at moderate voltage values. However, for the annealing temperature of 1050 ^{o}C, the resistivity of the implanted oxide layer increases due to coalescence of Si atoms dissolved in matrix to Si nanocrystals and recovery of the oxide bonds. In this case, charge injection and transport in the oxide become more difficult and most of the injected holes are in the nanocrystals that are close to oxide/substrate interface and a blue shift is seen with respect to PL peak position at 810 nm. As voltage value approaches 35 V, the EL peak position red shifted to PL peak position up to 795 nm, therefore it is inspected that at this voltage

value the substrate side of NC distribution is dominantly populated by holes. Increase in annealing duration from 2 h to 4 h at 1050 ^{o}C results in the further enhancement in the resistivity of nanocrystal/oxide system, therefore hole injection into the oxide and transport through it becomes more difficult than the sample annealed for 2 h. When Figures 3.14 (a) and (b) are compared we see that the amount of redshift in the EL peak with increasing bias is more in the 2 h annealed sample than 4 h one. Another important observation is that EL emission start to saturate and then drops after 30 V in the sample annealed for 4 h. This may be due the Auger relaxation that takes place as a result of over population of holes in nanocrystals located closer to the substrate.

Although the present explanation of the observed red shifts in EL is based on the size distribution of the nanocrystals and variations in the charge transport in the oxide matrix with annealing, contribution of other possible mechanisms could not be totally excluded. These effects are energy barrier lowering between nanocrystal and oxide matrix due to potential drop on oxide which causes reduction in confinement effect and results in a red shift in EL spectra.

3.8.3.2. MOS-LEDs with higher excess Si on p-type substrate

When the concentration of excess Si is increased, it brings out some new observations in the EL results. In Figure 3.15 below, EL results of M4 samples annealed at 900 ^{o}C and as-implanted one are shown. For all samples of M4 series, EL was observed only under forward bias condition of p-type Si with a 40 nm oxide. Like the other sample (M2), the emission from NBOHC with the same peak position was observed under PL measurements. For the devices from the samples annealed at 900 ºC, (for this sample there is no PL result to compare, PL measurement accidentally forgotten before device fabrication), recognizable changes has occurred in the EL spectra compared to the as-implanted ones. Width of the spectrum is narrowed by ~ 100 nm from high energy side, indicated that, annealing eliminated or decreased the concentration of defects which have the emission band at higher energy. At up to 22 V of bias, peak position shows red shifts from 725 to 740 nm, and intensity increases relatively; with bias voltage of 22 V the peak shifts suddenly to 595 nm. Further, increase in voltage first causes the EL peak to blueshift to 535

nm, and then redsift to 570 nm and is stable there. It is seen from Figure 3.15 (b) that the width of the spectrum follows the increase in the voltage. Contrary to this, relative intensity of lower energy side tail decreases as the peak start to shift to high energy side.

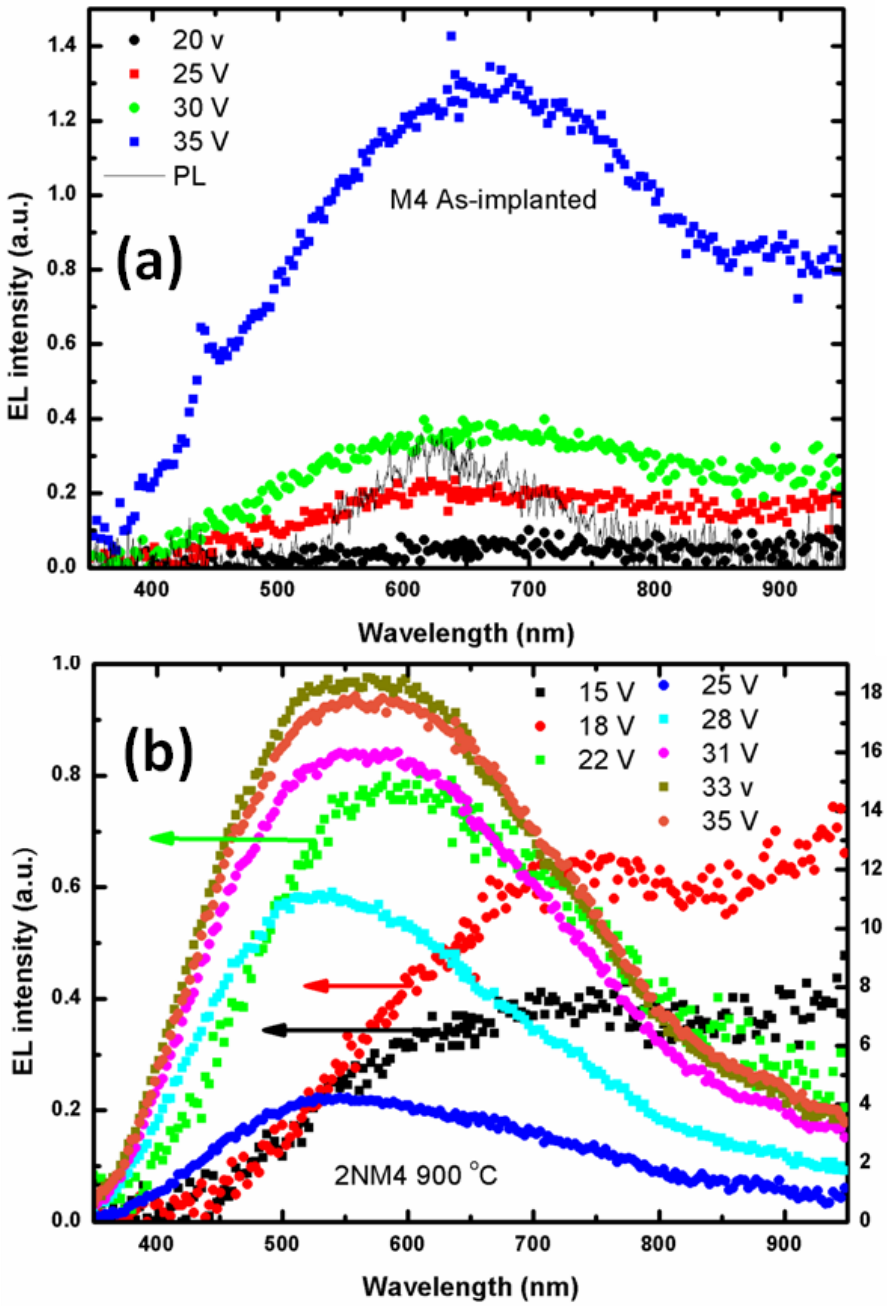

Figure 3.15. EL results observed from the samples of M4 under forward bias, (a) as-implanted and (b) annealed at 900 ^{o}C for 2h. The samples with 40 nm oxide on p-type Si substrate were implanted with Si having dose of 5x10^{16} cm^{-2}.

The main reason of this emission is the larger content of Si in the oxide (and we discuss briefly without any details here). As the Si content increases defect related yellow-blue emission increases, oppositely the emission at red decreases [98]. During the Si implantation and the following annealing processes, oxygen deficiency related centers and E′ centers are formed. It is suggested that hole trapping states at the Si − Si bond of oxygen deficient centers (here we can say precursor states) are broken and change to E′ centers [174]. Therefore, as the applied bias voltage increases, tunneling of holes from the substrates to these precursor centers increases, then, at the expense of luminescence peak around 740 nm from the amorphous clusters, the yellow-green emission increases to much higher level. At moderate bias voltages, this process is thought to be the precursor of the breakdown initiation of the device. It is also seen from Figure 3.15 (b) that the intensity of the emission decreased from 33 V to 35 V. This results from the leakage current path formation that would either saturate or decrease the emission intensity. Also, formation or increase in the number of non radiative defects by hot carriers could cause degradation of the emission from the device.

For the samples M4 annealed at 1100 ºC for 2h, these almost show the same tendency as was observed in M2 series as can be seen from Figure 3.16 (a). The EL peaks increased following the increase in voltage and exhibits a blue shift of about 45 nm with respect to the PL data. However some differences from M2 series can be seen at high voltages. In this regime, a new emission band emerged at around 500 nm due to oxygen deficient centers. For the sample annealed for 4 h, this behavior starts at lower threshold voltages (see Figure 3.16 (b)). We also see that the emission from the substrate is suppressed when this defect related emission is triggered. Two emission bands seen at high voltages are related with E′ and B2 defect centers. It is hard to figure out the exact structural reason for this defect related EL emission without supportive diagnostic measurements. However, we can suggest that during the ripening process of nanocrystals, there could be an inverse Ostwald ripening process under which the nanocrystals release some of their Si atoms back to the SiO_2 matrix where these atom forms weak Si-Si bonds which is more pertinent for the sample annealed for 4h. Under the hole injection from the substrate these weak bonds trap holes and are easily broken and then converted to light emissive E′ or B2

defects. The new emission bands seen at high voltages are associated with the formation of these defects.

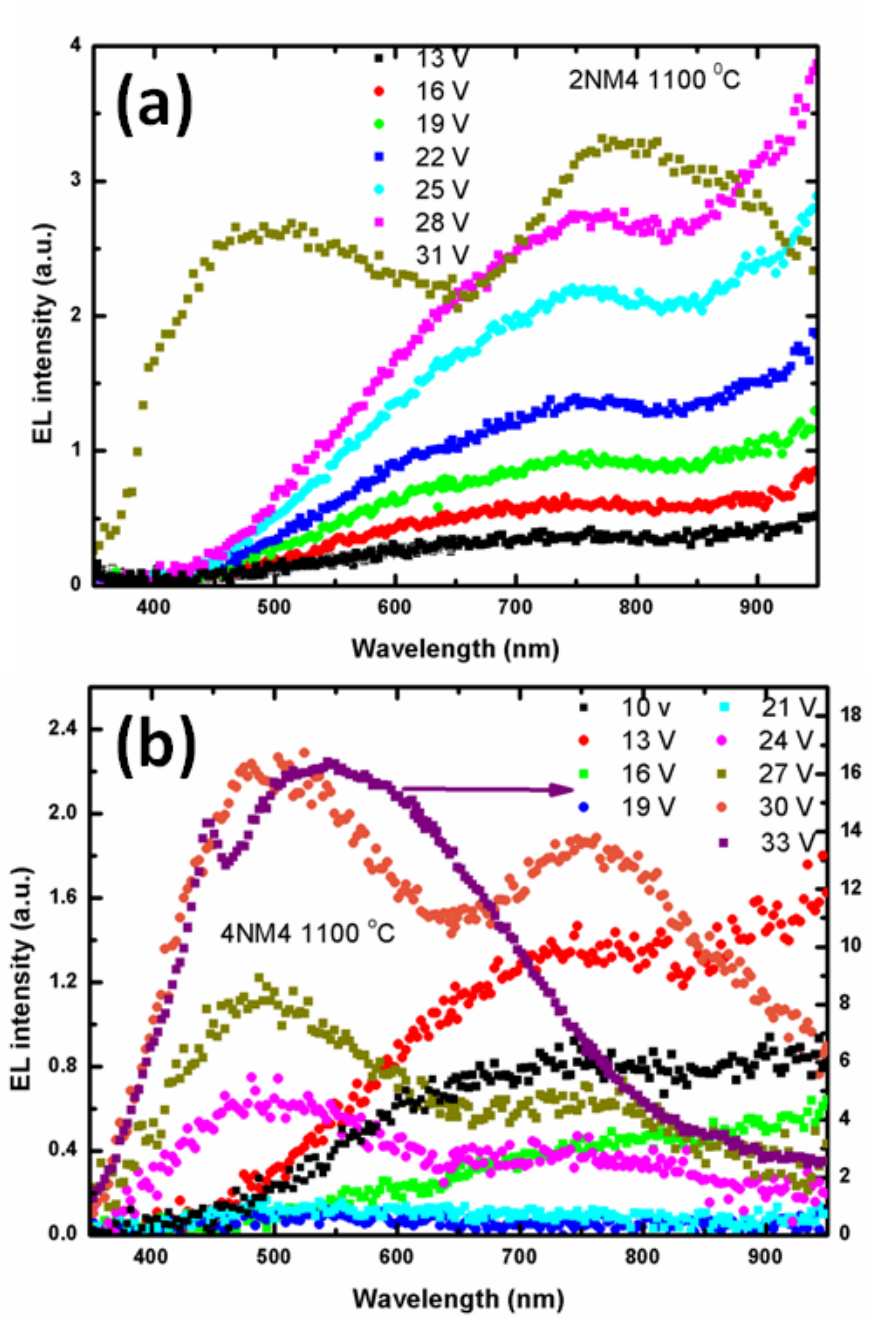

Figure 3.16. EL results of samples of series M4 at higher annealing temperature, under forward bias at room temperature. (a) Annealed at 1100 ^{o}C for 2h and (b) annealed at 1100 ^{o}C for 4h. Underlying Si substrate is p-type with 40 nm oxide layer.

3.8.4. PL results and discussions on Tb doped Si rich SiO_2

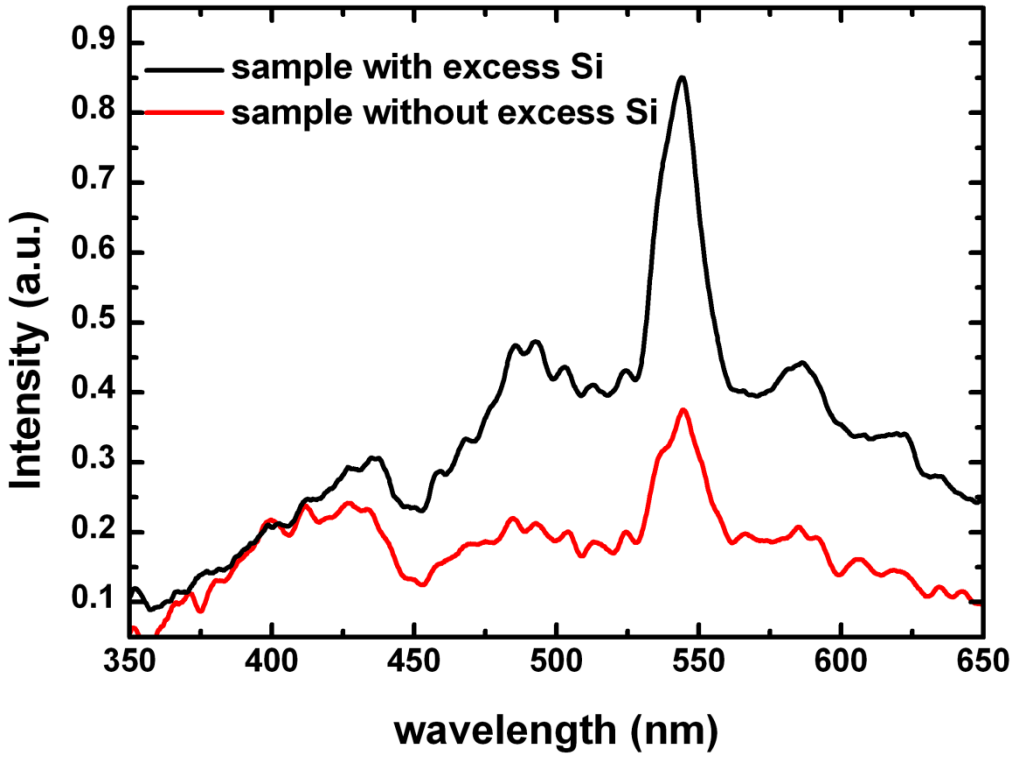

Figure 3.17. Room temperature PL spectrum of the samples on n-type Si substrates annealed at 900 ^{o}C.

Photoluminescence (PL) spectra of Tb doped SiO_2 layers annealed at 900 ^{o}C and 1050 ^{o}C are presented in Figures 3.17 and 3.18, respectively. No PL signal was detected for the as-deposited samples. Upon annealing at or above 900 ^{o}C, the characteristics emission bands of Tb3+ ions emerge in all samples. As shown in Figures 3.17 and 3.18 four emission bands originating from the Tb^{3+} atomic transitions can be identified easily. These bands seen around 622 nm, 588 nm, 545 nm and 490 nm are corresponding to the atomic transitions $^{5}D_4$-$^{7}F_{3,}$ $^{5}D_4$-$^{7}F_{4,}$ $^{5}D_4$-$^{7}F_{5,}$ and $^{5}D_4$-$^{7}F_6$. In the case of low temperature annealing at 900 ^{o}C, these emission bands are superimposed on a broad background signal which is usually attributed to high density of oxygen deficiency and/or non-bridged chemical bonds in the Si-O system. This broad matrix related emission is even stronger in the Si rich sample and often disappears when the stoichiometry of the system is improved with further heat treatments at high temperatures.

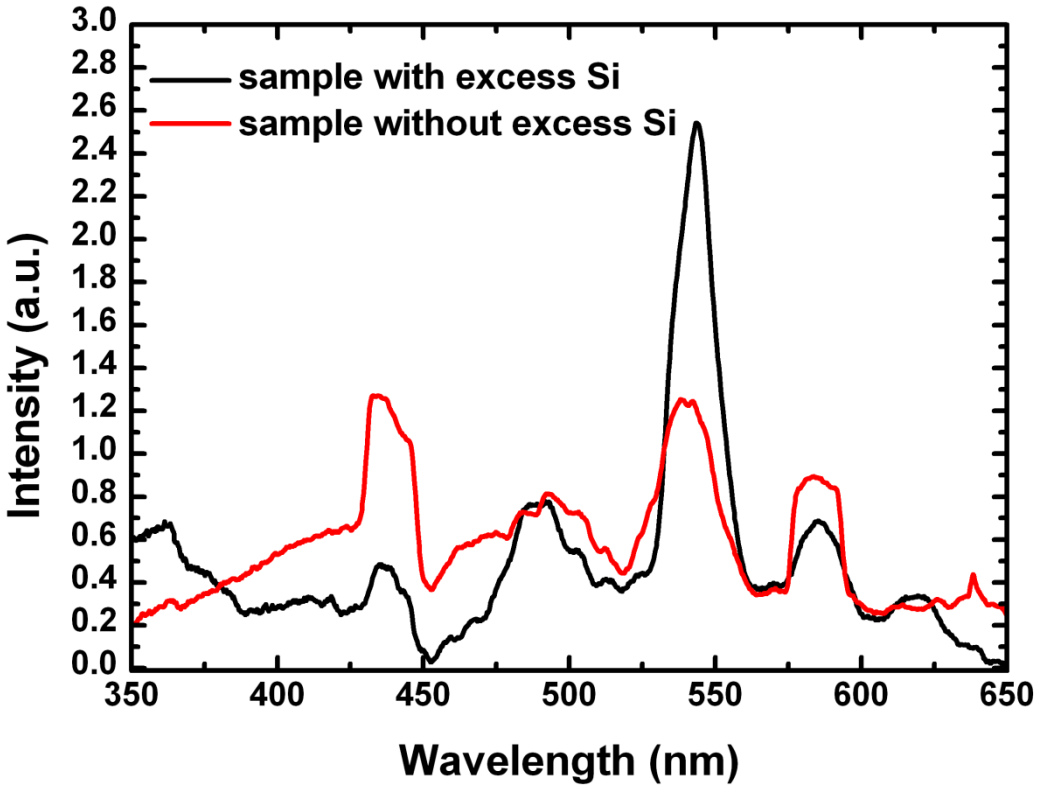

Figure 3.18. Room temperature PL spectrum of the samples on n-type substrate annealed at 1050 ^{o}C.

In the present case, as seen from Figure 3.18, the annealing at 1050 ^{o}C reduces the intensity of this broad peak. The high temperature annealing process eliminates most of the matrix related defects and brings the matrix to a more stoichiometric form. For the case of Tb doped Si rich sample, we can expect a phase separation resulting in formation of Si nanocrystals and/or TbSiO clusters in the matrix.

We have generally observed that light emission from the Tb^{3+} ion is very sensitive to its chemical configuration in the oxide matrix. A special composition of Tb-Si-O is likely to create the necessary route for light emission, charge transfer to Tb^{3+} ion, and finally atomic transition. Therefore absolute positioning of Tb^{3+} energy levels with respect to host media is very crucial in the performance of luminescence, luminescence quenching and charge trapping phenomena. Contrary to the sensitivity

of the signal intensity on the chemical environment, the peak position of the PL signal is not very sensitive to the chemical formation due to the atomic nature of the transitions.

However, depending on the matrix type, slight shifts in the peak positions can be observed. As being outer levels, the D states could interact with the surrounding matrix through so-called ligand field, [157] and this interaction or any additional charges around Tb^{3+} ions could cause small shifts in the host sensitive D state energy levels. On the other hand, F energy levels are being inner, more strongly localized and shielded by outer energy levels and thus unaffected by external effects like the ligand field of the matrix. In this study, no $^5D_3$ related emission was observed in the luminescence results. It is known that when the concentration of Tb^{3+} in matrix exceeds 0.1-0.3 % limit, the emission from $^5D_3$ level is quenched by a cross relaxation (concentration quenching) process due to resonant energy transfer between Tb^{3+} ions that populate the $^5D_4$ level. In this study, the Tb concentration is estimated to be around %3 which is far more than the concentration limit for the onset of the cross relaxation process.

3.8.5. Electroluminescence from Tb doped MOS-LED devices with and without excess Si.

EL measurements were conducted on all samples at both forward and reverse bias conditions. For the devices fabricated on p-type Si we could not measure any detectable Tb^{3+} atomic emission. In agreement with the observed PL spectra reported above a weak signal related to the matrix effect was the only detectable signal in the p-type samples. For n-type samples, EL signal was systematically obtained under the reverse bias condition.

Figure 3.19 (a), (b) and (c) show the EL spectra of the n-type samples before annealing, without and with excess Si, respectively. All processed samples have the same amount of Tb doping. During the measurements, the current density was kept constant at four representative values under the reverse bias condition.

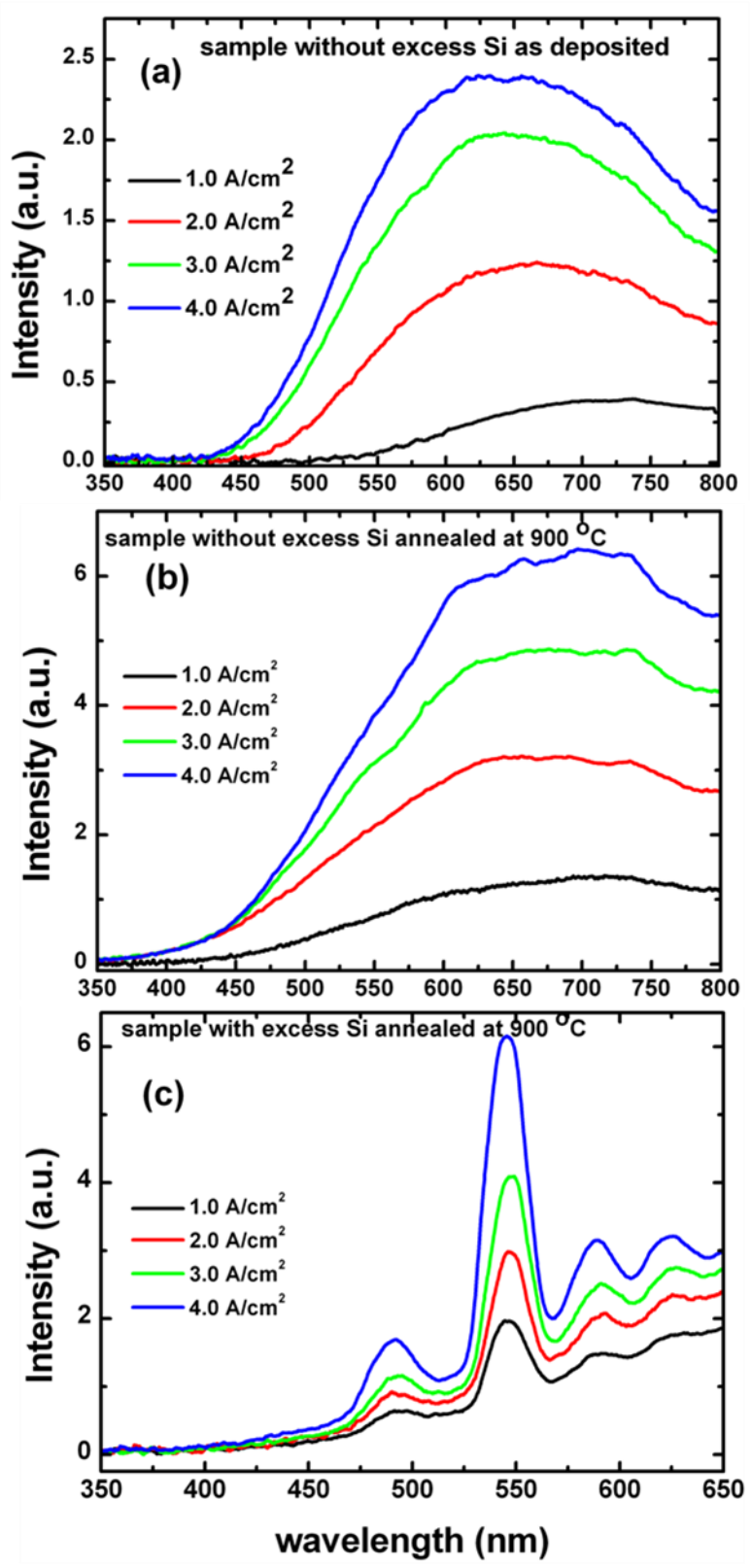

Figure 3.19. Electroluminescence spectrum of a) as deposited sample without excess Si b) sample without excess Si annealed at 900 ^{o}C. c) sample with excess Si annealed at 900 ^{o}C. All samples were prepared on n-type substrate and measured under reverse biased condition with different current injection levels.

In the as-deposited sample, the EL emission is dominated by a broad signal peaked around 700 nm, which is consistent with the above PL results. This is apparently related to the well known defect centers of non bridging oxygen hole center. Increased current injection results in increased EL intensity with a small blue shift suggesting that the excitation mechanism is impact ionization by energetic electrons. No Tb related signal was detected in the samples before the annealing. In these samples, Tb emission is either lost in the matrix-related emission or does not exist due to the fact that Tb^{3+} ions need to be in a suitable chemical configuration for an efficient energy transfer from the host matrix. When the samples are annealed at 900 ^{o}C, which is moderately high value at which one might expect the onset of Si clustering, we observe different behavior for the samples with and without excess Si.

There is no clear Tb related signal seen in the spectrum of the sample without excess Si even after 900 ^{o}C annealing. As in the as-deposited sample, signal coming from the oxide related defects dominates the whole spectrum. However, the signal intensity increased and the peak position of the EL spectrum shifted to red in the annealed sample (Figure 3.19 (b)) compared to the as-deposited sample. The increase in the signal intensity and the observed shift are due to the enhanced emission from the Si clusters formed in the matrix at 900 ^{o}C. It was previously shown that Si nanocluster formation and a light emission peaked around 750 nm can be observed after an annealing at 900 ^{o}C [167]. The increase in the EL signal can also be related to the suppression of the nonradiative states with the annealing process.

The sample with excess Si generated a different EL spectrum as shown in Figure 3.19 (c). In this case, the emission bands from $^{5}D_4$ - $^{7}F_j$ energy levels of Tb^{3+} ion are clearly seen. They are superimposed on another very broad emission signal extending to higher wavelengths. The dynamics of this broad emission is probably different than the previous case. This emission could be related either to amorphous Si nanoclusters or to another defect center related to excess Si in the matrix.

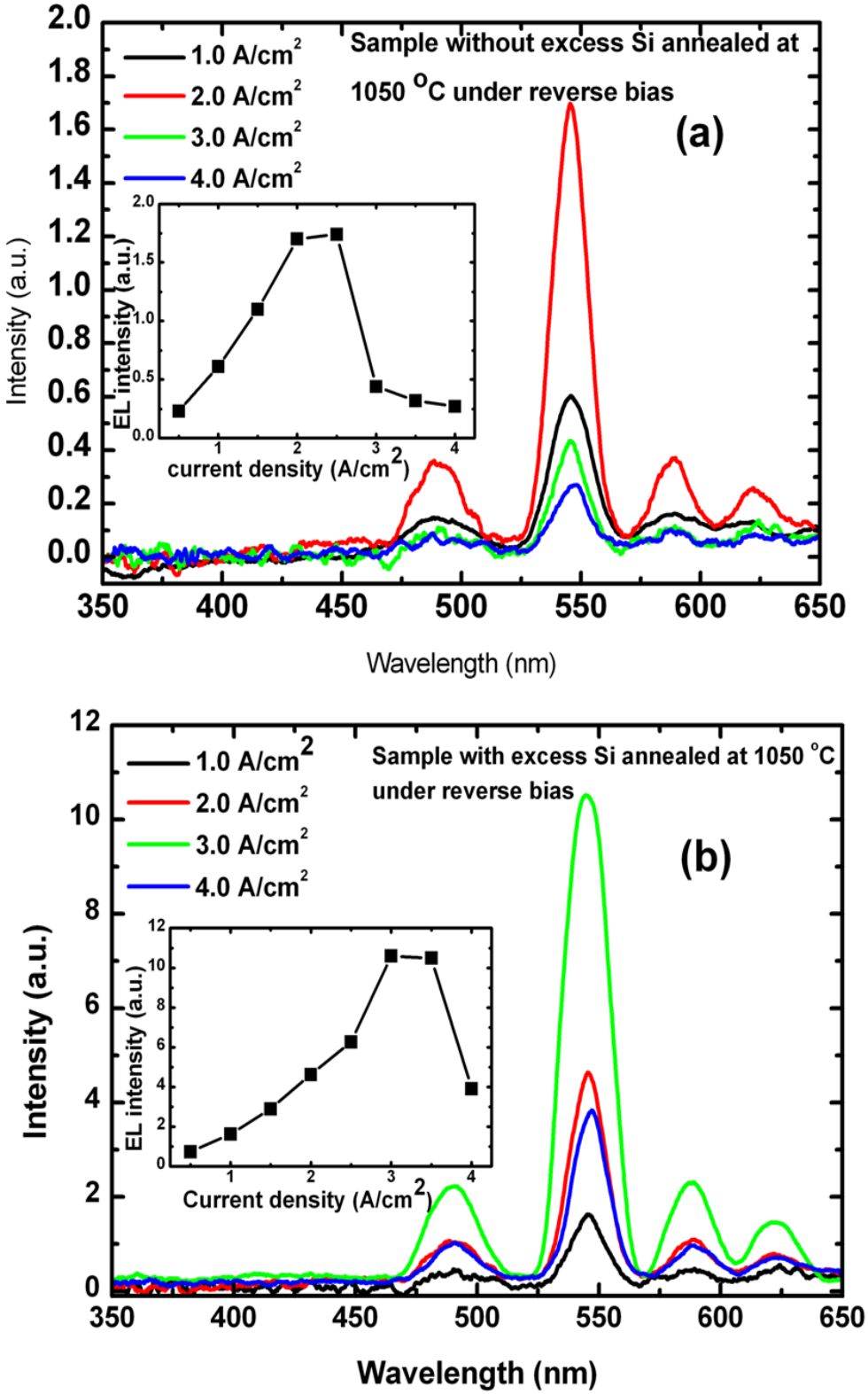

Figure 3.20. Room temperature EL results of a) the n-type sample without excess Si and b) the n-type sample with excess Si. Both samples were annealed at 1050 °C and measured under reverse bias at different current densities. Respective EL intensities with changing current density are given in the insets.

When the annealing temperature is increased to 1050 ^{o}C, defect related EL signals vanish in the spectra of the both kind of samples. As shown in Figure 3.20, only Tb related emissions remained in the observed EL spectra. At such a high temperature annealing process, SiO_2 matrix turns into a fully stoichiometric form accompanied by a phase separation process forming the Si cluster. We previously showed that this transformation can be well identified using Fourier Transform Infrared Spectroscopy (FTIR) [175]. The defect related broad light emission disappears when this transformation is completed. As a result, Tb related atomic emission lines are clearly visible without any parasitic defect emissions. When we compare the results presented in Figure 3.20 (a) and (b), the sample with excess Si incorporation is seen to generate much higher EL signal intensity. This result suggests that Tb^{3+} ions have more chance to form the desired chemical combination in the Si rich environment. Alternatively, the current injection into the Tb cluster is enhanced in the Si rich matrix as discussed below.

An interesting feature of the measured EL spectra is the turn over point seen in the variation of EL signal with the current density. The intensity of the light emission increases first with the current injection and then starts to decrease with the increased current density. Moreover, the current density corresponding to this turnover in the EL spectra is around 2.5 and 3.5 A.cm^{-2} for the samples without and with excess Si, respectively (see the insets in the figure). This is showing that the Si incorporation into the oxide matrix greatly enhances the EL efficiency with increased tolerable current density as one could expect. The maximum obtained EL efficiency was less than 0.1 % for the device with excess Si inclusion. The EL quenching at high current injection level may have resulted from the cross relaxation (up conversion quenching) between two neighboring excited Tb^{3+} ion at $^5D_4$ level [176]. This cross relaxation is different from the relaxation that results in depopulation of $^5D_3$ level described above. In the present case, one of the excited Tb^{3+} ions at $^5D_4$ level is further excited to some upper level most probably to ^7D level at the expense of at least one of the emissions from $^5D_4$-^7F_j transitions. As the injected current level increases accompanying more and more excited Tb^{3+} ions, the up conversion quenching might become more probable. Another possible explanation of the EL quenching is the loss of energy through the energy states of the host matrix during

energy migration between Tb^{3+} ions [141,157]. In addition, the local heating of the device due to high injection can depopulate $^5D_4$ level by thermally activated ionization to any nonradiative states around the Tb^{3+} ion. The small redshift observed at the high injection current regime in both kinds of devices are either due to heating of the devices or perturbation in the surrounding ligand field.

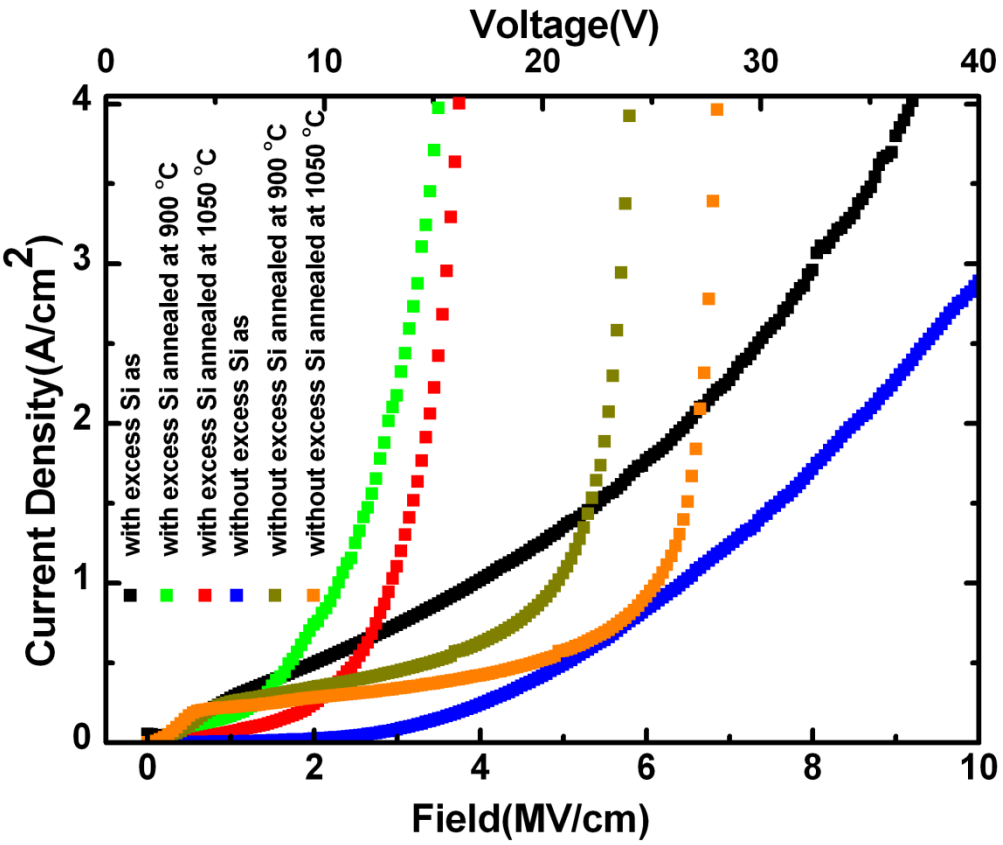

Figure 3.21. Current density vs applied field distribution of all annealed and as deposited samples of the light emitting devices.

The current density vs applied electric field on the samples is shown in Figure 3.21. It is seen that the current is mostly in the space charge limited regime for the level of detectable EL signal in the high field region, which suggests that most of the current is due to electron injection from ITO electrode towards substrate. The turn on voltage of the EL emission is clearly reduced by the excess Si incorporation in to the Tb doped matrix due to lowered injection barrier to the active region. The turn on voltage for the devices with excess Si is reduced to 10 V which is a significant

improvement compare to its counterparts without inclusion of excess Si. We can suggest that the EL emission is due to excitation of Tb^{3+} ions as a result of either direct impact excitation of Tb^{+3} ions or indirect excitation through impact excitation of host matrix by hot electrons. We suggest that the Si nano cluster/crystal sensitization could be the possible explanation for the enhancement of EL emission for the devices with excess Si. If this is so, for the devices with excess Si, an indirect excitation of Tb^{3+} ions through impact ionization of Si nanocrsytals would be the dominant mechanism.

3.9. Conclusions

In this part of the thesis we have presented an extensive and detailed study on electroluminescence from Si based material system with and without inclusion of Tb ions. This content could have an important impact on Si based LED technology. Below we highlight the major findings and conclusions reached during this study.

Contrary to the reported literature, we have observed a strong EL emission related to Si substrate at low energy side of the LED spectra in both n and p-type samples. It is assumed here that this emission is a result of the tunneling of electrons from top contact through the Si nanocrystal oxide layer into Si substrate where they recombine with holes accumulated in the inversion or accumulation layer at the SiO_2/Si interface, depending on the type of the substrate. Any quantum confinement effect especially under inversion condition might modify this emission toward high energy tail due to the increase in the energy difference between quantized levels. It is qualitatively concluded that the major transport through the oxide layer is the electron transport. Electrons injected from the top contact or from the substrate recombine partly in the oxide and partly in the Si substrate. Most of these recombinations in the substrate should be non-radiative as the substrate is indirect gap material, only small percentage would be radiative. This condition may be one of the reasons that decrease the efficiency of Si nanocrystal EL in the MOS-LED structure.

In this work, we have also studied possibility of light emission from MOS type LED fabricated on Tb doped SiO_2 matrix with and without excess Si. Successful device operation has been obtained under certain experimental conditions. Characteristic emission bands of Tb^{3+} ions have been observed clearly in the EL spectra of all reverse biased devices fabricated on n-type Si under excitation with hot electron injection from ITO window to the active layer. The light emission has been found to be sensitive to the Si amount in the oxide layer. Excess Si incorporation significantly increases electroluminescence efficiency accompanied by significant decrease in turn on voltage and increased tolerance to high current injection.

.

CHAPTER 4

QUANTUM CONFINED STARK EFFECT IN SILICON NANOCRYSTALS

4.1. Introduction

Nanocrystals or quantum dots could exhibit many effects of standard atomic/molecular physics due to the confinement of charge carriers in three dimensions. However, unlike single atoms, nanocrystals are usually not identical to each other due to phonons, surface effects and bulk disorders which play important roles on their electronic and optical properties. Nevertheless, a nanocrystal can be considered as a giant artificial atom, which has an adjustable quantized energy spectrum controlled by its size. Therefore, it enjoys prospects for an increasing range of future applications. Thanks to the progress of semiconductor growth technology during the early eighties, various low dimensional systems emerged whose quantum size effects mostly were elaborated through optical measurements. Among many other important features of nanoscrystals, a particular interest lies in the interaction with light under external field giving rise to so called quantum confined stark effect (QCSE). Due to the potentially important technological applications in new generation of devices, the effects of an electric field on the electronic and optical properties of semiconductor nanocrystals have been investigated for the last few years [41, 177-183].

In crystalline bulk semiconductors, the absorption spectrum has a characteristic absorption edge which is at approximately the wavelength corresponding to the band gap energy (Figure 4.1.). In bulk semiconductor, application of an electric field induces a small shift in the exciton absorption/emission peak to longer wavelengths because the polarization induced by the external field reduces the total energy of the

excitons. The effect is called the Franz-Keldysh effect or by analogy with the Stark shift in the absorption/emission lines of a hydrogen atom in the presence of an electric field, the phenomenon is also called just Stark effect. Besides the decrease in binding energy of excitons (tend to increase the threshold energy) the effective energy gap or the photon absorption threshold energy is reduced when the energy bands are tilted under the applied field and the conduction and valance band wave functions have tails in the forbidden energy gap with some overlap (the partial tunneling of wave functions into forbidden gap can be assisted by photons). However, in bulk semiconductors, the small stark shift is masked by the broadening of exciton peak due to ionization (dissociation) of excitons under relatively low field values which should also compete with thermal dissociation of excitons and push the observation of Stark shift to rather low temperatures. Therefore, it is not very useful to exploit the Stark effect for practical applications except the possibility of enhancement in the sensitivity of photon detector operating at a wavelength near the semiconductor absorption edge [184].

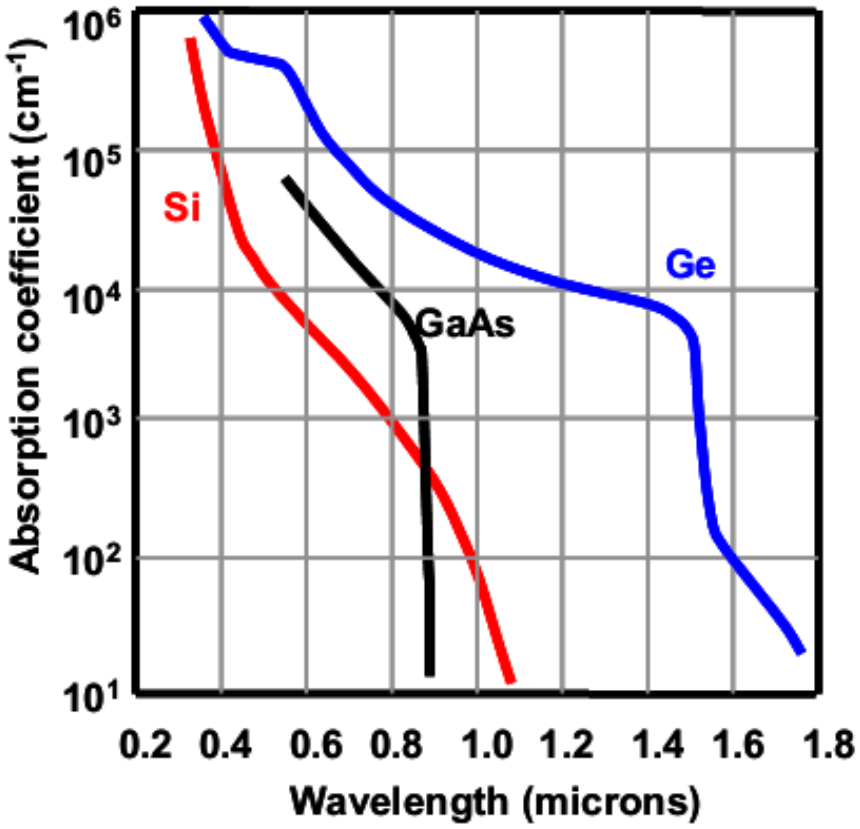

Figure 4.1 Optical absorption spectra of Si, GaAs, and Ge [185].

After first Stark effect studies and suggestions (Franz and Keldysh separately) for bulk crystals in the late of fifties (1958), the effect has been tested for several bulk semiconductor crystals in the following years mostly in the first half of the sixties including Si and Ge mostly through electro-absorption and electro reflection-measurements [186]. Later it has become a one of the useful spectroscopic tools for understanding and characterization of the crystalline semiconductors [187-190]. In 1968 electro-absorption of CdS micro-crystals embedded in glass matrix was demonstrated using AC external field, which might be accepted as starting step towards to more rigorous form of Stark effect for lower dimensional systems as called QCSE later [191].

With the sophistication of crystal growth techniques (like molecular beam epitaxy (MBE)), the Stark effect was demonstrated for quantum well structures of III-V semiconductor systems and first practical working modulator structures was demonstrated from these structures in early eighties in accordance with the theoretical developments of its theory [192-194]. Today several types of modulator structures based on III-V direct gap semiconductors are utilizing QCSE for signal modulation in telecommunication. As seen in Figure 4.1, the band edge absorption in direct band gap material (GaAs) is very sharp. In Ge, a strong absorption is observed at its direct band gap of 0.8 eV with an indirect band-gap (0.67 eV) absorption shoulder. In the case of Si, the absorption at the band edge is not strong up to the visible spectrum because of its indirect band gap at around 1.12 eV. Therefore in practical applications, very efficient optical signal modulation devices that depends on electro-absorption/QCSE phenomena uses direct band gap materials. Recently modulator structures made of Ge using its direct band-gap which is inherently in the telecommunication working window well have been shown to compete with the III-V systems [9, 195]. Besides the quantum well structures, QCSE has been demonstrated in nanocrystals of various materials including Si as well. Nanocrystals are expected to be superior over other low dimensional system due to the three dimensional confinement of wave functions [42]. One of the big advantages is that, they do not suffer polarization dependency which is typically observed in 2D structures. The advantage of using nanocrystal systems for exploiting the Stark effect will be briefly discussed in the forthcoming section.

4.2. On the aspects of QCSE in nanocrystals

It is remarkably known that, excitonic effects are much stronger in fully confined systems than bulk crystals and other low dimensional systems, since the quantum confinement reduces the spatial extension of the exciton wave-function that results in an enhancement in the oscillator strength. As discussed before, Stark effect in bulk semiconductors is limited to low external field that is in the order of 10^3-10^4 V.cm^{-1} depending on the material. In a stronger applied field, excitons easily dissociate and do not enable the intensity modulation. On the other hand, the situation is quite different in nanocrystals/quantum dots. Large electric field can be applied (the applied electric field can be 100 to 1000 times higher than 3D case), since the electron-hole wave functions will collapse to the opposite sides of the nanocrystal while retaining finite electron-hole wave function overlapping. Thus exciton is polarized but not ionized under a high field and therefore the large oscillator strength of the exciton is retained. It is known that the intensity of the absorbed and the emitted light is directly proportional to the oscillator strength of the exciton. At the same time, the envelope wave functions of electrons and holes as well as confining potential undergo deformations as shown in the schematic illustration in Figure 4.2.

The external field that induces change in exciton energy comprises three contributing terms:

$$\Delta E_{exct} = \Delta E_e + \Delta E_h - \delta\varepsilon \tag{4.1}$$

Where $\Delta E_{e,h}$ are the changes in single particle electron-hole energies and $\delta\varepsilon$ is the change in exciton binding energy (or change in Coulomb interaction energy). However, QCSE shift mainly results from the first two contributions.

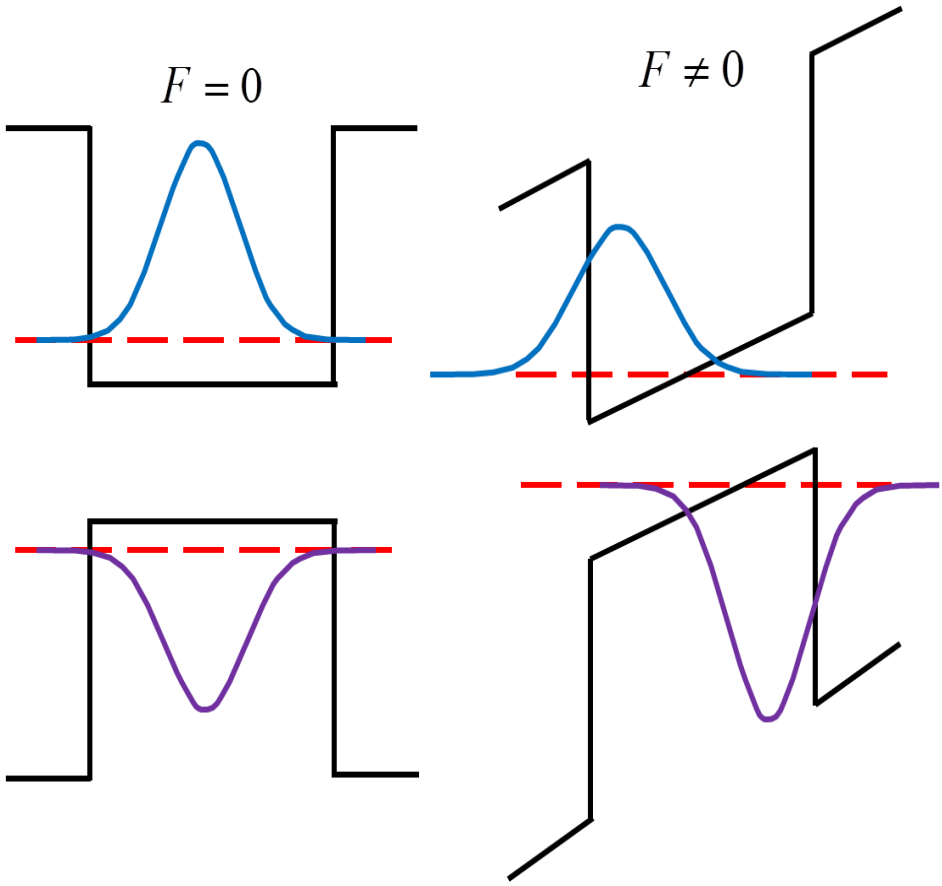

Figure 4.2. Schematic illustration of electron and hole wave functions for the lowest confined state in the nanocrystal; (left) in the absence of external electric field and (right) with the application of external field.

For an arbitrary value of externally applied electric field, one should solve the following Schrodinger equation:

$$(H_e + H_h + V_c) \Psi (r_e, r_h) = E \Psi (r_e, r_h) \qquad (4.2)$$

with V_c is the Coulomb interaction term, and assuming the electric field in z direction

$$H_{e,h} = \frac{P_{e,h}^2}{2\, m_{e,h}^*} + V_{e,h} (r_{e,h}) \mp eFz_{e,h} \qquad (4.3)$$

Where $H_{e,h}$ and $V_{e,h}$ are the single electron-hole Hamiltonian and confinement potentials respectively, and F is the applied field to the nanocrystal. The $\mp$ sign indicates energy change in electron and holes due to polarization under field. The energy change due to Stark effect given in Equation (4.1), is then equal to the differences between the energy levels calculated from the solutions of the equation (4.2) and the energy of the exciton system without an external field. The energy shift could be calculated by non-degenerate perturbation approach or by exact solution of general equation given above [196, 42]. Below the general perturbation approach is summarized:

In the non-degenerate perturbation approach for the ground state of nanocrystal, the electron-hole Hamiltonian can simply be written as:

$$H = H_0 + H' \tag{4.4}$$

Here, the perturbation term eFr should be smaller than the ground state of the exciton or band gap of the optical transition, where r is the radius of the nanocrystal. In the above equation, the first term is unperturbed and H' = eFz is the perturbation term due to electric field in z direction, with $E_o \gg E'$, where E_o is the ground energy of exciton without perturbation. Using the second order perturbation theory, the change in the ground state energy of exciton can be written as:

$$\Delta E = eF < z_{e,h} > + eF^2 < \Psi^o_{e,h}|z|\Psi'_{e,h} > \tag{4.5}$$

and the ground state exciton wave function $\Psi_{e,h}$ with the first order correction:

$$\Psi_{e,h} = \Psi^o_{e,h} + F\Psi'_{e,h} \tag{4.6}$$

Where $< z_{e,h} > = < \Psi^o_{e,h}|z|\Psi^o_{e,h} > = < \Psi^o_h|z|\Psi^o_h > - < \Psi^o_e|z|\Psi^o_e > = < z_h > - < z_e >$ is the average electron hole separation in the direction of applied field. The

second term in equation (4.5) can be written also for electron and hole terms separately as:

$$eF^2 < \Psi^o_{e,h}|z|\Psi'_{e,h} > = eF^2(< \Psi^o_h|z|\Psi'_h > + < \Psi^o_e|z|\Psi'_e >) \quad (4.7)$$

Inserting equation (4.6) into (4.7), one can get the second order correction to the exciton energy change easily. Finally, the total energy change of exciton can be simplified in more compact form as [196]:

$$\Delta E = pF + \beta F^2 \quad (4.8)$$

The linear coefficient *p* is the built in dipole moment which reflects the initial electron-hole separation i.e. inherently present ground state dipole moment of the nanocrystal without any external applied field. The quadratic term β represents the polarizability of the ground state electron hole wave functions under applied field. The quadratic second term βF^2 is proportional with ($m_e^* + m_h^*$) r^4 [194]. For a large nanocrystal or extremely large fields this approximation would not be satisfied and contribution from higher order terms should also be expected.

In the nanocrystal system having inversion symmetry in which the ground state has even parity, the linear term should be zero (like in the case of hydrogen atom ground state). However, in reality as the nanocrystals are not homogeneous in shape distribution, polarity differences between nanocrystals and surrounding media and charged defects around the nanocrystals breakes the inversion symmetry. In some highly polar materials, the built in fields could be so high that (even built in field reach MeV.cm^{-1}), the linear term is much stronger than that of square term, which results in a blue shift in observed spectrum rather than a red shift [197]. One can easily conclude that, the second order effect increases with m^* and has a strong dependence on the nanocrystal size. Having a larger effective mass compared to electrons, most of the energy change of QCSE comes from the hole polarization under an external field. Moreover, the results observed suggest that, for best

modulation depth, larger nanocrystals should be used. However, in larger nanocrystals, exciton absorption/emission decreases. Therefore for modulator applications, the optimization of nanocrystal size is a crucial issue.

The effect of external field on the confined nanocrystal systems can be summarized as follows:

The significant effect of the field is the change in the inter-subband separation between conduction and valance band states. As the field pushes the electron and hole wave functions to the opposite side of nanocrystal with a deformation in the envelope wave functions, the ground state inter-subband separation becomes smaller (see Figure 4.2). This effect is the dominant term in the variation of exciton transition energies, i.e. the QCSE is mainly determined by inter-subband effects. The separation of electron-hole wave function leads to a reduction in the binding energy of excitons due to weakening in the coulombic interection between electrons and holes. The change in the exciton binding energy is about 2-3 meV (or more), while the change in inter-subband energies could be up to 100 meV, depending on the strength of surrounding potential barrier and nanocrystal size. Moreover, the spatial separation between the wave functions leads to an increase in the life time of excitons and consequently decreases the oscillator strength of the transitions. As the carriers are confined in a potential well, the change in oscillator strength and life time could saturate at certain value, under high field regimes if tunneling out of carriers has not taken place. Under applied field, the inner spherical symmetry of nanocrystals breaks down which results in a relaxation in the selection rules between the transitions because the field mixes the states with different parity, and thus some transitions become possible which are forbidden for F=0. Besides all effects described above, the exciton spectrum is broadened due to involvement of increased surface scattering resulting from the localization of wave function to respective corners of well. Also a sharp decrease of the life time is commonly observed as a result of carrier sweep out by tunneling at high applied fields that is another source of broadening over uncertainty relation.

4.2. QCSE in Si nanocrystals based structures

Franz-Kelydsh (stark) effect studies in Si dates back to the 1960s when the planar Si integrated circuit technology was born. However, since the exciton binding energy of Si is about 10 meV, which prevents high field application and requires relatively very low temperature for experimental observations. In addition to this difficulty, the indirect nature of band structure of the bulk Si is another obstacle for practical applications [195]. As discussed above, either porous or embedded Si nanostructures overcome this burden with relatively high quantum yield of direct-like transition. First attempts of exploiting this structures for light modulation by external field were just few years later than the observation of strong light emission from nanostructured porous Si [198-200]. However, lack of barrier layer results in high conductance through the porous layer which screens the adequate field formation for the observation. And the interference of other effects due to strong carrier injections such as Auger recombination makes the observation of QCSE almost impossible for those structures. The only observed phenomenon in this case was the selective Auger recombination under carrier injection, where the Auger recombination starts with bigger nanocrystals and continues with smaller ones with increasing bias. Under this condition, only a blue shift was seen in the emission spectrum while the emission from bigger nanocrystals was quenched by Auger effect. In one exceptional study on porous Si, the PL peak shift with applied voltage was attributed to the QCSE without having the expected quadratic relation between energy variation and the applied field [201].

On the other hand, Si nanocrystals buried in SiO_2 matrix offers advantageous over the porous one: they are well passivated by surrounding matrix, and due to presence of high band offset between both the conduction and valance bands of Si nanocrystals and the SiO_2 bands, the escape or sweep out of generated carriers from the nanocrystals could be hindered even at relatively high field levels. Moreover, excitons would survive in buried Si nanocrystals at room temperature as the exciton binding energy of a Si nanocrystal is expected to be between 50 and 100 meV due to confinement for a nanocrystal size whose diameter is in the range of 2-5 nm [202,203]. Therefore one expects that for Si nanocrystal in SiO_2 , the excitons could survive at elevated temperature beyond the room temperature. Like porous Si, the

electric field effect on Si nanocrystal SiO_2 system has been studied by a few groups. Under strong illumination, Lin et al. indirectly announced QCSE observation, that was assumed to be due to the charge accumulation and trapping around the Si nanocrystal which results in an internal field formation that could lead to 11 nm change in the emission spectrum [204]. In another study, under external field, it was observed that there was a small red shift from Si nanocrystal for small electric fields. In this study the spectrum was blue shifted for moderate and high field levels [205]. They interpreted this blue shift resulted from a combination of strong carrier injection following selective Auger recombination rather than the QCSE, which was dictated at relatively high field regime. Moreover, the observation was done at relatively high field levels of few $MeV.cm^{-1}$, and they observed strong aging effect on their devices which was not reversible. In 2008, we demonstrated the first clear observation through well designed experiment on ion implanted samples which were later consistently supported theoretically by Bulutay et al. in 2010 [42].

4.3. Experimental procedure

P-type (1-10 Ω cm) (100) Si wafers with thermally grown 250 nm thick SiO_2 film were used. SiO_2 film was implanted with ^{28}Si ions at energy of 100 keV with an implantation dose of $1x10^{17}$ cm^{-2} and then annealed at 1100 ^oC for 2 h under N_2 atmosphere to induce nanocrystal formation. Si nanocrystals with a mean size of 3.2 nm with a deviation of 1.1 nm were observed in our previous study [206] with transmission electron microscope (JEOL2010F transmission electron microscope (TEM) equipped with a Gatan Imaging Filter (GIF)). Whereas using the theoretical approaches from the peak position of PL emission spectrum, Si nanocrystals were found to be around 5 nm [204]. We found that the shapes of the nanocrystals are either spherical or elongated in one direction. There was however no evidence for any preferential orientation of these elongated structures. In a similar study published recently by others, the calculated mean nanocrystal size was found to be 3.3 nm for samples annealed at 1100 ^oC [207] which is very close to our mean crystal size of 3.2 nm. Nanocrystals are buried at a mean depth of 140 nm from the film surface. Having an active layer buried between well isolating thermally grown oxide layers is an advantage of ion implantation for the high field applications. Metal oxide semiconductor (MOS) device structures were fabricated by evaporating 500 nm thick aluminum for back contact and by sputtering a 100 nm thick indium tin oxide (ITO) film for front contact. ITO film served as both electrical contact for the field application and a window for the PL measurements. The schematic illustration of the fabricated devices is shown in Figure 4.3. PL measurements were performed under external dc bias in the range of 0-34 V in closed cycle helium cryostat, by using 532 nm continuous NdYAG laser as an excitation source with an intensity of 0.7 $W\text{-}cm^{-2}$ and emitted light was detected with a spectrometer equipped with a CCD camera. PL measurements were conducted by applying first forward then followed by reverse bias for each voltage values. As an indication of the expected reliability and controllability of our sample preparation, we mention that we have also performed an experiment with two different samples and these results show consistent behavior as reported here. We have repeated PL measurement at different temperatures on these devices and obtained similar results in all experiments.

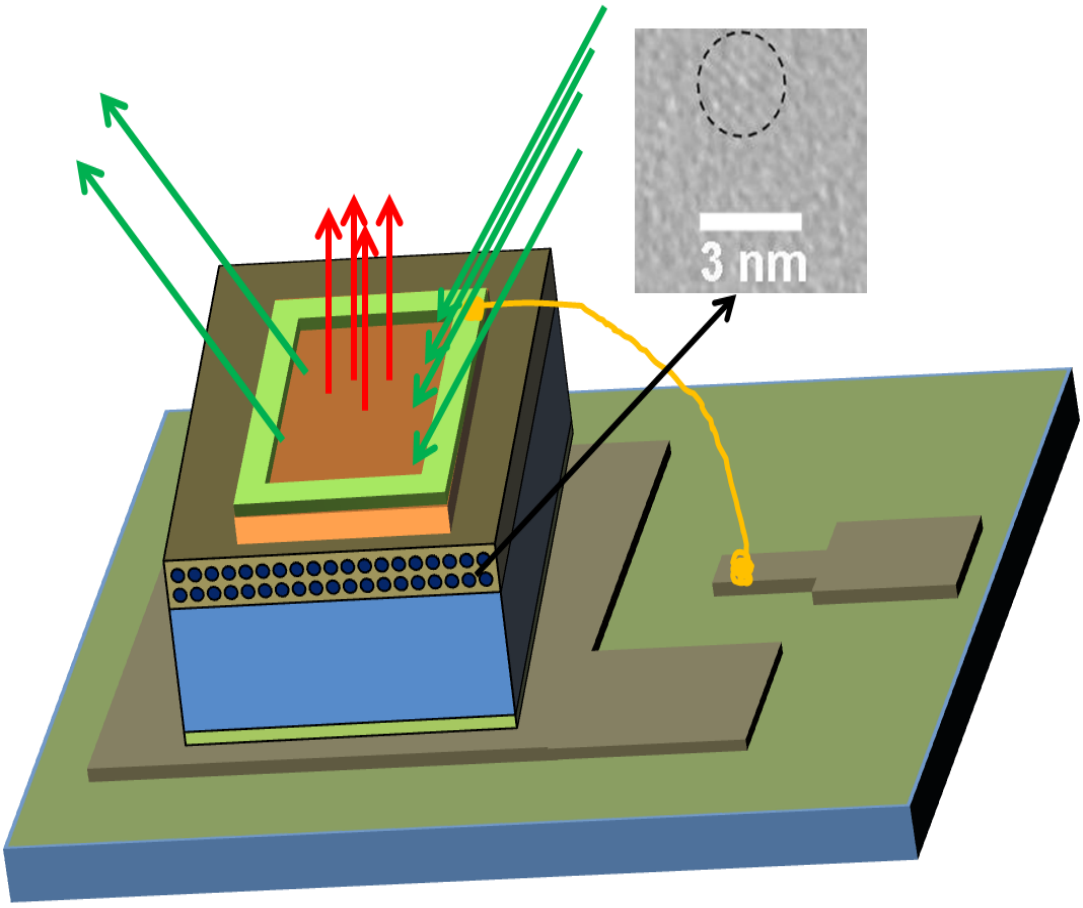

Figure 4.3. Cross-sectional schematic illustration of the devices for QCSE measurements. Green arrows indicate incoming and reflected laser light, and red arrows indicate modulated light emissions from Si nanocrystals under external electric field. At the upper right of the figure TEM image of Si nanocrystal is shown.

4.4. Results and Discussions

4.4.1. Observation of QCSE and temperature dependence

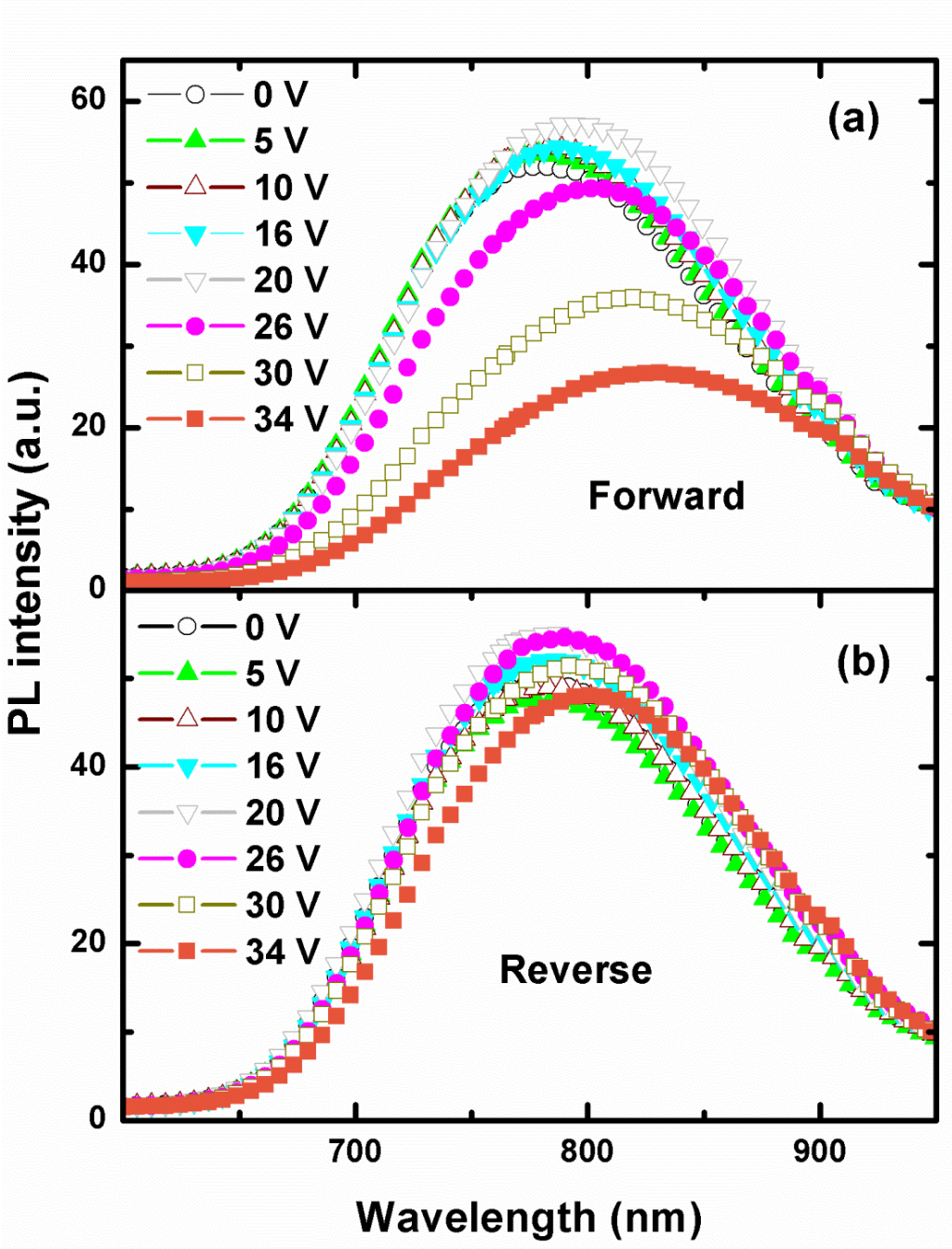

Figure 4.4. PL spectra of the sample implanted with Si^+ with a dose of $1x10^{17}$ cm^{-2} and annealed at 1100 ^oC for 2 h and measured at a temperature of T=30 K under (a) forward, and (b) reverse bias, within the range of 0-34 V. For the clarity of figure, selected voltage values are shown.

For the observation of QCSE in Si nanocrystals reported here, we had to use PL experiment due to the structure of the devices. The QCSE is generally demonstrated with the characterization techniques such as electro photo-absorption/transmission, electro-reflectance and -luminescence [208-210]. Electro-absorption is the most generally used technique for this type of studies, as the PL technique is relatively difficult compared to the absorption techniques for the Si nanocrystals as well as other materials. Absorption is the direct interaction of light with material system whose analysis is relatively straightforward. In contrary, PL emission is a secondary effect after the light absorption, which is very susceptible to the temperature and various relaxation pathways inherently present in the material system. This brings significant difficulties in both measurement and analysis of experimental data. Moreover, the effect of the field on the initial absorption that can alter the emission properties might be easily overlooked in the PL experiments.

In Figure 4.4., PL spectra of forward (accumulation) and reverse (inversion) biased samples measured at 30 K are presented. For the forward biased sample the PL peak is red shifted from ~780 nm to ~820 nm with increasing applied voltage from 0 to 34 V corresponding to an average electric field of 0-840 kV/cm across the nanocrystals.

The average electric field across the nanocrystals is calculated by assuming that all of the applied voltage drops across the Si nanocrystal dispersed oxide layer in the forward (accumulation) regime. The field across the nanocrystals is then found by an estimation based on the volume ratio of the Si nanocrystals to SiO_2 matrix. In this calculation, taking the dose of the implantation as $1x10^{17}$ atoms/cm^2 and atomic concentration of Si crystal as $5x10^{22}$ atoms/cm^3, the implanted ions corresponds roughly to a continuous Si layer of 20 nm. Applying the boundary condition for perpendicular component of electric displacement vector, the electric field across the nanocrystals was then estimated from the relation $F_{Si} * \varepsilon_{Si} = F_{SiO_2} * \varepsilon_{SiO_2}$, where F is the electric field and ε is the dielectric constant which was taken to be 11.9 and 3.9 for Si and SiO_2 , respectively [165]. The red shift in the PL peak position is accompanied with an increase in the width of the spectrum as can be seen from Figure 4.4 (a). On the other hand, the PL intensity stays almost constant up to a certain bias value where it starts to decrease with increasing applied voltage. Similar

PL characteristics were observed under reverse bias except that the red shift and the variation in the PL intensity are less than those observed in the case of forward bias (see Figure 4.4 (b)). When the applied voltage was turned-off, both PL intensity and peak position return to the unbiased values. Namely, no aging effect was observed as it was reported by Kamenev et al. [205].

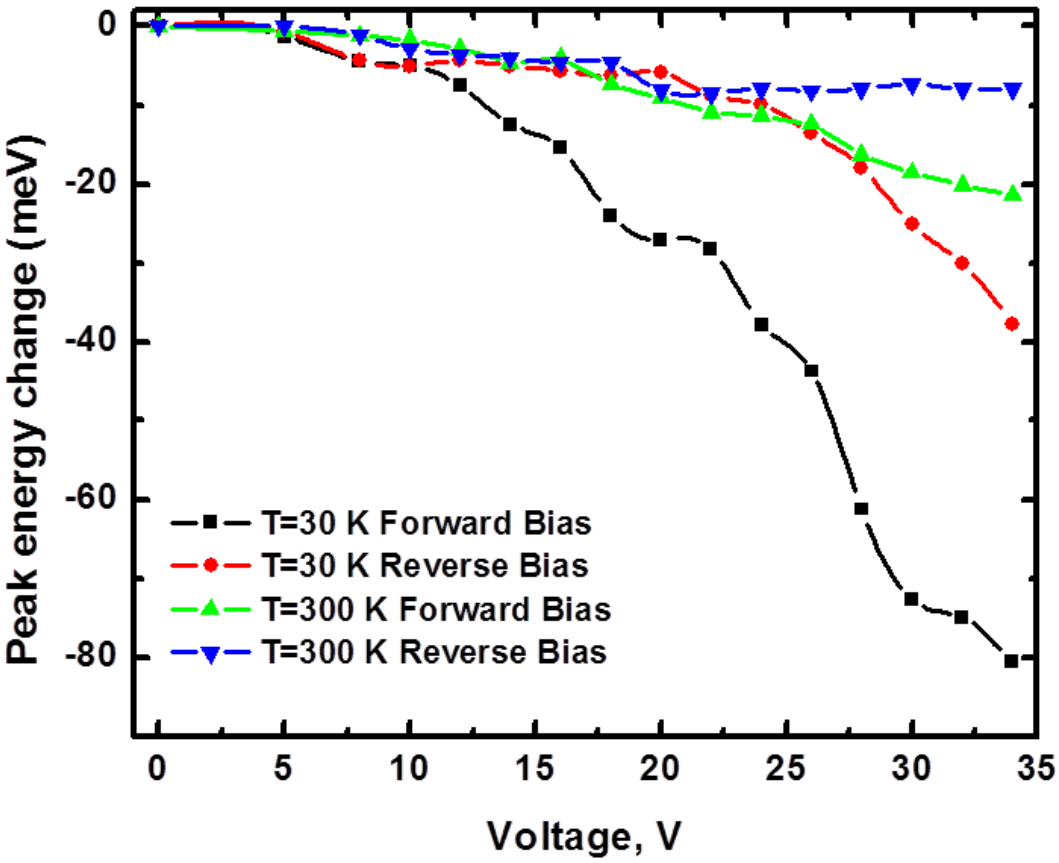

Figure 4.5. Shift in PL peak energy under forward and reverse bias at T=30 and 300 K.

Figures 4.5 and 4.6 show the variation of the peak position and the intensity of the PL signal as a function of the applied voltage. We see that both peak position and intensity are strongly dependent on the polarity of the external bias and the temperature of the sample. The peak shift at room temperature is rather small and difficult to measure. The peak shift increases with decreasing temperature and reaches a maximum value of 80 meV at T = 30 K under forward bias for a potential

difference of 34 V. The intensity variation exhibits a different feature as can be seen in Figure 4.6. At T= 30 K, the intensity tends to remain constant with small oscillations or slightly increase up to a certain voltage value (i.e. 22 V) beyond which a sudden decrease is observed. At room temperature, the PL intensity remains almost constant for the reverse bias while it decreases slightly for the forward bias case.

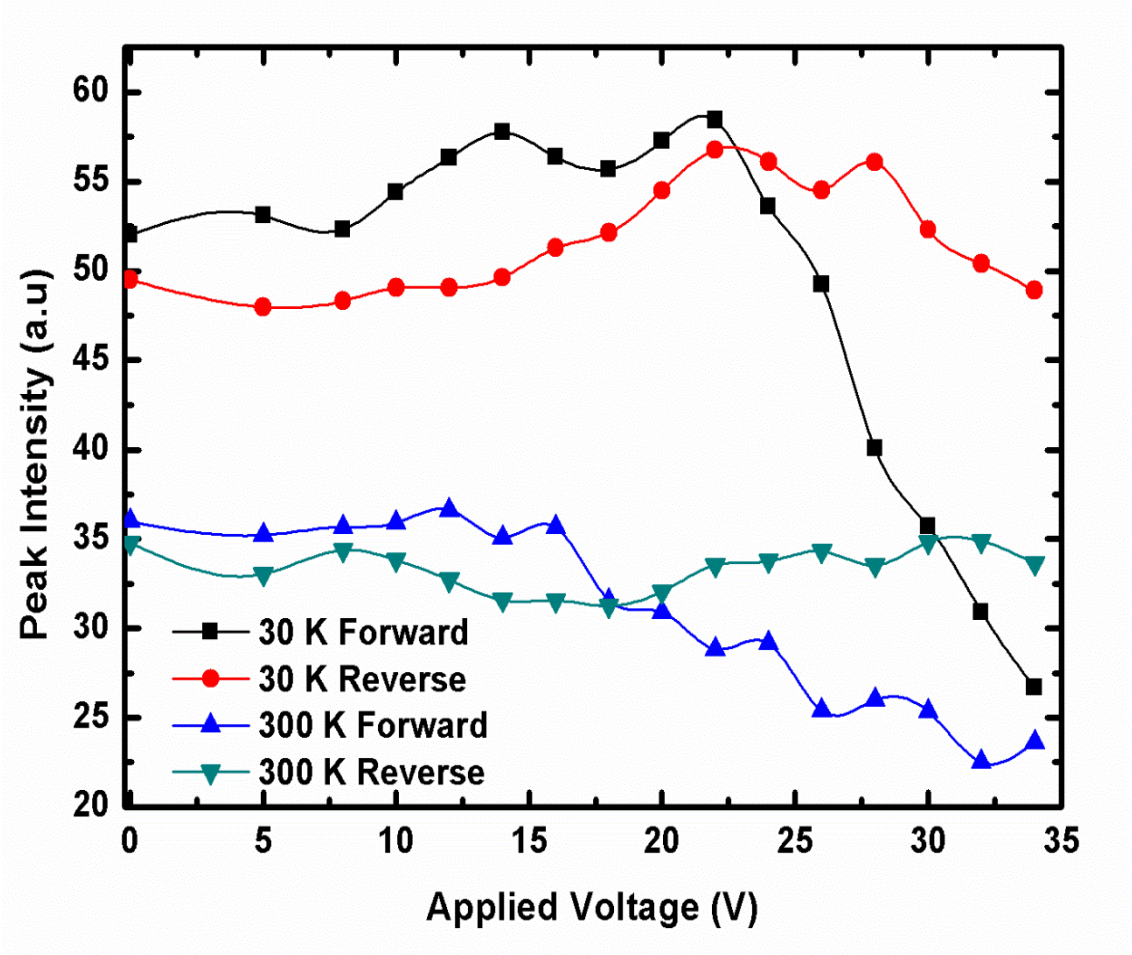

Figure 4.6. PL peak intensity variation as a function of applied voltage measured at T=30 and 300 K under forward and reverse bias.

Both the peak shift and the intensity variation are larger in the forward bias than that in the reverse bias. This asymmetry in the energy shift is related to the oxide charges formed at the SiO_2/Si interface either during the nanocrystal formation or by charge injection during the measurement. In order to reveal the type and the amount of oxide charges and estimate their effect on peak energy shift shown in Figure 4.5, we

performed capacitance-voltage (C-V) measurements at 300 K and 30 K with and without laser illumination. It can be seen from Figure 4.7 that the device is exhibiting typical C-V characteristics under light irradiation with a significant flat band shift in the negative direction. Without illumination, devices went to deep depletion regime due to lack of adequate generation of minority carriers (electrons) that respond to applied signal. This shows that the device is not leaky but charged positively either during device processing or measurements.

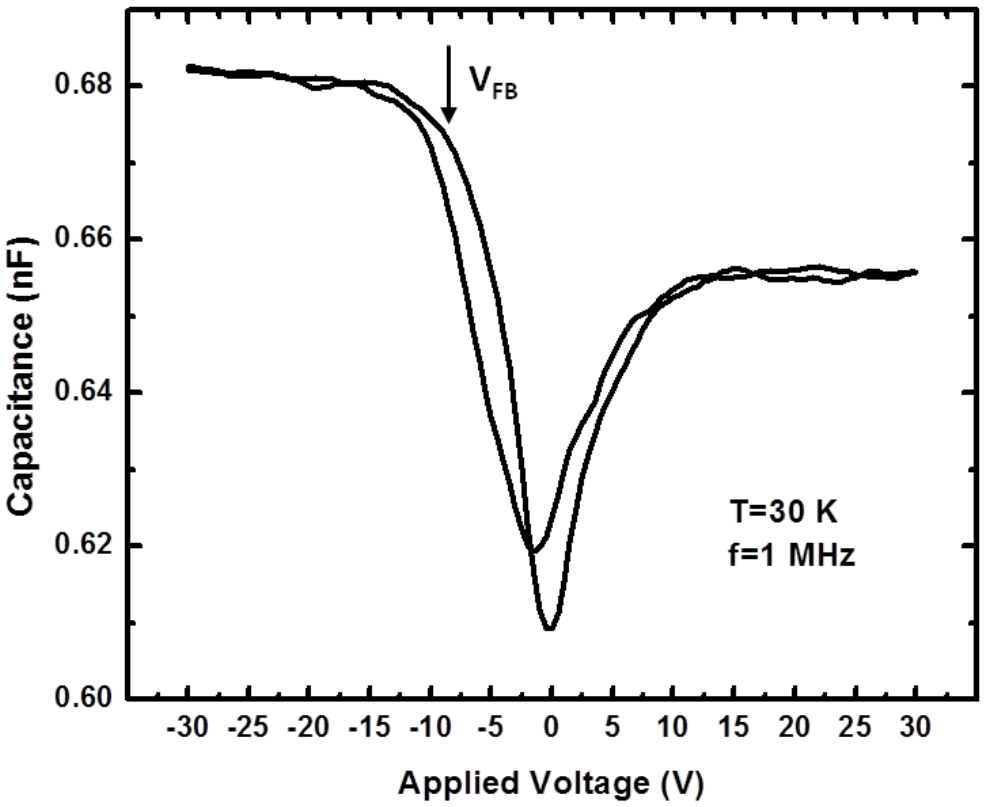

Figure 4.7. C-V curves measured at 30 K under laser illumination. The curves were obtained by sweeping the voltage from -30 V top +30 V and back from +30 V to -30 V at a frequency f = 1 MHz.

The flat band voltage, whose position on the voltage axis is a measure of oxide charges, was found to be shifted up to about -9 V showing that the oxide layer is positively charged. The voltage drop across the oxide layer is then not symmetrical around zero volt. In the reverse bias regime, the external voltage is partly screened by the local field developed by the oxide charges near the Si/SiO_2 interface. In

addition, it is expected that about 0.5 V of the applied voltage drops across the depletion region formed in the substrate under reverse bias. This is the typical voltage drop that can easily be calculated for a given substrate doping for a MOS device. As can be observed from Figure 4.5 the PL peak shift reaches about 38 meV at 34 V under reverse bias which corresponds to a value of 24 V for the forward bias case. The difference between these applied voltages (i.e. 10 V) is roughly same as the flat band voltage shift determined from the C-V measurements. This voltage shift explains the observed asymmetry in the QCSE with respect to the polarity of the applied voltage.

QCSE in quantum dots has been studied theoretically and experimentally for semiconductor systems like InAs/GaAs [179] and CdSe [180]. It is known, from the second order perturbation theory, that the change in band gap energy due to QCSE can be expressed by the following general expression:

$$\Delta E = pF + \beta F^2 \tag{4.8}$$

Where F is applied electric field, p and β are the dipole moment and the polarizability of the electron-hole system along the applied field, respectively. The linear term in this expression corresponds to presence of built-in dipole moment in the system. Such a built-in dipole moment was identified in the pyramidal InAs-GaAs and CdSe quantum dots where the inversion symmetry is not present [180]. For a fully isotropic and relaxed system, this linear term should be negligible.

QCSE manifests itself as the reduction of the effective energy difference between valence and conduction bands with the applied field. Any transition (absorption/emission) between these two bands should then be a function of the field strength, correspondingly. One important consideration is the temperature dependence of the QCSE, which can shed light on the polarization mechanism of the electron-hole pair within the quantum dot. QCSE is primarily determined by the spatial distribution of the electron-hole wave function. As described in detail by de Sousa et. al., Si quantum dot has closely spaced sub-bands in the conduction and valence bands [211]. The spatial distribution of the wave function corresponding to

these states within the nanocrystal depends on the external field. The electron/hole wave function corresponding to the lowest energy level is expected to have greatest localization and thus largest spatial separation from its counterpart under the external field. The polarization is then expected to be largest for the lowest energy level. Carriers residing at higher energy levels spread across the dot leading to less polarization. The QCSE should then increase with decreasing temperature as the relative population of the lower energy level increases. This was indeed observed in the InAs-GaAs dot system where the QCSE was studied by photocurrent experiments as a function of temperature [179]. In line with the expectations based on this qualitative description, we see from Figure 4.8, that QCSE is significantly larger at cryogenic temperature than at room temperature.

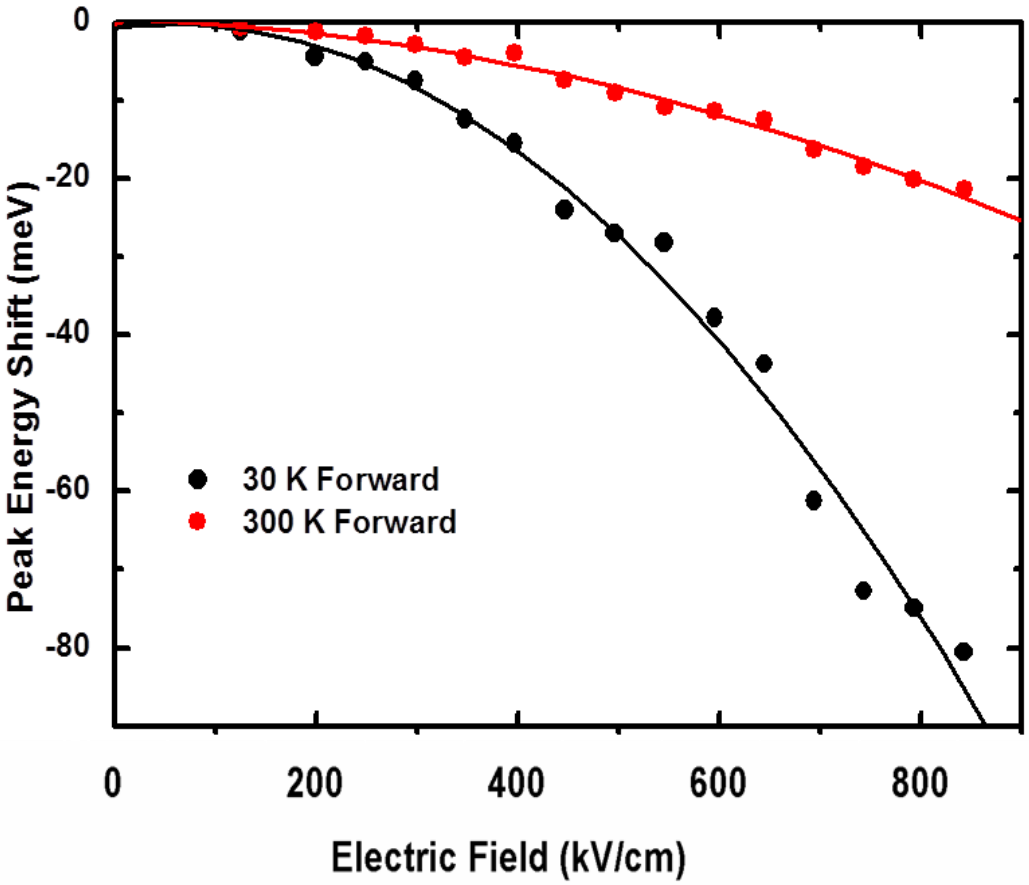

Figure 4.8. Shift in peak energy with respect to field across Si nanocrystals at forward bias for T=30 K and 300 K. Solid lines represent the theoretical fit by using Equation (4.8).

A good agreement is obtained by fitting the data in Figure 4.8 with equation (4.8) for both high and low temperature cases. The estimated values are 8.77×10^{-32} C-cm^2/V and 1.74×10^{-32} C-cm^2/V for the polarization constant β for 30 K and 300 K, respectively. Polarization constant β decreases with increasing temperature, reflecting the variation in the observed QCSE. The built-in dipole moment values are estimated as 4.83×10^{-27} C-cm and 1.31×10^{-27} C-cm for 30 K and 300 K, respectively. Decrease in both polarization constant and dipole moment is obvious as the temperature increases due to more spreading of electron/hole wave function over the nanocrystal with increasing temperature. The average separation between electrons and holes are then calculated as 0.302 and 0.082 nm for 30 and 300 K, respectively from p = er, where e is the electron's charge and r is the average distance between electron and hole. These values are small compared to the average nanocrystal size which was determined to be in the range of 3-5 nm for the similar samples studied here. A built-in dipole moment is normally not expected in an ideal nanocrystal system embedded in the SiO_2 matrix due to the inversion symmetry of the Si. However, interface states, which are believed to play an important role in nanocrystals, may act as trapping centers forming a built-in dipole moment. The presence of such a built-in dipole moment has been attributed to interface states in previous studies [183, 212]. In the present case, the estimated electron hole separations point to a modest effect of built-in dipole moment as expected from a system having inversion symmetry.

The intensity of the PL signal remains almost at the same level for all voltage values under reverse bias (see Figure 4.6). In the case of forward bias, the intensity either remains constant or increases slightly up to 22 and 16 V at T=30 K and room temperature, respectively. Above these voltages, the PL intensity drops monotonically with the applied voltage. The slight increase in the PL intensity at low voltage values might be due to the saturation of trap states with the low level injection. The low level of carrier injection might saturate trap states causing enhancement of PL intensity [213]. Moreover, the oscillatory behavior of emission intensity is due to the field induced parity change between the transitions as discussed before, this oscillatory behavior is also supported by theoretical calculations given in the following section. However, at higher voltages, PL

intensity quenches due to separation of electron/hole wave function and sweeping out of carriers from Si nanocrystals. Also increase in field strength could enhance cross-talk between nanocrystals, under which circumstances carrier migration to neighboring nanocrystals cause to lower PL efficiency [214]. It is quite understandable that onset of the carrier escape starts at lower voltages at room temperature with the help of thermal excitation to higher energy states within the nanocrystal. Any defect states at nanocrystal/SiO_2 interface or in SiO_2 matrix could facilitate this escape or tunnel out. Moreover overcharging nanocrystals could also cause significant reduction in PL intensity through Auger recombination [200, 215]. However, in our devices the Auger effect is expected to have almost no influence considering the charge injection from the device terminals. Finally, it is important to note that the observed energy shift is independent from the variation of the PL intensity which indicates that observed shift is related to QCSE rather than variation in the carrier population caused by over carrier injection/escape as proposed in the case of porous Si.

The effect of nanocrystal size on QCSE should also be studied for a complete understanding. However, the Gaussian distribution of the implanted Si atoms in the matrix, which is usually obtained from the ion implantation process, leads to the formation of nanocrsytals with different sizes. Larger nanocrystals are expected to be formed around at the peak of the Gaussian (i.e. ~140 nm from the optical window), and their sizes reduces gradually towards the tails of distribution. The emission spectrum is very broad as the total spectrum includes emission from all nanocrystals with different size. The field effect on PL emission varies also with nanocrystal size as we confirmed by a theoretical analysis and experimental observations in the next section.

4.4.2. Theoretical calculations on QCSE of Si nanocrystals embedded in SiO_2 and comparing with experimental observations

To support the experimental observation given above and to understanding the atomistic picture of the Si nanocrystals embedded in SiO_2, theoretical calculations was also conducted. The interested readers can find the details of calculations in studies of Ceyhun Bulutay and his group's publications [42,116,215,216]. The calculations here conducted by this group were on a single representative Si nanocrytstal embedded in uniform SiO_2 insulating matrix which resembles the actual samples used in our measurements. In the frame of theoretical calculations; electric field dependence of emission rate through oscillator strength, polarizability of carrier wave fuctions under applied field with the inclusion of Coulomb interaction, and field induced crossing in the energy levels were clearly elaborated and demonstrated for the first time. In the calculations for the valance band, the heavy-light hole mixing effect and the electron-phonon interactions were excluded. Therefore, the spin-orbit interactions and splitting in valance band were not calculated, meaning that the Hamiltonian was invariant under spin space rotations. These simplifications are not expected to have any significant effect on the outcomes of the computation.

The theoretical computation is a combination of semiempirical pseudopotential based atomistic Hamiltonian with the combination of LCBB (linear combination of bulk Bloch bands) as the expansion basis [217]. It is like analogy of tight binding method, but use bulk Bloch bands as a basis instead of atomic orbitals. External field is directly included into the Hamiltonian without any perturbation approximation. The computation technique is very powerful on the calculations of systems even made of several thousand atoms. The method was first tested on embedded group IV nanocrystals systems for various physical phenomena: such as, inter- and intra-band transitions, Auger recombination and carrier multiplication, non linear optical properties and then finally applied to Stark effect. Further technical details of the calculations can be found in reference [42].

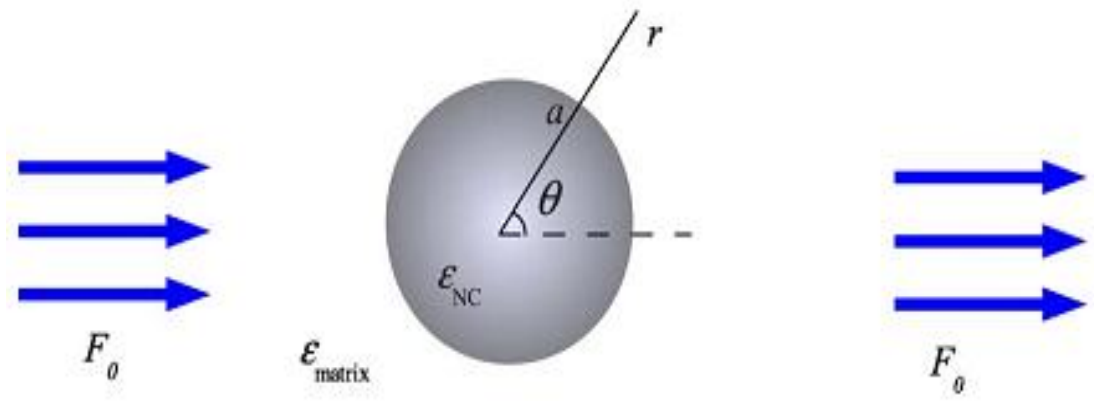

Figure 4.9. Electrostatic construction of single Si nanocrystal/SiO_2 system under uniform external field [42].

Figure 4.9 represents the single spherical nanocrystal embedded in a SiO_2 dielectric matrix with a constant permittivity and assumed to be well separated from other nanocrystals i.e. there is no interaction between the nanocrystals, which is believed to be the case in the actual experiments. The electrostatic potential is solved for the nanocrystal in spherical coordinates under uniform field F_o applied to the oxide layer using the dielectric ratio between nanocrystal and SiO_2. This potential energy is incorporated to the potential term of Hamiltonian as an external field effect.

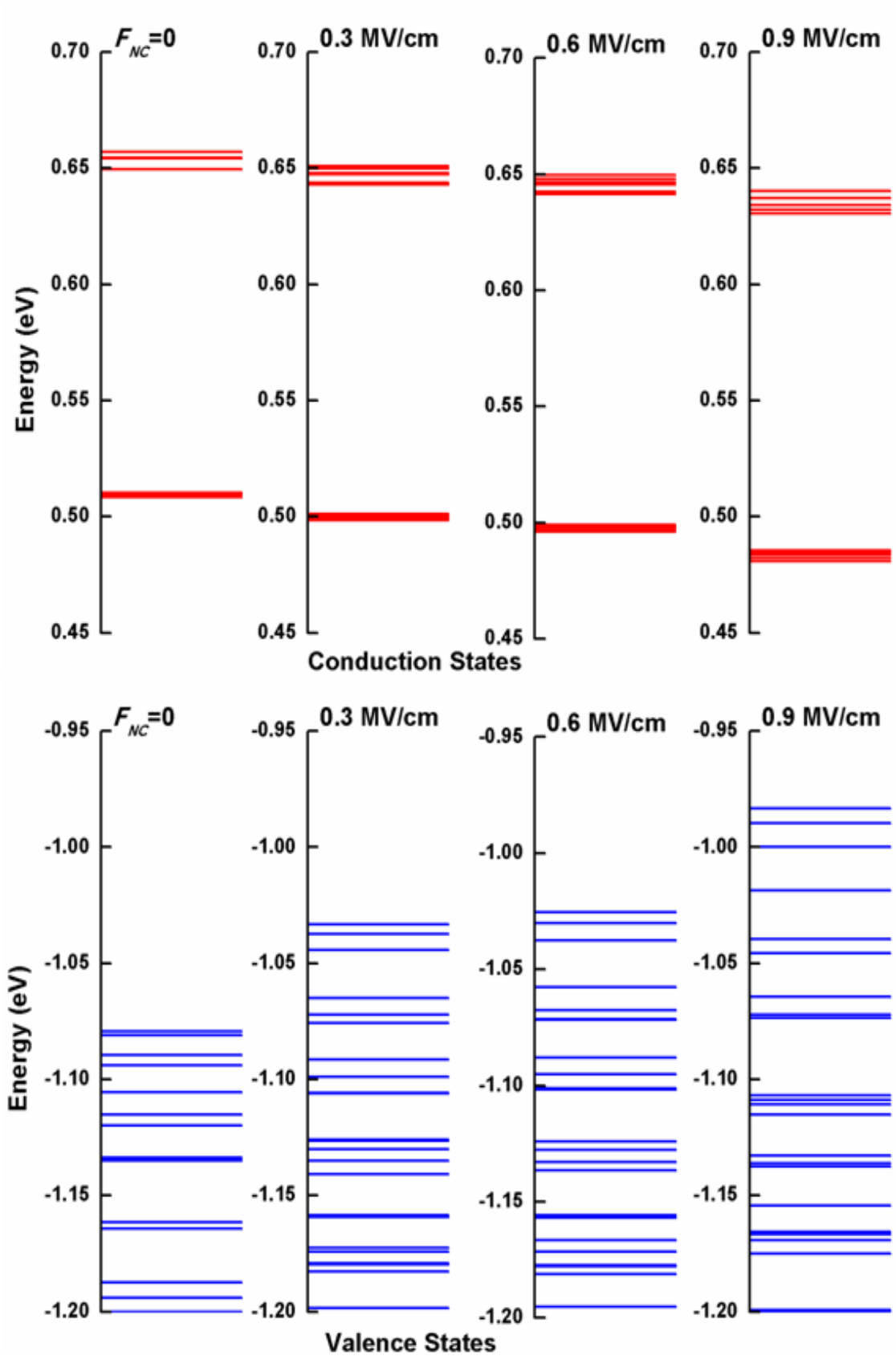

Figure 4.10. Single particle energy levels: for electrons (upper-red) and for holes (lower-blue) under various external field values. Si nanocrystal radius is 5.6 nm. [42].

Using the peak position of PL emission which is located at 780 nm, the calculated average size of nanocrystal is around 5.6 nm for computation. The size is extracted through theoretical model [116]. For this size of Si nanocrystal, single particle energy states of electrons and holes under different values of applied external field is displayed in Figure 4.10. The computational results clearly reveal that valance bands states are more prone to Stark shift which was also observed to be the case in InP quantum dots [218]. It is also known from the perturbation theory that as the holes have larger effective mass compare to the electrons, they are much more localized. Therefore under the applied field, holes are more polarized and contribute to the total Stark shift much more than the electrons.

The field dependence of oscillator strength for Si nanocrystal with diameter of 5.6 nm is given in Figure 4.11. Oscillator strength is the measure of overlap between electron and hole wave functions, which determines the strength of the transition rate of the emission/absorption. In the zero field un-distorted case, the wave functions are mostly localized and distributed as discrete like around the center of the nanocrystal. Under applied voltage of 34 V, the wave functions respond to the electric field as seen in Figure 4.11 (b). Hole wave function is strongly localized at nanocrystal dielectric interface in the direction of the external field. On the other hand electron wave function is almost staying symmetric around the center without localization to the opposite side of nanocrystal. The only insignificant change is the broadening in the distribution of wave function with changing its shape. Moreover, it is easily seen that under the external field the overlap between electron and hole wave functions significantly reduced, thereby result in quenching in the emission rate.

In Figure 4.12 the comparison of experimental QCSE red shift in the emission energy measured from Si nanocrystals at 30 K under forward bias with the results obtained from theoretical model is given. The forward bias regime of the measurement was chosen as it reflects the same scenario constructed in the theoretical approach. To correlate with the experimental results and account for the thermal effects as well as each excited state recombination, radiative recombination energy and oscillator strength were averaged by using Boltzmann factor with using

canonical partition function formalism. Moreover, same averaging also applied to the electron–hole Coulomb interaction energy. It is revealed in the Figure 4.12 that, the contribution from Coulomb interaction to the total Stark shift is not negligible. The energy change of single particle level could not be fully described without Coulomb interaction term. This significant contribution from Coulomb interaction is mostly

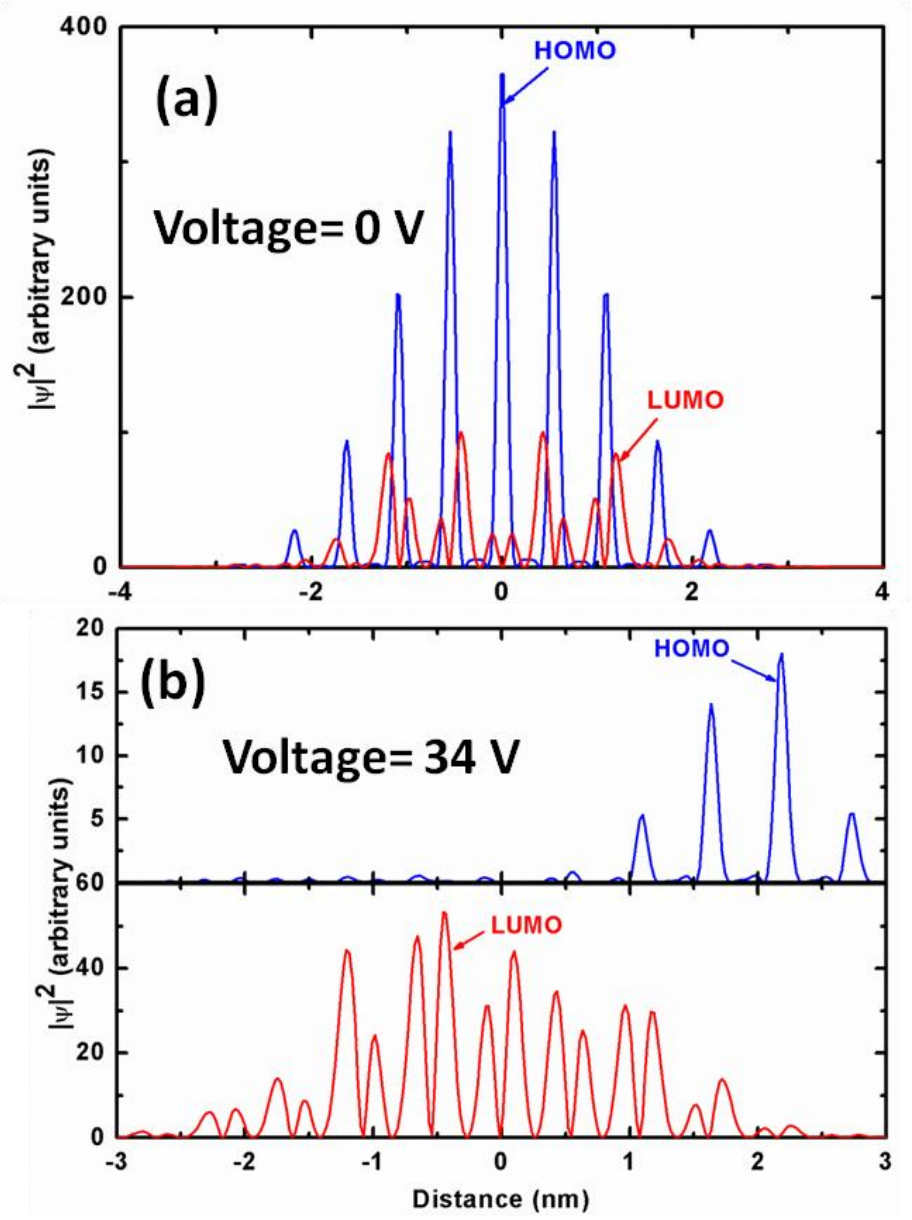

Figure 4.11. Oscillator strength (overlap of carrier wave functions): (a) without any bias wave functions are distributed symmetrically around center of the nanocrystal. (b) with the application of voltage hole wave function become more opposite and localized towards interface, while the electron wave function opposite parts turn same sign and stay symmetric around the center. The blue colored distribution represents hole while red one is representation of absolute value of electron wave function.

due to high band offsets of both conduction and valance bands between Si nanocrystal and SiO_2 insulating matrix. This shows that, even under high field regimes excitons are not totally ionized due to huge potential barrier. Under this scenario, one can expect that Coulombic term of the Stark shift is more pronounced for bigger Si nanocrystals compared to smaller ones, in which carriers see higher potential barrier and spatially more localized in nanocrystal volume.

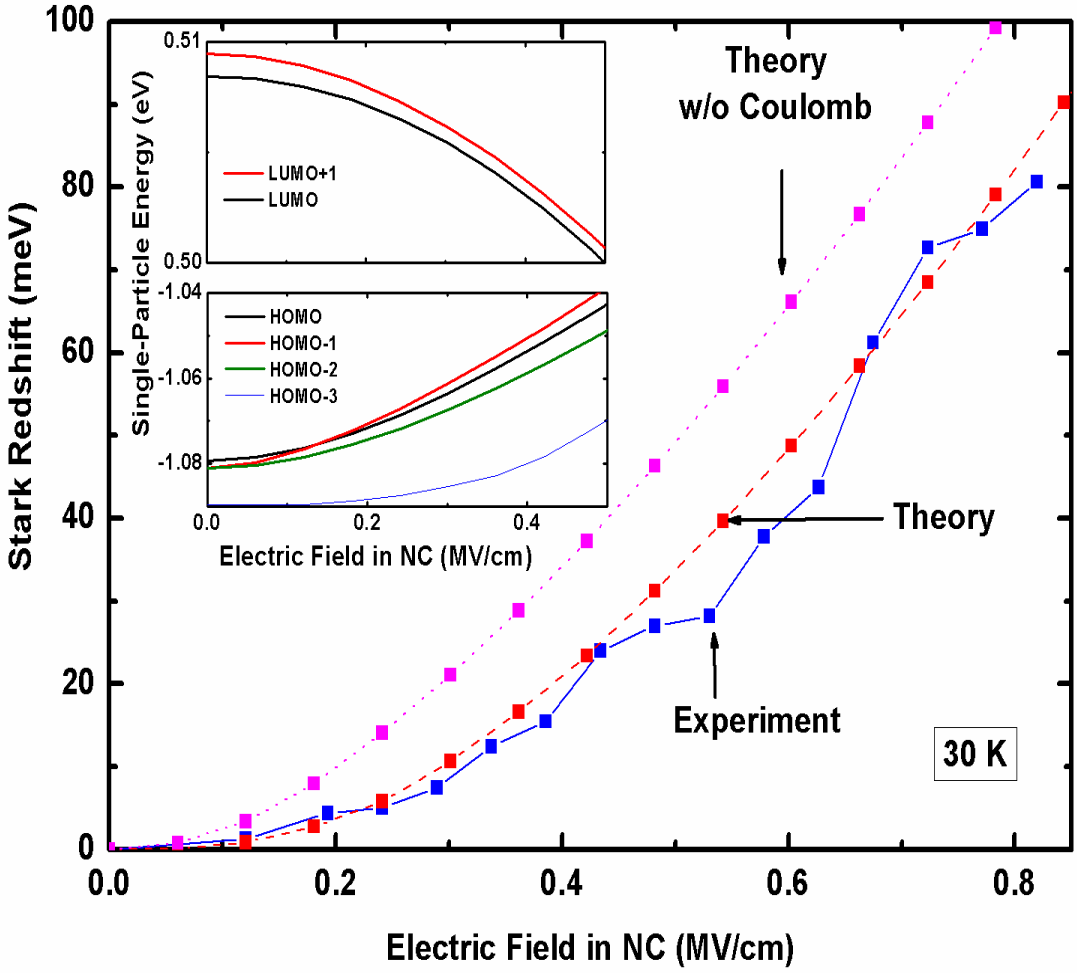

Figure 4.12. Comparison of experimental (forward bias case) and theoretical red shift due to QCSE of 5.6 nm Si nanocrystal at 30 K. The pink colored curve is only including single particle energy change of electrons and holes without coulomb interaction. In the red curve coulomb interaction is also taken into account. In the inset single particle stark shifts of the band edge states for conduction and valance bands are given (upper inset and lower inset respectively) [42].

No dipolar linear term has been observed from theoretical results as in the case of experimental observations in which the dipolar term was very small compared to the quadratic shift. This means that, although several effects were overestimated in the theory such as nanocrystal size inhomegenity, interface states between nanocrystal and SiO_2, carrier phonon interaction and the strain effect, the theory fairly supports the experimental findings. In the lower inset of Figure 4.12, the energy level crossing is seen in the evolution of valance band single particle states of Si nanocrystal with diameter of 5.6 nm at field strength of about 150 $kV.cm^{-1}$.

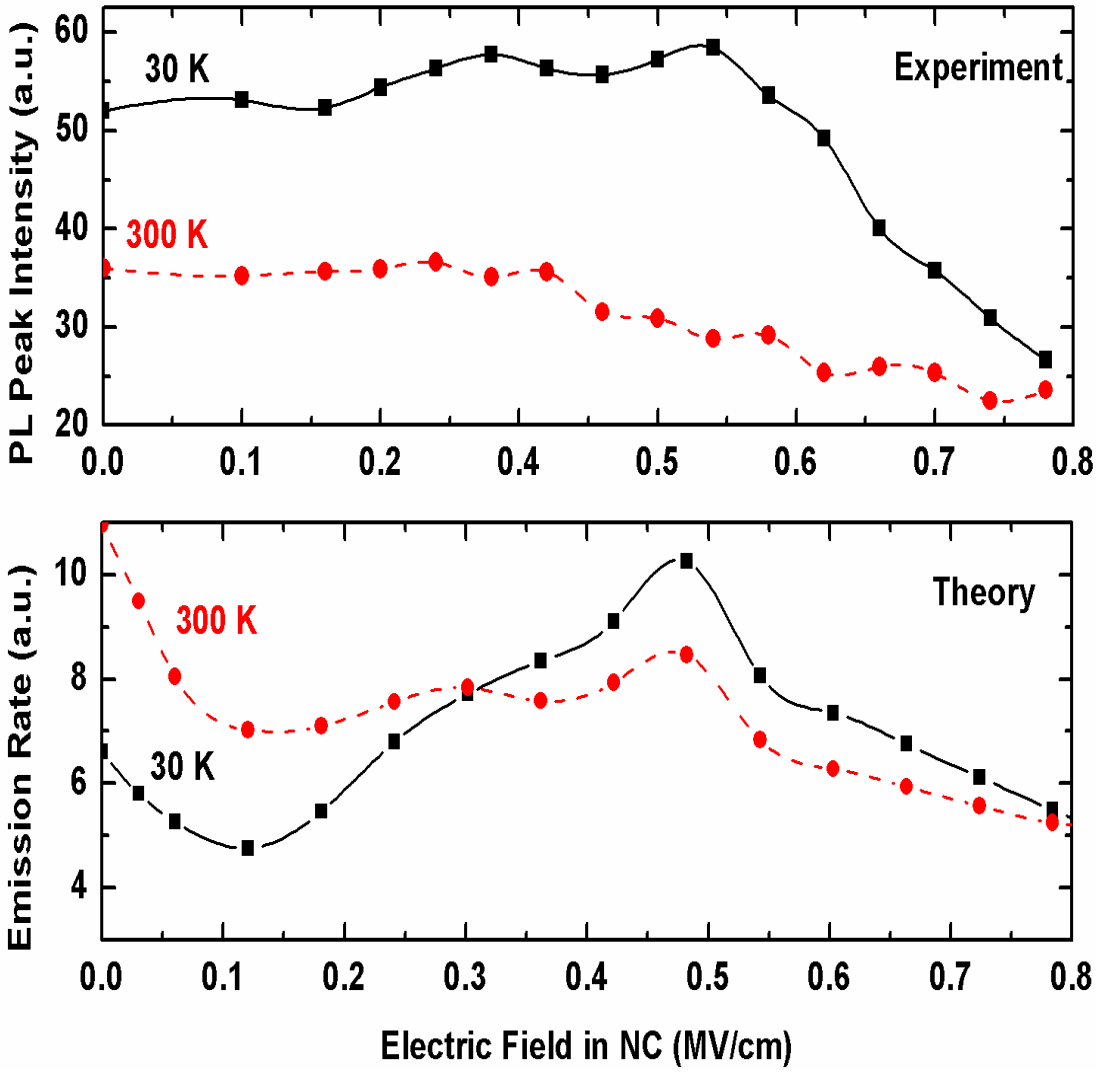

Figure 4.13. Experimental PL intensity and theoretical emission rate change under different field values for Si nanocrystal at 30 K and room temperature. Red colored spectrum represent at room temperature while black one represents at 30 K respectively [42].

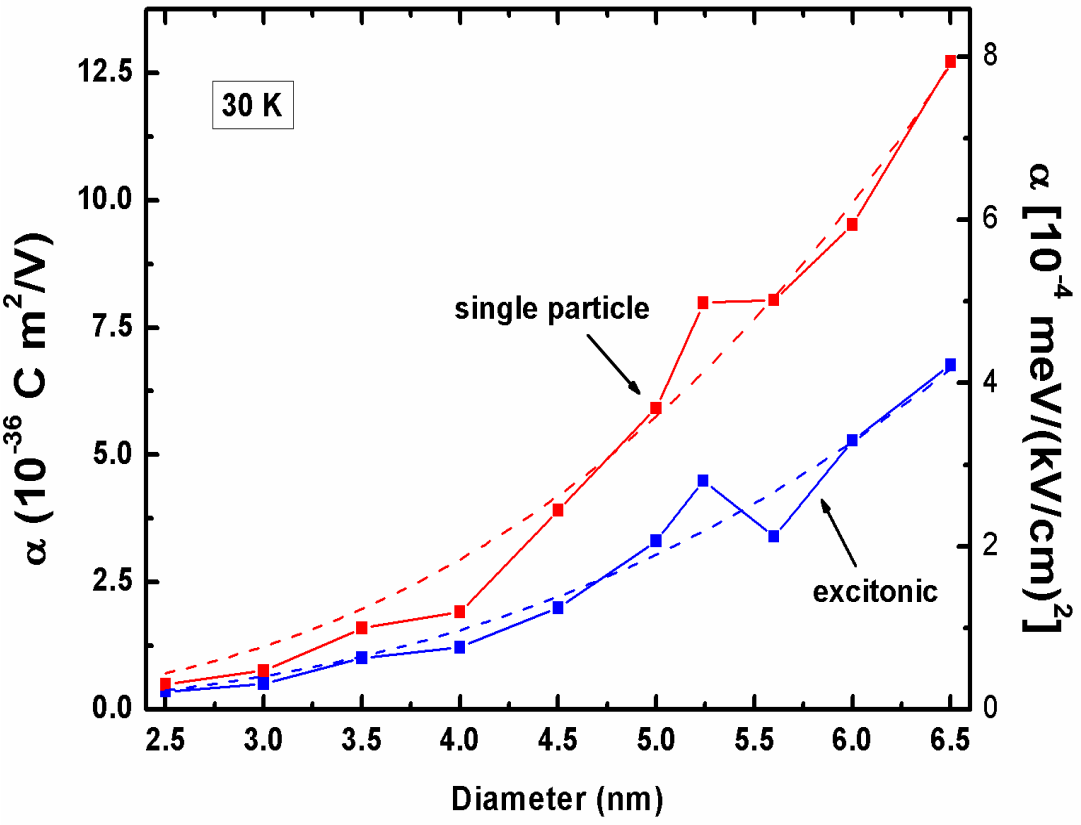

Figure 4.14. Dependence of polirizability on Si nanocrystal size, with and without Coulomb interaction at 30 K. The applied field is fixed at 0.5 MeV/cm. The dashed lines indicate cubic fits to the computed results.

In Figure 4.13, comparison of PL intensity of experimental result with the theoretical emission rate is given for various applied external field values. The oscillatory non-monotonic behavior in the emission peak intensity was observed in both experimental and theoretical results. This means that the intensity variations in the observed PL intensity are qualitatively estimated by theoretical computations. However, contrary to what we observed experimentally, for relatively small field levels, the theoretical results estimate the emission intensity to be much higher at room temperature than at 30 K. This might be due to thermally activated processes which degrade the emission intensity at higher temperature regime. Moreover, as the theoretical computation was done on a single Si nanocrystal, any resonant and non-resonant coupling between nanocrystals or between nanocrystals and point defects that could be present in the matrix, were not included in the theory.

As discussed before, QCSE strongly depends on the size of the nanocrystal, and the contribution of hole states is much larger than that of electrons due to their relatively larger effective mass. The quadratic term which reflects the polarizability of electron hole wave functions by the external field increases with increasing nanocrystal size accordingly. Up to now theoretical results were restricted to single diameter value of 5.6 nm which was extracted from the PL peak position of the experimental data. In the calculations, semi-Gaussian size distribution of the nanocrystals in the actual sample was ignored. Next, we have extracted the size dependence of the polarizability of Si nanocrystals, defined as $\Delta E = -\alpha F^2$, where ΔE is overall Stark shift in the emission energy, α is polarizability constant and F is the electric field inside the nanocrystal. In Figure 4.14, the excitonic polarizability is given with and without Coulomb interaction at 30 K. It is seen that, for relatively larger nanocrystals, the actual value of polarizability is significantly overestimated without inclusion of a change in the exciton binding energy (or Coulomb interaction between electrons and holes). Both curves display a small oscillatory non-monotonic behavior in the polarizability with respect to nanocrystal size. Like the basic dipole polarizability, both curves can be easily fitted by a cubic dependence of nanocrystal diameter as $\alpha = c\ R^3$, where R is nanocrystal diameter. Using the fit function, the value of c were found to be 2.43×10^{-11} and 4.61×10^{-11} C/(V.m) for the excitonic and single particle cases respectively.

4.4.3. Size and temperature effect

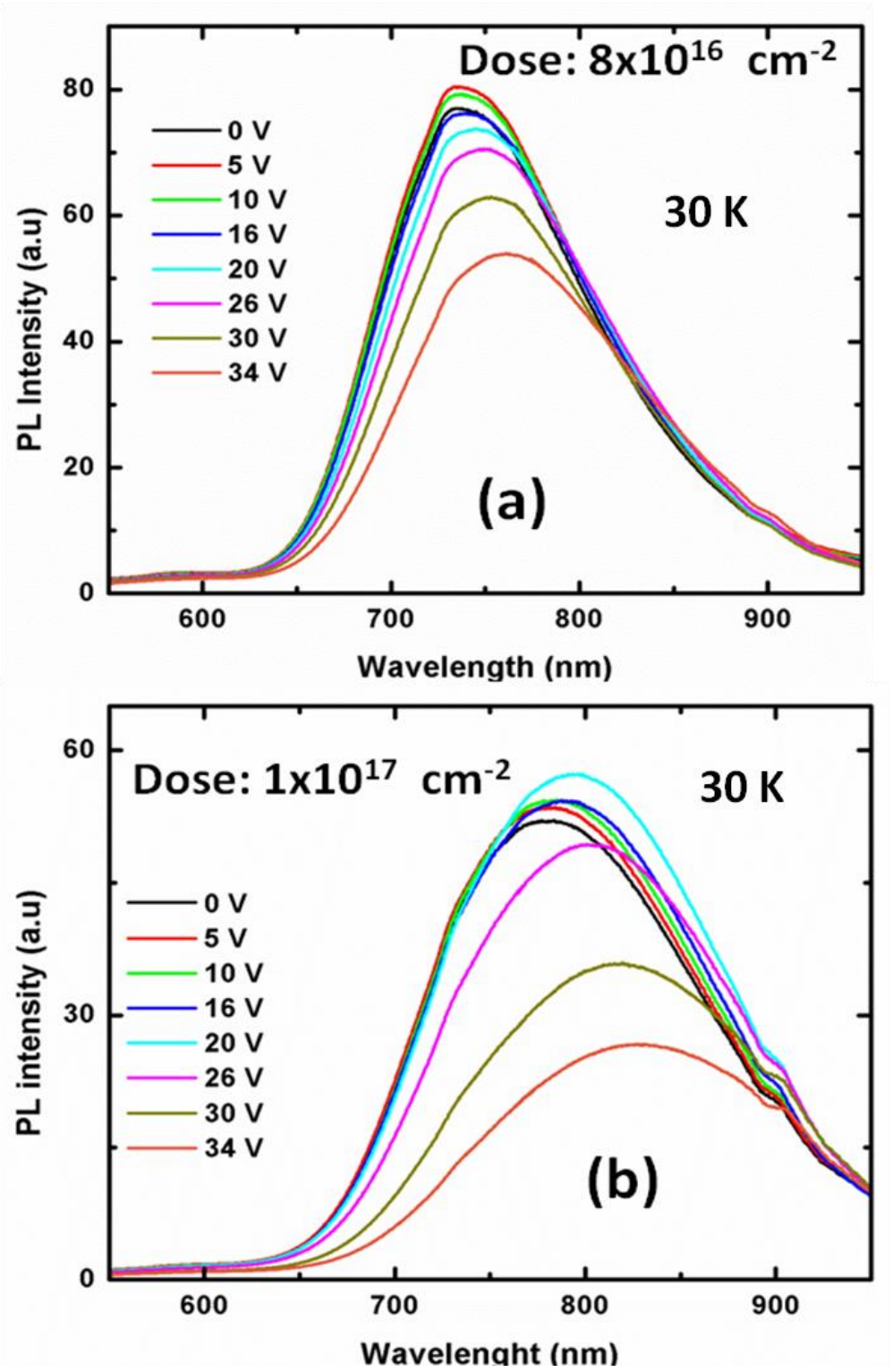

Figure 4.15. PL spectra of the samples implanted with a Si dose of (a) $8x10^{16}$ cm^{-2} and (b) $1x10^{17}$ cm^2 at a temperature of 30 K. The annealing temperature for the samples is 1100 ^{0}C with the duration of 2 h. Measurements were conducted under forward bias in a range of 0 – 34 V. For clarity, only selected voltage values are shown.

Following the observations on QCSE in Si nanocrystals reported above, we have conducted further experiments and theoretical calculations on the size and temperature effects on the QCSE. We built devices with different nanocrystal sizes varied by the dose of the implantation. We measured the QCSE through PL emission at different temperatures between 20 and 300 K on those devices and all related parameters were extracted systematically. Most of these data and corresponding theoretical calculations are still being processed and not included in this thesis. Some representative results are presented and shortly discussed below for the sake of completeness.

In Figure 4.15, PL results of the samples with different Si implantation dose measured at 30 K are given. In the nanocrystal formation process, the size of the nanocrystal could be determined by changing the amount of excess Si incorporated into the SiO_2 layer. Therefore, relatively smaller nanocrystals in average size synthesized with lower dose of implanted Si atoms. The excess Si was chosen as $8x10^{16}$ and $1x10^{17}$ cm^{-2} for the starting sample whose implantation energy, annealing temperature and duration were same. The PL peak position of the sample with lower implantation dose is around 735 nm while it is around 780 nm for the sample with higher Si content without any applied electric field. It is reasonable that, the emission energy is blue shifted by lowering the amount of excess Si thereby the average size of the nanocrystals is reduced and concequently the quantum confinement effect on the band gap is pronounced. For the applied external voltage of 34 V in the forward bias, the total red shift in PL peak position is 25 and 40 nm for the smaller and larger nanocrystals, respectively.

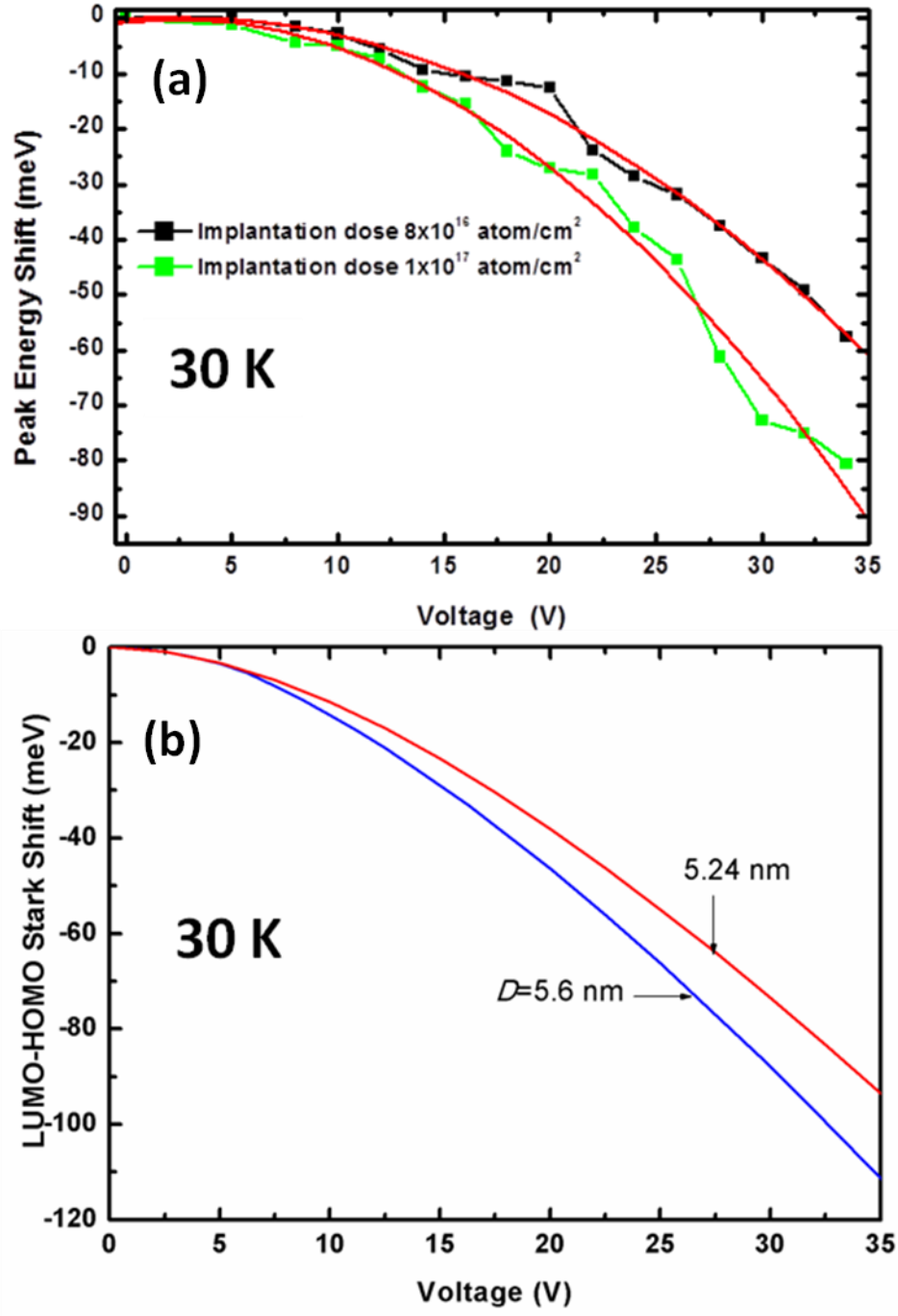

Figure 4.16. Shift in PL peak energy as a function of applied voltage at a temperature of 30 K (a) depicted from experimental results of Si implanted samples of both low and high dose, the red solid line is quadratic fit of the Equation (4.8). (b) Theoretically computed Stark shift without Coulomb interaction for smaller and larger Si nanocrystals.

In Figure 4.16, the theoretical and experimental data for the red shift in the emission energies due to the QCSE in the smaller and larger Si nanocrystals are given. The strong size dependence of the Stark shift to the nanocrystal size is seen in both experimental and theoretical results. Using the quadratic fit to the experimental curves, built-in dipole moments and the polarization constants were extracted. The polarization constants were found to be 7.63×10^{-32} and 5.71×10^{-32} ($C.cm^{-2}.V^{-1}$) for larger and smaller nanocrystals, respectively. Like in the previous analysis, we found minor contributions from linear term with dipole moments as 4.67×10^{-27} and 4.22×10^{-27} (C.cm) for large and small nanocrystals, respectively. With the inclusion of Coulomb term, theoretical calculation is very successful to explain the theoretical observations of Stark effect for both large and small nanocrystals. However, more studies are needed to further elaborate the effect of size and temperature on the QCSE in nanocrystals.

4.5. Conclusions

The effect of electric field on the PL from Si nanocrysals formed in SiO_2 has systematically been studied at both cryogenic and room temperatures. It was observed that PL peak position was red shifted by increasing external voltage without any aging effects on luminescence properties of the sample after voltage was cut off. The field effect on the PL peak position and intensity have been discussed and attributed to QCSE in Si nanocrystals. It was shown that there is a fairly good agreement between theoretical model from second order non-degenerate perturbation theory and our experimental results. In addition to quadratic term which reflects polarizability of electron/hole due to spatial separation under electric field, we observed a minor contribution from a linear term originated from the built in dipole moment which is related to either defect states at Si nanocrystal/SiO_2 interface or anisotropic shape distribution of the nanocrystal. Both built-in dipole moment and polarizability decrease with increasing temperature due to spreading of electron/hole wave functions in the quantum well as the statistical distribution of carriers at higher energy levels increased. We have observed an asymmetric red shift in PL peak between the measurement conducted at forward and reverse bias which is considered

as a result of the internal electric field generated by the hole injection and trapping at substrate/oxide interface.

Using atomistic pseudopotential model with combination of LCBB as an expansion basis, QCSE was theoretically computed without perturbation approaches by the theory group led by Dr. Ceyhun Bulutay, who has been our collaborating partner during this work. In the theoretical model, the inhomogeneity in the size distribution, interface states, coupling between the nanocrytals and strain effects were excluded as minor contribution was expected. Size of the nanocrystal used in computation was determined using the PL peak position of the experimental result. It was demonstrated that Coulomb interaction term has a significant effect on the total Stark shift. Without excitonic term, single particle Stark shift overestimates the experimental results. Nonmonotonic behavior observed in PL emission under external field was also estimated by the theory. One of the interesting outcomes of the theory was that, unlike the rigidity of conduction band states most of the system response to the external field comes from the valence band states. Strong size dependence of the polarizability suggested by the computational result was verified by the experimental observations.

In this part of our work, we have reported the first clear observation of QCSE in Si nanocrystals based on PL measurements. We believe that this result is an important contribution to the present understanding of the electronic and optical properties of Si nanocrystals. The next step would be to transfer these fundamental demonstrations to the technological applications. The obvious outcome of this work would be the fabrication of electro-optical devices such as optical modulator, which will be revolutionary in the silicon based photonics.

CHAPTER 5

SILICON NANOWIRES FOR PHOTOVOLTAIC APPLICATIONS

5.1. Introduction

5.1.1. Nanowires, their properties and applications:

Recently, modern physical methods have been developed mostly at physics laboratories to fabricate a new class of materials having dimensions at nanometer scale. Consequently, interesting new properties that include the structural, electronic, optical, thermal behaviors etc. have emerged from the quantum world of this new material class. To understand these new properties occurring at nanoscale new scientific disciplines called nanophysics, nanochemistry, nanoelectronics etc. have been developed [219].

Semiconductor nanostructures which have at least one dimension in the order of nm scales have attracted much interest due to the unique quantum confinement effects emerging at this length scales. Such nanostructures include two dimensional (2D) quantum wells, one dimensional (1D) quantum wires (nanowires) and zero dimensional (0D) quantum dots (nanocrystals), each having unique electrical and optical properties. The terminology quantum refers to the fact that electronic properties become quantized as the size of the structure is reduced to the nanometer scale.

Nanowires are the high aspect ratio structures whose diameters are of nm size (1-500 nm) and lengths up to hundreds μm (even few mm). They are perhaps the most versatile building blocks for nanoscale device applications in various fields. In the nanowires, the translational invariance still exists in one direction (along the

nanowire) for particles. However, due to the confinement in other two dimensions, electrons, holes, photons, phonons and other quasi-particles exhibit many interesting features, which do not exist in the three dimensional form [220]. Different types of 1D nanostructures (here we call all of them shortly as nanowires) are illustrated in Figure 5.1. The unique properties of nanowires depend not only on their sizes, (length, diameter and axis of orientation) but also strongly depend on the materials used. Currently, numerous applications of nanowires to devices are being investigated and developed across by many groups worldwide.

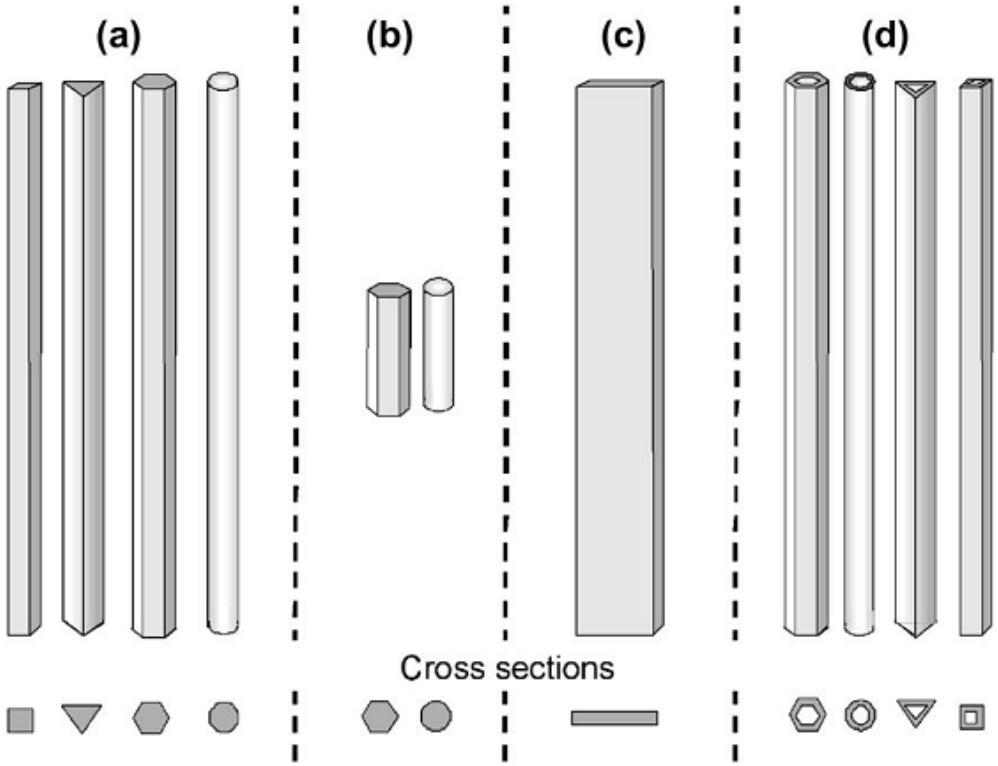

Figure 5.1. Illustration of different types of 1D nanostructures depending on their morphologies: (a) nanowires (nanofibres or whiskers), (b) nanorods, (c) nanobelts (nanoribbons) and (d) nanotubes [221].

To date, as a result of advances in crystal growth technology, a wide variety of materials (elemental metals, wide range of semiconductors including group IV, III-V, II-VI, oxides, carbides, nitrides, phosphides, etc.) have been successfully grown in

the form of nanowires or whiskers as individual structures or as an array on a substrate [221,222]. Accommodation of higher level of strain without the formation of dislocations allows them to be fabricated on almost any kind of substrates easily. Carbon nanotubes have been the most known 1D nanostructures over the last two decades. However, semiconducting based nanowire structures will dominate the applications due to some advantages over the carbon nanotubes. Unlike the carbon nanotubes which have electronic properties depending on the less controllable chirality of the nanotubes, the electronic properties of semiconducting nanowires can be controlled by the choice of semiconductors, doping or the variation of the diameter.

In addition to their new physical and chemical features brought by 2D carrier confinement, their large surface to volume ratio compared to their bulk form makes the nanowires very useful in numerous electronic, photonic, spintronic, biological, chemical, photovoltaic and sensor applications [220]. For example, due to their large and active surfaces, the contrast ratio (sensitivity) of the nanowire based sensors that are sensitive to either physically adsorbed or chemisorbed agents is expected to be much higher compared to their bulk counterpart [223]. Moreover, arrays of nanowire sensors could in principle achieve nanometer scale spatial resolution and therefore provide accurate real-time information regarding not only the concentration of a specific analyte, but also its spatial distribution, as well as providing the corresponding information on other analytes within the same volume [219].

Nanowires are expected to become important functional components in future opto- and micro-electronic technologies. In this manner various nanowire based field effect transistors, nanolasers using nanowires as a cavity, and LED applications have been demonstrated [45, 224-226]. Nanowires have also been proposed for applications associated with extraordinarily high piezoresistive nanomaterials and superconductors [227,228]. Furthermore, they have been used as good electron field emission sources for flat panel displays, because their small diameter and large curvature at the tip reduce the threshold voltage for the electron emission and display remarkable field emission characteristics [229].

Recently, nanowire based solar cells have also become one of the hot topics. With remarkable electrical and optical contributions, these systems do not have any upper boundaries for both effectiveness and integration to daily usage. Nanowires in a core-shell structure in type-II band alignment could be effectively utilized for photovoltaic applications; which allows separation of created electron-holes in different materials (core or shell) transported axially to the respective terminals thereby the recombination losses can be decreased. This scheme could be adapted to the inorganic/organic hybrid solar cell applications where the three dimensionality of the nanowire junction can be exploited [230].

The devices and potential applications mentioned above are all proof of principle devices and their industrial applications can not compete with the existing planar and top-down technologies due to excessive production time and cost. The main challenges of the industrial use of nanowires in practical applications lie in the fields of the manipulation, positioning and processing of large amount of nanowires as well as the precise control over the diameter and doping levels. It is obvious that neither carbon nanotubes nor the semiconducting nanowires could be a competitor to today's Si-CMOS IC technology for electronic application of massive integration and computing. However, they would find a place some in practical sensing and photovoltaic applications in the near future.

For the synthesizing nanowires two basic approaches are followed: top-down and bottom-up. In a traditional top-down method, nanowires are typically realized by a combination of high resolution lithography followed by physical or chemical etching. In the bottom-up approaches, nanowires are synthesized through the combination of constituent ad-atoms from the initial seed nucleation. Various lithographic techniques can be employed to define the position and dimensions of the nanowires before the growth process.

5.1.2. Si nanowires and production methods

As Si is the most important semiconducting material for IC technology which has been considered as one of the greatest success of the last 60 years, nanowires made of Si have been the most attractive choice for the realization of various novel device applications. First report on Si nanowire (whisker) growth is dated to 1964 by Wagner and Ellis [80] long before the announcement of carbon nanotube by Iijima in 1991 [231]. Even earlier study of Treuting and Arnold reported in 1957 can be taken as the first study on Si nanowire growth [232]. In 1975, the growth mechanism of Si whiskers was elucidated by Givargizof [233]. The research on Si wire growth had flourished after 1964, however until the mid nineties the research activities were almost in standby. The publication of Morales and Lieber in Science in 1998 [234] gave a big impetus to the research and investigations on Si nanowires extensively grew up.

Successful utilization of Si nanowires has been demonstrated in field effect transistors, chemical and biological sensors, field emitters, high performance lithium ion batteries, photo detectors, LEDs, thermoelectric systems, and solar cells [235-242].

In this study, we focused on the utilization Si nanowires in photovoltaic applications. Si nanowire solar cells with coaxial and radial heterojunctions offer unique advantages over thin film solar cells due to allowance of three dimensional junction formations with careful engineering of nanowire size, doping and junction depth. Moreover, vertically aligned arrays of Si nanowire enable orthogonal photon absorption and carrier collection. This allows enhanced optical absorption due to light trapping and improved carrier collection where the carrier collection distances can be much less than the minority carrier diffusion lengths [243]. With these properties, nanowire based solar cell technologies have a great potential for new breakthrough discoveries towards very efficient photovoltaic devices.

Using both bottom-up and top-down strategies, there are different methods developed to produce silicon nanowire arrays. Among them, the most commonly used silicon nanowire production method has been Vapor-Liquid-Solid (VLS) which

is a bottom-up approach as discussed in Chapter 2. Other bottom-up alternatives that have been extensively used can be listed as: chemical vapour deposition (CVD) [244], plasma enhanced chemical vapor deposition (PECVD) [245], thermal evaporation [246], molecular beam epitaxy (MBE) [247], metal organic vapor phase etitaxy (MOVPE) [248], solution based synthesis [249], and laser ablation [250]. Alternatively, silicon nanowires can be produced by top-down approaches. Many of these methods have employed various lithographical methods followed by a reactive ion etching (RIE) [251]. However, although it is excellent for the proof of concept studies, DRIE is certainly not suitable for large area applications which are necessary for the PV industry. A novel etching technique called either Metal Assisted Etching (MAE) or electroless etching has recently been developed for the production of vertically aligned Si nanowires on Si substrate. MAE is attracting much attention because it is easy, cheap, and fully compatible with the existing large area production stepts of c-Si solar cell production.

Bottom-up methods usually require complex and expensive equipments, involve high temperatures and high vacuum processes with the use of hazardous silicon precursors, all of which drastically increase the cost of the processes. Moreover, silicon nanowire production over large areas is not possible due to limitations in the growth processes. Contrarily MAE offers a low temperature, cost effective and solution based methodology that enables production of vertically aligned silicon nanowire arrays over large areas. In addition, silicon nanowires formed by MAE method have exactly the same properties with the starting substrate (i.e. doping type, direction and density), while those synthesized with bottom-up approaches may need to be tuned for the desired characteristics. Considering these important advantages, MAE method is expected to become the major choice for the production of arrays of silicon nanowires for industrial applications.

5.2. Si nanowire production by MAE method

The solution based MAE method was first introduced by Dimova Malinovska et. al. in 1997 [252] and called as metal assisted chemical etching (MAE). The idea was to obtain porous silicon by etching an Al covered silicon substrate in a water based solution containing HF, HNO_3. Later, developments in both metal assisted chemical etching method and porous silicon characteristics directed many research groups to study this cost effective method. The etching process in the MAE method can be summarized as follows: the silicon substrate which is partly covered by a noble metal is exposed to HF and an oxidizing agent; silicon underneath the noble metal was much rapidly etched compared to the parts without metal coating. This causes the nobel metal to sink through the initially created pores and form a porous or columnar structure.

In 2002, Peng et. al. who investigated the MAE method extensively, proposed a single step process which does not require any pre-coating process [43]. In this approach, the silicon substrate is placed in a $HF/AgNO_3$ solution where Ag coating and silicon etching took place simultaneously. They called this single step process as electroless etching method in their later works. Following these pionering studies, several other attempts understanding the mechanism and gained control over the resultant structure were carried out [253-257]. Besides Ag, other noble metals (Au, Pt, Fe, etc.) have been tested in the MAE of Si for nanowire formation. In addition to this single step etching, the two step etching process (which is much faster than single step one) has also been successfully adapted to Si nanowire formation. In this case, the first step is the deposition of Ag on to the Si substrate either by evaporation/sputtering or by using solution of $AgNO_3$ and then the second step is the immersion of this metal covered substrate in to the solution consisting of HF, H_2O_2 and water.

There are mainly two models suggested in the literature to explain the formation of Si nanowire through electroless etching methods. However, lacking and difficulty in the in-situ diagnostics of chemical reactions taking place during the nanowire formation, there is no conclusive evidence to support these proposed models. Therefore the kinetics of the reaction at the atomic scale has been an open question

up to now. The first model is based on a self-assembled localized micro electrochemical cell model where spontaneous micro/sub-micro cathode-anodes formed between metal and Si [256]. At the initial stage, silicon etching and silver deposition occur simultaneously on the Si wafer surface. The deposited Ag atoms coming into contact with silicon nucleate the growth of Ag nanoclusters which are distributed throughout the surface of the silicon wafer spontaneously. These silver nanoclusters and the Si surrounding these silver nuclei act as the local cathode and anode in the electrochemical redox reaction respectively. Therefore, having the higher electro negativity, Ag ions are reduced by capturing electron from Si valance band, leading to oxidation of Si locally under the Ag nanoparticles. The exact chemical reaction chain is not known, but it could be simplified as by a clever guess as:

At the cathode (Ag): $$Ag^{+} + e^{-} \rightarrow Ag_{(s)} \quad (5.1)$$

At the anode (Si):
$$Si_{(s)} + O_{2(aq)} \rightarrow SiO_2 + 4e^{-} \ (V_B)$$
$$SiO_2 + 6HF \rightarrow H_2SiF_6 + 2\ H_2O \quad (5.2)$$

These nanometer-sized, free standing excessive numbers of electrolytic cells could be spontaneously assembled on the surface of the substrate. As silver is deposited, the surrounding silicon acting as the anode is oxidized to SiO_2 and etched away with F^{-} supplied by HF in the solution. As this reaction goes on spontaneously distributed pits immediately form beneath the Ag nanoparticles accordingly. As a result of having a higher electronegativity, the Ag particles trapped in these pits do not move horizontally and at the end, collective combination of all pits leave the Si surface decorated with nanowires [258]. With longer immersion times in the $HF/AgNO_3$ solution, the Ag particles that do not enter the pits would grow into very thick and branched silver dendrites over the Si nanowire layer. The process steps proposed by this model is schematically illustrated in Figure 5.2

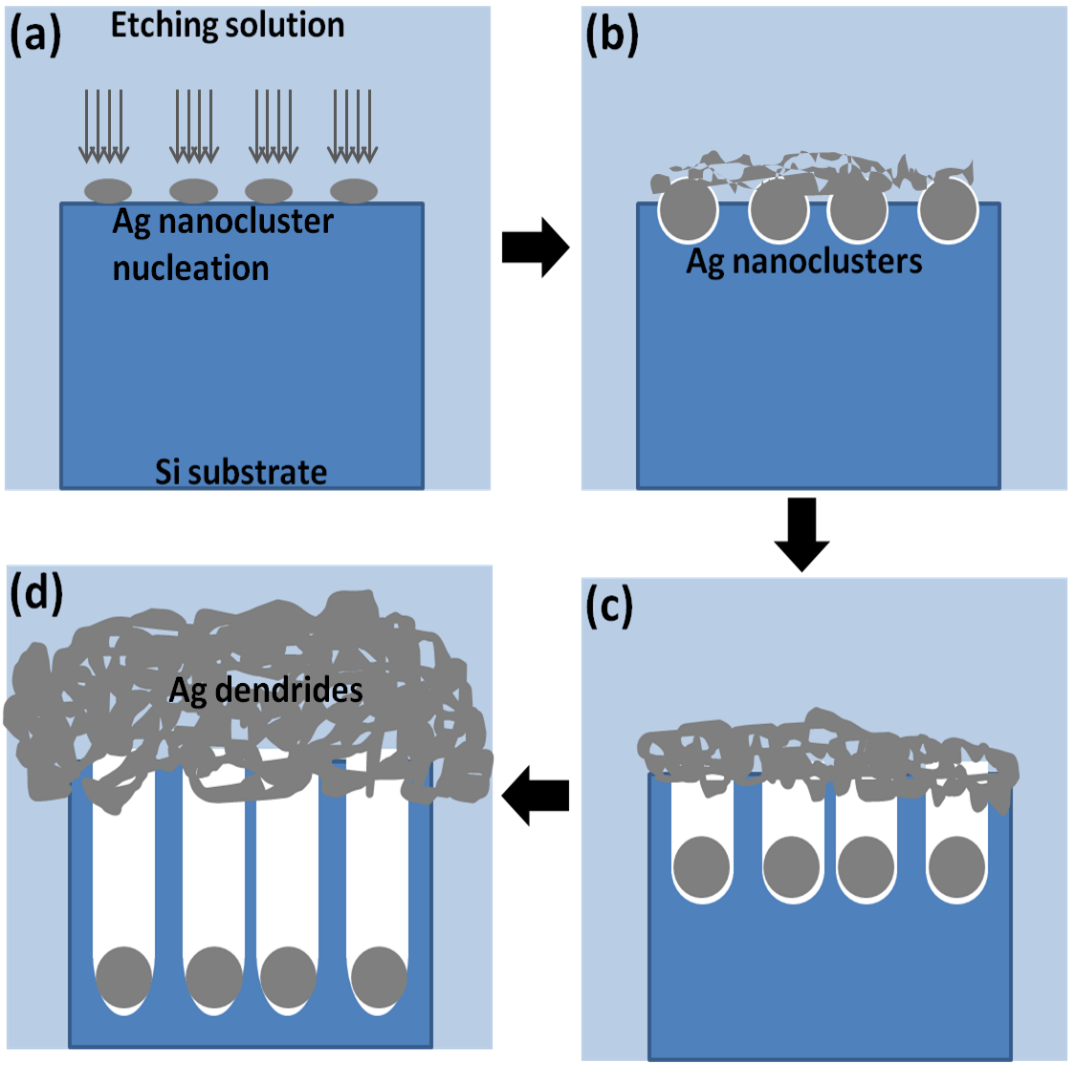

Figure 5.2. Crosssectional schematic illustration of nanowire formation mechanisms in single step approach: (a) spontenous Ag nanocluster nucleation through redox reactions, (b) pit formation under Ag nanoclusters, (c) and (d) nanowire formation in different length depending on etching time. The thick dentritic Ag film formed during the process at the top.

The second model proposed for the MAE is based on the mass transfer during the chemical etching [259]. Si atoms in contact to Ag or other noble metals are dissolved in the metal, transported to the metal-solution interface, oxidized by the solution, and finally etched away. The second model has generally been less popular compared to the first one. Schematic illustration of these two models is represented in Figure 5.3.

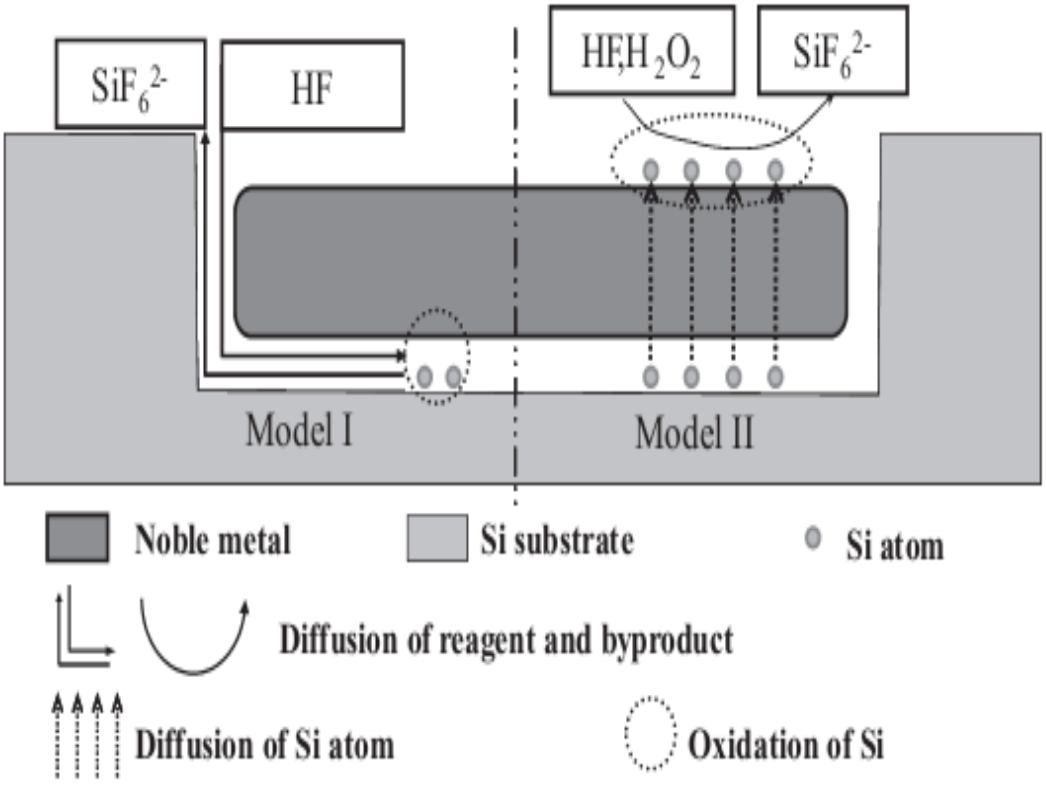

Figure 5.3. Schematic illustration of two models: Model I represent the galvanic replacement between Ag ions and Si substrate, the reagents and by products of reaction diffuse in/out along the interface between the metal and wall of etched Si. Model II, Si atoms are dissolved into metal diffuse to metal/solution interface and are oxidized on the metal surface [259].

5.3. Experimental details of Si nanowire production

We have systematically studied MAE properties of Si for the formation of Si nanowires over sixty runs of different experimental conditions. Effects of temperature, time, solution concentration, Si substrate types, doping concentration on the morphological structure of nanowires were studied.

The chosen Si substrates are mostly single side polished with a thickness of around 400 μm. Usually the polished front side of the wafers was used for the etching studies. Si wafers with different doping types (n-type, p-type), resistivities (0.1-1Ω.cm, 1-10 Ω.cm), crystal structure (monocrystalline, multicrystalline) and crystallographic orientations ((100), (111)) were selected as the starting substrates.

In order to obtain homogenously distributed nanowire formation, the surface should be well cleaned homogeneously. Otherwise during the galvanic etching, spontaneous nucleation of Ag nanocrystallites can be inhibited by the contaminants, which might results in less yield or totally useless pattern formation. Therefore etching process requires well controlled cleaning procedure to avoid any failure. All equipment (beakers, gloves, tweezers etc.) should be very clean during all processes.

In the chemical cleaning process, Si substrates were consecutively sonicated in acetone, 2-propanol and de-ionized water baths for 10-15 minutes each. This step was followed by immersion in to piranha solution prepared by mixing of sulfuric acid (H_2SO_4) and hydrogen peroxide (H_2O_2) in 3:1 volume ratio for 20 minutes at a temperature of around 85 ^oC. Then the samples were removed out of the piranha solution, rinsed under de-ionized water and sonicated in de-ionized water for 15 minutes, and finally dipped into dilute hydrofluoric acid solution (5-10%)for 2 minutes to remove the native oxide and allow the substrate surface to become hydrophobic.

The chemically cleaned silicon substrates were then immersed in the electroless etching solution which consists of $AgNO_3$ and HF for the one step etching process used in this study. The schematics of the experimental setup is given in Figure 2.6

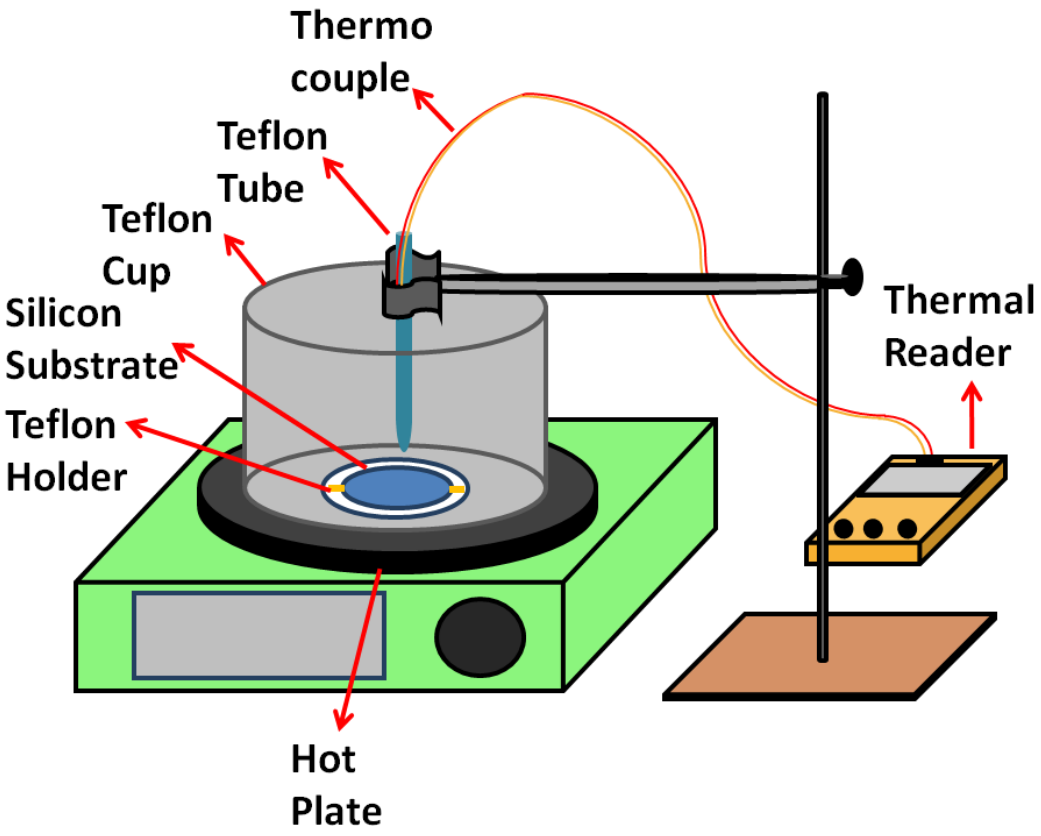

Figure 5.4. Schematic illustration of the handmade experimental setup for MAE etching.

To study the effect of different process parameters, cleaned silicon substrates were immersed into the solution having different concentrations, for various durations (up to 10 hours), at different temperatures (2-55°C).

The morphologic properties of etched Si were investigated by scanning electron microscope (SEM) and the reflection properties were studied using integrating sphere and calibrated Si detector attached to monochromator. In Figure 5.5 (a) and (b), SEM images of vertically aligned Si nanowires produced by MAE are given. The SEM images were taken before Ag removal process by nitric acid (HNO_3).

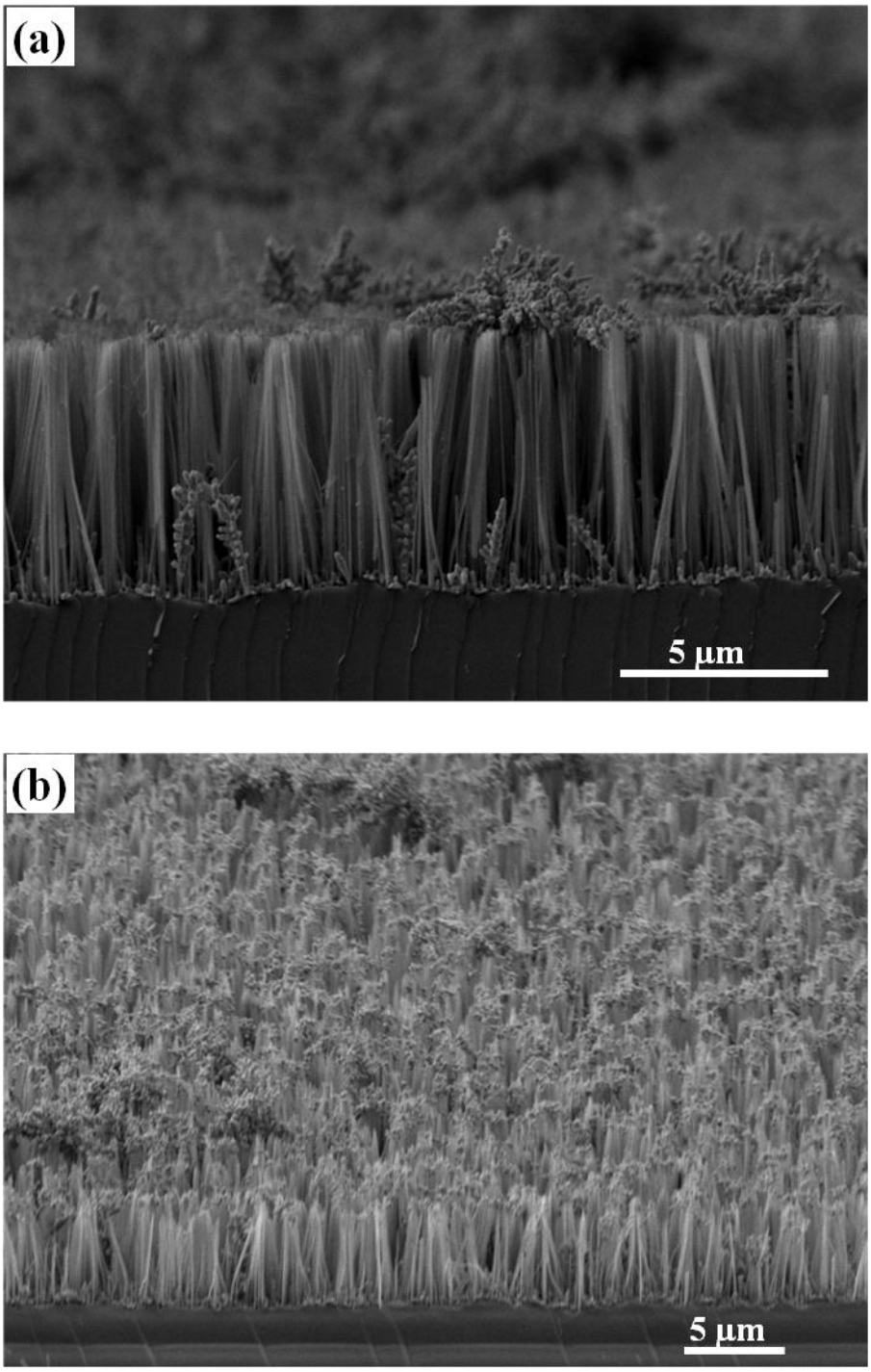

Figure 5.5. Cross-sectional SEM images of a silicon samples containing 8µm long silicon nanowire arrays prepared by MAE.

5.4. Results and discussions

5.4.1. Effects of MAE parameters on Si nanowire morphology

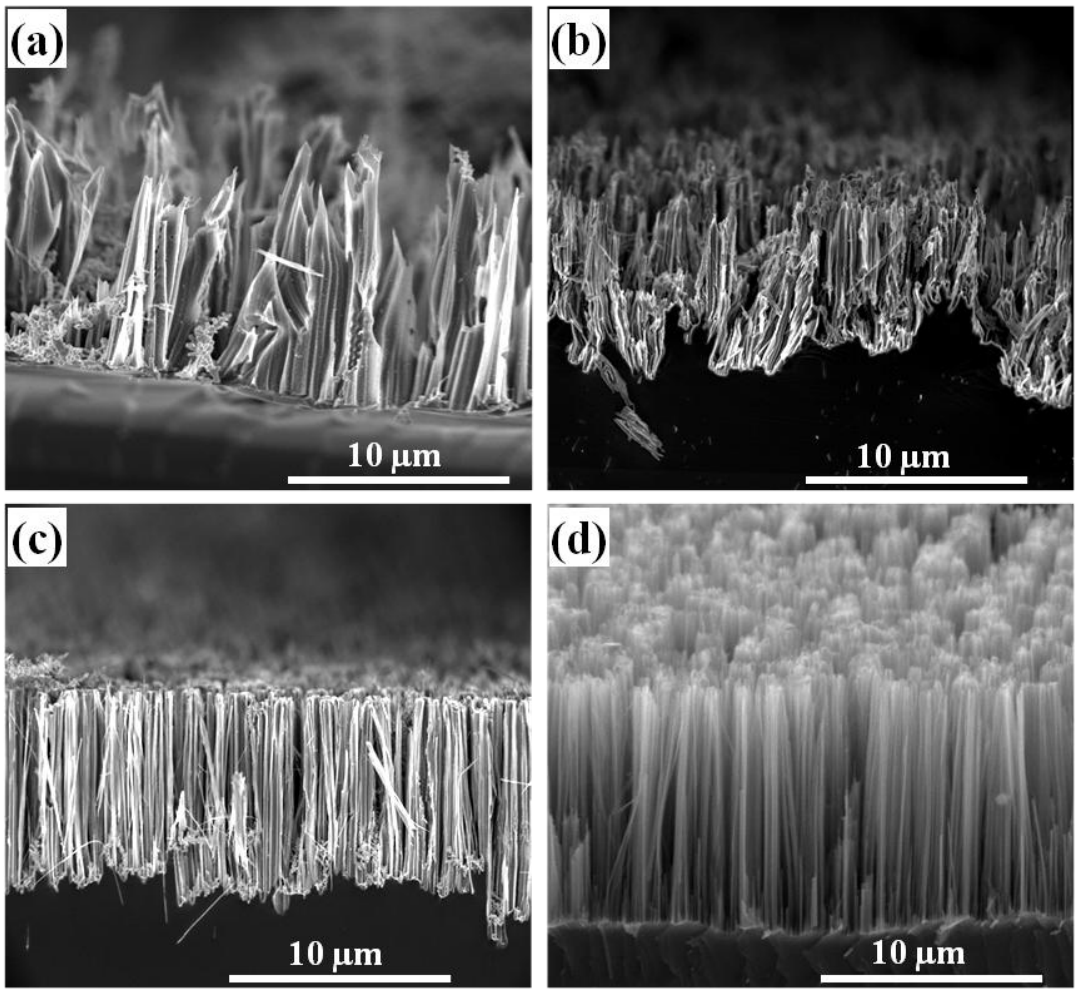

Figure 5.6. Cross sectional SEM images of samples that were etched in solutions having different concentrations, all samples were prepared from p-type Si substrate with a resistivity of 5-10 ohm-cm and with the direction of (100): (a) 0.01M AgNO3 / 4.6 M HF, (b) 0.02 M AgNO3 / 7 M HF, (c) 0.04 M AgNO3 / 4.6 M HF, (d) 0.02 M AgNO3 / 4.6 M HF.

Maybe the most crucial parameter for the resultant Si nanowire structure is the chemical properties of the solution. Relative concentration of additives in the etching solution determines the final structure. Also, the amount of the solution over the Si substrate is critically important for a good aligned nanowire synthesis. We have investigated the effect of solution concentration by changing the concentrations

of $AgNO_3$ and HF one at a time. In all cases a more disrupted structure was obtained after the concentration was changed. The results of several attempts in optimization of the solution concentration are given in Figure 5.6. It is apparent that the Si nanostructures shown in Figure 5.6 (a), (b) and (c) do not have well alignment and sharp nanowire morphologies, (d) on the other hand, the sample shown in Figure 5.6 (d) exhibit vertically well aligned silicon nanowires with a homogeneous distribution. Therefore the chemical composition used for this sample, which is 0.02 M $AgNO_3$ / 4.6 M HF was chosen to study other parameters. However, in reality it is hard to obtain the same structure even for the same procedure. Extreme care is needed to repeat similar experiments. The results given in Figure 5.6 reflect an averaged behavior of several etching procedures using the same solution concentration values for each.

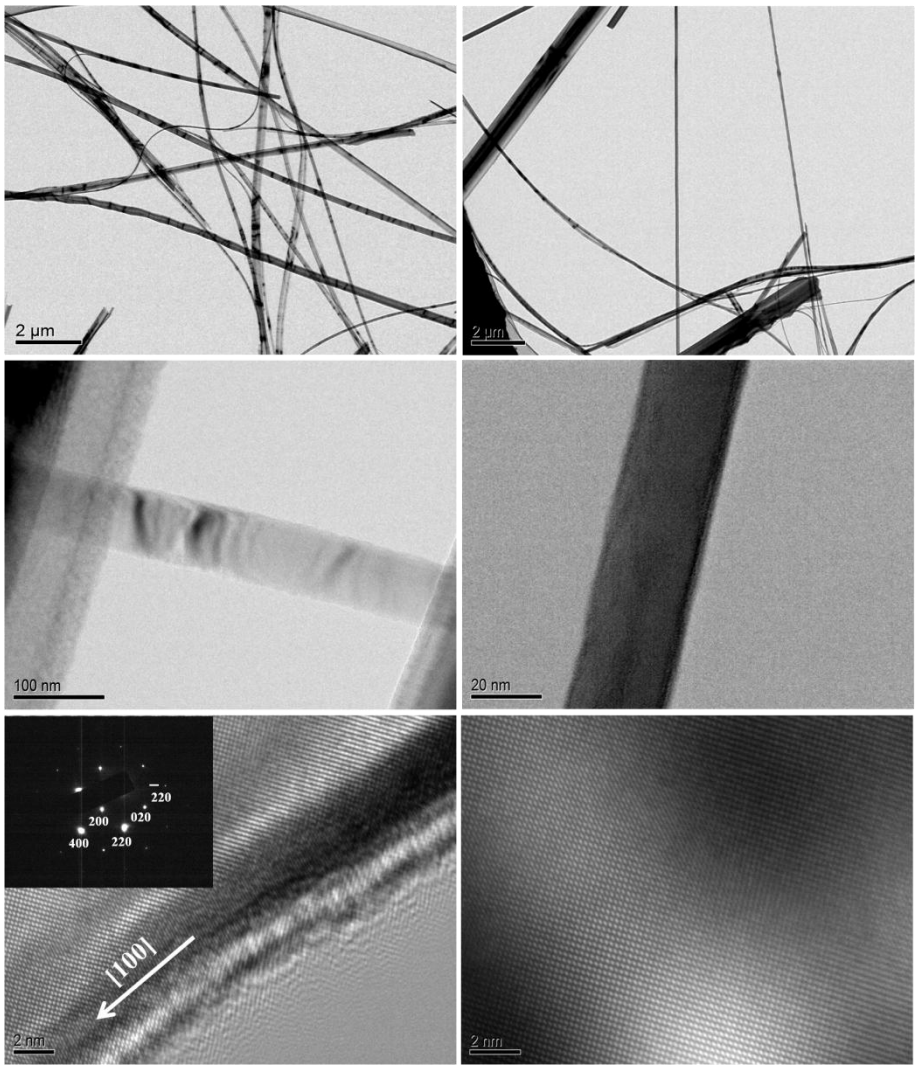

Figure 5.7. Representative TEM images of the samples produced in 0.02M AgNO3 / 4.6M HF solution using (100), 5-10 ohm-cm p-type Si.

In Figure 5.7, Transmission electron microscope (TEM) images are shown for the samples produced in 0.02M AgNO3 / 4.6M HF solution kept at 40 ^{o}C for an hour. As the nanowires etched through (100) directional substrate, the crystalline direction of nanowires was also at the same direction from the diffraction pattern. It is seen from the Figure 5.7 (lower parts) that the nanowire surface is rough, although this is not the case for all samples, some portion of many nanowires exhibit a similar structure shown in this figure.

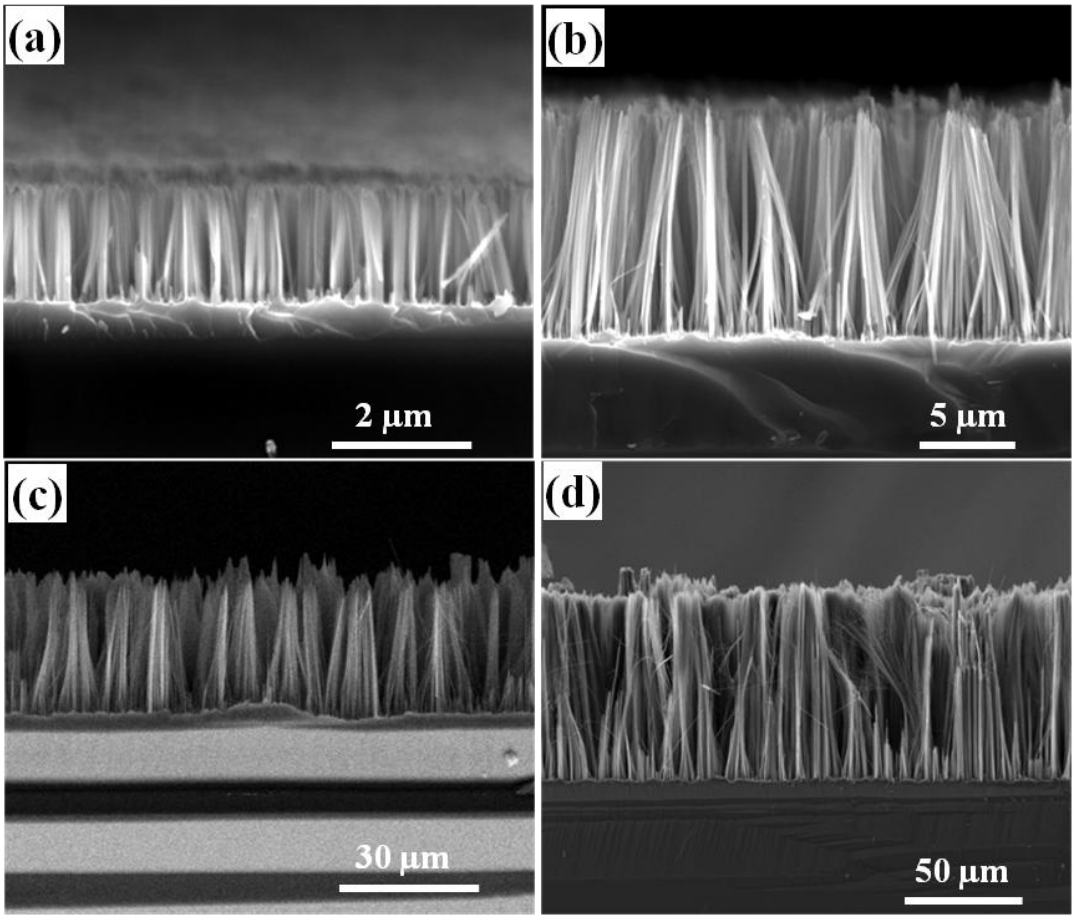

Figure 5.8. Cross sectional SEM images of the vertically standing silicon nanowire arrays obtained by electroless etching at 40^{0}C in a solution containing 4.6 M HF / 0.02 M $AgNO_3$ for (a) 8 min., (b) 40 min., (c) 120 min., (d) 360 min.

Etching time is another factor that directly affects the resultant nanowire lengths. Nanowires were fabricated within etching durations of 8, 16, 40, 60, 120, 180, 240, 360, 450 and 600 min., while maintaining the solution concentration at 4.6 M HF/ 0.02 M $AgNO_3$ and temperature at 40°C. From this sample set SEM images of the silicon nanowires, fabricated within 8, 40, 120 and 360 min., respectively are shown in Figure 5.8. Vertically aligned silicon nanowire arrays can be clearly seen in all images. The dependence of the nanowire length on the etching time is shown in Figure 5.9.

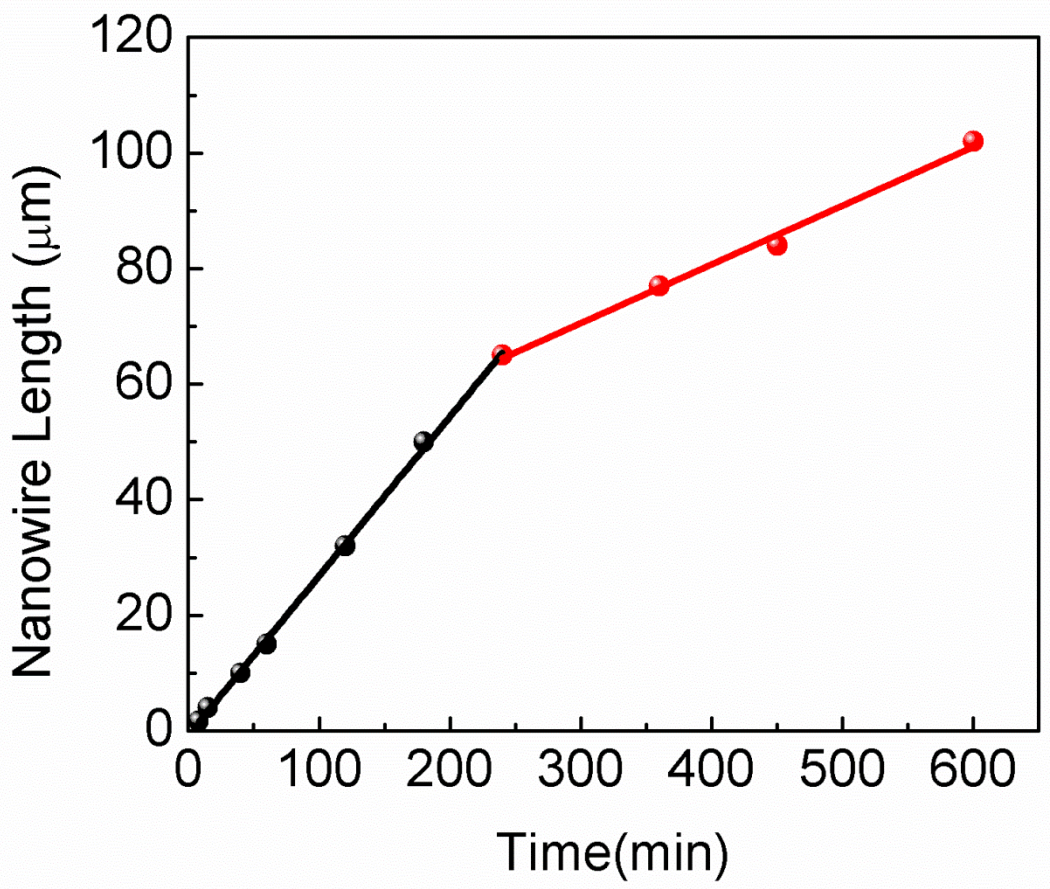

Figure 5.9. Variation in the nanowire length with etching time. The etching processes were conducted at 40 ^{o}C, with (100) directional p-type samples with a resistivity of 5-10 Ohm-cm.

As seen in the Figure 5.9, a linear relationship between etching time and nanowire length was obtained for etching duration up to 4 h with an etching rate of 0.25 μm/min. This high etching rate value indicates the rapidity of MAE process. Further etching, beyond 4 h, was again developed with a linear relationship with a change in

the etching rate as shown in the same figure. Etching rate of the nanowires in this regime was determined as 0.1 μm/min. This clearly indicates that the reaction slows down due to decrease in the reaction kinetics. This decrease in the rate reaction can be attributed to two main effects : Firstly, since HF in the solution are used up and/or evaporates as the time goes on during the etching process its amount is reduced, the etching rate is not determined by the reaction kinetics anymore when its amount drops below certain threshold value. In another word SiO_2 formation beneath the Ag cluster is much faster than the etching of this oxide layer when the HF amount is not sufficient (reaction is limited by HF diffusion to Si Ag nanocluster interface). Secondly, the decrease in the etch rate can also be attributed to the difficulty of Ag sinking to the bottom of the nanowire arrays, causing insufficient Ag concentration at the bottom. Since the reduction-oxidation of galvanic reaction selectively takes place at the interface between the bottom of the nanowires and the top of the bulk substrate, the drop in Ag concentration causes the etching rate to slow down. Although both suggestions could play a role in the rate reduction, the effect of first suggestion is more likely. The lack of in-situ measurement prevents the understanding of the exact mechanisms for this slow down effect.

Another aspect seen from the time dependence measurements is the distribution and alignment of the resultant nanowires. As a outcome of the MAE method, the nanowires tend to form bundles (like American Indian tepees) due to the capillary forces upon pulling them out from the etching solution, as also observed by others [260]. The other reason is that the nanowires are so elastic that, they could not stand alone after a certain length. As the nanowire length increases with etching time, these factors become more effective resulting in a bundled structure rather than vertically aligned individual nanowire arrays, presented in Figure 5.10 (a). The effects of forming several tens of microns long nanowire bundles on reflectivity are also discussed with the reflectivity measurements below.

For some applications, longer Si nanowires may be required. Even though the reaction kinetics slow down and the nanowires tend to form bundles, individually standing nanowires could still be obtained. Figure 5.10. (b) and (c) shows SEM images of silicon nanowire containing samples having more than 100 micron lengths.

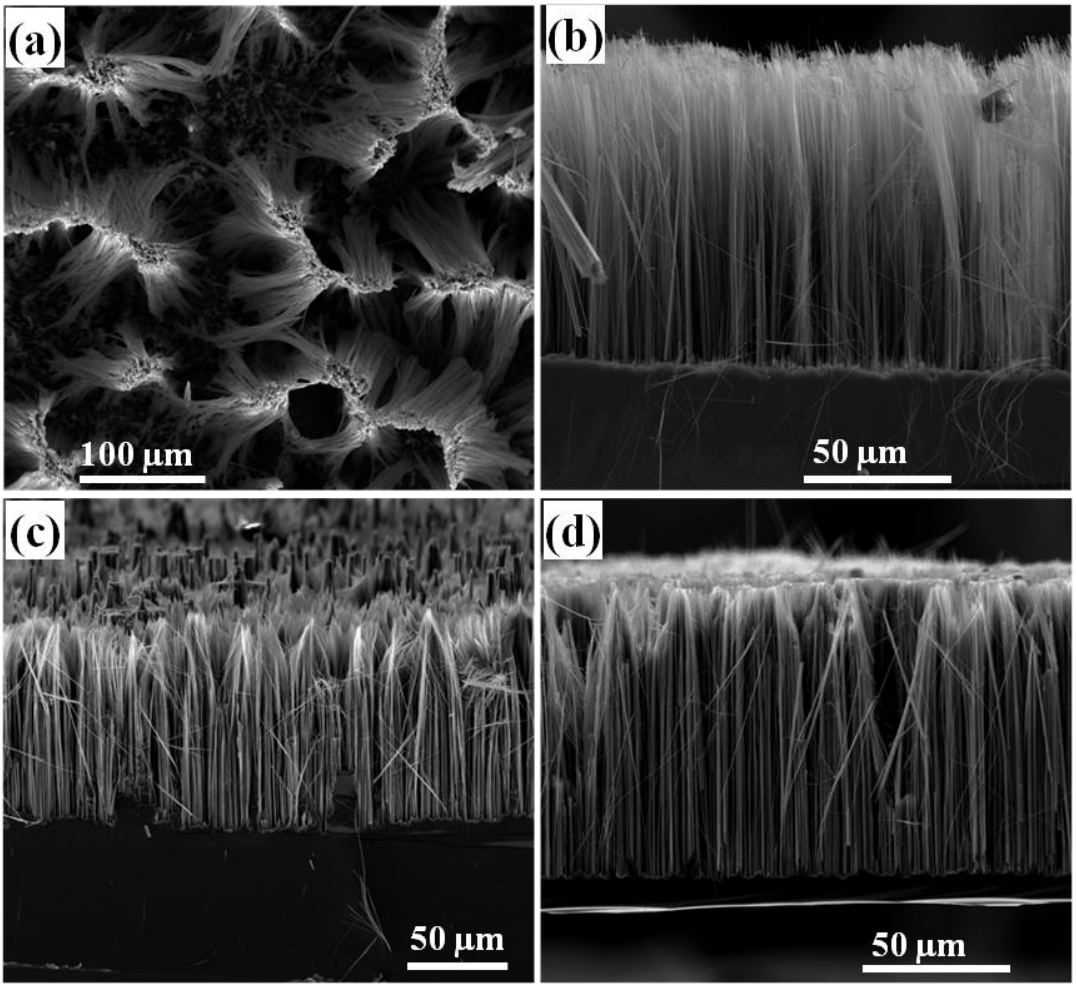

Figure 5.10. (a) SEM image of a substrate showing the connected top portions of approximately 80 µm long nanowires. (b) and (c) are cross sectional SEM images of samples containing over 100 µm long nanowires. (d) MAE etching of a thin silicon wafer was carried out and this image was obtained just before the substrate was converted completely into free standing nanowires.

Especially for the sample in Figure 5.10 (a), the bundle formation is clearly seen. In addition to nanowires attached to underlying Si substrate, we have conducted nanowire etching studies on 110 µm thick Si wafer in order to obtain complete etching of the substrate and get a free standing network of 110 µm long silicon nanowires dispersed in a solution. However, the etching processes halted before the substrate was completely converted into nanowires because Ag dendrite film completely covered the reacting interface and stopped the reaction from proceeding further. SEM image in Figure 5.10 (d) shows that the sample had 100 µm long

nanowires standing on top of only 10 μm thick bulk substrate just before complete etching of the substrate.

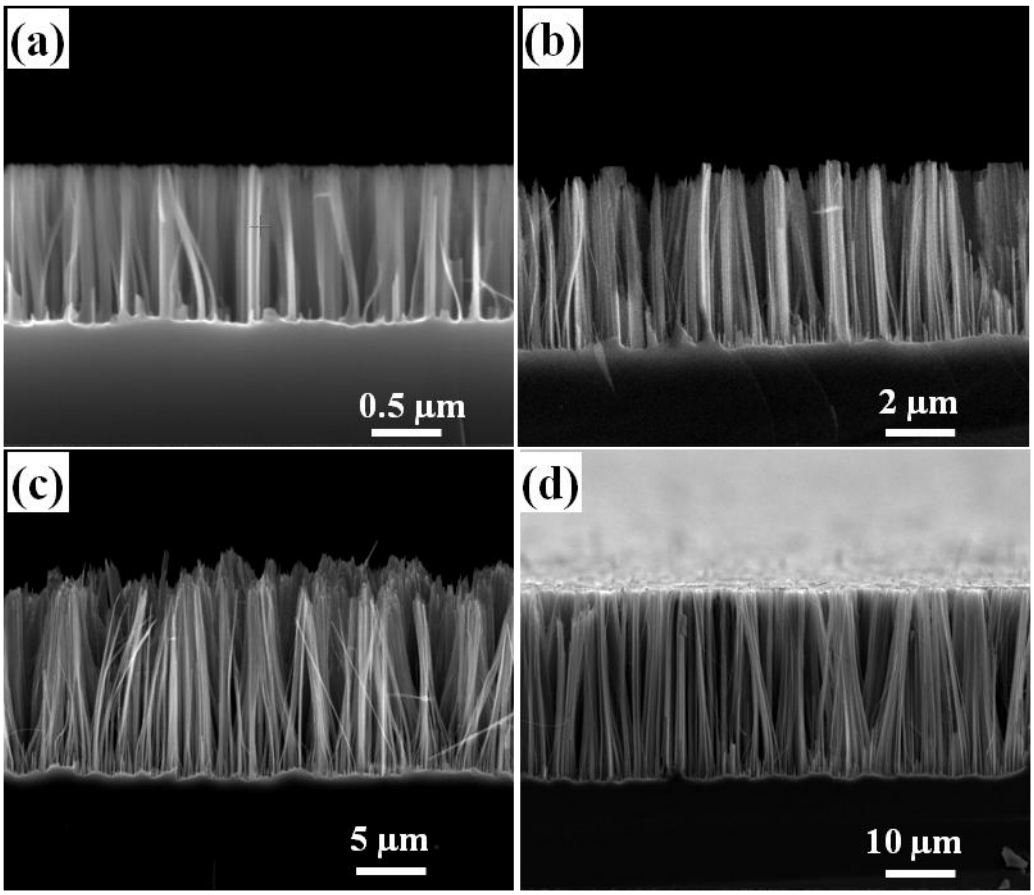

Figure 5.11. Cross sectional SEM images of silicon nanowire arrays obtained by MAE method conducted at (a) 0 ^{0}C, (b) 10 ^{0}C, (c) 25 ^{0}C and (d) 50 ^{0}C upon 1 h etching in a solution containing 4.6 M HF / 0.02 M AgNO3.

Chemical reactions are exponentially dependent to the temperature and described by the Arrhenius relation. Therefore, temperature dependence of MAE is another critical factor to be determined which has a direct influence on nanowire length and the resulting morphology due to changes in the kinetics of the galvanic reactions during the etching process. SEM images of the silicon nanowires fabricated for an hour duration at temperatures of 2, 10, 25 and 50 °C, are shown in Figure 5.11. Nanowire length as a function of varying temperature is plotted in Figure 5.12. We see that, contrary to the expectation, the length of the silicon nanowires was found to be

linearly dependent on the solution temperature. We have avoided temperatures in excess of 50 °C due to safety reasons and to keep solution concentration stable. Also, taking into account that one of the great advantages of this process is the ability to work at low temperatures, we focused on the low temperature applications.

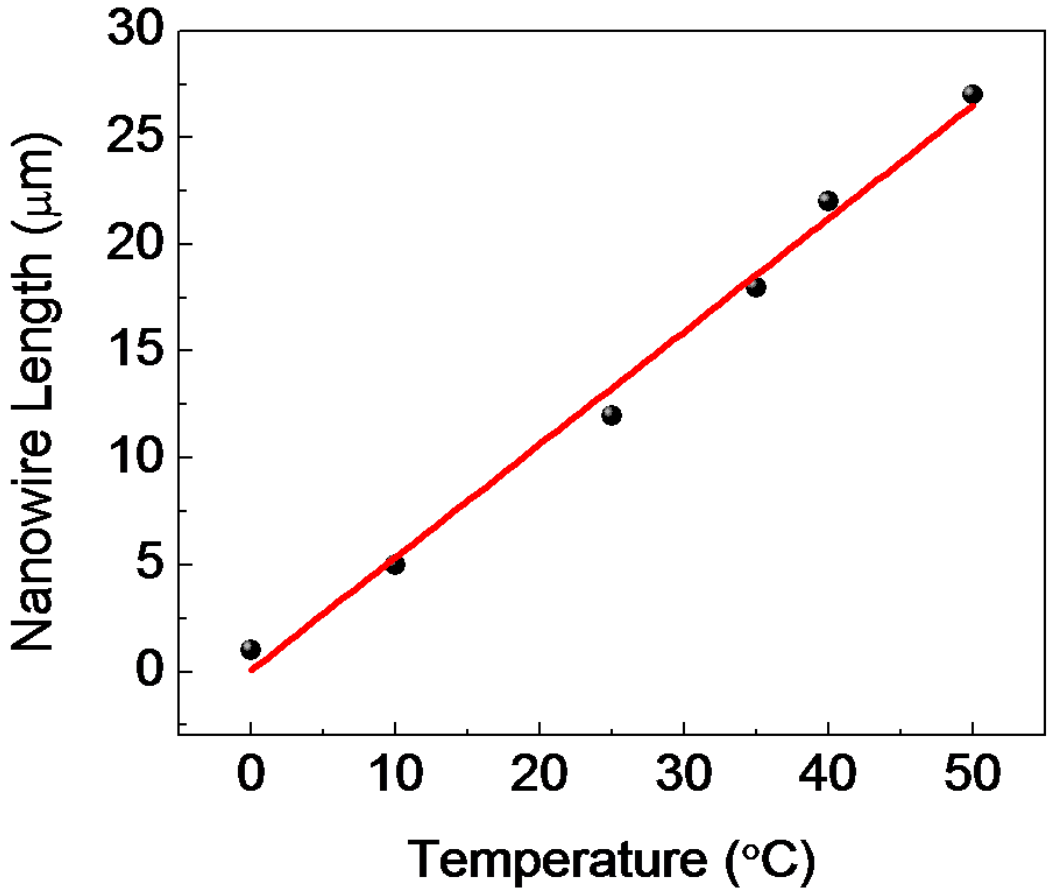

Figure 5.12. Variation in nanowire length with solution temperature for an etching time of 1 h in a solution containing 4.6 M HF / 0.02 M AgNO3.

Similar to the effect seen with longer etching durations, conducting the process at high temperatures causes nanowires to get stuck to each other, while at lower solution temperatures and slower reaction kinetics yields well aligned nanowires distributed uniformly throughout wafer surface.

The physical features of the starting Si substrates in terms of doping type and density, crystallographic orientation and resistivity were expected to affect the etching rate and the morphological structure of the nanowires. This prediction is

based on the fact that n-type silicon would have a larger number of electrons available at the surface. Thus, the Fermi energy level in n-type wafer is higher than p-type wafer, which should then lead to an easier electron extraction from the wafer during galvanic replacement reactions. In one of the previous studies [258] on the doping type dependence, it was concluded that silver distribution density became higher for n-type silicon wafers, whereas silver particle sizes were found to be relatively larger on the p-type silicon substrates. However, the results of our successive experiments revealed that the etching mechanism of silicon nanowires do not have an obvious dependence on the doping type in the samples that we used in this experiment. SEM images of p-type and n-type silicon wafers are given in Figure 5.13. We see that the difference between p-type and n-type samples is not significant. It should be noted that the resistivity of the samples we used in the range of 1-20 Ohm-cm, and the doping dependence might be observable in another resistivity interval.

In order to search for the doping dependence, we have conducted etching experiment with n-type Si substrates with a very low resistivity (one of them at 40 ^{o}C and the other one at room temperature). Surprisingly, we have obtained no nanowire or nanowire like structures on the surface. We have observed formation of continuous Ag film on the surface. It is likely that the galvanic etching path is blocked by an aggressive Ag deposition on the Si surface. When the Ag layer is etched by HNO_3, it was observed by SEM images that the surface is almost as smooth as the starting substrate. Due to lack of p-type wafer with very low resistivity, we could not make comparative experiments for this sample.

It was suggested by the earlier reports that the crystallographic orientation of the monocrystalline silicon wafer affects the alignment of the silicon nanowires produced by MAE method. We have investigated this feature by etching silicon wafers with (100) and (111) crystallographic orientations under the same conditions. SEM images of the resultant structures are given in Figure 5.13. The nanowire alignment was vertical in both cases, therefore we conclude that Si wafers with (100) and (111) directions have similar reaction kinetics giving the same vertical nanowire

alignment and same length. Interestingly, nanowires were not only formed vertically on the top surface but were also formed on the surface of the edge of the samples.

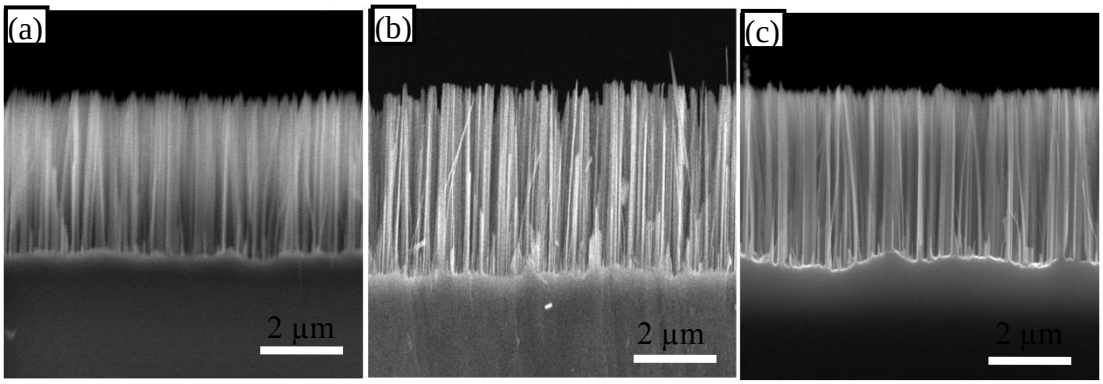

Figure 5.13. Cross sectional SEM images of electroless etched (a) n-type (100), (b) p-type (100) and (c) n-type (111) silicon wafers having 1-5 Ω.cm, 10-20 Ω.cm and 10-20 Ω.cm resistivities respectively

The results presented up to this point were obtained from electronic grade Si substrates. In the following, the effect of crystallinity of the starting substrate on the morphologies of MA etched mono- and multicrystalline silicon wafers that are used in photovoltaic industry, will be presented.

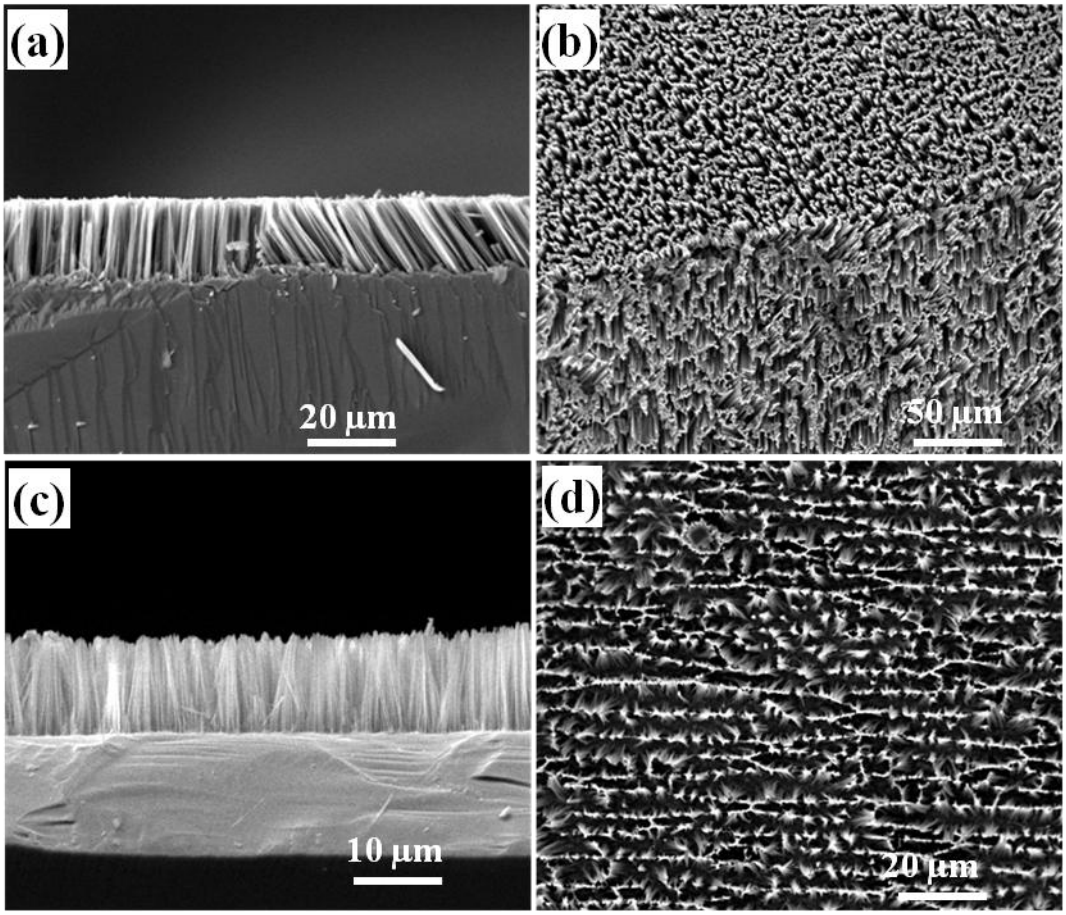

Figure 5.14. (a) cross-sectional view and (b) top view of multicrystalline silicon substrate; (c) cross-sectional view and (d) top-view of monocrystalline silicon substrate, etched under the same conditions.

We have shown that etching single crystalline substrates with both (100) and (111) crystallographic orientations yields vertically aligned nanowires on the surface. The applicability of Si nanowire fabrication procedure to multicrystalline Si is important for solar cell applications, since the production costs of the multicrystalline silicon wafers are relatively lower compared to the single crystalline ones. Furthermore, there were very limited studies that involve etching of multicrystalline silicon wafers in the literature. Cross-sectional and top view SEM images of the silicon nanowires etched from multicrystalline and monocrystalline silicon wafers, are shown in Figures 5.14. (a) – (d) by MAE method. These images clearly demonstrate that silicon nanowire arrays can be formed on multicrystalline substrates following the same experimental procedures.

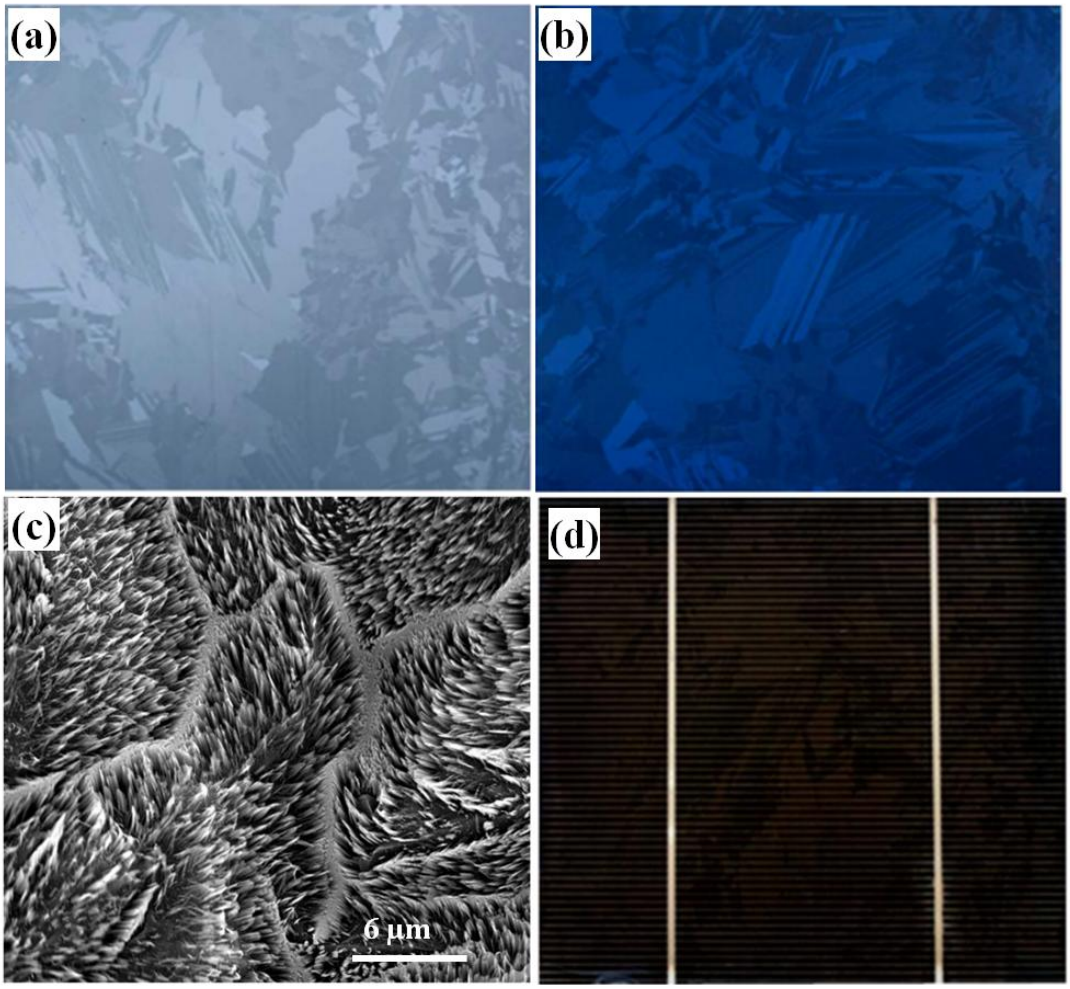

Figure 5.15. Images of 156x156 mm^2 multicrystalline Si wafers: (a) pristine as-cut wafer, (b) anti reflective Si-nitrate deposited, (c) top view SEM image of Si nanowires on multicrystalline wafer, and (d) full size Si solar cell with nanowire decorated surface.

Figure 5.14.(a) reveals that alignment and length of the nanowires are different in each grain, showing that the etching rate changes with crystallographic orientation (other than (100) and (111)) due to different chemical reactivity of the grains. On the other hand, the distribution of the nanowires and their length within each grain was found to be very homogeneous, similar to the ones fabricated from monocrystalline silicon. Grains with different orientations and the grain boundaries are easily distinguishable. Grains with sizes less than 1 µm can easily be identified from the directional difference occurred during MAE.

In the grain boundaries, the surfaces contain numerous high energetic surfaces which significantly increase the density of Ag nucleation with smaller sizes via increased

redox reaction. We observed that the density of nanowires is much higher than that of those formed inside the grains, or sometimes they are almost like a continuous Si belt surrounding each island.

These features of nanowires formation at grain boundaries might bring about a new potential application which can be very useful for the characterization of crystallinity and grain size distribution in the multicrystalline Si wafers. For example, we have identified that the investigated multicrystalline wafers contain various grain islands with directions different than (100) and (111).

In the earliest studies on chemical etching of silicon wafers, a two-step process was often used. In the first step, a metal thin film is deposited on the Si surface, and then in the second step, an electrochemical etch process is used to form the nanowires. Several researchers continued to work with this method even after the development of the single step process. Ag was often preferred as the coating material and HF/H_2O_2 solution was used as the etching solution. In this work we studied this method for the sake of completeness and comparison with the single step process. Ag coating was carried out using both thermal evaporation of Ag film with a thickness of 15 nm and deposition by $AgNO_3$ solution. Both samples were than immersed in a solution containing 5 M HF and 0.5M H_2O_2 at room temperatures for 10 min. Although a very homogeneous structure was obtained, the Si nanostructures are not standing as individual, they include larger columnar structures as well as nanowires. The SEM images displayed in Figure 5.16 show that rather than individual nanowire arrays, a thin film-like structure is obtained. Also, in accordance with the previous reports [261], higher etching rates were obtained using this process compared to single step due to catalyzing the reaction by very oxidative H_2O_2 being used in the solution. We believe that, two step etching of Si nanowires could yield better results than one step etching through optimization by carefully designed experiments.

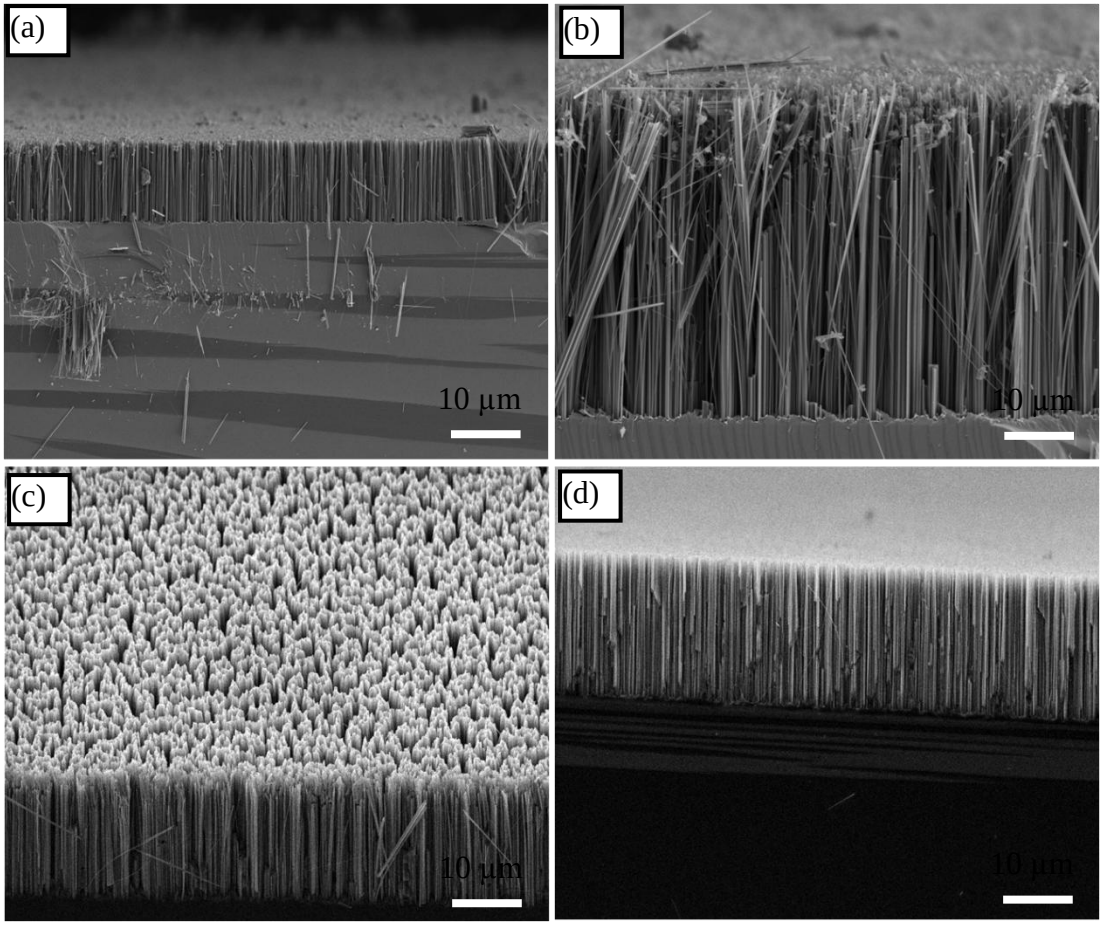

Figure 5.16. Cross-sectional SEM images of the Si samples (p-type, (100) with 5-10 Ohm-cm resistivity) etched using the two step method. The images are taken from different samples with different etching solution recipes for ten minutes at room temperature. (a), (b), (c) Ag deposited by $AgNO_3$ solution, and (d) deposited by thermal evaporation.

MAE technique does not allow a precise control over the silicon nanowire diameter and density, although nanowire alignment and lengths are well controlled. As confirmed by the SEM analysis, the resultant silicon nanowire diameters are generally in the range of 30-250 nm. On the other hand, using nanosphere lithography technique well-controlled nanowire arrays both in diameter and periodicity can be produced with a two step technique. In this procedure, homogenous nanospheres of either silica or polystyrene are uniformly distributed on the Si surface as a two dimensional hexagonally close packed crystal structure. Then the size of the nanospheres is reduced either by HF or O_2 plasma depending on the used nanosphere type. The desired diameter and periodicity of the nanowires can be determined either using this reduction technique or by changing the nanosphere size

(it can be between several tens of nm to few μm depending on purpose). First, Ag or Au is deposited on this layer, and then nanospheres are dissolved in an appropriate etchant. Finally, the wafer is immersed in to HF-H_2O_2 solution for etching. However, defect free and single layer covering of the surface by nanospheres is difficult, and in the best cases only few cm^2 areas can be covered with the desired properties. In our preliminary study, we have managed to cover about 40 cm^2 Si surface with 500 nm diameter polystyrene nanospheres. However deposited layer had both line defects and two layer formation. In Figure 5.17 SEM image of the nanowires that we obtained via nanosphere patterning is given. We see that Si formation is very uniform and extremely well aligned. This result shows that nanosphere lithography is a promising technique in the nanowire formation. However, it needs to be optimized for large area for practical applications.

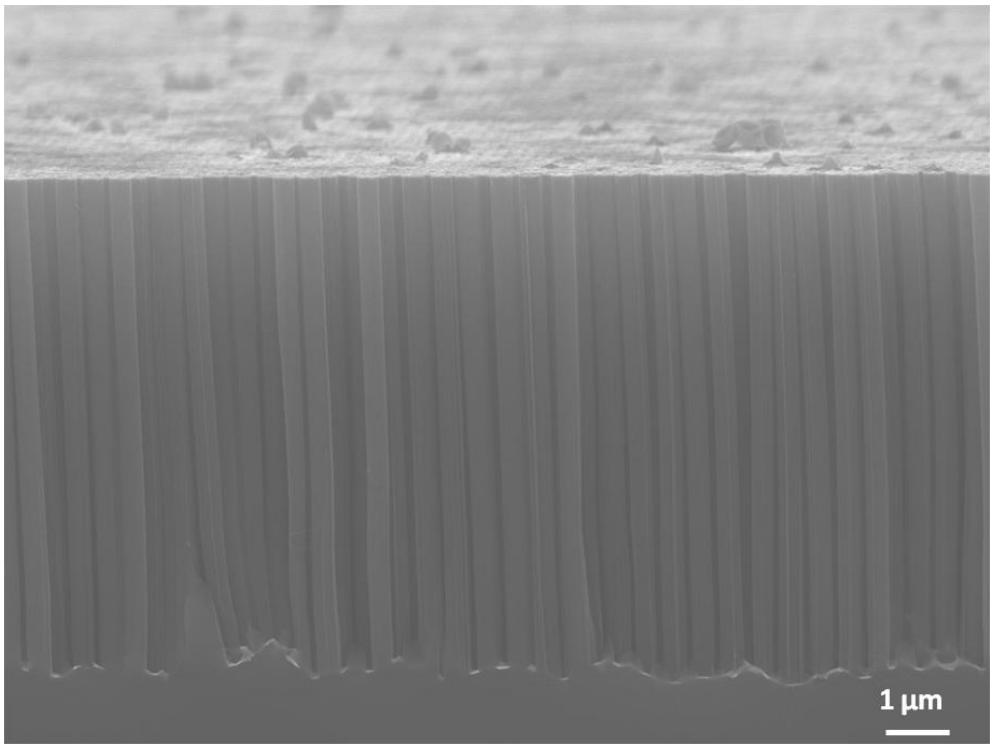

Figure 5.17. Si nanowires produced by two step process using nanosphere lithography, the diameter of nanowires is determined by polystyrene nanospheres with diameter of 500 nm.

5.4.2. Reflection properties of Si nanowires produced by MAE technique

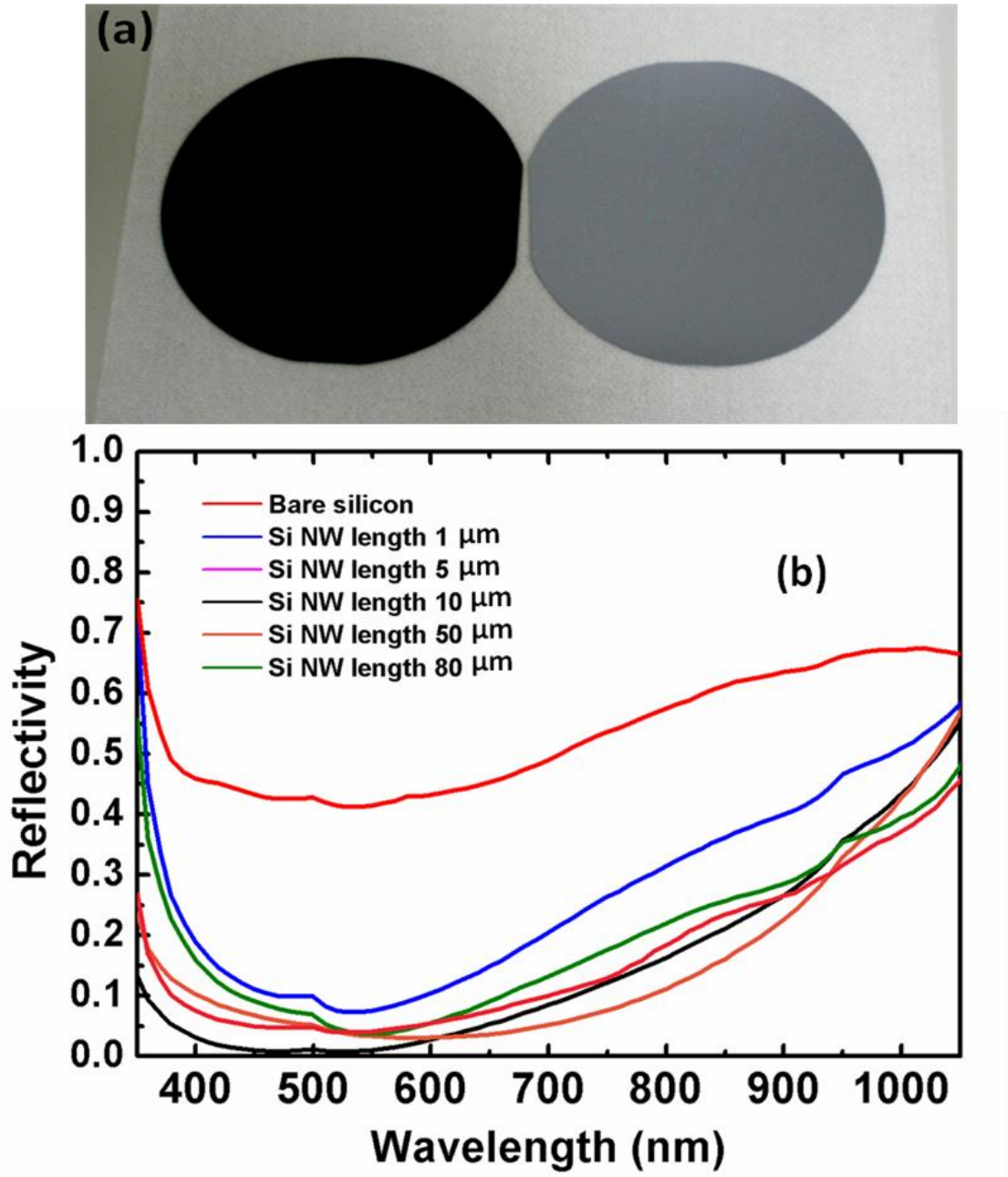

Figure 5.18. (a) Photographs of 4-inch Si wafer before (on the right) and after (on the left) Si nanowire fabricated by MAE. (b) Optical reflectivity measurements results of bare silicon and silicon samples containing various lengths of silicon nanowire arrays in a 350-1050 nm spectral window.

One of the most important features of vertically aligned Si nanowires is their unique and remarkable antireflective properties. The optical photographs of the Si substrate

taken before and after Si nanowire formation are given in Figure 5.18 (a). The shiny and reflective grey colored surface of the substrate turns into a black and dull appearance after nanowire formation. This significantly low reflectivity, already visible by naked eye, was also measured in a reflectivity setup. Reflectivity measurements of the bare Si wafer compared to Si wafers with different lengths of Si nanowires are given in Figure 5.18 (b). We see that that Si nanowire arrays significantly reduces the reflectivity of the surface in a wide spectral range. The reflectivity values as low as 1.16% has been observed. These measurements were carried out on the samples, which were produced by a solution concentration of 4.6 M HF, 0.02 M $AgNO_3$ processed at 40 °C for different etching durations. Reflectivity of these samples were measured at a wavelength of 500 nm with respect to the nanowire length is plotted in Figure 5.19. A sharp decrease in reflectivity with nanowire length was observed up to a nanowire length of 10 μm. These results are consistent with the previously reported reflectivity dependence on the nanowire length [262]. We have further extended this work and examined the reflectivity values for longer Si nanowires. Further increase in the nanowire length resulted in a slight increase in the reflectivity of the samples. This could be due to the bundle formation and nanowire loss, which decreases the uniformity of the distribution of nanowires and increases the void space. As indicated before, Si nanowire arrays transforms into bundles with the increase in the length. The top view of the surface from the SEM images given in the inset of Figure 5.19 shows the bundling of the nanowires clearly. The sample with 10 μm long nanowires has a stronger light trapping feature due to its higher nanowire density, small void space and homogeneous nanowire distribution, giving the best antireflective performance. For the case of multicrystalline Si, due to the different directional alignment of the nanowires depending on the crystalline direction of the grains, the reflection from the wafer depends on the vision angle.

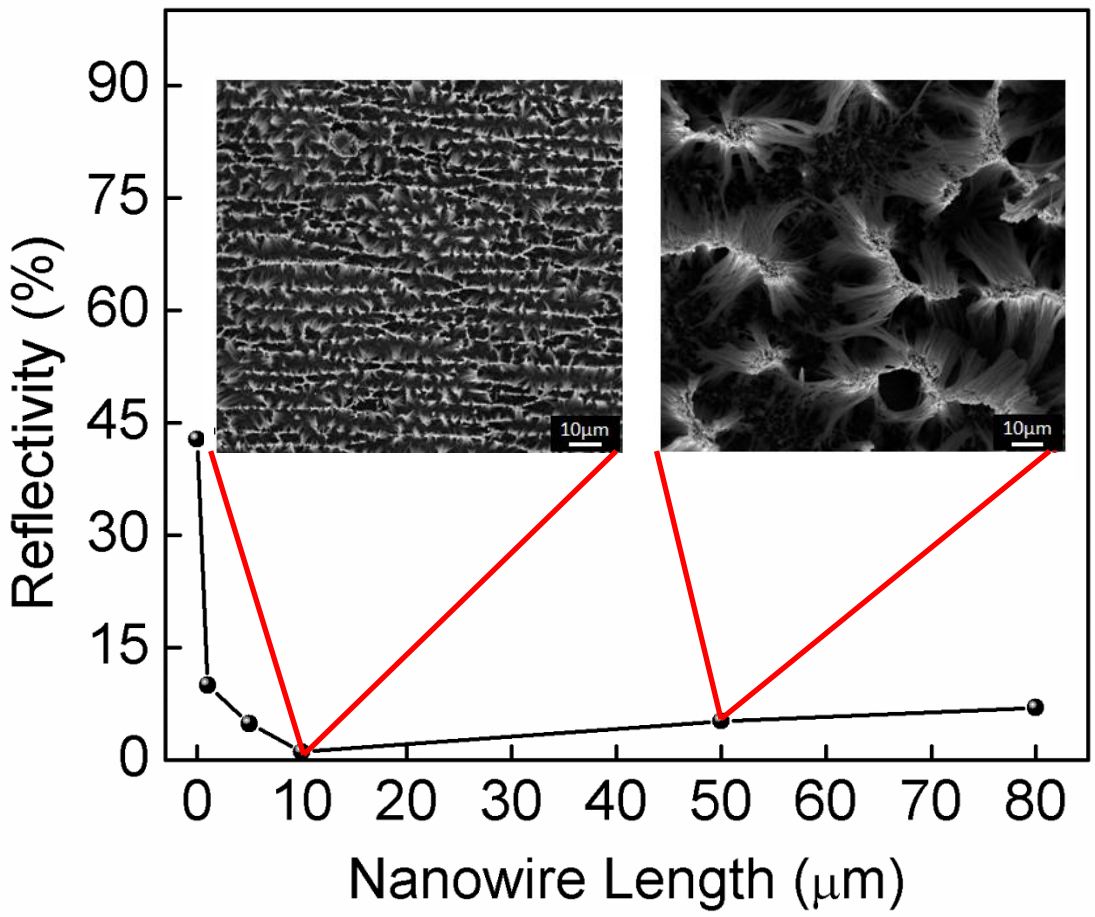

Figure 5.19. The dependence of the reflectivity on the nanowire length at the wavelength of 500 nm. The SEM images in the inset of the graph are obtained from the etched silicon samples containing 10 and 50 μm long silicon nanowire arrays.

The absorption enhancement phenomenon in solar cells has been studied for many years. One of the most efficient and widely used methods is to increase the total internal reflection of the systems by texturing the surface. To maximize the light trapping and absorption on the surface many studies have been carried out on the use of nanostructures including nanowires / nanorods structures.Total internal reflection is simply equivalent to the integral of the energy transferred by the photons via scattering events taking place at the surface or inside the medium. Maximum achievable absorption of light by a planar sheet absorber is ideally described by random Lambertian light trapping mechanism [263]. It was found that the absorption strength of a nanowire array exceeds the planar light trapping limit leading to a greater absorption per material volume than achievable by any textured surface [264], especially in the photon energies near the band gap of the absorber [242]. This behavior makes nanostructures like nanowires/nanorods very promising for solar cell

applications. In particular, silicon nanowires, having the same material structure, are the most appealing candidate for this application. In the following sections we present the application of Si nanowires to large area solar cells.

5.5. Si nanowire based large area solar cells

Crystalline solar cells overwhelmingly dominate the photovoltaic market today. However, high material and processing costs do remain as the two important drawbacks for these systems. It was realized that in order to reduce the material costs, new designs involving thinner silicon wafers should be used rather than the conventional silicon wafers. However, as an indirect band gap material, silicon is not capable of absorbing the whole solar spectrum as the wafer thickness drops below 200 μm in conventional cells. To address this issue and the efficiency improvement in general, there are several studies related to light trapping techniques, increasing the path length and the number of scattering events of the incident photons using total internal reflections, thereby increasing the light absorption. Surface texturing and anti reflection coatings have been commonly used for such purposes [265, 266].

Among nanostructures, silicon nanowires have been investigated for solar cell applications, owing to the fact that silicon is the most suitable semiconductor with superior and easily tunable properties for photovoltaic applications. Moreover, they could be formed as vertically aligned and integrated arrays on the solar cell surface, which was found to bring remarkable light trapping strength to the system, providing reflectivities as low as 1% [257]. Following the realization of enhanced light trapping and charge transfer properties of silicon nanowires [267], many different silicon nanowire related studies have been reported. In these studies several different methods to synthesize silicon nanowire arrays have been used, such as vapor-liquid-solid [268], laser ablation [250], direct reactive ion etching [251] and MAE/electroless etching [269-271]. Among these methods, MAE stands as the most appealing one. MAE is a solution based method, meaning that the nanowire formation would have a minor contribution to the overall processing cost. Moreover, unlike the conventional nanowire fabrication methods, silicon nanowires with desired properties and doping levels can be produced over large areas using this

technique. As a consequence of developing such a cost effective silicon nanowire fabrication method enabling large-scale and large-area production in a controlled manner, it could be claimed that silicon nanowire based solar cell production has a great potential to be adapted to industry-scale works. With this point of view, there are several reports focusing on the photovoltaic properties of large area silicon nanowire solar cells [272,273]. These studies revealed that significant developments could be achieved with further optimizations in the process. It was claimed that the presence of silicon nanowire arrays lead to an increase in the short circuit current, but the overall power conversion efficiencies cannot be improved. This is due to surface recombination mechanisms actively taking place along the nanowire surfaces decreasing the fill factor and open circuit voltage of the solar cells. Another challenge for the solar cell performance is the high series resistance due to aggravated top contact-nanowire interface. Passivation of nanowire surfaces has been investigated to reduce surface recombination [274] in addition to the attempts for decreasing the series resistance at the contacts [275].

With the presence of silicon nanowires on the surface, several different types of junctions could be formed depending on the doping process. A radial p-n junction could be formed by doping only the surface of the nanowires [276], or a planar p-n junction could be formed by doping the entire nanowire arrays. In the former case, a three dimensional radial p-n junction can be created. The device physics of both types of solar cells have been compared and a great improvement in the charge transport and collection mechanisms in the case of radial p-n junction solar cells compared to the planar junction solar cells have been reported [243]. In fact, silicon nanowires provide several alternative radial p-n junction solar cell designs. In addition to radial p-n homojunction solar cells, radial p-n heterojunction solar cells have also been widely investigated [277,278]. In a recent work, we have shown that remarkable improvement in the photovoltaic conversion efficiency can be obtained in certain device structures [279].

In this part of the thesis, we report on industrial size (156 mm x 156 mm) monocrystalline silicon solar cells with vertically aligned random nanowire arrays formed on their surface by MAE. To our knowledge, this is the first demonstration of

the nanowire application on a solar cell with this size. Various lengths of vertically aligned silicon nanowire arrays have been formed on monocrystalline silicon wafers through a cost effective procedure and the effect of silicon nanowire length on the solar cell characteristics have been investigated. The light trapping and antireflective properties of the silicon solar cells have been investigated and compared with conventional texturing techniques. The quantum efficiency (QE) measurements have been carried out comparatively. The technical procedures presented here are fully compatible with the present monocrystalline silicon solar cell production lines with minimal cost.

5.5.1. Experimental details and solar cell fabrication

For mono-crystalline solar cell production, Czochralski grown, 200 μm thick, p-type as cut silicon wafers with (100) crystallographic orientation, 4 Ω-cm resistivity and 156x156 mm^2 size were used. The procedure begins with saw-damage-etching of the wafers in order to eliminate the surface damage that resides from mechanical sawing. For this purpose, the wafers were shiny etched in a hot potassium hydroxide (KOH) solution. Following this step, an HCl cleaning followed by an HF cleaning was used to remove metallic contaminants and silicon oxide formed on the surface. As a result of these pre-treatments, the wafer surfaces gained a proper form for the further processing. Two separate groups of substrates were prepared to compare the effect of conventional surface texturing and nanowire formation on the solar cell performance. Surface texturing was carried out for the wafers in the first group again in a hot KOH solution with facilitating a random pyramid formation and then, the same cleaning steps with the previous KOH treatment were used. The second group of wafers was not subjected to any alkaline texturing process. Instead, vertically aligned silicon nanowire arrays were formed on their surface by MAE process as described in previous section. In brief, an etching solution of 0.02 M silver nitrate ($AgNO_3$) and 4.6 M hydrofluoric acid (HF) at 20 °C was prepared and the wafers were kept inside this solution for 10 to 50 min. depending on desired length of nanowires. At the end of the process silver dendrite layers were removed by nitric acid (HNO_3). After conventional alkaline texturing and nanowire fabrication by MAE, the wafers were n-type doped by phosphorus diffusion to a sheet resistance of 50 Ω/□ (Ω/cm^2) as

determined by a four point probe measurement. After removal of the phosphorus glass by dipping into 5% HF, wafers were coated with 80 nm of silicon nitride (Si_3N_4) in plasma enhanced chemical vapor deposition (PE-CVD) system for surface passivation. This also acts as an anti-reflection (AR) coating. The front silver and back aluminum metal contacts were then screen printed and co-fired. Finally, edge isolation was performed with laser scribing. The flowchart of the fabrication processes of solar cells is given in Figure 5.20.

We have fabricated nanowire decorated solar cells both on mono and multicrystalline Si wafers. Most of the systematic studies have been carried out on mono-crystalline solar cells due to the uniformity of this type of wafer. A few multi-crystalline solar cells have been processed to demonstrate the feasibility of the production on this type of wafer. Multi-crystalline wafers were also subjected to same procedure of production with mono-c wafers. We have found that nanowire decoration work better for multicrystalline based solar cell than that for mono crystalline.

The resultant surface texturing features and silicon nanowires were monitored by Scanning Electron Microscope (SEM). Cross-sectional SEM images were obtained from the cleaved edges of the silicon substrates. Reflection measurements were made through calibrated integrated sphere which also takes into account the diffuse reflectance. The device characterization was carried out by obtaining the current-voltage characteristics of the devices in a standard solar simulator (AM1.5G). Minority carrier life-time measurements were conducted using a Sinton lifetime tester. The quantum efficiency measurements were done using a set-up equipped with a monochromator, a chopper and lock-in amplifier system and a calibrated light detector.

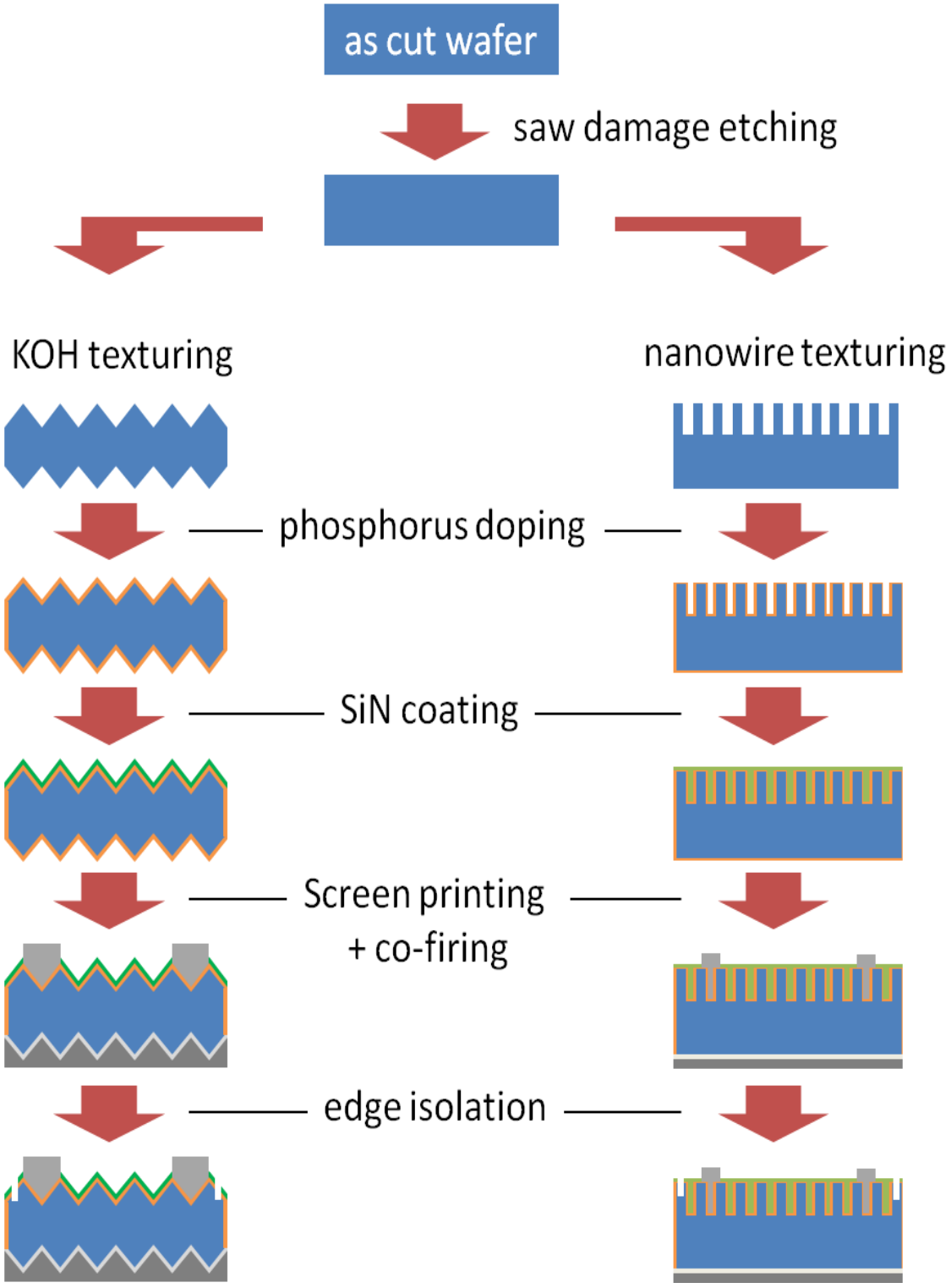

Figure 5.20. Flowchart of processes, during the fabrication of the both conventional alkaline textured (left part) and nanowire decorated solar cells (right part).

5.5.2. Features of nanowire synthesis on standard Si wafers.

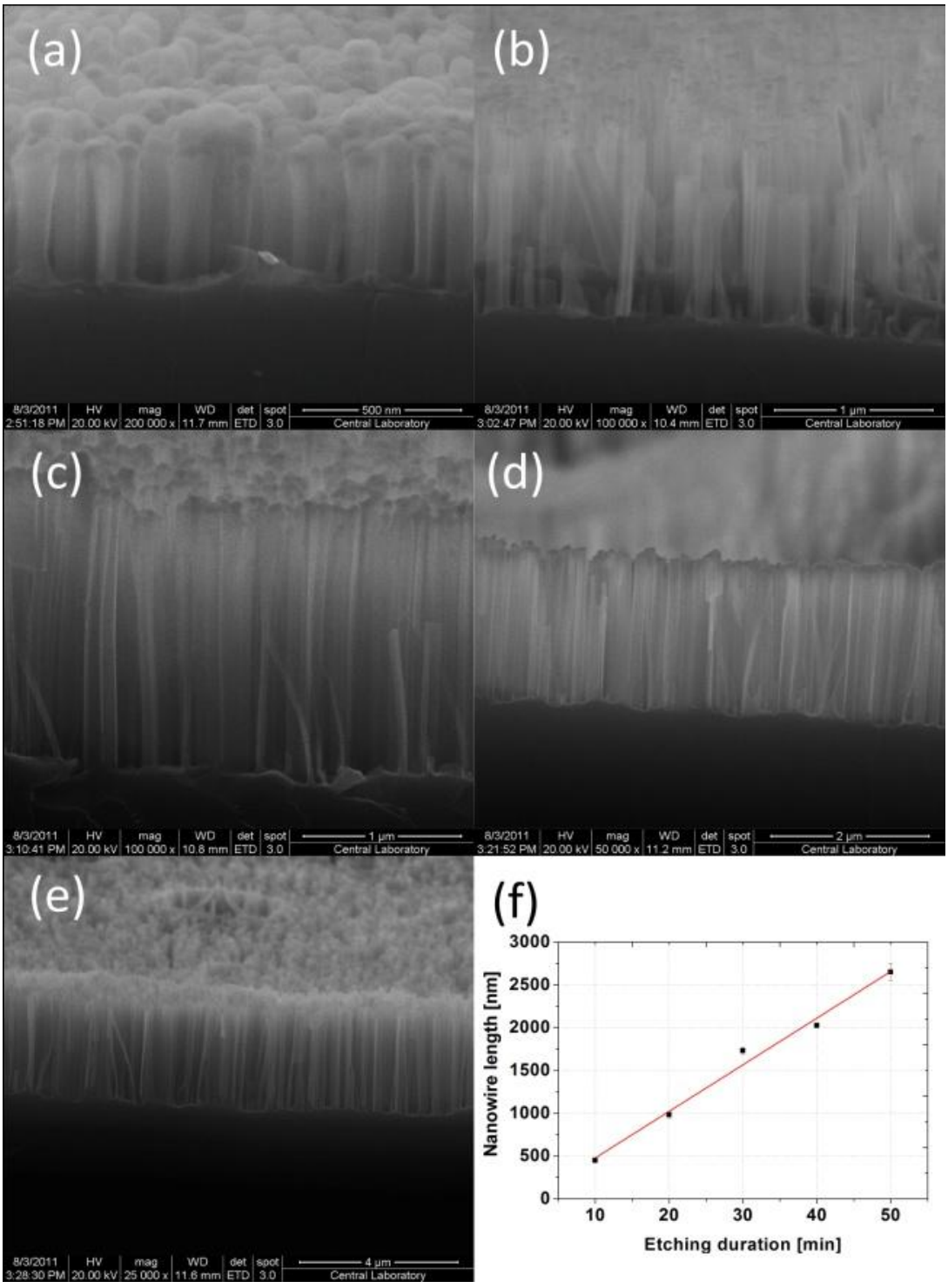

Figure 5.21. Cross sectional SEM images of silicon nanowires fabricated, a) 10 min, b) 20 min, c) 30 min, d) 40 min, e) 50 min of etching. F) An almost linear relationship was obtained between etching time and nanowire length.

The MAE process was applied to both monocrystal and multicrystal wafers. The relationship of Si nanowire length and distribution with each process parameters, namely etching time, solution temperature and concentration, wafer orientation, resistivity and doping type was described above. In this part of the thesis, we studied 5 different sample types with different nanowire lengths. As shown in the SEM images (Figure 5.21), vertically aligned and well-controlled Si nanowires were formed on the device surface. Detailed SEM analysis revealed that the length, shape and distribution of the nanowires were found to be uniform all across the wafer. SEM images of the nanowires fabricated within 10, 20, 30, 40 and 50 min. are shown in Figures 5.21. (a)-(e), respectively. The nanowire length as a function of etching time is plotted in figure 5.21(f).

5.5.3. Reflection from wafer surface

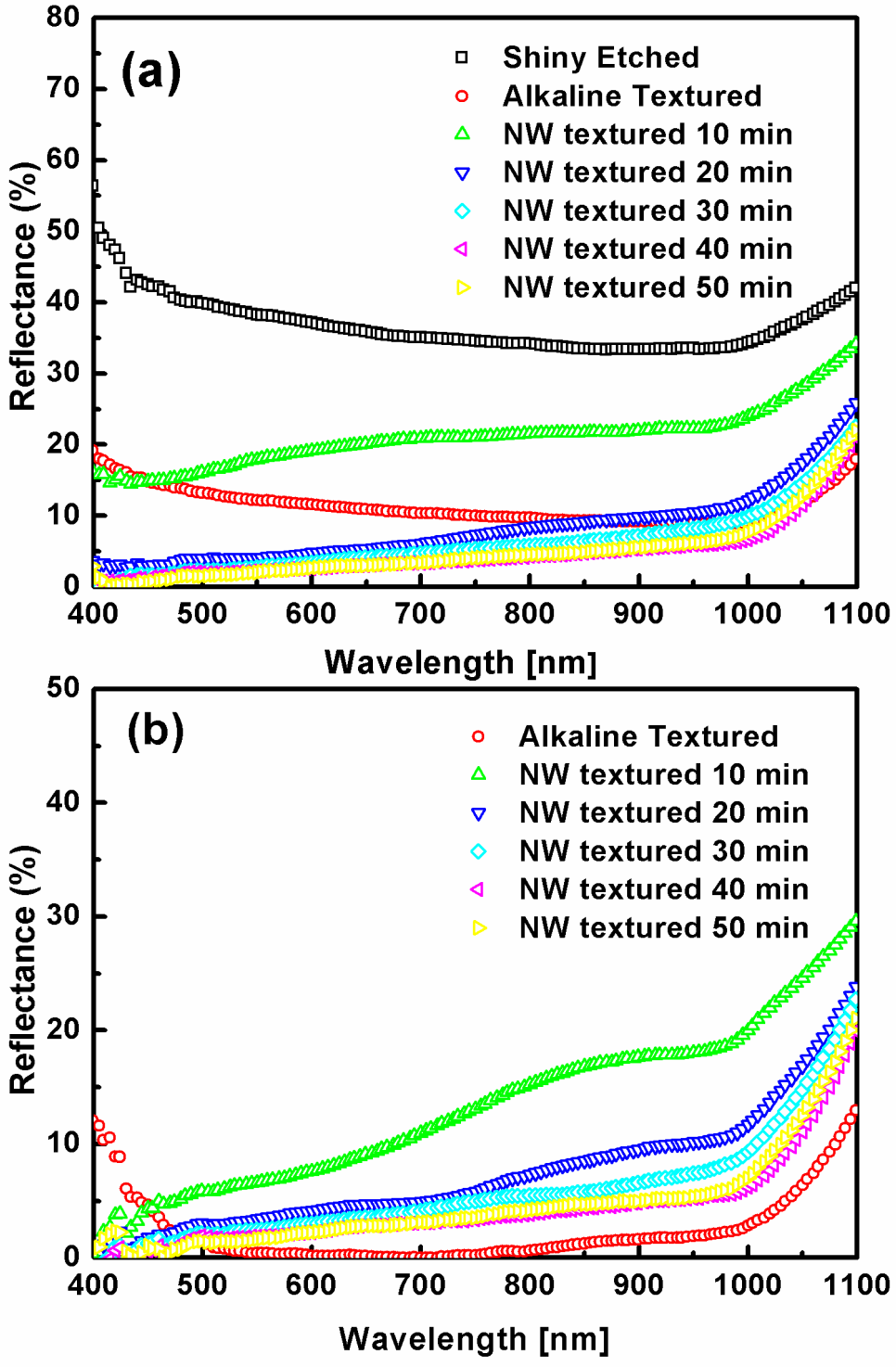

Figure 5.22. Reflection spectrum of samples (a) before and (b) after Si_3N_4 coating. All nanowire textured samples except 10 min. of etching has lower reflection than alkaline textured sample (a). Alkaline textured sample has the lowest reflection while nanowire textured samples do not show significant difference after AR coating (b)

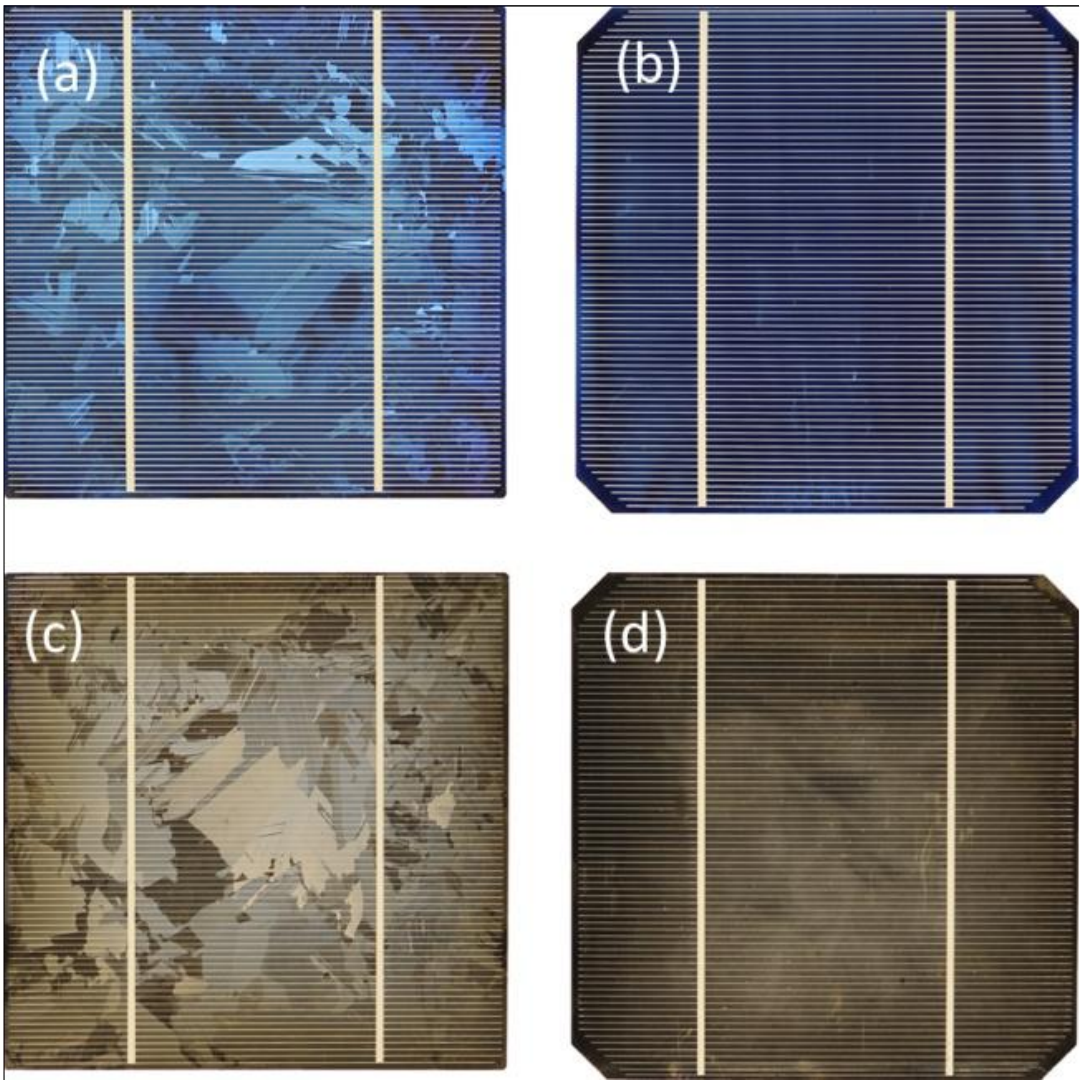

Figure 5.23. Images of the fully processed solar cells. There is a significant color change between conventionally textured cells (a) and (b), when compared to nanowire textured cells (c) and (d), due to absorption enhancement for wavelengths smaller than 450 nm.

The optical reflection spectra of textured/silicon nanowire containing silicon wafers prior to and after AR coating are shown in Figures 5.22 (a) and (b), respectively. As the nanowire length increases, the reflectivity of the wafers decreases accordingly. Without the presence of AR coating on the surface, all nanowire coated wafers, except the one fabricated within 10 min., exhibit lower optical reflection than the standard pyramid textured wafer. However, following AR coating, the pyramid textured wafer exhibits the lowest reflection for the wavelengths higher than 450 nm while nanowire textured wafers, except the one fabricated within 10 min., do not

show any significant difference. Average reflection results are tabulated in Table 1. For the wavelengths smaller than 450 nm, the samples with nanowires exhibit very low reflectivity, showing excellent light trapping properties in the blue part of the spectrum. This feature can be seen from the color of the fully processed mono and multicrystalline Si solar cells shown in Figure 5.23. The surface of the monocrystalline Si solar cells is entirely blackened by the presence of nanowires, while we see some color variations due to the orientation difference of different polysilicon domains in the multicrystalline wafer. The dependence of the nanowires formation on the crystalline orientation was discussed in the previous sections.

Table 5.1. Average reflection values for pyramid and nanowire textured samples throughout the whole spectrum before and after AR coating. The net difference in average reflection has also been listed before and after AR coating.

	Textured	10 min	20 min	30 min	40 min	50 min
Before AR	11.4 %	21.1 %	8.3 %	6.3 %	4.8 %	5.0 %
After AR	2.3 %	13.3 %	7.4 %	5.9 %	4.3 %	4.6 %
Difference	9.1 %	7.8 %	0.9 %	0.4 %	0.5 %	0.4 %

A numerical tabulation for the average reflectivity data corresponding to the 350-1100 nm wavelength range is given in Table 5.1. We see that the effect of nitride coating is gradually decreasing with the length of the nanowires. For the samples with longest nanowires prepared within 30 to 50 min. of etching, the effect of nitride coating on the reflectivity is insignificant. The absence of AR effect of the nitride layer for long nanowires can be attributed to a change of refractive index on nanowire coated surfaces. As the nanowire length is increased, the effective refractive index of the surface changes removing the condition for the destructive interference condition for AR coatings. Therefore, the net difference between reflectance before and after AR coating decreases with increasing wire length for shorter nanowires and stabilizes for longer nanowires fabricated for longer than 30 min. of etching, as shown in Table 5.1.

5.5.4. Solar Cell Device Performance

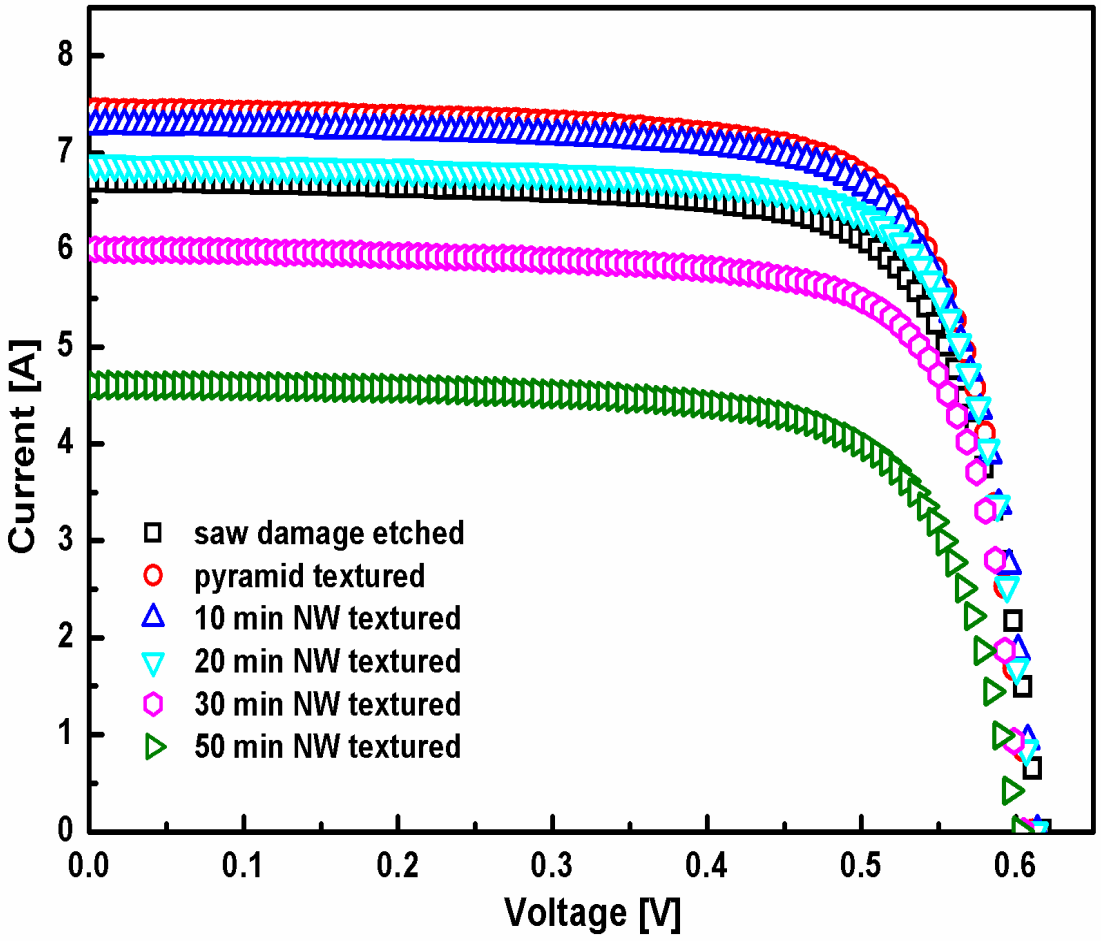

Figure 5 I-V characteristics of different samples under standard testing conditions (AM1.5G, 100W/cm^2, 25 °C).

Current-voltage (I-V) curves of the solar cells fabricated in this work are shown in Figure 5.24. The highest power conversion efficiency of %14.2 was obtained for the standard pyramid textured solar cell. The nanowire textured samples with shortest investigated etch time (10 min.) approaches the same performance as the pyramid textured device. Although further optimizations still need to be done to improve the reported performance, our result proves the successful implementation of Si nanowire to the standard solar cell devices on an industrial scale.

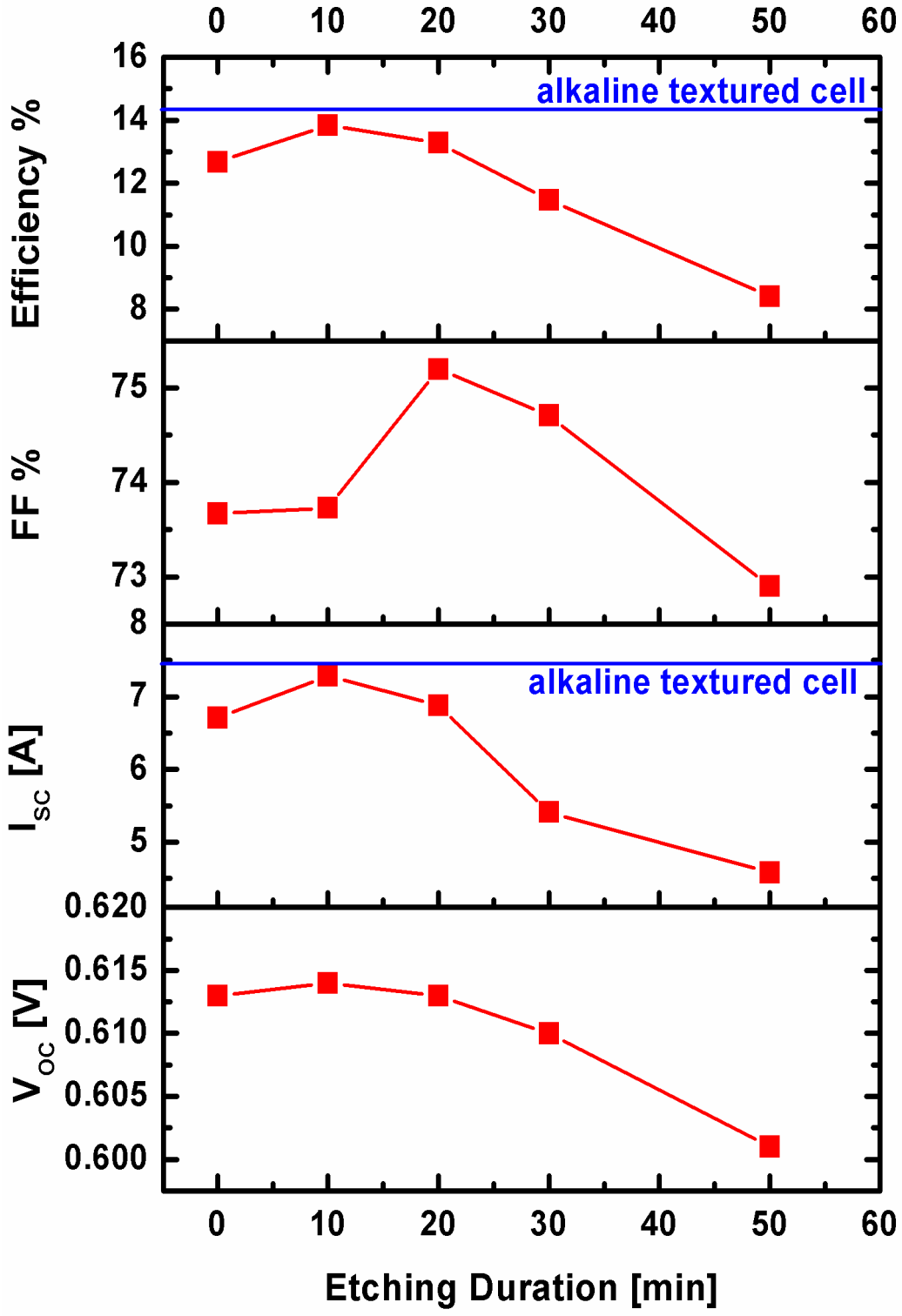

Figure 5.25. The effect of etching duration on different solar cell parameters. 0 min. of etching corresponds to only saw damage etched cell and textured solar cell parameters are inserted as a reference line on efficiency and I_{SC} graphs.

The solar cell device parameters such as photovoltaic conversion efficiency, fill factor, short circuit current and open circuit voltage extracted from the I-V analysis are shown in Figure 5.25. It is clear that the short circuit current and open circuit voltage increase initially with the introduction of nanowires on to the solar cell surface, and then they both decrease with the nanowire length leading to a reduction in the overall power conversion efficiency. This can be attributed to the increased surface recombination processes along the nanowire surfaces. As a consequence of the MAE, broken/dangling silicon bonds are generated on the nanowire surfaces, which constitute trap energy levels for the photo generated charge carriers. This becomes more of an issue for longer nanowires, since the density of recombination sites increase with the nanowire length.

The effect of Si nanowire length on the carrier lifetime was measured and correlated to the solar cell parameters. Figure 5.26 shows the minority carrier lifetime values for samples measured by Sinton lifetime tester. As a consequence of the surface recombination, lower minority carrier lifetimes were obtained for solar cells with relatively longer silicon nanowire arrays. The decrease in the minority carrier lifetime was the main reason for the reduction of V_{oc} and I_{sc} with increasing nanowire length. Better cell performance should be expected with improved passivation of the nanowire surfaces.

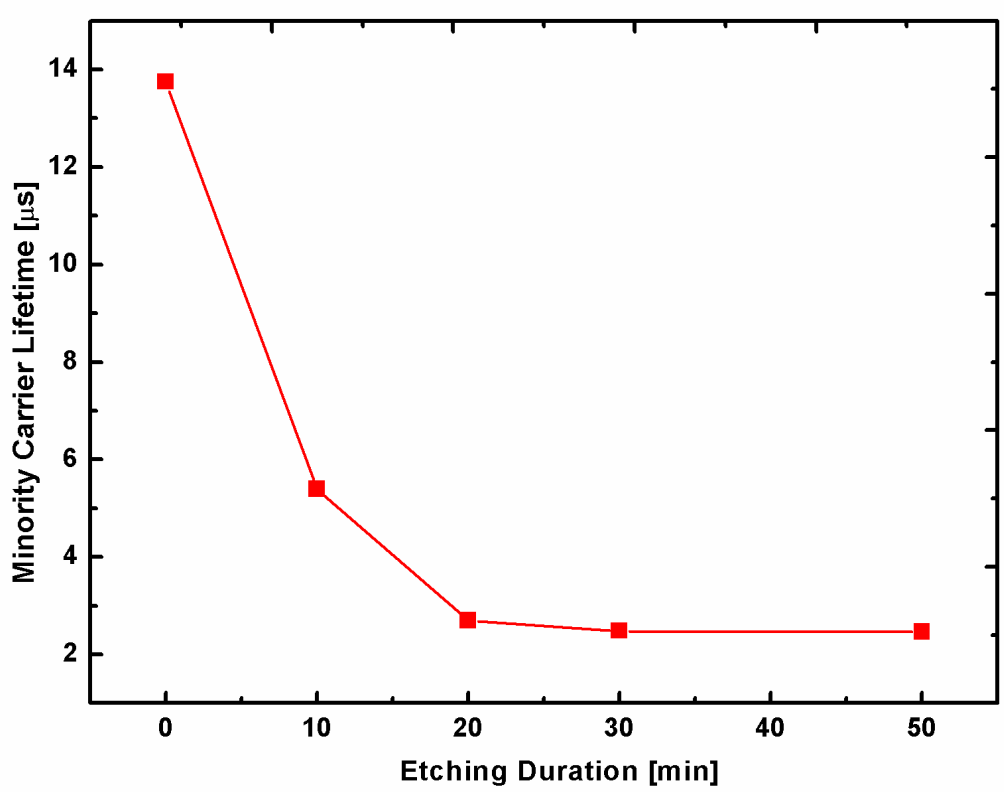

Figure 5.26. Minority carrier lifetimes for lifetime samples prepared by both sides coated with Si-nitrate. 0 min. of etching corresponds to saw damage etched wafer.

Although the cells with etching time of 20 min. exhibit lower reflectance values, the short circuit current from those cells are low compared to the 10 min. etched and alkaline textured cells. The reason for this may be three fold: i) poor contact formation over long nanowires, ii) poor absorption due to thinned bulk for longer wires, or iii) poor blue response of cells due to high absorption on long nanowires.

In order to investigate the decrease in I_{sc} with increasing nanowire length and the dependence of the solar cell performance on the wavelength in general, quantum efficiency (QE) measurements were conducted. External and internal quantum efficiency (EQE and IQE) results are displayed in Figure 5.27, respectively. It is seen that the QE results correlates in general with the other solar cell parameters presented above. The QE values drop with the increasing nanowire length as a consequence of poor carrier collection on long nanowires. However, the blue response of cells fell down more rapidly, showing that photo-generated carriers are lost more easily for this part of the spectrum.

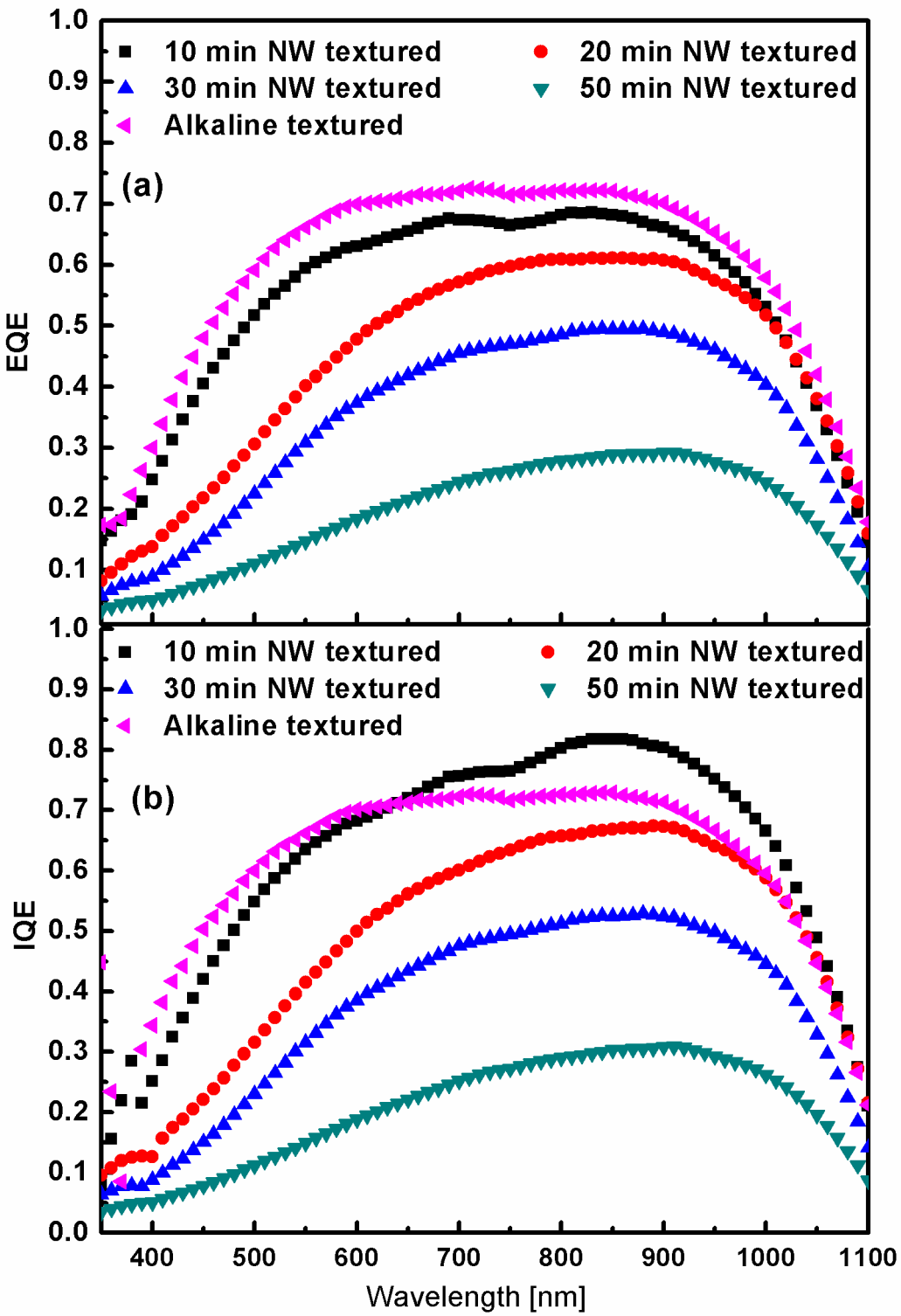

Figure 5.27. (a) External Quantum Efficiency results for different textured samples without bias light. The decrease in blue response is very clear with increasing wire length. (b) IQE analyses reveals that 10 min. of nanowire texturing has better long wave response which is attributed to better light trapping.

This is a result of the fact that blue part solar radiation is absorbed at the very top region of the nanowires due to the higher absorption coefficient of Si in this region, and a carrier created there has to travel along the long nanowire and reach the bulk region where junction is formed. Since the nanowire has a very high surface to volume ratio and is highly doped, the diffusion length of the carrier is very low and as a result, the collection efficiency is very low especially for the blue part of the spectrum. Although, the anti-reflecting properties of nanowires are seemingly superior for the blue light (see Figure 5.22), the absorbed light are not effectively used for the photo-current generation in the nanowire coated solar cells. We believe that improvement in the surface passivation and a better control over the nanowire doping will lead to better cell performance for the blue region of the spectrum.

When the IQE of the samples are analyzed, we see that the sample with 10 min. of nanowire formation has better long wave response when compared to the alkaline textured sample (Figure 5.27b). This result may be attributed to the better light trapping and/or scattering ability of nanowire textured sample. While the nanowires are formed only on the front side of the cell, the back side of the device acts as a perfect reflector especially for the red and infrared part of the spectrum, and hence improves the solar cell performance.

The quality of the metal contact is crucially important for an efficient charge collection in the solar cells. The nanostructures surface of the cell might require a new approach for the metallization scheme. For this reason, metal contact formation was investigated through cross sectional SEM images as shown in Figure 5.28 (a), (b) and (c) for the saw damage etched sample and samples with nanowires respectively. As revealed from the SEM images, while silver metal paste forms proper metallization on the standard solar cell, it fails to stick properly to the solar cells with nanowires. This might indeed be expected due to the low effective contact area and the hydrophobic nature of the nanowires and could be the main reason for decrease in fill factor with nanowire length as shown in Figure 5.25. The major contribution to the increase in the series resistance (Figure 5.29) with nanowire texture might be from the poor metallization. In order to improve the device

characteristics, effective charge collection through optimized electrical contacts should be investigated.

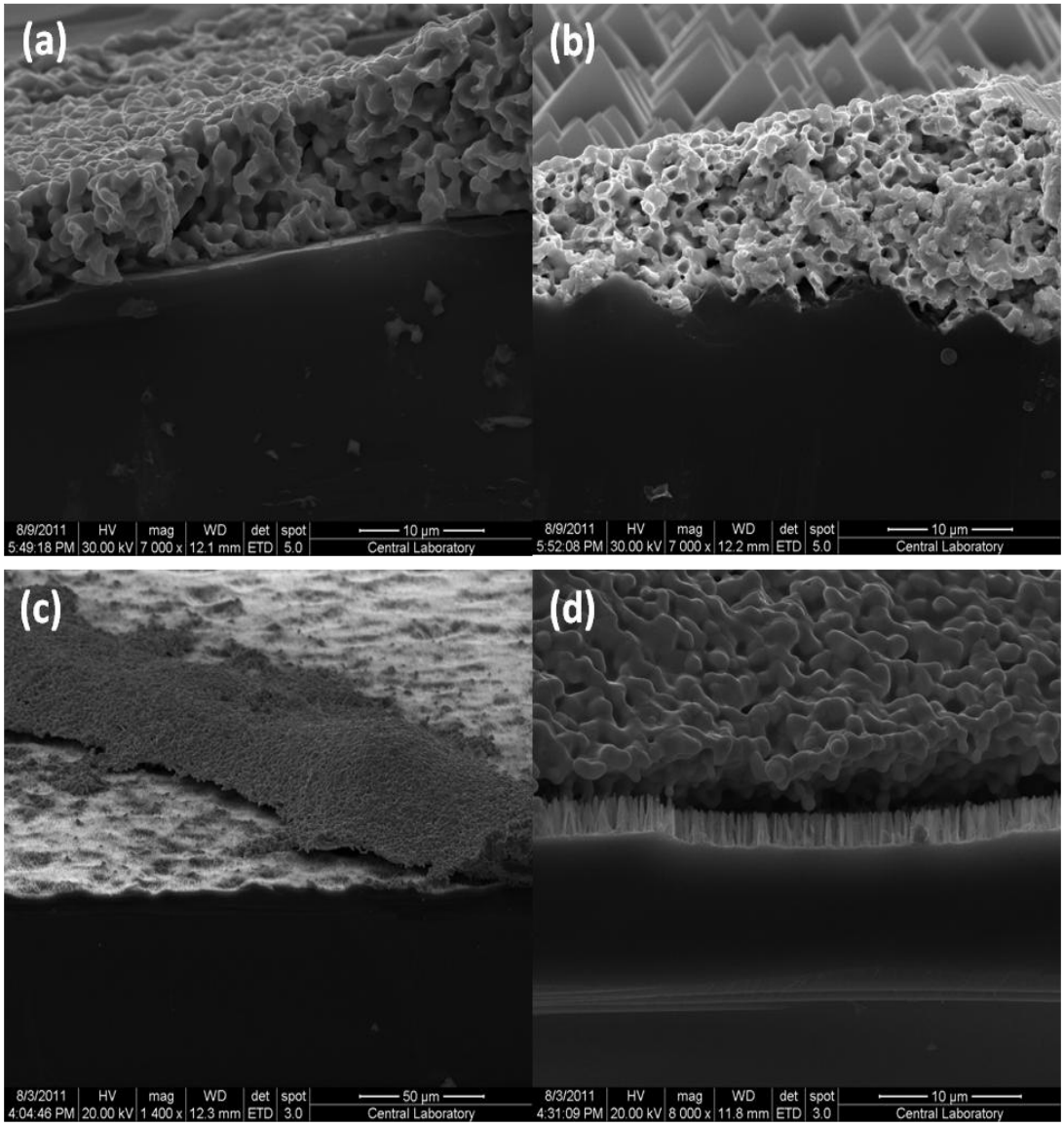

Figure 5.28 Front side silver contact formation on (a) saw damage etched surface, (b) pyramid textured sueface, (c) and (d) nanowire textured surface. The silver finger sticks to surface properly in (a) and (b), while the finger does not diffuse in between but rather floats on nanowires as shown in (b) and (c).

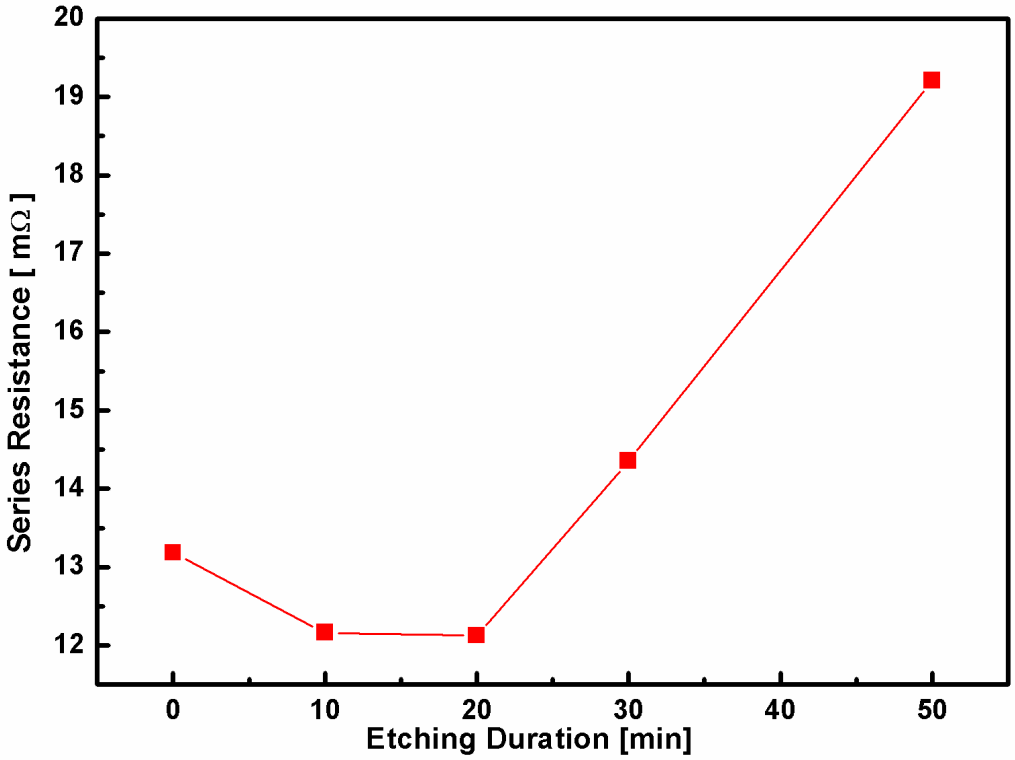

Figure 5.29. Change of series resistance with increased etching durations. 10 and 20 min. of etching has lower R_s values, evidence for better contact formation while higher etching times result in higher R_s due to floating contacts on nanowires.

5.5.5. Conclusions

In this chapter, we have presented an extensive study on the fabrication, characterization and application of Si nanowire to Si solar cells. We have shown that Si nanowires can be fabricated by MAE which is an easy, cheap and very appropriate technique for industrial applications. We studied the effect of process parameters like etch duration, solution temperature, solution chemistry on the structure of the nanowires formed. The length of the nanowire was shown to be controlled easily with these parameters. However, the diameter of the nanowires was hardly controllable by these parameters. Nanowire decorated surfaces exhibited excellent light trapping properties. The reflection from the surface, especially in the wavelength interval where the solar radiation is most efficient, can be made extremely low by nanowire application.

We then demonstrated the first application of Si nanowires to industrial size (156 mm x 156 mm) crystalline Si solar cells. We showed that nanowire formation process could successfully be integrated to the standard solar cell production line. We concluded that the use of nanowires on large area crystalline solar cells is technically feasible. We have observed an improvement in the solar cell efficiency compared to the solar cells with flat surface. However, the efficiency remained under that of standard solar cell with alkaline textured surface. Both efficiency and the quantum efficiency values dropped with the increasing nanowire length. This is mainly due to the poor charge collection ability along the nanowire. The charge collection efficiency can be improved by surface passivation of the nanowires and possibly by reducing the doping in them. The screen print metallization using standard Ag paste was found to create poor contact to the top of the nanowires due to the low contact area. We concluded that a new metallization scheme, possible with a more suitable Ag paste, needs to be developed to improve the metallization on the nanowire-decorated surfaces.

CHAPTER 6

CONCLUSIONS, OPEN ISSUES AND SUGGESTIONS FOR FUTURE WORKS

6.1. Conclusions

In this thesis, we studied Si nanostructured based sytems for electro-optical and photovoltaic applications. Each chapter was organized independently from each other. In reality, our studies were well beyond the results given here, for the sake of completeness and compactness we had to put some representative findings only; may be each chapter with all data obtained could be an another thesis individually. In Chapter 2, we could only represent one of four of all related studies. In Chapter 3, we discarded half of the total related studies including detailed investigation of transport properties whose results were only reported qualitatively in one page. In Chapter 4, we had to discard detailed temperature and size dependence of Stark effect including theory, in Chapter 5, we discard Si nanowire decorated large area solar cell on electronic grade and multi-crystalline substrates. Moreover, a chapter on Si nanowire/chalcopyrite heterojunction structures for solar cell applications was totally eliminated from the thesis: that study consisted of detailed investigation of Si nanowire/$AgInSe_2$ heterojuctions through electro-optical, electrical (I-V, C-V in full temperature range and their modeling) and structural analysis. Beyond those, we also left out Si nanowire-organic hetero junction based solar cells, Si nanowire/ZnO, Si nanowire/CdTe and ZnO nanowire/ CdTe heterojunction devices. Below, we present general conclusion of the thesis.

In Chapter 2 we presented and discussed ZnO nanocrystal/Si heterojunction based LED structures. ZnO nanocrystals were synthesized by VLS method on p- and n-type Si substrate with and without thin SiO_2 layer. Using these samples, LED structures were fabricated and EL measurements were carried out at room

temperature. In addition to ZnO/Si heterojunction devices, control devices without any nanocrystals were also fabricated and tested to understand the EL mechanisms of LED structures. Throughout the EL study presented, some conclusive results have been obtained.

Contrary to the clear observation of UV emission from the band edge of ZnO in PL measurements, almost all EL emissions were in the visible region, which are related to the native defect levels (vacancies and interstitials) located in the band gap of ZnO. The dominance of these visible EL emissions was attributed to either to the structural changes during the device fabrication processes or to the different nature of the excitation mechanisms of electron hole pair under the applied voltage.

Devices having oxide buffer layer seem to have more tolerance to higher voltage-applications and more reliable compared to the devices having no SiO_2 buffer layer. Therefore SiO_2 buffer layer acts as a controller and regulator for the charge transport which results in more reliable and efficient EL devices by preventing over injection and breakdown. For an efficient device operation; hole injection from the substrate is required (forward bias condition for the devices on p-type and reverse bias condition for the devices n-type Si substrate respectively) over the hole accumulation layer in the p-type substrate and from the inversion layer in n-type substrate. In this biasing scheme, the dominant mechanism for the EL emission is the bipolar injection of carriers into the ZnO crystal layer. In the case of electron injection from the Si substrate, the light emission mechanism should be impact ionization, because of the difficulties of hole injection from ITO layer. In this case hot electrons should be supplied by the Si substrate.

Finally, ZnO nanocrystal/Si heterostructures can be exploited for fabrication of light emitting devices with optimized growth condition and device design. Because ZnO/Si heterostructures combines the advantages of the large band gap and exciton binding energy of ZnO and maturity of Si technology with cheap and large size substrate they have a great potential for future silicon based LED applications. By controlling defect to band edge emissions ratio with process control and non-defective encapsulation of ZnO nanocrystals with some delicate new approaches,

efficient white LEDs with low cost, which do not require extra phosphor light converting layer, would be produced.

In Chapter 3 of the thesis we have presented an extensive and detailed study on electroluminescence from Si based material system with and without inclusion of Tb ions. This content could have an important impact on the Si based LED technology. Below we highlight the major findings and conclusions reached during this study.

Contrary to the reported literature, we have observed a strong EL emission related to Si substrate at low energy side of the LED spectra in both n and p-type samples. It is assumed here that this emission is a result of the tunneling of electrons from top contact through the Si nanocrystal oxide layer into Si substrate where they recombine with holes accumulated in the inversion or accumulation layer at the SiO_2/Si interface, depending on the type of the substrate. Any quantum confinement effect especially under inversion condition might modify this emission toward high energy tail due to the increase in the energy difference between quantized levels. It is qualitatively concluded that the major transport through the oxide layer is the electron transport. Electrons injected from the top contact or from the substrate recombine partly in the oxide and partly in the Si substrate. Most of these recombinations in the substrate should be non-radiative as the substrate is indirect gap material, only small percentage would be radiative. This condition may be one of the reasons that decrease the efficiency of Si nanocrystal EL in the MOS-LED structure.

In Chapter 3, we have also studied possibility of light emission from MOS type LED fabricated on Tb doped SiO_2 matrix with and without excess Si. Successful device operation has been obtained under certain experimental conditions. Characteristic emission bands of Tb^{3+} ions have been observed clearly in the EL spectra of all reverse biased devices fabricated on n-type Si under excitation with hot electron injection from ITO window to the active layer. The light emission has been found to be sensitive to the Si amount in the oxide layer. Excess Si incorporation significantly increases electroluminescence efficiency accompanied by significant decrease in turn-on voltage and increased tolerable high current injection.

In Chapter 4, effect of electric field on the PL from Si nanocrysals formed in SiO_2 has been systematically studied at both cryogenic and room temperatures. It was observed that PL peak position was red shifted by increasing external voltage without any aging effects on luminescence properties of the sample after voltage was cut off. The field effect on the PL peak position and intensity have been discussed and attributed to QCSE in Si nanocrystals. It was shown that there is a fairly good agreement between theoretical model from second order non-degenerate perturbation theory and our experimental results. In addition to quadratic term which reflects polarizability of electron/hole due to spatial separation under electric field, we observed a minor contribution from a linear term originated from the built in dipole moment which is related to either defect states at Si nanocrystal/SiO_2 interface or anisotropic shape distribution of the nanocrystal. Both built-in dipole moment and polarizability decrease with increasing temperature due to spreading of electron/hole wave functions in the quantum well as the statistical distribution of carriers at higher energy levels increased. We have observed an asymmetric red shift in PL peak between the measurement conducted at forward and reverse bias which is considered as a result of the internal electric field generated by the hole injection and trapping at substrate/oxide interface.

Using atomistic pseudopotential model with combination of LCBB as an expansion basis, QCSE was theoretically computed without perturbation approaches. Size of the nanocrystal used in computation was determined using the PL peak position of the experimental result. It was demonstrated that Coulomb interaction term has a significant effect on the total Stark shift in Si nanocrystals. Nonmonotonic behavior observed in PL intensity under external field was also estimated by the theory. One of the interesting outcomes of the theory was that, unlike the rigidity of conduction band states most of the system response to the external field comes from the valence band states. Strong size dependence of the polarizability in Si nanocrystals suggested by the computational result was verified by the experimental observations.

In this part of our work, we have reported the first clear observation of QCSE in Si nanocrystals based on PL measurements. We believe that this result is an important contribution to the present understanding of the electronic and optical properties of

Si nanocrystals. The next step would be to implement the predicted applications in the technological fields. The obvious outcome of this work would be the fabrication of electro-optical devices such as optical modulator, which will be revolutionary in the silicon based photonics.

In Chapter 5, we have presented an extensive study on the fabrication, characterization and application of Si nanowire to Si solar cells. We have shown that Si nanowires can be fabricated by MAE which is an easy, cheap and very appropriate technique for industrial applications. We studied the effect of process parameters like etch duration, solution temperature, solution chemistry on the structure of the nanowires formed. The length of the nanowire was shown to be controlled easily with these parameters. However, the diameter of the nanowires was hardly controllable by these parameters. Nanowire decorated surfaces exhibited excellent light trapping properties. The reflection from the surface, especially in the wavelength interval where the solar radiation is most efficient, can be made extremely low by nanowire application.

We then demonstrated the first application of Si nanowires to industrial size (156 mm x 156 mm) crystalline Si solar cells. We showed that nanowire formation process could successfully be integrated to the standard solar cell production line. We concluded that the use of nanowires on large area crystalline solar cells is technically feasible. We have observed an improvement in the solar cell efficiency compared to the solar cells with flat surface. However, the efficiency remained under that of standard solar cell with alkaline textured surface. Both efficiency and the quantum efficiency values dropped with the increasing nanowire length. This is mainly due to the poor charge collection ability along the nanowire. The charge collection efficiency can be improved by surface passivation of the nanowires and possibly by reducing the doping in them. The screen print metallization using standard Ag paste was found to create poor contact to the top of the nanowires due to the low contact area. We concluded that a new metallization scheme, possible with a more suitable Ag paste, needs to be developed to improve the metallization on the nanowire-decorated surfaces.

6.2. Open Issues and Suggestions for Future Works

In this thesis, we have studied ZnO nanocrystals/Si heterojunctions for LED applications. We have observed light emissions resulted from defect states of ZnO nanocrystal, under an electrical excitation. No reliable UV emission from ZnO band edge has been observed. It was shown that, with the presence of oxide buffer layer between ZnO and Si LED the performance of the device was significantly improved both in efficiency and in tolerance to maximum applied voltage levels. Our results suggest that, a good thin pasivation layer is required for ZnO nanocrystal using nondestructive techniques. This result can be further elaborated by studying the effect of thickness of the barrier oxide layer.

Our LED studies on Si nanocrystals revealed that the EL spectrum originated directly from the Si nanocrystals is very broad, which means that Si nanocrystal emission is not useful in photonic applications. However, doping of Si nanocrystal environment with rare earth elements seems feasible for Si based photonics. In this thesis we have studied with Tb for narrow emission, and significant enhancement in light emission was observed under electrical excitation compared to the optical one. Optimization of active light emitting region with respect to the amount of excess Si can lead to an improved efficiency in light emitting characteristics. This will also help us finding optimum bias region for the applications. Furthermore, the matrix material used in the active region can be replaced by a low band gap material like SiC in order the make the electronic transport easier. Besides we also suggest that using well defined Si nanowire arrays could enhance the charge injection in to the active region, thereby either turn-on voltage can be decreased or thickness of the active region can be increased at the same turn-on voltage, which should enhance the amount of light emission. This will be tested in new LED devices soon in our laboratories.

QCSE is an important physical phenomenon for technological applications. We have clearly demonstrated this effect in the Si nanocrystals buried in SiO_2. This observation can be a basis of new studies towards Si based modulator applications. Use of SiO_2 matrix has a big advantage in modulation depth due to the very high energy offsets in both conduction and valence bands of between Si nanocrystals and SiO_2. However, this high band offsets is a significant obstacle for high speed

application. Besides, Si nanocrystals do not have totally direct like optical transitions which are also an important obstacle for high speed applications. However this obstacle can be overcome by plasmonic enhancement in the life time. The difference in the dielectric constant between Si nanocrystal and surrounding oxide is an important issue, this cause to increase in applied voltage as the 66% of total field is screened by Si nanocrystals. As a working modulator, our studied system could be placed in an either mach-zender type or in a bidirectional coupler or it can be placed in a gate region of MOS-FETs which has a superiority of signal amplification as a side effect.

In the last part of this thesis study, we have shown that Si nanowires by MAE method are very suitable for large scale industrial applications. To prove this, we used nanowires as an antireflective layer on the large area Si solar cells. Our results showed that, nanowires could be utilized with further enhancement on the system. However, two problems have to be overcome: first one is that, new passivation approach is needed to reduce aggressive recombination over the nanowire surface. This can be done by oxidizing the nanowire surface in few nanometers before nitrate coating. The other problem that has to be overcome is the screen printed contact formation is not suitable for nanowire textured surfaces. This contact problem could be overcome by buried contact formation using solution based methods.

Our preliminary studies showed that, using nanowires in multicrystalline wafers is more feasible compare to the monocrystalline ones. We are now systematically studying on multicrystalline wafer texturing by Si nanowire formation. However, we believe that, instead of regular nanowires using non-homogenous surface texturing with small aspect ratios could be very useful in light trapping, in this context we developed new approach for surface texturing by changing the properties of solution used in the nanowire. Besides nanowire formation, we applied MAE method to nanohole formation; we have obtained good results from them as an antireflective behavior and we are currently testing them in large area solar cell applications.

REFERENCES

[1] P. Ruch, T. Brunschwiler, W. Escher, S. Paredes, and B. Michel, "Toward five-dimensional scaling : How density improves efficiency in future computers," *IBM Journal of Research and Development*, vol. 55, no. 5, pp. 1-13, 2011.

[2] J. A. Davis, V. K. De, and J. D. Meindl, "A Stochastic Wire-Length Distribution for Gigascale Integration (GSI)— Part I : Derivation and Validation," *IEEE Transactions on Electron Devices*, vol. 45, no. 3, pp. 580-589, 1998.

[3] D. A. B. Miller, "Device Requirements for Optical Interconnects to Silicon Chips," *Proceedings of the IEEE*, vol. 97, no. 7, 2009.

[4] J. D. Meindl, "Interconnect Opportunities for Gigascale İntegration," *IEEE Micro*, pp. 28-35, 2003.

[5] M. E. Groenet, "Monolithic Heteroepitaxial Integration of III-V Semiconductor Lasers on Si Substrates," *Phd. Thesis*, 2002.

[6] Y. Halioua, A. Bazin, P. Monnier, T. J. Karle, G. Roelkens, I. Sagnes, R. Raj, and F. Raineri "Hybrid III-V semiconductor/silicon nanolaser.," *Optics express*, vol. 19, no. 10, pp. 9221-31, May 2011.

[7] S. Balakumar, S. Peng, K. M. Hoe, G. Q. Lo, and R. Kumar, "Fabrication of thick SiGe on insulator (Si[sub 0.2]Ge[sub 0.8]OI) by condensation of SiGe/Si superlattice grown on silicon on insulator," *Applied Physics Letters*, vol. 90, no. 19, p. 192113, 2007.

[8] N. Izhaky, M. T. Moore, S. Koehl, O. Cohen, D. Rubin, A. Barkai, G. Sarid, R. Cohen, and M. J. Panicca, "Development of CMOS-Compatible Integrated Silicon Photonics Devices," *IEEE Journal of Selected Topics in Quantum Electronics*, vol. 12, no. 6, pp. 1688-1698, 2006.

[9] Y. H. Kuo, Y. K. Lee, Y. Ge, S. Ren, J. E. Roth, T. I. Kamins, D. A. B. Miller, J. S. Harris, "Strong quantum-confined Stark effect in germanium quantum-well structures on silicon," *Nature*, vol. 437, pp. 1334-1336, 2005.

[10] C. W. Liu, M. H. Lee, M. j. Chen, C. F. Lin, and M. Y. Chern, "Roughness-Enhanced Electroluminescence from Metal Oxide Silicon Tunneling Diodes," *IEEE Electron Device Letters*, vol. 21, no. 12, pp. 601-603, 2000.

[11] C. W. Liu, M. H. Lee, S. T. Chang, M. J. Chen, and C. F. Lin, "'Room-Temperature Electroluminescence from Metal-Oxide-Silicon-Tunneling Diodes on (110) Substrates'," *Applied Physics*, vol. 39, no. 10, pp. 1016-1018, 2000.

[12] H. Aharoni and M. du Plessis, "Low-Operating-Voltage Integrated Silicon," *IEEE journal of Quantum Electronics*, vol. 40, no. 5, pp. 557-563, 2004.

[13] O. Boyraz and B. Jalali, "Demonstration of a silicon Raman laser," *Optics express*, vol. 12, no. 21, pp. 5269-73, Oct. 2004.

[14] H. Rong et al., "A continuous-wave Raman silicon laser," *Nature*, vol. 433, pp. 725-728, Feb. 2005.

[15] H. K. Han, S. Y. Seo, and J. H. Shin, "Optical gain at 1.54 μm in erbium-doped silicon nanocluster sensitized.pdf," *Applied Physics Letters*, vol. 79, no. 27, p. 5568, 2001.

[16] J. M. Sun, W. Skorupa, T. Dekorsy, M. Helm, L. Rebohle, and T. Gebel, "Efficient ultraviolet electroluminescence from a Gd-implanted silicon metal–oxide–semiconductor device," *Applied Physics Letters*, vol. 85, no. 16, p. 3387, 2004.

[17] Z. Yuan, D. Li, M. Wang, D. Gong, P. Cheng, P. Chen, and D. Yang, "Photoluminescence of Tb3+-doped SiNx films with different Si concentrations," *Materials Science and Engineering: B*, vol. 146, no. 1-3, pp. 126-130, Jan. 2008.

[18] Z. Yuan, A. Anopchenko, N. Daldosso, R. Guider, D. N. Urrios, A. Pitanti, R. Spano, and L. Pavesi,"Silicon Nanocrystals as an Enabling Material for Silicon Photonics," *Proceedings of the IEEE*, vol. 97, no. 7, 2009.

[19] R. J. Walters, "Silicon Nanocrystals for Silicon Photonics", Phd. Thesis, 2007.

[20] L. T. Canham, "Silicon quantum wire array fabrication by electrochemical and chemical dissolution of wafers," *Applied Physics Letters*, vol. 57, no. 10, p. 1046, 1990.

[21] R. J. Zhang, Y. M. Chen, W. J. Lu, Q. Y. Cai, and Y. X. Zheng, "Influence of nanocrystal size on dielectric functions of Si nanocrystals embedded in SiO[sub 2] matrix," *Applied Physics Letters*, vol. 95, no. 16, p. 161109, 2009.

[22] Z. Wan, S. Huang, M. a Green, and G. Conibeer, "Rapid thermal annealing and crystallization mechanisms study of silicon nanocrystal in silicon carbide matrix.," *Nanoscale research letters*, vol. 6, no. 1, p. 129, Jan. 2011.

[23] P. Basa, P. Petrik, M. Fried, L. Dobos, B. Pecz, and L. Toth, “Si nanocrystals in silicon nitride: An ellipsometric study using parametric semiconductor models,” *Physica E: Low-dimensional Systems and Nanostructures*, vol. 38, no. 1-2, pp. 76-79, Apr. 2007.

[24] S. Yerci, I. Yildiz, M. Kulakci, U. Serincan, M. Barozzi, M. Bersani, and R. Turan, “Depth profile investigations of silicon nanocrystals formed in sapphire by ion implantation,” *Journal of Applied Physics*, vol. 102, no. 2, p. 024309, 2007.

[25] M. Yedji, J. Demarche, G. Terwagne, R. Delemare, D. Flandre, D. Barba, D. Koshel, and G. G. Ross, “Method for fabricating third generation photovoltaic cells based on Si quantum dots using ion implantation into SiO2,” *Journal of Applied Physics*, vol. 109, no. 8, p. 084337, 2011.

[26] G. Zatryb, a Podhorodecki, X. J. Hao, J. Misiewicz, Y. S. Shen, and M. a Green, “Correlation between stress and carrier nonradiative recombination for silicon nanocrystals in an oxide matrix.,” *Nanotechnology*, vol. 22, no. 33, p. 335703, Aug. 2011.

[27] C. Y. Hsiao, C. F. Shih, S. H. Chen, and W. T. Jiang, “Comparison of silicon nanocrystals embedded silicon oxide films by sputtering and PECVD,” *Thin Solid Films*, vol. 519, no. 15, pp. 5086-5089, May 2011.

[28] N. Saxena, A. Agarwal, D. M. Phase, R. Janey Choudhary, and D. Kanjilal, “Controlled formation of silicon nanocrystals by dense electronic excitation in PLD grown SiOX films,” *Physica E: Low-dimensional Systems and Nanostructures*, vol. 42, no. 9, pp. 2190-2196, Jul. 2010.

[29] Q. Wan, T. H. Wang, M. Zhu, and C. L. Lin, “Resonant tunneling of Si nanocrystals embedded in Al[sub 2]O[sub 3] matrix synthesized by vacuum electron-beam co-evaporation,” *Applied Physics Letters*, vol. 81, no. 3, p. 538, 2002.

[30] J. S. Biteen, D. Pacifici, N. S. Lewis, and H. A. Atwater, “Enhanced radiative emission rate and quantum efficiency in coupled silicon nanocrystal-nanostructured gold emitters,” *Nano letters*, vol. 5, no. 9, pp. 1768-73, Sep. 2005.

[31] L. Pavesi, L. Dal Negro, C. Mazzoleni, G. Franzò, and F. Priolo, “Optical gain in silicon nanocrystals.,” *Nature*, vol. 408, no. 6811, pp. 440-4, Nov. 2000.

[32] B. M. Monroy, O. Crégut, M. Gallart, B. Hönerlage, and P. Gilliot, “Optical gain observation on silicon nanocrystals embedded in silicon nitride under femtosecond pumping,” *Applied Physics Letters*, vol. 98, no. 26, p. 261108, 2011.

[33] T. Creazzo, B. Redding, E. Marchena, J. Murakowski, and D. W. Prather, “Pulsed pumping of silicon nanocrystal light emitting devices.,” *Optics express*, vol. 18, no. 11, pp. 10924-30, May 2010.

[34] M. Kulakci, U. Serincan, and R. Turan, “Electroluminescence generated by a metal oxide semiconductor light emitting diode (MOS-LED) with Si nanocrystals embedded in SiO 2 layers by ion implantation,” *Semiconductor Science and Technology*, vol. 21, no. 12, pp. 1527-1532, Dec. 2006.

[35] R. J. Walters, J. Carreras, T. Feng, L. D. Bell, and H. A. Atwater, “Silicon Nanocrystal Field-Effect Light-Emitting Devices,” *IEEE Journal of Selected Topics in Qunatum Electronics*, vol. 12, no. 6, pp. 1647-1656, 2006.

[36] V. Beyer, B. Schmidt, K.-H. Heinig, and K.-H. Stegemann, “Light emitting field effect transistor with two self-aligned Si nanocrystal layers,” *Applied Physics Letters*, vol. 95, no. 19, p. 193501, 2009.

[37] J. Carreras, C. Bonafos, J. Montserrat, C. Domínguez, J. Arbiol, and B. Garrido, “Auger quenching-based modulation of electroluminescence from ion-implanted silicon nanocrystals.,” *Nanotechnology*, vol. 19, no. 20, p. 205201, May 2008.

[38] R. J. Walters, P. G. Kik, J. D. Casperson, H. A. Atwater, R. Lindstedt, M. Giorgi, and G. Bourianoff, “Silicon optical nanocrystal memory,” *Applied Physics Letters*, vol. 85, no. 13, p. 2622, 2004.

[39] K. Imakita, M. Ito, M. Fujii, and S. Hayashi, “Nonlinear optical properties of Si nanocrystals embedded in SiO[sub 2] prepared by a cosputtering method,” *Journal of Applied Physics*, vol. 105, no. 9, p. 093531, 2009.

[40] S. A. Fischer, A. B. Madrid, C. M. Isborn, and O. V. Prezhdo, “Multiple Exciton Generation in Small Si Clusters: A High-Level, Ab Initio Study,” *The Journal of Physical Chemistry Letters*, vol. 1, no. 1, pp. 232-237, Jan. 2010.

[41] M. Kulakci, U. Serincan, R. Turan, and T. G. Finstad, “The quantum confined Stark effect in silicon nanocrystals.,” *Nanotechnology*, vol. 19, no. 45, p. 455403, Nov. 2008.

[42] C. Bulutay, M. Kulakci, and R. Turan, “Stark effect , polarizability , and electroabsorption in silicon nanocrystals,” *Physical Review B*, vol. 81, p. 125333, 2010.

[43] K. Q. Peng, Y. J. Yan, S. P. Gao, and J. Zhu, “Synthesis of Large-Area Silicon Nanowire Arrays,” *Advanced Materials*, vol. 14, no. 16, p. 1164, 2002.

[44] U. Özgür, Y. I. Alivov, C. Liu, A. Teke, M. A. Reshchikov, S. Dogan, V. Avrutin, S. J. Cho, and H. Morkoc, “A comprehensive review of ZnO materials and devices,” *Journal of Applied Physics*, vol. 98, no. 4, p. 041301, 2005.

[45] D. Vanmaekelbergh and L. K. van Vugt, “ZnO nanowire lasers.,” *Nanoscale*, vol. 3, no. 7, pp. 2783-800, Jun. 2011.

[46] C. W. Litton, D. C. Reynolds, and T. C. Collins, Eds., *Zinc Oxide Materials for Electronic and Optoelectronic Device Applications*. Chichester, UK: John Wiley & Sons, Ltd, 2011.

[47] B. V. Avrutin, D. J. Silversmith, and H. Morkoc, “in ZnO : Current Status and Outlook,” *Proceedings of the IEEE*, vol. 98, no. 7, pp. 1269-1280, 2010.

[48] U. Rössler, “Energy Bands of Hexagonal II-VI Semiconductors,” *Physical Review*, vol. 184, no. 3, p. 733, 1969.

[49] S. P. Chennupati Jagadish, *Zinc Oxide Bulk, Thin Films and Nanostructures: Processing Properties and Applications*. Elsevier, 2006.

[50] M. E. Burnett and S. Q. Wang, “Current sunscreen controversies: a critical review.,” *Photodermatology, photoimmunology & photomedicine*, vol. 27, no. 2, pp. 58-67, Apr. 2011.

[51] N. H. Nickel and E. Terukov, Eds., *Zinc Oxide- A material for Micro- and Optoelctronic Applications*. Dortrecht Netharlands: Springer, 2005.

[52] P. A. Rodnyi and I. V. Khodyuk, “Optical and luminescence properties of zinc oxide (Review),” *Optics and Spectroscopy*, vol. 111, no. 5, pp. 776-785, Dec. 2011.

[53] Y. Yoshino, “Piezoelectric thin films and their applications for electronics,” *Journal of Applied Physics*, vol. 105, no. 6, p. 061623, 2009.

[54] A. Klein, A. C. Korber, A. Wachaw, F. Sauberlich, Y. Gessenbaur, S. P. Harvey, D. E. Proffit, and T. O. Mason, “Transparent Conducting Oxides for Photovoltaics: Manipulation of Fermi Level, Work Function and Energy Band Alignment,” *Materials*, vol. 3, no. 11, pp. 4892-4914, Nov. 2010.

[55] H. Frenzel, A. Lajn, H. V. Wenckster, M. Lorenz, F. Schein, Z. Zang, and M. Grundmann, “Recent progress on ZnO-based metal-semiconductor field-effect transistors and their application in transparent integrated circuits.,” *Advanced materials*, vol. 22, no. 47, pp. 5332-49, Dec. 2010.

[56] A. Menzel, K. Subannajui, F. Güder, D. Moser, O. Paul, and M. Zacharias, “Multifunctional ZnO-Nanowire-Based Sensor,” *Advanced Functional Materials*, p. n/a-n/a, Oct. 2011.

[57] Z. Dai, A. Nurbawono, A. Zhang, M. Zhou, Y. P. Feng, G. W. Ho, and C. Zhang, “C-doped ZnO nanowires: electronic structures, magnetic properties, and a possible spintronic device.,” *The Journal of chemical physics*, vol. 134, no. 10, p. 104706, Mar. 2011.

[58] M. Ahmad and J. Zhu, “ZnO based advanced functional nanostructures: synthesis, properties and applications,” *Journal of Materials Chemistry*, vol. 21, no. 3, p. 599, 2011.

[59] I. Drapak,“Visible Luminescence of a ZnO-Cu2O Hetero junction,” *Semiconductors*, vol. 2, p. 624, 1968.

[60] L. V. K. and P. G. P. A. E. Tsurkan, N.D. Fedotova, “Injection Electroluminescence Emitted by n-ZnO-p-ZnTe Heterojuntions,” *Semiconductors and Semimetals*, vol. 6, p. 1183, Apr. 1975.

[61] H. Ohta, K.-ichi Kawamura, M. Orita, M. Hirano, N. Sarukura, and H. Hosono, “Current injection emission from a transparent p–n junction composed of p-SrCu[sub 2]O[sub 2]/n-ZnO,” *Applied Physics Letters*, vol. 77, no. 4, p. 475, 2000.

[62] Y. I. Alivov, J. E. Van Nostrand, D. C. Look, M. V. Chukichev, and B. M. Ataev, “Observation of 430 nm electroluminescence from ZnO/GaN heterojunction light-emitting diodes,” *Applied Physics Letters*, vol. 83, no. 14, p. 2943, 2003.

[63] Q.X. Yu, B. Xu, Q. H. Wu, Y. Liao, G. Z. Wang, R. C. Fang, H. Y. Lee, and C. T. Lee, “Optical properties of ZnO/GaN heterostructure and its near-ultraviolet light-emitting diode,” *Applied Physics Letters*, vol. 83, no. 23, p. 4713, 2003.

[64] H. Long, G. Fang, H. Huang, X. Mo, W. Xia, B. Dong, X. Meng, and X. zhao, “Ultraviolet electroluminescence from ZnO/NiO-based heterojunction light-emitting diodes,” *Applied Physics Letters*, vol. 95, no. 1, p. 013509, 2009.

[65] Y. T. Shih, M. K. Wu, M. J. Chen, Y. C. Cheng, J. R. Yang, and M. Shiojiri, “ZnO-based heterojunction light-emitting diodes on p-SiC(4H) grown by atomic layer deposition,” *Applied Physics B*, vol. 98, no. 4, pp. 767-772, Nov. 2009.

[66] Y. I. Alivov, E. V. Kalinina, A. E. Cherenkov, D. C. Look, B. M. Ataev, A. K. Omaev, M. V. Chukichev, and D. M. Bagnal, “Fabrication and characterization of n-ZnO/p-AlGaN heterojunction light-emitting diodes on 6H-SiC substrates,” *Applied Physics Letters*, vol. 83, no. 23, p. 4719, 2003.

[67] P. Chen, X. Ma, and D. Yang, “Fairly pure ultraviolet electroluminescence from p-Si-based SiOx/ZnO/SiOx double-barrier device,” *Optics Communications*, vol. 283, no. 7, pp. 1359-1362, Apr. 2010.

[68] S. T. Tan, J. Zhao, S. Iwan, X. W. Sun, X. Tang, J. Ye, M. Bosman, L. Tang, G. Q. Lo, and K. L. Teo "n-ZnO/n-GaAs Heterostructured White Light-Emitting Diode : Nanoscale Interface Analysis and Electroluminescence Studies," *IEEE Transactions on Electron Devices*, vol. 57, no. 1, pp. 129-133, 2010.

[69] Z. Shi, L. Zhao, X. Xia, W. Zhao, H. Wang, J. wang, X. Dong, B. Zhang, and G. Du, "Effect of MgZnO barrier layer on the UV emission of n-ZnO/p-Si heterojunction diodes," *Journal of Luminescence*, vol. 131, no. 8, pp. 1645-1648, Aug. 2011.

[70] Z. Yang, S. Chu, W. V. Chen, L. Li, J. Kong, J. Ren, P. K. L. Yu, and J. Liu, "ZnO:Sb/ZnO:Ga Light Emitting Diode on c -Plane Sapphire by Molecular Beam Epitaxy," *Applied Physics Express*, vol. 3, no. 3, p. 032101, Mar. 2010.

[71] C.-T. Lee, Y.-H. Lin, L.-W. Lai, and L.-R. Lou, "Mechanism Investigation of p-i-n ZnO-Based Light-Emitting Diodes," *IEEE Photonics Technology Letters*, vol. 22, no. 1, pp. 30-32, Jan. 2010.

[72] X. Fang, J. Li, D. Zhao, D. Shen, B. Li, and X. Wang, "Phosphorus-Doped p-Type ZnO Nanorods and ZnO Nanorod p−n Homojunction LED Fabricated by Hydrothermal Method," *The Journal of Physical Chemistry C*, vol. 113, no. 50, pp. 21208-21212, Dec. 2009.

[73] M.T. Chen, M. P. Lu, Y. J. Wu, J. Song, C. Y. Lee, M. Y. Lu, Y. C. Chang,, L. J. Chou, Z. L. Wang, and L. J. Chen, "Near UV LEDs made with in situ doped p-n homojunction ZnO nanowire arrays.," *Nano letters*, vol. 10, no. 11, pp. 4387-93, Nov. 2010.

[74] O. Lupan, T. Pauporté, and B. Viana, "Low-voltage UV-electroluminescence from ZnO-nanowire Array/p-GaN light-emitting diodes.," *Advanced materials*, vol. 22, no. 30, pp. 3298-302, Aug. 2010.

[75] Y. Chen, H. Shih, C. Wang, C. Hsieh, C. Chen, Y. Chen, and T. Lin, "Ultraviolet electroluminescence from hybrid inorganic/organic ZnO/GaN/poly(3-hexylthiophene) dual heterojunctions.," *Optics express*, vol. 19 Suppl 3, no. May, pp. A319-25, May 2011.

[76] J. Liu, Y. H. Ahn, J.-Y. Park, K. H. Koh, and S. Lee, "Hybrid light-emitting diodes based on flexible sheets of mass-produced ZnO nanowires.," *Nanotechnology*, vol. 20, no. 44, p. 445203, Nov. 2009.

[77] M. a. Zimmler, T. Voss, C. Ronning, and F. Capasso, "Exciton-related electroluminescence from ZnO nanowire light-emitting diodes," *Applied Physics Letters*, vol. 94, no. 24, p. 241120, 2009.

[78] S. W. Lee, H. D. Cho, G. Panin, and T. Won Kang, "Vertical ZnO nanorod/Si contact light-emitting diode," *Applied Physics Letters*, vol. 98, no. 9, p. 093110, 2011.

[79] B. Ling, J. L. Zhao, X. W. Sun, S. T. Tan, Y. Yang, and Z. L. Dong, "Electroluminescence From Ferromagnetic Fe-Doped ZnO Nanorod Arrays on p-Si," *IEEE Transactions on Electron Devices*, vol. 57, no. 8, pp. 1948-1952, 2010.

[80] R. S. Wagner and W. C. Ellis, "Vapor-Liquid-Solid Mechanism of Single Crystal Growth," *Applied Physics Letters*, vol. 4, no. 5, p. 89, 1964.

[81] M. Willander, Q. Zhao, and O. Nur, "Zinc oxide nanostructures at the forefront of new white light- emitting technology," *SPIE: Newsroom*, pp. 1-3, 2007.

[82] G. R. Lin, "Improved blue-green electroluminescence of metal-oxide-semiconductor diode fabricated on multirecipe Si-implanted and annealed SiO[sub 2]/Si substrate," *Journal of Applied Physics*, vol. 95, no. 12, p. 8484, 2004.

[83] N. Akil, S. E. Kerns, D. V. Kerns, A. Hoffmann, and J.-pierre Charles, "A Multimechanism Model for Photon Generation by Silicon Junctions in Avalanche Breakdown," *IEEE Transactions on Electron Devices*, vol. 46, no. 5, pp. 1022-1028, 1999.

[84] S. Chang, K. Chen, C. Shie, C. Liu, M. Chen, and C. Lin, "The band-edge light emission from the metal-oxide-silicon tunneling diode on (110) substrates," *Solid-State Electronics*, vol. 46, no. 8, pp. 1113-1116, Aug. 2002.

[85] N. Bano, I. Hussain, O. Nur, M. Willander, P. Klason, and a Henry, "Study of luminescent centers in ZnO nanorods catalytically grown on 4H-p-SiC," *Semiconductor Science and Technology*, vol. 24, no. 12, p. 125015, Dec. 2009.

[86] N. H. Alvi, K. Ul Hasan, O. Nur, and M. Willander, "The origin of the red emission in n-ZnO nanotubes/p-GaN white light emitting diodes.," *Nanoscale Research Letters*, vol. 6, no. 1, p. 130, Jan. 2011.

[87] J. G. Zhu, C. W. White, J. D. Budai, S. P. Withrow, and Y. C. Chen, "Growth of Ge, Si and SiGe nanocrystal in SiO2 matrices," *Journal of Applied Physics*, vol. 78, no. 7, p. 4386, 1995.

[88] Y. Kanemitsu, T. Ogawa, K. Shiraishi, and K. Takeda, "Visible oxidized Exciton a," *Physical Review B*, vol. 48, no. 7, p. 4883, 1993.

[89] L. Pavesi and R. Turan, Eds., *Silicon Nanocrystals*. Weinheim, Germany: Wiley-VCH Verlag GmbH & Co. KGaA, 2010.

[90] M. Lopez, B. Garrido, C. Bonafos, A. P. Rodriguez, and J. R. Morate, “Optical and structural characterization of Si nanocrystals ion beam synthesized in SiO 2 : correlation between the surface passivation and the photoluminescence emission,” *Solid-State Electronics*, vol. 45, pp. 1495-1504, 2001.

[91] M. L. Brongersma, A. Polman, K. S. Min, and H. A. Atwater, “Depth distribution of luminescent Si nanocrystals in Si implanted SiO2 films on Si,” *Journal of Applied Physics*, vol. 86, no. 2, p. 759, 1999.

[92] J. Y. Zhang, X. M. Bao, and Y. H. Ye, “Synthesis of Ge nanocrystals in thermal SiO 2 films by Ge q ion implantation,” *Thin Solid Films*, vol. 323, pp. 68-71, 1998.

[93] H. Karl, W. Hipp, I. Großhans, and B. Stritzker, “Ion beam synthesis of buried CdSe nanocrystallites in SiO 2 on (100) -silicon,” *Materials Science and Engineering C*, vol. 19, pp. 55-58, 2002.

[94] U. V. Desnica, O. Gamulin, A. Tonejc, M. Iwanda, C. W. White, E. Sonder, and R. A. Zhur, “CdS nanocrystals formed in SiO2 substrates by ion implantation,” *Materials Science and Engineering C*, vol. 15, pp. 105-107, 2001.

[95] L. Hobbs, X. Yuan, and G. Pacchioni, *Defects in SiO2 and Related Dielectrics: Science and Technology*, vol. 516, no. 8. Kluwer Academic Publisher, 2000.

[96] L. W. Hobbs, C. E. Jesurum, V. Pulim, and B. Berger, “Local topology of silica networks,” *Philosophical Magazine A*, vol. 78, no. 2012, pp. 679-711, 1998.

[97] T. Bakos, *Defetcs in Amorphous SiO2*, no. June. Phd. Thesis Work, 2003.

[98] A. N. Trukhin, J. Jansons, H. J. Fitting, T. Barfels, and B. Schmidt, “Cathodoluminescence decay kinetics in Ge, Si, O implanted SiO2 layers,” *Journal of Non-Crystalline Solids*, vol. 331, pp. 91-99, 2003.

[99] Y. Sakurai and K. Nagasawa, “Correlation between the green photoluminescence band and the peroxy radical in γ-irradiated silica glass,” *Journal of Applied Physics*, vol. 88, no. 1, p. 168, 2000.

[100] S. T. Pantelides, “Defects in Amourphous Silicon: A New Perspective,” *Physical Review Letters*, vol. 57, no. 23, p. 2979, 1986.

[101] L. Skuja, “Optically active oxygen-de deficiency-related centers in amorphous silicon dioxide,” *Journal of Non-Crystalline Solids*, vol. 239, pp. 16-48, 1998.

[102] C. Barthou, P. H. Duong, A. Oliver, J. C. C. Wong, L. R. Fernandez, A. C. Sosa, T. Itoh, and P. Lavallard, "Silicon nanocrystals and defects produced by silicon and silicon-and-gold implantation in silica," *Journal of Applied Physics*, vol. 93, no. 12, p. 10110, 2003.

[103] S. M. Prokes and O. Glembocki, "Role of interfacial oxide-related defects in the red-light emission in porous silicon," *Physical Review B*, vol. 49, no. 3, pp. 2238-2241, 1994.

[104] I. M. Lifshitz and V. V. Slyozov, "The kinetics of precipitation from super saturated solid solutions," *Journal of Physics and Chemistry of Solids*, vol. 19, no. 1-2, pp. 35-50, Feb. 1961.

[105] A. F. Le, L. N. Safronov, and G. A. Kachurin, "Modeling Si nanoprecipitate formation in SiO 2 layers with excess Si atoms," *Semiconductors*, vol. 33, no. 4, 1999.

[106] T. Müller, K.-H. Heinig, and W. Möller, "Size and location control of Si nanocrystals at ion beam synthesis in thin SiO[sub 2] films," *Applied Physics Letters*, vol. 81, no. 16, p. 3049, 2002.

[107] G. A. Kachurin, K. S. Zhuraulev, N. A. Pazdnikov, A. F. Leier, I. E. Tyschenko, V. A. Volodin, W. Skorupa, and R. A. Yankov, "Annealing effects in light-emitting Si nanostructures formed in SiO2 , by ion implantation and transient preheating," *Nuclear Instruments and Methods in Physics Research Section B: Beam Interactions with Materials and Atoms*, vol. 127/128, pp. 583-586, 1997.

[108] P. Mutti, G. Ghislotti, S. Bertoni, L. benoldi, G. F. Cerefolini, L. Meda, E. Grilli, and M. Guzzi, "Room Temperature Visible Luminescence From Silicon Nanocrystals in Silicon Implanted SiO2 Layers," *Applied Physics Letters*, vol. 66, no. 7, pp. 851-853, 1995.

[109] Y. Kanemitsu and S. Okamoto, "Phonon structures and Stokes shift in resonantly excited luminescence of silicon nanocrystals," *Physical Review B*, vol. 58, no. 15, pp. 9652-9655, 1998.

[110] D. Kovalev, H. Heckler, G. Polisski, and F. Koch, "Optical Properties of Si Nanocrystals," *Physica Status Solidi (B)*, vol. 215, no. 2, pp. 871-932, Oct. 1999.

[111] M. S. Hybertsen, "Absorption and Emission of Light in Nanoscale Silicon Structures," *Physical Review Letters*, vol. 72, no. 10, pp. 1514-1517, 1994.

[112] C. Garcia, B. Garrido, P. Pellegrino, R. Ferre, J. A. Moreno, and L. Pavesi, "Absorption cross-sections and lifetimes as a function of size in Si nanocrystals embedded in SiO 2," *Physica E*, vol. 16, pp. 429-433, 2003.

[113] D. Kovalev, H. Heckler, M. Ben-Chorin, G. Polisski, M. Schwartzkopff, and F. Koch, "Breakdown of the k-Conservation Rule in Si Nanocrystals," *Physical Review Letters*, vol. 81, no. 13, pp. 2803-2806, Sep. 1998.

[114] R. J. Needs, S. Bhattacharje, K. N. Nash, A. Oteish, A. J. Read, and L. T. Canham, "First-principle calculations of band-edge electronic states of silicon quantum wire," *Physical Review*, vol. 50, no. 19, p. 2803, 1994.

[115] T. Y. Kim, N. M. Park, K. H. Kim, G. Y. Sung, Y. W. Ok, T. Y. Seong, and C. J. Choi, "Quantum confinement effect of silicon nanocrystals in situ grown in silicon nitride films," *Applied Physics Letters*, vol. 85, no. 22, p. 5355, 2004.

[116] C. Bulutay, "Interband, intraband, and excited-state direct photon absorption of silicon and germanium nanocrystals embedded in a wide band-gap lattice," *Physical Review B*, vol. 76, p. 205321, Nov. 2007.

[117] T. Arguirov, T. Mchedlidze, M. Kittler, M. Reiche, T. Wilhelm, T. Hoang, J. Holleman, and J. Schmitz, "Silicon based light emitters utilizing radiation from dislocations; electric field induced shift of the dislocation-related luminescence," *Physica E: Low-dimensional Systems and Nanostructures*, vol. 41, no. 6, pp. 907-911, May 2009.

[118] S. Saito, T. Takahama, K. Tani, M. Takahashi, T. Mine, Y. Suwa, and D. Hisamoto, "Stimulated emission of near-infrared radiation in silicon fin light-emitting diode," *Applied Physics Letters*, vol. 98, no. 26, p. 261104, 2011.

[119] B. H. Lai, C. H. Cheng, and G. R. Lin, "Multicolor ITO / SiO x / p-Si / Al Light Emitting Diodes with Improved Emission Efficiency by Small Si Quantum Dots," *IEEE journal of Quantum Electronics*, vol. 47, no. 5, pp. 698-704, 2011.

[120] A. A. Shklyaev, F. N. Dultsev, K. P. Mogilnikov, A. V. Latyshev, and M. Ichikawa, "Electroluminescence of dislocation-rich Si layers grown using oxidized Si surfaces," *Journal of Physics D: Applied Physics*, vol. 44, no. 2, p. 025402, Jan. 2011.

[121] Z. Liu, J. Huang, P. C. Joshi, A. T. Voutsas, and J. Hartzell, "Polarity-controlled visible/infrared electroluminescence in Si-nanocrystal/Si light-emitting devices," *Applied Physics Letters*, vol. 97, no. 7, p. 071112, 2010.

[122] J. Potfajova, B. Schmidt, H. Helm, T. Gemming, M. Benyoucef, A. Rastelli, and O. G. Schmidt, "Microcavity enhanced silicon light emitting pn-diode," *Applied Physics Letters*, vol. 96, no. 15, p. 151113, 2010.

[123] T. Hong, T. Chen, G. Z. Ran, J. Wen, Y. Z. Li, T. Dai, and G. G. Qin, "Enhanced electroluminescence from nanoscale silicon p+ -n junctions made with an anodic aluminum oxide pattern.," *Nanotechnology*, vol. 21, no. 2, p. 025301, Jan. 2010.

[124] M. Suzuno, T. Koizumi, and T. Suemasu, "p-Si/β-FeSi2/n-Si double-heterostructure light-emitting diodes achieving 1.6 micro meter electroluminescence of 0.4 mW at room temperature," *Applied Physics Letters*, vol. 94, p. 213509, 2009.

[125] C. M. Sun, H. K. Tsang, S. P. Wong, W. Y. Cheung, N. Ke, M. Lourenco, and K. P. Homewood, "Electroluminescence from metal–oxide–silicon tunneling diode with ion-beam-synthesized β-FeSi2 precipitates embedded in the active region," *Nuclear Instruments and Methods in Physics Research Section B: Beam Interactions with Materials and Atoms*, vol. 267, no. 7, pp. 1081-1084, Apr. 2009.

[126] A. G. Macedo, A. E. de Vasconcelos, R. Valaski, F. Muchenski, E. F. da Silva Jr., A. F. da Silva, and L. S. Roman, "Enhanced lifetime in porous silicon light-emitting diodes with fluorine doped tin oxide electrodes," *Thin Solid Films*, vol. 517, no. 2, pp. 870-873, Nov. 2008.

[127] S. Adachi and T. Kubota, "Electroluminescence from porous silicon formed by photoetching in an HF/I2 solution," *Journal of Porous Materials*, vol. 15, no. 4, pp. 427-431, May 2008.

[128] F. Iacona, A. Irrera, G. Franzo, D. Pacifici, I. Crupi, M. Mritello, C. D. Presti, and F. Priolo, "Silicon-Based Light-Emitting Devices : Properties and Applications of Crystalline , Amorphous and Er-Doped nanoclusters," *IEEE Journal of Selected Topics in Quantum Electronics*, vol. 12, no. 6, pp. 1596-1606, 2006.

[129] J. Carreras, C. Bonafos, J. Montserrat, C. Domínguez, J. Arbiol, and B. Garrido, "Auger quenching-based modulation of electroluminescence from ion-implanted silicon nanocrystals.," *Nanotechnology*, vol. 19, no. 20, p. 205201, May 2008.

[130] G. Franzò, A. Irrera, E. C. Moreira, M. Mritello, F. Iacona, D. Sanfilippo, G. D. Stefano, P. G. Fallica, and F. Priolo, "Invited paper Electroluminescence of silicon nanocrystals in MOS structures," *Applied Physics A: Materials Science and Processing*, vol. 74, pp. 1-5, 2002.

[131] Y. Liu, L. Ding, M. Yang, J. I. Wong, C. Y. Ng, S. F. Yu, Z. X. Li, C. Yen, F. R. Zhu, M. C. Tan, and S. Fung, "Influence of charge trapping on electroluminescence from Si-nanocrystal light emitting structure," *Journal of Applied Physics*, vol. 101, no. 10, p. 104306, 2007.

[132] J. M. Sun, W. Skorupa, T. Dekorsy, M. Helm, L. Rebohle, and T. Gebel, "Efficient ultraviolet electroluminescence from a Gd-implanted silicon metal–oxide–semiconductor device," *Applied Physics Letters*, vol. 85, no. 16, p. 3387, 2004.

[133] R. J. Walters, J. Carreras, T. Feng, L. D. Bell, and H. A. Atwater, "Silicon Nanocrystal Field-Effect Light-Emitting Devices," *IEEE Journal of Selected Topics in Quantum Electronics*, vol. 12, no. 6, pp. 1647-1656, 2006.

[134] N. Yang, W. K. Henson, J. R. Hauser, J. J. Wortman, and S. Member, "Modeling Study of Ultrathin Gate Oxides Using Direct Tunneling Current and Capacitance – Voltage Measurements in MOS Devices," *IEEE Transactions on Electron Devices*, vol. 46, no. 7, pp. 1464-1471, 1999.

[135] P. Olivo, J. Sune, and B. Ricco, "Determination of the Si- SiO , Barrier Height from the Fowler -Nordheim Plot," *IEEE Electron Device Letters*, vol. 12, no. 11, p. 620, 1991.

[136] G. Liu and B. Jacquier, Eds., *Spectroscopic Properties of Rare Earths in Optical materials*. Springer, 2004.

[137] A. R. Zanatta, A. Khan, and M. E. Kordesch, "Red–green–blue light emission and energy transfer processes in amorphous SiN films doped with Sm and Tb," *Journal of Physics: Condensed Matter*, vol. 19, no. 43, p. 436230, Oct. 2007.

[138] M. J. F. Digonnet, Ed., *Rare-Earth-Doped Fiber Lasers and Amplifiers*, Second ed. Newyork- Basel: Marcel Dekker, Inc., 2001.

[139] J. Palm, F. Gan, B. Zheng, J. Michel, and L. Kimerling, "Electroluminescence of erbium-doped silicon.," *Physical review. B, Condensed matter*, vol. 54, no. 24, pp. 17603-17615, Dec. 1996.

[140] Y. Hori, T. Andreev, D. Jalabert, E. Monroy, L. S. Dang, B. Daudin, M. Tanaka, and O. Oda, "GaN quantum dots doped with Tb," *Applied Physics Letters*, vol. 88, no. 5, p. 053102, 2006.

[141] K. S. Sohn, Y. Y. Choi, K. H. Kim, S. Y. Choi, and H. D. Park, "Effect of inter-ionic interaction on photoluminescence property of yttrium aluminate garnet phosphors," *Journal of Materials Science: Materials in Electronics*, vol. 12, pp. 179-186, 2001.

[142] C. J. Liang, W. C. H. Choy, and C. Huang, "The Electroluminescent Decay Mechanism of Rare-Earth Ions in OLEDs Based on a Terbium Complex," *IEEE Photonics Technology Letters*, vol. 19, no. 15, pp. 1178-1180, Aug. 2007.

[143] F. Ze-Bo, T. Y. Sheng, L. X. Qin, Y. Y. Hu, and W. Y. Yue, "Preparation of transparent conductive ZnO:Tb films and their photoluminescence properties," *Chinese physics*, vol. 13, no. 8, pp. 1330-1334, 2004.

[144] O. Ntwaeaborwa, H. Swart, R. Kroon, P. Holloway, and J. Botha, "Enhanced luminescence and degradation of SiO2:Ce,Tb powder phosphors prepared by a sol–gel process," *Journal of Physics and Chemistry of Solids*, vol. 67, no. 8, pp. 1749-1753, Aug. 2006.

[145] A. J. Kenyon, "Recent developments in rare-earth doped materials for optoelectronics," *Progress in Quantum Electronics*, vol. 26, no. 4-5, pp. 225-284, 2002.

[146] J. M. Sun, S. Prucnal, W. Skorupa, T. Dekorsy, A. Muchlich, M. Helm, L. Rebohle, and T. Gebel, "Electroluminescence properties of the Gd[sup 3+] ultraviolet luminescent centers in SiO[sub 2] gate oxide layers," *Journal of Applied Physics*, vol. 99, no. 10, p. 103102, 2006.

[147] S. Yerci, R. Li, and L. Dal Negro, "Electroluminescence from Er-doped Si-rich silicon nitride light emitting diodes," *Applied Physics Letters*, vol. 97, no. 8, p. 081109, 2010.

[148] M. Fujii, S. Hayashi, and K. Yamamoto, "Excitation of intra-4 f shell luminescence of rare earth ions (Er 3 + and Yb 3 +) by the energy transfer from Si nanocrystals," *journal of Nanoparticle Research*, vol. 1, pp. 83-90, 1999.

[149] D. Pacifici, G. Franzò, F. Priolo, F. Iacona, and L. Dal Negro, "Modeling and perspectives of the Si nanocrystals–Er interaction for optical amplification," *Physical Review B*, vol. 67, no. 24, pp. 1-13, Jun. 2003.

[150] H. Rinnert, G. W. Adeola, and M. Vergnat, "Influence of the silicon nanocrystal size on the 1.54 μm luminescence of Er-doped SiO/SiO[sub 2] multilayers," *Journal of Applied Physics*, vol. 105, no. 3, p. 036101, 2009.

[151] A. Irrera, F. Iacona, G. Franzo, M. Miritello, R. L. Savio, M. E. Castagna, S. Coffa, and F. Priolo, "Influence of the matrix properties on the performances of Er-doped Si nanoclusters light emitting devices," *Journal of Applied Physics*, vol. 107, no. 5, p. 054302, 2010.

[152] S. Prucnal, J. M. Sun, L. Rebohle, and W. Skorupa, "Energy transfer from Gd to Er atoms in SiO2(GdEr)-MOSLEDs produced by ion implantation," *Materials Science and Engineering: B*, vol. 146, no. 1-3, pp. 241-244, Jan. 2008.

[153] S. Wang, H. Amekura, a Eckau, R. Carius, and C. Buchal, "Luminescence from Er and Tb implanted into MOS tunnel diodes," *Nuclear Instruments and Methods in Physics Research Section B: Beam Interactions with Materials and Atoms*, vol. 148, no. 1-4, pp. 481-485, Jan. 1999.

[154] S. Prucnal, J. M. Sun, W. Skorupa, and M. Helm, "Switchable two-color electroluminescence based on a Si metal-oxide-semiconductor structure doped with Eu," *Applied Physics Letters*, vol. 90, no. 18, p. 181121, 2007.

[155] A. Irrera, M. Mritello, D. Pacifici, G. Franzo, F. Priolo, F. Iacona, D. Sanfilippo, G. D. Stefano, and P. G. Fallica, "Electroluminescence properties of SiOx layers implanted with rare earth ions," *Nuclear Instruments and Methods in Physics Research Section B: Beam Interactions with Materials and Atoms*, vol. 216, pp. 222-227, Feb. 2004.

[156] J. M. Sun, W. Skorupa, T. Dekorsy, M. Helm, L. Rebohle, and T. Gebel, "Bright green electroluminescence from Tb[sup 3+] in silicon metal-oxide-semiconductor devices," *Journal of Applied Physics*, vol. 97, no. 12, p. 123513, 2005.

[157] S. Edition, *Phosphor Handbook*, Second edi. Boca Raton: CRC Press, Taylor and Francis Group, 2007.

[158] U. Serincan, G. Aygun, and R. Turan, "Spatial distribution of light-emitting centers in Si-implanted SiO2," *Journal of Luminescence*, vol. 113, no. 3-4, pp. 229-234, Jun. 2005.

[159] S. P. Withrow, C. W. White, A. Meldrum, J. D. Budai, D. M. Hembree, and J. C. Barbour, "Effects of hydrogen in the annealing environment on photoluminescence from Si nanoparticles in SiO[sub 2]," *Journal of Applied Physics*, vol. 86, no. 1, p. 396, 1999.

[160] U. Serincan, S. Yerci, M. Kulakci, and R. Turan, "Evolution of SiO2 matrix during the formation of Ge and Si nanocrystals by ion implantation," *Nuclear Instruments and Methods in Physics Research Section B: Beam Interactions with Materials and Atoms*, vol. 239, no. 4, pp. 419-425, Oct. 2005.

[161] I. Mihalcescu, J. C. Vial, and R. Romestain, "Absence of Carrier Hopping in Porous Silicon," *Transport*, pp. 13-16, 1998.

[162] K. K. Ng, *Complete Guide to Semiconductor Devices*. New York: McGraw-Hill Inc., 1995.

[163] M. P. Houng, Y. H. Wang, W. J. Chang, and I. Introduction, "Current transport mechanism in trapped oxides: A generalized trap-assisted tunneling model," *Journal of Applied Physics*, vol. 86, no. 3, pp. 3-6, 1999.

[164] S. Fleischer, P. T. Lai, and Y. C. Cheng, "A new method for extracting the trap energy in insulotors," *Journal of Applied Physics*, vol. 73, no. 1, p. 3348, 1993.

[165] S. M. Sze and K. K. Ng, *Physics of Semiconductor Devices*, Third Edit. John Wiley and Sons, Inc., 2007.

[166] T. Matsuda, "Blue electroluminescence from MOS capacitors with Si-implanted SiO2," *Solid-State Electronics*, vol. 48, no. 10-11, pp. 1933-1941, Nov. 2004.

[167] L. X. Yi, J. Heitmann, R. Scholz, and M. Zacharias, “Si rings, Si clusters, and Si nanocrystals—different states of ultrathin SiO[sub x] layers,” *Applied Physics Letters*, vol. 81, no. 22, p. 4248, 2002.

[168] T. Matsuda, H. Takata, M. Kawabe, and T. Ohzone, “Visible Electroluminescence from MOS Capacitors with Si-Implanted Si02 under Dynamic Operation,” *IEEE Transactions on Electron Devices*, vol. 85, no. 11, p. 821, 2001.

[169] M. Sopinskyy and V. Khomchenko, “Electroluminescence in SiOx films and SiOx -film-based systems,” *Current Opinion in Solid State and Materials Science*, vol. 7, no. June, pp. 97-109, 2003.

[170] C. J. Lin and G. R. Lin, “Defect-Enhanced Visible Electroluminescence of Multi-Energy Silicon-Implanted Silicon Dioxide Film,” *IEEE journal of Quantum Electronics*, vol. 41, no. 3, pp. 441-447, 2005.

[171] J. Valenta, N. Lalic, and J. Linnros, “Electroluminescence microscopy and spectroscopy of silicon nanocrystals in thin SiO 2 layers,” *Optical Materials*, vol. 17, pp. 45-50, 2001.

[172] J. Zhang, Y. Ye, X. Tan, and X. Bao, “Voltage-controlled electroluminescence from SiO 2 films containing Ge nanocrystals and its mechanism,” *Applied Physics A: Materials Science and Processing*, vol. 71, pp. 299-303, 2000.

[173] J. M. Mayer, J. A. Davies, and L. Erikson, *Ion Implantation in Semiconductors*, vol. 79, no. 1. New York: Academic, 1970.

[174] T. Gebel, L. Rebohle, J. Sun, W. Skorupa, A. N. Nazarov, and I. Osiyuk, “Correlation of charge trapping and electroluminescence in highly efficient Si-based light emitters,” *Physica E*, vol. 16, pp. 499-504, 2003.

[175] A. G. Imer, S. Yerci, A. S. Alagoz, M. Kulakci, U. Serincan, T. G. Finstad, and R. Turan, “Evolution of Vibrational Modes of SiO2 During the Formation of Ge and Si Nanocrystals by Ion Implantation and Magnetron Sputtering,” *Journal of Nanoscience and Nanotechnology*, vol. 10, no. 1, pp. 525-531, Jan. 2010.

[176] R. Rauea, K. Nieuwesteegb, and W. Busselta, “Saturation by resonant up-conversion in Th-doped phosphors,” *Journal of Luminescence*, vol. 49, no. 48 and 49, pp. 485-488, 1991.

[177] R. M. Kraus, P. G. Lagoudakis, A. L. Rogach, D. V. Talapin, H. Weller, J. M. Lupton, and J. Feldmann, “Room-Temperature Exciton Storage in Elongated Semiconductor Nanocrystals,” *Physical Review Letters*, vol. 98, no. 1, pp. 3-6, Jan. 2007.

[178] T. Nakaoka, S. Kako, and Y. Arakawa, “Unconventional quantum-confined Stark effect in a single GaN quantum dot,” *Physical Review B*, vol. 73, no. 12, pp. 4-6, Mar. 2006.

[179] P. W. Fry, I. E. Itskevich, D. J. Mowbray, M. S. Skolnick, J. J. Finley et al., “Inverted electron-hole alignment in InAs-GaAs self-assembled quantum dots.,” *Physical Review Letters*, vol. 84, no. 4, pp. 733-6, Jan. 2000.

[180] E. Menéndez-Proupin and C. Trallero-Giner, “Electric-field and exciton structure in CdSe nanocrystals,” *Physical Review B*, vol. 69, no. 12, pp. 1-9, Mar. 2004.

[181] J. Seufert, M. Obert, M. Schheibner, N. A. Gippius, G. Backer, A. Forchel, T. Passow, K. Leonardi, and D. Hommel, “Stark effect and polarizability in a single CdSe/ZnSe quantum dot,” *Applied Physics Letters*, vol. 79, no. 7, p. 1033, 2001.

[182] J. Müller, J. M. Lupton, P. G. Lagoudakis, F. Schindler, R. Koeppe, D. V. Talapin, and H. Weller, “Wave function engineering in elongated semiconductor nanocrystals with heterogeneous carrier confinement.,” *Nano letters*, vol. 5, no. 10, pp. 2044-9, Oct. 2005.

[183] S. A. Empedocles, “Quantum-Confined Stark Effect in Single CdSe Nanocrystallite Quantum Dots,” *Science*, vol. 2114, no. 1997, 2012.

[184] R. G. Hunsperger, *Integrated optics: Theory and Technology*, Fifth Edit., vol. 42, no. 3. Springer, 2002.

[185] D. A. B. Miller, “Germanium Quantum Wells for High-Performance Modulators in Silicon Photonics,” *Photonics Spectra*, vol. 83, no. September, pp. 80 - 83, 2007.

[186] M. Cordona, K. L. Shaklee, and F. H. Pollak, “Electroreflectance at a Semiconductor-Electrolyte Interface,” *Physical Review*, vol. 154, no. 3, p. 696, 1967.

[187] M. Chester and P. H. Wendland, “Electroabsorption Spectrum in Silicon,” *Physical Review Letters*, vol. 13, no. 6, p. 193, 1964.

[188] H. K. Rockstad, “Application of Electroabsorption Techniques to the Study of Crystal Particles in Glasses,” *Applied Optics*, vol. 7, no. 5, pp. 759-762, 1968.

[189] Y. Yacoby, “Bulk Measuremnt of the Franz-Keldysh Effect in Si,” *Physical Review*, vol. 142, no. 2, p. 1966, 1965.

[190] A. Frova, P. Handler, F. A. Germano, and D. E. Aspnes, “Electro-Absorption Effects at the Band Edges of Silicon and Germanium,” *Physical Review*, vol. 145, no. 2, p. 575, 1966.

[191] H. Search, C. Journals, A. Contact, M. Iopscience, and I. P. Address, "Electroabsorptive behaviour of semiconductor quantum dots in glass," vol. 631, pp. 6-9, 1990.

[192] D. S. Chemla, T. C. Damen, and D. A. B. Miller, "Electroabsorption by Stark effect on room-temperature excitons in GaAs/GaAlAs multiple quantum well structures," *Applied Physics Letters*, vol. 42, no. 10, p. 864, 1983.

[193] T. T. B. Laboratories and B. Laboratories, "Physical review letters 26," *Physical Review Letters*, vol. 53, no. 22, pp. 2173-2176, 1984.

[194] G. Bastard, E. E. Mendez, L. L. Chang, and L. Esaki, "Variational Calculations on a Quantum Well in an Electric Field," *Physical Review B*, vol. 28, no. 6, p. 3241, 1983.

[195] Y. H. Kuo, Y. K. Lee, Y. Ge, S. Ren, J. E. Roth, T. I. Kamins, D. A. B. Miller, and J. S. Harris, "Quantum-Confined Stark Effect in Ge / SiGe Quantum Wells on Si for Optical Modulators," *IEEE journal of Quantum Electronics*, vol. 12, no. 6, pp. 1503-1513, 2006.

[196] K. Janssens, B. Partoens, and F. Peeters, "Stark shift in single and vertically coupled type-I and type-II quantum dots," *Physical Review B*, vol. 65, no. 23, pp. 2-5, May 2002.

[197] J. Singh, *Electronic and Optoelectronic Properties of Semiconductor Structures*. New York: Cambridge University Press, 2003.

[198] H. Koyama, T. Oguro, and N. Koshida, "Electrical quenching of photoluminescence from porous silicon," *Applied Physics Letters*, vol. 62, no. 24, p. 3177, 1993.

[199] C. Allan, "Saturation porous-silicon," *Physical Review B*, vol. 51, no. 24, pp. 605-613, 1995.

[200] M. Parkinson, S. C. Bayliss, D. T. Clarke, D. Law, and G. Beamson, "An analysis of photoluminescence voltage quenching and band structure of nanoporous silicon," *Thin Solid Films*, vol. 326, no. 1-2, pp. 194-200, Aug. 1998.

[201] S. P. Mcginnis, B. Das, and M. Dobrowolska, "The effect of electric field on the photoluminescence and absorption spectra of porous silicon," *Thin Solid Films*, vol. 365, pp. 1-4, 2000.

[202] T. Takagahara and K. Takeda, "Theory of the quantum confinement effect on excitons in quantum dots of indirect-gap materials," *Physical Review B*, vol. 46, no. 23, pp. 578-581, 1992.

[203] M. N. Islam and S. Kumar, “Influence of surface states on the photoluminescence from silicon nanostructures,” *Journal of Applied Physics*, vol. 93, no. 3, p. 1753, 2003.

[204] G. R. Lin, K.-C. Yu, C.-J. Lin, H.-C. Kuo, and M.-C. Ou-Yang, “Pumping intensity dependent surface charge accumulation and redshifted microphotoluminescence of silicon-implanted quartz,” *Applied Physics Letters*, vol. 85, no. 6, p. 1000, 2004.

[205] B. Kamenev, D. N. Kouvatsos, and A. G. Nassiopoulou, “Influence of a high electric field on the photoluminescence from silicon nanocrystals in SiO 2,” *Materials Science and Engineering C*, vol. 101, pp. 324-328, 2003.

[206] J. Mayandi, T. G. Finstad, a. Thøgersen, S. Foss, U. Serincan, and R. Turan, “Scanning probe measurements on luminescent Si nanoclusters in SiO2 films,” *Thin Solid Films*, vol. 515, no. 16, pp. 6375-6380, Jun. 2007.

[207] Y. Q. Wang, R. Smirani, and G. G. Ross, “The effect of implantation dose on the microstructure of silicon nanocrystals in SiO 2,” *Nanotechnology*, vol. 15, no. 11, pp. 1554-1560, Nov. 2004.

[208] D. A. B. Miller, D. S. Chemla, T. C. Damen, T. H. Wood, C. A. Burrus, A. C. Gossard, and W. Wiegmann, “The Quantum Well Self-Electrooptic Effect Device : Optoelectronics Bistability and Oscillation, and Self-Linearized Modulation,” *IEEE journal of Quantum Electronics*, vol. 21, no. 9, p. 1462, 1985.

[209] H. J. Polland, L. Schultheis, J. Kuhl, E. O. Gobel, and C. W. Tu, “Lifetime Enhancement of Two-Dimensional Excitons by the Quantum-Confined Stark Effect,” *Physical Review Letters*, vol. 55, no. 23, pp. 2610-2613, 1985.

[210] T. Arakawa, Y. Kato, F. Sogawa, and Y. Arakawa, “Pkotoluminescence studies of GaAs quantum wires with quantum confined Stark effect,” *Applied Physics Letters*, vol. 70, no. 5, p. 646, 1997.

[211] J. de Sousa, J. P. Leburton, V. Freire, and E. da Silva, “Intraband absorption and Stark effect in silicon nanocrystals,” *Physical Review B*, vol. 72, no. 15, p. 155438, Oct. 2005.

[212] L.-wang Wang and L. Berkeley, “Calculating the Influence of External Charges on the Photoluminescence of a CdSe Quantum Dot,” *Journal of Physical Chemistry B*, vol. 105, no. 12, pp. 2360-2364, 2001.

[213] A. W. Achtstein, H. Karl, and B. Stritzker, “Electric-field-controlled photoluminescence of CdSe nanocrystal-doped SiO2 on Si,” *Journal of Luminescence*, vol. 121, no. 2, pp. 365-368, Dec. 2006.

[214] L. Pavesi, “Influence of dispersive exciton motion on the recombination dynamics in porous silicon,” *Journal of Applied Physics*, vol. 80, no. 1, p. 216, 1996.

[215] C. Sevik and C. Bulutay, “Auger recombination and carrier multiplication in embedded silicon and germanium nanocrystals,” *Physical Review B*, vol. 77, no. 12, pp. 14-17, Mar. 2008.

[216] H. Yıldırım and C. Bulutay, “Bound-state third-order optical nonlinearities of germanium nanocrystals embedded in a silica host matrix,” *Physical Review B*, vol. 78, no. 11, pp. 1-6, Sep. 2008.

[217] L. W. Wang, A. Franceschetti, and A. Zunger, “Million-Atom Pseudopotential Calculation of G-X Mixing in GaAs /AlAs Superlattices and Quantum Dots,” *Physical Review Letters*, vol. 78, no. 14, pp. 2819-2822, 1997.

[218] H. Fu, “Stark shifts, band-edge transitions, and intrinsic optical dipoles in spherical InP quantum dots under electric fields,” *Physical Review B*, vol. 65, no. 4, pp. 1-5, Jan. 2002.

[219] B. Bhushan, *Springer Handbook of Nanotechnology*, Second Edi. Springer, 2007.

[220] M. Law, J. Goldberger, and P. Yang, “Semiconductor Nanowires and Nanotubes,” *Annual Review of Materials Research*, vol. 34, no. 1, pp. 83-122, Aug. 2004.

[221] S. Barth, F. Hernandez-Ramirez, J. D. Holmes, and A. Romano-Rodriguez, “Synthesis and applications of one-dimensional semiconductors,” *Progress in Materials Science*, vol. 55, no. 6, pp. 563-627, Aug. 2010.

[222] K. Tomioka, T. Tanaka, S. Hara, K. Hiruma, and T. Fukui, “III – V Nanowires on Si Substrate : Selective-Area Growth and Device Applications,” *IEEE Journal of Selected Topics in Quantum Electronics*, vol. 17, no. 4, pp. 1112-1129, 2011.

[223] F. Shen, M. Tan, Z. Wang, M. Yao, Z. Xu, Y. Wu, J. Wang, X. Guo, and T. Zhu, “Integrating silicon nanowire field effect transistor, microfluidics and air sampling techniques for real-time monitoring biological aerosols.,” *Environmental science & technology*, vol. 45, no. 17, pp. 7473-80, Sep. 2011.

[224] A. Heinzig, S. Slesazeck, F. Kreupl, T. Mikolajick, and W. M. Weber, “Reconfigurable silicon nanowire transistors.,” *Nano letters*, vol. 12, no. 1, pp. 119-24, Jan. 2012.

[225] Y. Xiao, C. Meng, P. wang, Y. Ye, H. Yu, S. Wang, F. Gu, L. Dai, and L. Tong, “Single-nanowire single-mode laser.,” *Nano letters*, vol. 11, no. 3, pp. 1122-6, Mar. 2011.

[226] L. C. Chuang, F. G. Sedgwick, R. Chen, W. S. Ko, M. Moewe, K. W. Ng, T. T. D. Tran, and C. C. Hasnain, "GaAs-Based Nanoneedle Light Emitting Diode and Avalanche," *Nano Letters*, pp. 385-390, 2011.

[227] P. Neuzil, C. C. Wong, and J. Reboud, "Electrically controlled giant piezoresistance in silicon nanowires.," *Nano letters*, vol. 10, no. 4, pp. 1248-52, Apr. 2010.

[228] A. Bezryadin and P. M. Goldbart, "Superconducting nanowires fabricated using molecular templates," *Advanced Materials*, vol. 22, no. 10, pp. 1111-21, Mar. 2010.

[229] N. Liu, G. Fang, W. Zeng, H. Long, and X. Zhao, "Giant Enhancement of Field Emission from Selectively Edge Grown ZnO-Carbon Nanotube Heterostructure Arrays via Diminishing the Screen Effect," *The Journal of Physical Chemistry C*, vol. 115, pp. 14377-14385, 2011.

[230] W. U. Huynh, J. J. Dittmer, and a P. Alivisatos, "Hybrid nanorod-polymer solar cells.," *Science (New York, N.Y.)*, vol. 295, no. 5564, pp. 2425-7, Mar. 2002.

[231] S. Iijima, "Helical microtubules of graphitic carbon," *Nature*, vol. 354, p. 56, 1991.

[232] R. G. Treuting and S. M. Arnold, "Orientation habits of metal whiskers," *Acta Metallurgica*, vol. 5, no. 10, p. 598, Dec. 1957.

[233] E. I. Givargizov, "Fundamental aspects of VLS growth," *Journal of Crystal Growth*, vol. 31, pp. 20-30, Mar. 1975.

[234] A. Morales and C. Lieber, "A laser ablation method for the synthesis of crystalline semiconductor nanowires," *Science (New York, N.Y.)*, vol. 279, no. 5348, pp. 208-11, Jan. 1998.

[235] Y. Cui and C. M. Lieber, "Functional nanoscale electronic devices assembled using silicon nanowire building blocks," *Science*, vol. 291, pp. 851-3, Feb. 2001.

[236] A. I. Boukai, Y. Bunimovich, J. Tahir-Kheli, J.-K. Yu, W. a Goddard, and J. R. Heath, "Silicon nanowires as efficient thermoelectric materials.," *Nature*, vol. 451, no. 7175, pp. 168-71, Jan. 2008.

[237] J. Goldberger, A. I. Hochbaum, R. Fan, and P. Yang, "Silicon Vertically Integrated Nanowire Field Effect Transistors," *Nano Letters*, vol. 6, no. 5, pp. 973-977, May 2006.

[238] C. K. Chan, R. N. Patel, M. J. O'Connell, B. a Korgel, and Y. Cui, "Solution-grown silicon nanowires for lithium-ion battery anodes.," *ACS nano*, vol. 4, no. 3, pp. 1443-50, Mar. 2010.

[239] J. Bae, H. Kim, X. M. Zhang, C. H. Dang, Y. Zhang, Y. J. Choi, A. Nurmikko, and Z. L. Wang, "Si nanowire metal-insulator-semiconductor photodetectors as efficient light harvesters.," *Nanotechnology*, vol. 21, no. 9, p. 095502, Mar. 2010.

[240] F. Qian, S. Gradecak, Y. Li, C.-Y. Wen, and C. M. Lieber, "Core/multishell nanowire heterostructures as multicolor, high-efficiency light-emitting diodes.," *Nano letters*, vol. 5, no. 11, pp. 2287-91, Nov. 2005.

[241] Y. Cui, Q. Wei, H. Park, and C. M. Lieber, "Nanowire nanosensors for highly sensitive and selective detection of biological and chemical species.," *Science (New York, N.Y.)*, vol. 293, no. 5533, pp. 1289-92, Aug. 2001.

[242] E. Garnett and P. Yang, "Light trapping in silicon nanowire solar cells.," *Nano letters*, vol. 10, no. 3, pp. 1082-7, Mar. 2010.

[243] B. M. Kayes, H. a. Atwater, and N. S. Lewis, "Comparison of the device physics principles of planar and radial p-n junction nanorod solar cells," *Journal of Applied Physics*, vol. 97, no. 11, p. 114302, 2005.

[244] V. A. Nebol, A. A. Shchetinin, A. A. Dolgachev, and V. V. Korneeva, "Effect of the Nature of the Metal Solvent on the Vapor – Liquid – Solid Growth Rate of Silicon Whiskers," *Inorganic Materials*, vol. 41, no. 12, pp. 1425-1428, 2005.

[245] S. Sharma and M. K. Sunkara, "Direct synthesis of single-crystalline silicon nanowires using molten gallium and silane plasma," *Nanotechnology*, vol. 15, no. 1, pp. 130-134, Jan. 2004.

[246] X. L. Ma, Y. L. Zhu, and Z. Zhang, "Growth orientation of one-dimensional silicon nanowires prepared by thermal evaporation," *Philosophical Magazine Letters*, vol. 82, no. 8, p. 461, 2002.

[247] C. C. Büttner, N. D. Zakharov, E. Pippel, U. Gösele, and P. Werner, "Gold-enhanced oxidation of MBE-grown silicon nanowires," *Semiconductor Science and Technology*, vol. 23, no. 7, p. 075040, Jul. 2008.

[248] W. Seifert, M. Borgstrom, K. Deppert, K. A. Dick, J. Jhansson et al., "Growth of one-dimensional nanostructures in MOVPE," *Journal of Crystal Growth*, vol. 272, no. 1-4, pp. 211-220, Dec. 2004.

[249] J. D. Holmes, "Control of Thickness and Orientation of Solution-Grown Silicon Nanowires," *Science*, vol. 287, no. 5457, pp. 1471-1473, Feb. 2000.

[250] A. M. Morales, "A Laser Ablation Method for the Synthesis of Crystalline Semiconductor Nanowires," *Science*, vol. 279, no. 5348, pp. 208-211, Jan. 1998.

[251] Y. Q. Fu, A. Colli, A. Fasoli, J. K. Luo, A. J. Flewitt, A. C. Ferrari, and W. I. Milne, "Deep reactive ion etching as a tool for nanostructure fabrication," *Journal of Vacuum Science & Technology B: Microelectronics and Nanometer Structures*, vol. 27, no. 3, p. 1520, 2009.

[252] D. Dimova-Malinovska, M. Sendova-Vassileva, N. Tzenov, and M. Kamenova, "Preparation of thin porous silicon layers by stain etching," *Thin Solid Films*, vol. 297, no. 1-2, pp. 9-12, Apr. 1997.

[253] K. Peng, Y. Wu, H. Fang, X. Zhong, Y. Xu, and J. Zhu, "Uniform, axial-orientation alignment of one-dimensional single-crystal silicon nanostructure arrays.," *Angewandte Chemie (International ed. in English)*, vol. 44, no. 18, pp. 2737-42, Apr. 2005.

[254] S. L. Cheng, C. H. Chung, and H. C. Lee, "A Study of the Synthesis, Characterization, and Kinetics of Vertical Silicon Nanowire Arrays on (001)Si Substrates," *Journal of The Electrochemical Society*, vol. 155, no. 11, p. D711, 2008.

[255] C.-Y. Chen, C.-S. Wu, C.-J. Chou, and T.-J. Yen, "Morphological Control of Single-Crystalline Silicon Nanowire Arrays near Room Temperature," *Advanced Materials*, vol. 20, no. 20, pp. 3811-3815, Oct. 2008.

[256] T. Qiu, X. L. Wu, G. G. Siu, and P. K. Chu, "Intergrowth Mechanism of Silicon Nanowires and Silver Dendrites," *Journal of Electronic Materials*, vol. 35, no. 10, pp. 1-6, 2006.

[257] B. Ozdemir, M. Kulakci, R. Turan, and H. E. Unalan, "Effect of electroless etching parameters on the growth and reflection properties of silicon nanowires.," *Nanotechnology*, vol. 22, no. 15, p. 155606, Apr. 2011.

[258] K. Peng, H. Fang, J. Hu, Y. Wu, J. Zhu, Y. Yan, and S. T. Lee, "Metal-particle-induced, highly localized site-specific etching of Si and formation of single-crystalline Si nanowires in aqueous fluoride solution.," *Chemistry : A European Journal*, vol. 12, no. 30, pp. 7942-7, Oct. 2006.

[259] V. Schmidt, J. V. Wittemann, S. Senz, and U. Gösele, "Silicon Nanowires: A Review on Aspects of their Growth and their Electrical Properties," *Advanced Materials*, vol. 21, no. 25-26, pp. 2681-2702, Jul. 2009.

[260] S. H. Kang, B. Pokroy, L. Mahadevan, and J. Aizenberg, "Control of shape and size of nanopillar assembly by adhesion-mediated elastocapillary interaction.," *ACS nano*, vol. 4, no. 11, pp. 6323-31, Nov. 2010.

[261] Z. Huang, N. Geyer, P. Werner, J. de Boor, and U. Gösele, "Metal-assisted chemical etching of silicon: a review.," *Advanced materials (Deerfield Beach, Fla.)*, vol. 23, no. 2, pp. 285-308, Jan. 2011.

[262] S. K. Srivastava, D. Kumar, P. K. Singh, M. Kar, V. Kumar, and M. Husain, “Excellent antireflection properties of vertical silicon nanowire arrays,” *Solar Energy Materials and Solar Cells*, vol. 94, no. 9, pp. 1506-1511, Sep. 2010.

[263] P. Campbell and M. A. Green, “Light Trapping Properties of Pyramidally Textured Surfaces,” *Journal of Applied Physics*, vol. 62, no. 1, pp. 243-249, Aug. 1987.

[264] E. Yablonovitch, “Statistical ray optics,” *Journal of the Optical Society of America*, vol. 72, no. 7, pp. 899-907, 1982.

[265] M. A. Green, J. Zhao, A. Wang, S. R. Wenham, and S. Member, “Very High Efficiency Silicon Solar Cells — Science and Technology,” *IEEE Transactions on Electron Devices*, vol. 46, no. 10, pp. 1940-1947, 1999.

[266] J. Zhao, A. Wang, and M. A. Green, “24 . 5 % E □ ciency Silicon PERT Cells on MCZ Substrates and 24 . 7 % Efficiency PERL Cells on FZ Substrates,” *Progress in Photovoltaics: Research and Applications*, vol. 474, no. 7, pp. 471-474, 1999.

[267] J. Jie, W. Zhang, K. Peng, G. Yuan, C. S. Lee, and S.-T. Lee, “Surface-Dominated Transport Properties of Silicon Nanowires,” *Advanced Functional Materials*, vol. 18, no. 20, pp. 3251-3257, Oct. 2008.

[268] T. Stelzner, M. Pietsch, G. Andrä, F. Falk, E. Ose, and S. Christiansen, “Silicon nanowire-based solar cells.,” *Nanotechnology*, vol. 19, no. 29, p. 295203, Jul. 2008.

[269] A. Blanco, K. Q. Peng, Y. J. Yan, S. P. Gao, J. Zhu, “Synthesis of Large-Area Silicon Nanowire Arrays via Self-Assembly Nanoelectrochemistry,” *Advanced Materials*, vol. 14, no. 16, p. 1164, 2002.

[270] K. Peng, Y. Xu, Y. Wu, Y. Yan, S.-T. Lee, and J. Zhu, “Aligned single-crystalline Si nanowire arrays for photovoltaic applications,” *Small (Weinheim an der Bergstrasse, Germany)*, vol. 1, no. 11, pp. 1062-7, Nov. 2005.

[271] V. Sivakov, G. Andra, A. Gawlik, A. Berger, J. Plentz, F. Falk, and S. H. Christiansen, “Silicon nanowire-based solar cells on glass: synthesis, optical properties, and cell parameters.,” *Nano letters*, vol. 9, no. 4, pp. 1549-54, Apr. 2009.

[272] C. Chen, R. Jia, H. Yue, H. Li, X. Liu, D. Wu, W. Ding, T. Ye, S. Kasai, H. Tamotsu, J. Chu, S. Wang, “Silicon nanowire-array-textured solar cells for photovoltaic application,” *Journal of Applied Physics*, vol. 108, no. 9, p. 094318, 2010.

[273] H. Yue, R. Jia, C. Chen, W. Ding, Y. Meng, D. Wu, D. Wu, W. Chen, X. Liu, Z. Jin, W. Wang, and T. Ye, "Antireflection properties and solar cell application of silicon nanostructures," *Journal of Vacuum Science & Technology B: Microelectronics and Nanometer Structures*, vol. 29, no. 3, p. 031208, 2011.

[274] Y. Dan, K. Seo, K. Takei, J. H. Meza, A. Javey, and K. B. Crozier, "Dramatic reduction of surface recombination by in situ surface passivation of silicon nanowires.," *Nano letters*, vol. 11, no. 6, pp. 2527-32, Jun. 2011.

[275] C. Chen, R. Jia, H. Li, Y. Meng, X. Liu, T. Ye, S. Kasai, H. Tamatsu, N. Wu, S. Wang, and J. Chu, "Electrode-contact enhancement in silicon nanowire-array-textured solar cells," *Applied Physics Letters*, vol. 98, no. 14, p. 143108, 2011.

[276] E. C. Garnett and P. Yang, "Silicon nanowire radial p-n junction solar cells.," *Journal of the American Chemical Society*, vol. 130, no. 29, pp. 9224-5, Jul. 2008.

[277] J.-J. Chao, S.-C. Shiu, S.-C. Hung, and C.-F. Lin, "GaAs nanowire/poly(3,4-ethylenedioxythiophene):poly(styrenesulfonate) hybrid solar cells.," *Nanotechnology*, vol. 21, no. 28, p. 285203, Jul. 2010.

[278] Q. Shu, J. Wei, K. Wang, H. Zhu, Z. Li, Y. Jia, X. Gui, N. Guo, X. Li, C. Ma, and D. Wu, "Hybrid heterojunction and photoelectrochemistry solar cell based on silicon nanowires and double-walled carbon nanotubes.," *Nano letters*, vol. 9, no. 12, pp. 4338-42, Dec. 2009.

[279] B. Ozdemir, M. Kulakci, R. Turan, and H. Emrah Unalan, "Silicon nanowire - poly(3,4-ethylenedioxythiophene)-poly(styrenesulfonate) heterojunction solar cells," *Applied Physics Letters*, vol. 99, no. 11, p. 113510, 2011.

VITA

Author of this work achieved his BS degree in physics in June 2002, and MS degree in physics in September 2005 at METU. Currently, he has studying on nanostructured materials and their electro-optical and photovolataic applications at Center for Solar Energy Research and Applications (GUNAM).

List of publications:

1. M. F. Genisel, U. Md Nizam, Z. Say, M. Kulakci, R. Turan, O. Gulseren and E. Bengu, "Bias in bonding behavior among boron, carbon, and nitrogen atoms in ion implanted a-BN, a-BC, and diamond like carbon film", Journal of Applied Physics **110**, 074906 (2011)

2. B. Ozdemir, M. Kulakci, R Turan and H. E. Unalan, "Silicon nanowire - poly(3,4-ethylenedioxythiophene)-poly(styrenesulfonate) heterojunction solar cells", Applied Physics Letters **99**, 113510 (2011)

3. Y. S. Ocak, M. Kulakci, R. Turan, T. Kilicoglu and O. Gullu, "Analysis of electrical and photoelectrical properties of ZnO/p-InP heterojunction", Journal of Alloys and Compounds **505**, 6631 (2011)

4. B. Ozdemir, M. Kulakci, R. Turan and H. E. Unalan, "Effect of electroless etching parameters on the growth and reflection properties of silicon nanowires", Nanotechnology **22**, 155606 (2011)

5. C. Bulutay, M. Kulakci and R. Turan, "Stark effect, polarizability, and electroabsorption in silicon nanocrystals", Physical Review B **81**, 125333 (2010).

6. A. G. Imer, S. Yerci, A.S. Alagoz, M. Kulakci, U. Serincan, T. G. Finstad and R. Turan, "Evolution of Vibrational Modes of SiO2 During the Formation of

Ge and Si Nanocrystals by Ion Implantation and Magnetron Sputtering", Journal of Nanoscience and Nanotechnology **10**, 525 (2010)

7. Y. S. Ocak, M. Kulakci, T. Kilicoglu, R. Turan and K. Akkılıç, "Current-Voltage and capacitance-voltage characteristics of a Sn/Methylene Blue/p-Si Schottky diode", Synthetic Metals **159,** 1603 (2009)

8. M. Kulakci, U. Serincan, R. Turan and T. G. Finstad, "The quantum confined Stark effect in silicon nanocrystals", Nanotechnology **19,** 455403 (2008)

9. T. Colakoglu, M. Parlak, M. Kulakci and R. Turan, "Effect of boron implantation on the electrical and photoelectrical properties of e-beam deposited Ag-In-Se thin films", Journal of Physics D- Applied Physics **41**, 115308 (2008)

10. S. Yerci, M. Kulakci, U. Serincan, R. Turan, M. Shandalov and Y. Golan, "Formation of Ge Nanocrystals in Al_2O_3 Matrix", Journal of Nanoscience and Nanotechnology **8**, 759 (2008)

11. P. Basa, A. S. Alagoz, T. Lohner, M. Kulakci, R. Turan, K. Nagy and Zs. J. Horvarth, "Electrical and ellipsometry study of sputtered SiO_2 structures with embedded Ge nanocrystals" Applied Surface Science **254,** 3626 (2008)

12. S. Yerci, I. Yildiz, M. Kulakci, U. Serincan, M. Barozzi, M. Bersani ve R. Turan, "Depth profile investigations of silicon nanocrystals formed in sapphire by ion implantation," Journal of Applied Physics, **102**, 024309 (2007)

13. U. Serincan, M. Kulakci, R. Turan, S. Foss ve T. G. Finstad, "Variation of Photoluminescence from Si Nanostructures in SiO_2 Matrix with Si^+ Post Implantation," Nuclear Instruments and Methods in Physics Research B, **254**, 87 (2007)

14. M. Kulakci, U. Serincan ve R. Turan, "Electroluminescence Generated by Metal Oxide Semiconductor Light Emitting Diode (MOS-LED) with Si Nanocrystals Embedded in SiO_2 Layers by Ion Implantation," Semiconductor Science and Technology, **21**, 1527 (2006)

15. U. Serincan, S. Yerci, M. Kulakci ve R. Turan, "Evolution of SiO_2 Matrix During the Formation of Ge and Si Nanocrystals by Ion Implantation," Nuclear Instruments and Methods in Physics Research B, **239**, 419 (2005)

16. S. Yerci, I. Yildiz, A. Seyhan, ," Structural and optical properties of A12O3 with Si and Ge nanocrystals", Materials Research Society Proceedings **958**, 105 (2007)

17. T. Yıldırım, İ. Küçük, M. Kulakci, R. Turan and N. M. Gasanly, " Thermally Stimulated current measurements in N-implanted TlGaSeS layered single crystals" (Under Publication)

18. M. Kulakci, T. Colakoglu, B. Ozdemir, H. E. Unalan, M. Parlak and R. Turan, " Silicon nanowire-silver indium selenide heterojunction diode" (Submitted to Nanoscale)

19. M. Kulakci and R. Turan," Electroluminescence Properties of Tb^{+3} Doped SiO_2 and Si Rich SiO_2 by Sputtering Technique" (Submitted to Journal of Physics D-Applied physics)

20. M. Kulakci, F. Es, B. Ozdemir, H. E. Unalan and R. Turan," Industrial size (156 mm x156 mm) crystal silicon solar cells textured with nanowires by electroless etching", (Under evaluation at Progress in photovoltaics)

21. M. Kulakci, U. Keles, C. Bulutay and R. Turan, "Temperature and Size dependences of Quantum Confined Stark Effect in Si Nanocrystals" (Under Preperation)

22. B. Kaleli, M. Kulakci and R. Turan," Mechanisms of Light Emission from Terbium Ions (Tb^{3+}) Embedded in a Si Rich Silicon Oxide Matrix" (Ready to Submission)

Oral and Poster Presentations:

1. M. Kulakci, F. Es, B. Ozdemir, H. E. Unalan ve R. Turan, "Nanotellerle kaplanmış endüstriyel boyutlarda Kristal silisyum güneş gözeleri" 18. Yoğun Madde Fiziği- Ankara Toplatısı, ODTÜ-Ankara, Kasım (2011)

2. M. Kulakci, F. Es, B. Ozdemir, H. E. Unalan and R. Turan, "Application of Si Nanowires Prepared by a Novel Etching Technique to Standard Crystalline Silicon Solar Cells" PVSEC (26 th European Photovoltaic solar Energy Conference and Exhibition), Hamburg, Almanya, 5-9 Eylül 2011-06-09

3. B. Ozdemir, M. Kulakci, R. Turan and H. E. Unalan, "Hybrid Heterojunction Solar Cells Fabricated by Silicon Nanowires and PEDOT:PSS", PVSEC (26 th European Photovoltaic solar Energy Conference and Exhibition), Hamburg, Almanya, 5-9 Eylül 2011

4. O. Demircioglu, F. Es, M. Kulakci and R.Turan," Effects of Groove Geometry on the efficiency of Buried Contact C-Si Solar Cells", PVSEC (26 th European Photovoltaic solar Energy Conference and Exhibition), Hamburg, Almanya, 5-9 Eylül 2011

5. B. Ozdemir, M. Kulakci, R. Turan and H. E. Unalan, "Silicon Nanowire-PEDOT:PSS Heterojunction Solar cells ", NANO TR 7, Istanbul, 27 Haziran-1 Temmuz 2011

6. B. Ozdemir, M. Kulakci, R. Turan and H. E. Unalan, "Silicon Nanowire-PEDOT:PSS Heterojunction Solar Cells", E-MRS (Europian Materials Research Society) 2011 Spring Meeting, Nice, France, 9-13 Mayıs 2011

7. B. Ozdemir, M. Kulakci, R. Turan and H. E. Unalan, "Fabrication of Silicon Nanowires and Determination of the Process parameters" IMMC (International Metallurgical and Materials Congress), İstanbul, Türkiye, 11-13 Kasım 2010

8. B. Ozdemir, M. Kulakci, R. Turan and H. E. Unalan," Fabrication of Silicon Nanowires and Determination of the Process Parameters", E-MRS (Europian Materials Research Society) 2010 Spring Meeting, Strasbourg, France, 7-11 Haziran 2010

9. B. Ozdemir, M. Kulakci, R. Turan and H. E. Unalan,"Fabrication of Silicon Nanowires and Investıgation of Their Photovoltaic Applications" SOLAR TR 6, Ankara, Turkiye, 29-30 Nisan 2010

10. Y. S. Ocak, M. Kulakcı, T. Kılıçoğlu, R. Turan, G. Topal and K. Akkılıç, " A Novel Organometal Mn Complex for Electrical and Photovoltaic Applications" SOLAR TR 1, Ankara, Türkiye, 29-30 Nisan 2010

11. B. Kaleli, M. Kulakci and R. Turan, "Photoluminescence and Electroluminescence from Tb Doped Silicon Rich SiO_2 Prepared by Magnetron Sputtering" MRS (Material Research Society), Boston, USA, 29 kasım – 2 Aralık 2010

12. U. Keles, C. Bulutay, M. Kulakci and R. Turan, " Stark effect, polarizability and electroabsorption in silicon nanocrystals" ", E-MRS (Europian Materials Research Society) 2010 Spring Meeting, Strousbourg, France, 9-13 Mayıs 2010

13. C. Bulutay, M. Kulakci and R. Turan, " Stark effect, polarizability and electro absorption in nanocrystals", APS (American Physical Society) March Meeting, Portland, Oregon, USA, 15-19 Mart 2010

14. M. Kulakci, C. Bulutay, U. Serincan and R. Turan, "Quantum Confined Stark Effect on Silicon Nanocrystals Embedded in SiO_2 : Computational and Experimental Aspects", ", E-MRS (Europian Materials Research Society) 2009 Spring Meeting, Strasbourg, France, 8-12Haziran 2009

15. M. Kulakci, U. Serincan, C. Bulutay and R. Turan, "Modulation of Light Emission from Si Nanocrystals by Quantum Confined Stark Effect", MRS (Material Research Society), Boston, USA, 1-5 Aralık 2008

16. U. Guler, S. Ozturk, M. Kulakci, S. Canli, R. Turan, "Effect of using thin transparent conductive layer on plasmonic oscillations of nanoparticles fabricated by e-beam lithography," International Conference on Materials for Advanced Technologies 2009, June 28 – July3, 2009, Singapore

17. B. Kaleli, M. Kulakci and R. Turan, "Effect of Annealing Conditions on Light Emission from Terbium Ions (Tb^{3+}) Embedded in a Matrix" NANO TR 5, Anadolu Üniversitesi, Eskişehir, 8-12 Haziran 2009

18. M. Kulakci, U. Serincan, C. Bulutay, T. G. Finstad and R. Turan, "Quantum Confined Stark Effect in silicon Nanocrystals Embedded in SiO_2", Workshop on Nanoelectronics and Nanophotonics, Ilgaz, Türkiye, 26-28 Ocak 2009

19. I. Dogan, M. Kulakci, S. Yerci, A. G. Imer, I. Yildiz, A. Seyhan and R. Turan, "Si, Ge and SiGe Nanocrystals Formed in Transparent Matrices for the Next Generation Solar Cell Applications", International Workshop on Advanced Materials and Devices for Photovoltaic Applications (NANOMAT 2008), Ankara, Türkiye, Nisan 2008

20. R. Turan, M. Kulakci, S. Yerci, I. Doğan, A. G. Imer, I. Yildiz and A. Seyhan, " Si, Ge and SiGe Nanocrystals Embedded in tranparent Matrices for Light Conversion for Solar Cell Applications" EMRS (Material Research Society) Spring Meeting, San Fransisco, CA, USA, Mart 2008

21. A. G. Imer, A. S. Alagoz, A. Seyhan, M. Kulakci and R. Turan, " Effects of hydrogen annealing on the photoluminescence Characteristics of Si nanocrystals produced by ion implantation and magnetron sputtering", International workshop on SEMIconductor NANOstructures (SEMINANO 2007), Bad Honnef, Almanya, Haziran 2007

22. I. Dogan, S. Yerci, I. Yildiz, M. Kulakci, U. Serincan, R. Turan, M. Shandalov and Y. Golan, " Formation and characterisation of silicon and germanium nanocrystals in Al_2O_3 matrix by ion implantation", International workshop on SEMIconductor NANOstructures (SEMINANO 2007), Bad Honnef, Almanya, Haziran 2007

23. M. Kulakci, A. Seyhan, R. Turan and U. Serincan, "Electric Field Dependence of photoluminescence from Si Nanocrystals Embedded in SiO_2 matrix", International workshop on SEMIconductor NANOstructures (SEMINANO 2007), Bad Honnef, Almanya, Haziran 2007

24. A. Seyhan, S. Yerci, M. Kulakci, R. Turan, A. Erbil and A. Aydinli, U. Serincan, R. Turan, M. Shandalov and Y. Golan, "Visible Photoluminescence form Al_2O_3 containing Ge nanocrystals," International workshop on SEMIconductor NANOstructures (SEMINANO 2007), Bad Honnef, Almanya, Haziran 2007

25. A. G. Imer, A. S. Alagoz, A. Seyhan, M. Kulakci and R. Turan, " Photoluminescence Emission from Silicon nanocrystals Embedded in SiO_2: The role of hydrogen", NANO TR 3, Ankara, Türkiye, Haziran 2007

26. S. Yerci, I. Yildiz, A. Seyhan, M. Kulakci, U. Serincan, M. Shandalov, Y. Golan and R. Turan, "Structural and Optical Properties of Al_2O_3 with Si and Ge Nanocrystals," Mater. Res. Soc. Symp. Proc., Vol. 958, *L07-06,* Boston, USA, 2006.

27. M. Kulakci, U. Serincan and R. Turan, "Electroluminescence properties of Si implanted SiO_2 Layers," Proc. the International Conference on Superlattices, Nano-Structures and Nano-Devices, S. 126, İstanbul, Türkiye, 2006

28. M. Kulakci, U. Serincan and R. Turan, "Electroluminescence (EL) Properties of Silicon Implanted SiO_2 on n-type and p-type Silicon Substrates and Mechanisms of EL Emissions," The E-MRS 2006 Spring Meeting, Nice, France, May 29 – June 2, 2006

29. U. Serincan, M. Kulakci and R. Turan, "Luminescence Properties of Ion Irradiated and Annealed Si Nanocrystals in SiO_2 Matrix," The 1st International Workshop on Semiconductor Nanocrystals, *SEMINANO 2005*, Budapest, Hungary, September 10-12, 2005

30. Yerci, S., U. Serincan, A. Aydinli, F. Ay, M. Kulakcı and R. Turan, "Evolution of Si-O-Si stretching mode of SiO_2 during the formation of Ge and Si nanocrystals by ion implantation," Proc. 1st International Workshop on Semiconductor Nanocrystals, SEMINANO 2005, Vol II, 223-226, Budapest, Hungary, 2005

31. U. Serincan, S. Yerci, M. Kulakci, A. Seyhan and R. Turan, "PL and FTIR Analysis of Ge and Si Implanted SiO_2 Layers," The Optical Interconnects 3rd Optoelectronic & Photonic Winter School 2005, Sardagna (Trento), Italy, February 27 – March 4, 2005

32. R. Turan, H. E. Unalan, B. Ozdemir, and M. Kulakcı, "Nanoteknoloji Güneş Enerjisi Dönüşümünde Yeni Ufuklar Açıyor", Bilim ve Teknik Dergisi, TÜBİTAK yayınları, sayı 523, Haziran 2011